The Aerogravity Assist

Combined Atmospheric and Interplanetary Trajectory Optimization.

Iosto Fodde

Aerospace Engineering
Spaceflight
Space Exploration

TU Delft

The Aerogravity Assist

Combined Atmospheric and Interplanetary Trajectory Optimization.

by

Iosto Fodde

to obtain the degree of Master of Science
at the Delft University of Technology,
to be defended publicly on Tuesday November 6, 2018 at 9:30 AM.

Student number:	4283422	
Thesis committee:	Dr. ir. D. Dirkx	TU Delft, supervisor
	Dr. ir. E. Mooij	TU Delft
	Dr. A. Menicucci	TU Delft
	Prof. dr. ir. P.N.A.M. Visser	TU Delft, chairman

An electronic version of this thesis is available at `http://repository.tudelft.nl/`.

TU Delft

Preface

This thesis marks the end of my Aerospace Engineering Master at the TU Delft. The goal of this thesis is mainly to increase the current knowledge on the topic handled in this research project: the aerogravity assist. However, it also serves to show everything that I have learned over the last two years during my time at the TU Delft.

I would like to sincerely thank my supervisor Dr. Dominic Dirkx. Our (often lengthy) weekly meetings have helped me tremendously for my thesis and understanding Tudat, but also your recommendation for the Alpbach Summer School and tips on how to look for possible PhD projects after I graduate have helped me a lot. Furthermore, I would like to thank Erwin Mooij for his help in finding the right research project, and for giving feedback on several problems that I had at the start of my research project.

Finally, I would also like to thank my parents and girlfriend for their support and encouragement during the complete duration of my Master thesis.
Credit cover figure: DARPA.

Iosto Fodde
Delft, October 22, 2018

Contents

List of Symbols

A	Illuminated area.	[m^2]
a	Semi-major axis.	[m]
$\boldsymbol{a}$	To be estimated variables vector.	[-]
atm	Atmospheres (pressure).	[-]
B	Impact parameter.	[m]
CA	Control Action.	[-]
$C(A,B)$	Coverage of Pareto front B compared to A.	[-]
$C^{A/B}$	transformation matrix of frame B to frame A.	[-]
C_D	Drag force coefficient.	[-]
C_L	Lift force coefficient.	[-]
C_{nm}	Spherical Harmonics gravitational constant.	[-]
C_p	Pressure coefficient.	[-]
C_R	Reflectivity coefficient.	[-]
C_r	Crossover rate.	[-]
C_S	Side force coefficient.	[-]
$C_{x/y/z}$	Elementary rotation matrices.	[-]
C_τ	Shear stress pressure coefficient.	[-]
c	Speed of light in vacuum.	[m/s]
c	Chord.	[m]
$\boldsymbol{c}$	Constraint vector.	[-]
c_0	Mass fraction.	[-]
D	Aerodynamic drag force.	[N]
E	Specific energy.	[J/kg]
e	Eccentricity.	[-]
F	Differential weight.	[-]
$\boldsymbol{F}$	Force vector.	[N]
$F(Kn)$	Aerodynamic Bridging function.	[-]
$\boldsymbol{f}$	Fitness function.	[-]
$f(V)$	Radiative heating velocity function.	[-]

G	Universal gravitational constant.	[$m^3\ kg^{-1}\ s^{-2}$]
g	Gravitational acceleration.	[m/s^2]
g_{load}	Mechanical load.	[-]
H	Scale height.	[m]
h	Enthalpy.	[J]
h	Height above surface variable.	[m]
i	Inclination.	[°]
J_n	Spherical harmonics constant.	[-]
Kn	Knudsen number.	[-]
k	Thermal conductivity.	[$kg\ m\ s^{-3}\ K^{-1}$]
k_h	Sutton-Graves heating constant.	[-]
L	Aerodynamic lift force.	[N]
M	Mach number.	[-]
m	Mass variable.	[kg]
$\mathcal{N}_n$	Guidance node.	[-]
n_b	Neighbourhood size.	[-]
n_p	Population size.	[-]
Pr	Prandtl Number.	[-]
P_{nm}	Legendre polynomial.	[-]
p	Pressure.	[kg/m^2]
Q	Collisional operator.	[-]
Q_{stag}	Stagnation point heat load.	[J/cm^2]
q	Heating rate.	[W/cm^2]
q_∞	Dynamic pressure.	[$kg\ m^{-1}\ s^{-2}$]
R	Radius of an object.	[m]
R	Universal gas constant.	[$J\ mol^{-1}\ K^{-1}$]
R_N	Nose radius.	[m]
$\boldsymbol{r}$	Position vector.	[m]
r	Radial distance variable.	[m]
S	Aerodynamic side force.	[N]
S	LSQ error variable.	[-]
S	Non-dominated space of a Pareto front.	[-]
S_i	Spline of section i.	[-]
S_{nm}	Spherical Harmonics gravitational constant.	[-]
S_{ref}	Vehicle reference area.	[m^2]
s	Freestream molecular speed ratio.	[-]
T	Temperature variable.	[K]
t	time variable.	[s]
U	Potential energy.	[J]
u	Argument of latitude.	[°]
V	Velocity variable.	[m/s]

$V(a)$	Covariance matrix of a.	[-]
V_{esc}	Escape velocity.	[m/s]
V_∞	Hyperbolic Excess Velocity.	[m/s]
v	Normalized velocity.	[-]
W	LSQ weight matrix.	[-]
$\boldsymbol{w}$	Weight vector.	[-]
$\boldsymbol{x}$	Optimization population.	[-]
x, y, z	Cartesian position components.	[m]
α	Angle of attack.	[°]
β	sideslip angle.	[°]
Γ	Guidance matrix.	[-]
γ	Flight path angle.	[°]
γ	Specific heat ratio.	[-]
γ_0	Transport parameter.	[-]
Δt	Time-step of simulation.	[s]
δ	Velocity bending angle.	[°]
Θ	Longitude.	[°]
θ	Atmospheric bending angle.	[°]
θ_p	Perigee bending angle.	[°]
λ	Weight vector.	[-]
μ	Planetary gravitational parameter.	[$m^3\ s^{-2}$]
ρ	Density.	[kg/m^3]
σ	Bank angle.	[°]
σ	Momentum accommodation parameter.	[-]
σ_p	Collisional diameter particle.	[m^2]
τ	Shear stress pressure.	[N/m^2]
χ	Heading angle.	[°]
Φ	Solar flux.	[W/m^2]
ϕ	Latitude.	[°]
Ω	Population space.	[-]
ω	Rotational rate.	[°/s]
$-$	Incoming indication superscript.	[-]
$+$	Outgoing indication superscript.	[-]

List of Abbreviations

AGA	Aerogravity Assist.
AU	Astronomical Unit.
com	centre of mass.
DP	Dormand-Prince integrator.
DSMC	Direct Simulation Monte Carlo.
EMCD	ESA Mars Climate Database.
EOM	Equations of motion.
ESA	European Space Agency.
FMF	Free Molecular Flow.
GA	Gravity Assist.
GRAM	Global Reference Atmospheric Model.
GTOP	Global Trajectory Optimization Problems.
GUACA	Global Upper Air Climate Atlas.
HTV	Hypersonic Test Vehicle.
IHS	Improved Harmony Search.
LSQ	Least Squared fitting.
lb	Lower bound.
MAP	Middle Atmosphere Program.
MER	Mars Exploration Rover.
MET	Marshall Engineering Thermosphere.
MEX	Mars Express.
MGCM	Mars Global Circulation Model.
MGS	Mars Global Surveyor.
MJD2000	Modified Julian Date 2000.
MN	Modified Newtonian.
MO	Mars Odyssey

MOEA/D	Multi-Objective Evolutionary Algorithm based on Decomposition.
MRO	Mars Reconnaissance Orbiter.
MSL	Mars Science Laboratory.
MTGCM	Mars Thermospheric General Circulation Model.
NASA	National Aeronautics and Space Administration.
NGA	National Geospatial-Intelligence Agency.
NRL	Naval Research Laboratory.
NSGA-II	Non-dominated Sorting Genetic Algorithm.
PVO	Pioneer Venus Probes and Orbiter
RAAN	Right Ascension of the Ascending Node.
RK	Runge-Kutta integrator.
RKF	Runge-Kutta-Fehlberg.
SOI	Sphere of influence.
SPARTA	Stochastic Parallel Rarefied-gas Time-accurate Analyzer.
TOF	Time-Of-Flight.
TPS	Thermal Protection System.
TRL	Technological Readiness Level.
Tudat	TU Delft Astrodynamics Toolbox.
UV	Ultraviolet.
ub	Upper bound.
VEX	Venus Express.
VeRa	Venus express Radio science experiment.
VIRA	Venus International Reference Atmosphere.
VLBI	Very Long Baseline Interferometry.
VTC	Variable Transpiration Cooling.

Abstract

Currently one of the major drawbacks of interplanetary travel is the cost of these types of missions. Mission to extra-terrestrial bodies require a large amount of propellant to complete, which often takes up a large part of the mass budget of the spacecraft. This requires larger launchers to be used to get the spacecraft into the required orbit, which increases the cost of these missions. An often used method to decrease the propellant used during an interplanetary mission is the gravity assist. The gravity assist uses the gravitational influence of a planetary body to increase its heliocentric velocity. This is done by exchanging some of the planets momentum as it orbits the Sun to the spacecraft. The increase in velocity is limited by several factors: the gravitational influence of the body, the closest distance possible between the body and the spacecraft, and the orientation of the planetary bodies relative to each other. A new method has been proposed by McRonald and Randolph [1990] called the aerogravity assist, which improves upon the gravity assist by increasing the angle over which the spacecraft can turn using the aerodynamic forces it experiences while travelling through the atmosphere of the planetary body. This increase in the velocity bending angle increases the heliocentric velocity compared to the gravity assist, and also allows for changes in inclination of the interplanetary orbit using less propellant. This report investigates both the atmospheric and interplanetary trajectory of the aerogravity assist, and combines them to understand the benefit of the aerogravity assist for interplanetary trajectories.

A modular simulation environment is designed using the TU Delft Astrodynamics Toolbox to simulate the atmospheric trajectory of the aerogravity assist. This simulator allows the selection of different types of acceleration and environment models. The waverider is selected to be the vehicle used during the aerogravity assist, as it is able to obtain high lift-over-drag ratios which reduce the drag losses during the atmospheric section of the maneuver. The specific aerodynamic characteristics and heating models of the selected vehicle are evaluated and incorporated into the simulator. From this simulation environment, the optimal atmospheric trajectories were investigated using an optimization algorithm. It was found that this specific problem is extremely sensitive to the selected optimization algorithm, the tuning parameters of the optimization algorithm, and the objecive and decision variables that are used. The MOEA/D algorithm was selected to find the optimal atmospheric trajectories for Mars, Earth, and Venus, where the objective variables were chosen to be the atmospheric bending angle and the incoming and out-going inclination difference. It was found that using the angle-of-attack and bank angle as control variables, an atmospheric bending angle of 120.5 degrees and an inclination difference of 0.2 degrees could be obtained at Mars. Using the control action instead of the inclination difference as objective variable at Mars showed that the atmospheric bending could be increased to 151.2 degrees while maintaining an inclination difference of below 3 degrees, and smoothed the trajectory in the process. For Earth and Venus the same optimization scheme was employed. They were able to obtain atmospheric bending angles between 70 and 50 degrees, while obtaining inclination differences below 1.5 degrees. For Venus, the heat load was also optimized instead of the inclination difference and it was found that the peak heat flux decreased by around 1000 W/cm^2, while decreasing the atmospheric bending angle by around 10 degrees.

A mission planner was designed to be able to investigate the effect of the aerogravity assist on interplanetary trajectories. To increase the accuracy of this mission planner, the numerically found atmospheric trajectories are used to determine the possible interplanetary trajectories. Pareto fronts were created for Mars, Earth, and Venus for a range of incoming velocities that showed the possible velocity bending angles and outgoing velocities that can be achieved using an aerogravity assist. These Pareto fronts were then implemented in the mission planner to determine the influence of the AGA on an interplanetary trajectory. Several different interplanetary trajectories were investigated using both gravity and aerogravity assists. It was found that due to the fact that for Earth and Venus higher velocities are needed to travel through the atmosphere, the aerogravity assist would lose too much velocity and thus not improve upon the gravity assist. However, for Mars an increase was found of 4 km/s compared to the gravity assist for a trajectory to Saturn using fly-by's at Mars and Jupiter. Taking into account the extra mass of the thermal protection system, the decrease of mass was found to be around 60 percent, which could be used to lower the cost of the launcher or increase the scientific output of the mission by adding instruments to the payload.

1 Introduction

1.1. Background

In the field of space exploration travelling to other solar system bodies to investigate their properties has been an important goal for many years. These bodies can tell us more on important scientific topics such as: the origin of life [Ehrenfreund and Charnley, 2000], where the water on Earth originates from [Altwegg et al., 2015], how the solar system evolved over time [Porco, 2006], and many others. Furthermore, technological advances that come along with these interplanetary missions not only benefit the space industry, but also everyday life on Earth[1]. The private sector is now also getting involved in travelling to extra-terrestrial bodies, as some companies enter the field of asteroid mining[2] or space tourism[3]. These activities all require physical exploration of the body, as remote sensing is not able to reach the accuracy of having instruments, or humans, on the body itself.

There are several methods to reach extra-terrestrial bodies. The simplest method, which has been used extensively in the past, is the high thrust impulsive maneuver. This method uses an engine to deliver a high amount of thrust for a short period of time to reach an interplanetary transfer orbit towards the target body. This method can only be used to reach bodies that are close to Earth and in a similar orbit, e.g. Mars, Venus, or the Moon. Reaching bodies that are further away requires a large amount of propellant, which takes up mass and thus requires a larger (more expensive) launch vehicle. There are other options like low thrust trajectories [Breakwell and Rauch, 1966], which use a continuous low thrust maneuver to steer the spacecraft to the target body. This method shows a lot of promise; however, the high power requirements when a spacecraft is far away from the Sun limits the possibilities as larger and more efficient solar panels are required. Another method is the solar sail [Leipold et al., 2003], which uses the momentum exchange of photons originating from the Sun to propel the spacecraft. This method, however, is not as widely used as other methods and requires extensive research and testing before it can be used.

A method that is currently frequently used to reach bodies that are further away is the gravity assist [Battin, 1959]. When a spacecraft, on a hyperbolic trajectory, makes a close approach with a large body an exchange of momentum occurs between the two bodies. In the reference frame of the larger body, the spacecraft enters the gravitational sphere of influence while accelerating towards the body and exits it again while decelerating. No change in velocity has occurred from the stand point of the large body. However, if observed from the Sun's reference frame, i.e. the heliocentric or ecliptic reference frame, the spacecraft does experience a change in velocity due to the fact that the larger body is also moving in an orbit around the Sun. The velocity gain of the spacecraft is proportional to the amount over which the velocity vector is turned during its encounter with the larger body. To increase the heliocentric velocity of the spacecraft it approaches behind the body, and to decrease the heliocentric velocity (to move towards the Sun) the spacecraft needs to approach the body from the front.

An analogy that can help understand the gravity assist is that of a ball bouncing of the front of a train. Imagine a ball being thrown from a train station at 30 km/h towards a train moving at 50 km/h in the direction

[1] `https://www.nasa.gov/sites/default/files/files/Benefits-Stemming-from-Space-Exploration-2013-TAGGED.pdf`, Benefits Stemming from Space Exploration, ISECG, September 2013, accessed: October 22, 2018

[2] `https://www.planetaryresources.com/`, Planetary Resources, accessed: October 22, 2018

[3] `https://www.spacex.com`, SpaceX, accessed: October 22, 2018

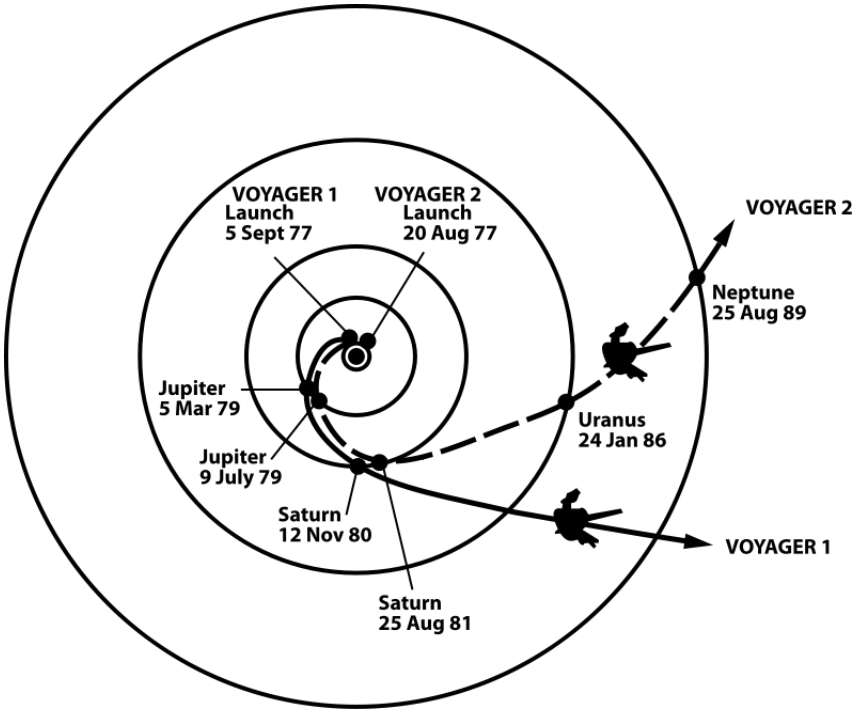

Figure 1.1: The paths of both Voyager mission through the Solar System. Courtesy of NASA.

of the train station. The train driver will see the ball moving towards the train at 80 km/h, and see the ball bounce off the train again at 80 km/h. However, the people at the train station will see the ball leave the train station at 30 km/h, and see the bounce ball off the train (assuming no energy loss) with 130 km/h (the 80 km/h of the ball bouncing in the trains reference frame, and the 50 km/h of the trains movement combined), which is a 100 km/h increase. In this analogy the train is the large planetary body, the ball is the spacecraft, and the train station is the Sun.

There are many missions that have used (multiple) gravity assists to reach the target body. One example is the Rosetta mission [Villefranche et al., 1997], which used two gravity assists around Earth and one gravity assist around Mars to reach the comet 67p/Churyumov-Gerasimenko. A more complex example is that of Voyager 2, which performed gravity assist around Jupiter, Saturn, Uranus, and Neptune to escape the gravitational influence of the Sun (see figure 1.1).

A problem of the gravity assist is the limitation in the possible velocity bending angle. The velocity bending angle determines the velocity increase of the spacecraft and is proportional to the gravitational influence of the large body and the closest distance between the spacecraft and the planetary body. The gravitational influence is set by the body that is used for the gravity assist and the spacecraft-body separation is limited due to several factors. One is the environment of the larger body, which could cause damage to the spacecraft (e.g. electronics could be damaged due to harsh radiation environments at Jupiter), or negatively affect the velocity of the spacecraft (e.g. drag of the atmosphere when this is not desired). This bending angle limitation is the main drawback of the gravity assist, as it limits the velocity gain, and requires very specific configurations of planets. For example, Voyager 2's trajectory (shown in figure 1.1), called "the Grand Tour", allowed the use of several gas giants for gravity assists. However, this will only be possible again in around 200 years [Flandro, 1966].

These limitations led to the development of a new maneuver called the aerogravity assist by McRonald and Randolph [1990]. This maneuver works using the same principle of the gravity assist. However, it uses the atmosphere of the body to increase the velocity bending angle of the spacecraft. Using the aerodynamics of the vehicle, it counteracts the centrifugal force that is trying to move the vehicle away from the body by pointing the lift vector towards the center of the body. This allows the vehicle to turn over a larger angle compared to a gravity assist. The drag experienced when flying through the atmosphere needs to be limited as this can diminish the performance of the maneuver if it outweighs the gain in velocity due to the bending angle. Furthermore, the velocity difference between the body, and the spacecraft that is on a hyperbolic orbit is extremely large, thus the heating that occurs during atmospheric flight can be a large problem for the design

of the vehicle.

The aerogravity assist belongs to a class of maneuvers called the aero-assisted maneuvers. These maneuvers use the atmosphere of a planet to alter the orbit of the spacecraft. One of these maneuvers is called aerobraking, and uses the atmosphere to lower the apoapsis of the orbit [Spencer and Tolson, 2007]. When arriving at an orbit around the planet, the spacecraft can enter the atmosphere at periapsis and use the drag experienced during atmospheric entry to change the height at the point furthest from the planet, which is called the apoapsis. This maneuver is more efficient then using an impulsive thrust to lower the apoapsis, but it does require the spacecraft to have systems in place that can overcome the high mechanical loads and the heating that occurs during entry of the atmosphere. Several missions have used the aerobraking maneuver [Spencer and Tolson, 2007]. The Magellan mission used aerobraking successfully at Venus, where it performed 730 atmospheric passes, and saved 1.2 km/s in ΔV. Additionally, the Mars Global Surveyor (MGS), and the Mars Reconnaissance Orbiter (MRO) both used aerobraking to reach their desired scientific orbit around Mars. The other aero-assisted maneuver is called an aerocapture [Spilker and R., 2005]. This maneuver uses the atmosphere of a planet to change the orbit of the spacecraft from a hyperbolic one, to an elliptical orbit (changing from an interplanetary orbit to an orbit around the target planet). This maneuver has not been performed yet as the mechanical and heat loads are significantly higher then for aerobraking, thus extensive research and development on trajectory and subsystem analyses needs to be performed first.

The vehicle required for the aerogravity assist has to have several capabilities that previously used space vehicles did not posses. Gliding at high altitudes requires the vehicle to generate a significant amount of lift in low density conditions [Huang et al., 2011]. As the speeds at these altitudes tend to be high, the shape of the vehicle should also minimize the drag experienced at these high velocities. These types of vehicles have been studied extensively as they could allow the development of hypersonic planes and re-usable space launch capabilities (see e.g. Nonweiler [1959], Tincher and Burnett [1994], and McClinton et al. [2005]). In recent years several test flights of these hypersonic vehicle have been performed in combination with aero-breathing propulsion [McClinton et al., 2005]. The X-43 vehicle is a NASA project that was designed to perform hypersonic research and test several different aero-breathing propulsion systems [Voland et al., 2006]. It showed to be able to fly at a peak Mach number of 7 and keep within the allowable constraints. Another flight tested vehicle is the Hypersonic Test Vehicle 2 (HTV-2) [Walker, 2008]. The HTV-2 test vehicle was designed by DARPA to investigate the capabilities of a hypersonic glider to reach any location on Earth within one hour. The design of a vehicle specific for an aerogravity assist has only been performed in theory (see e.g. Anderson et al. [1991] and Armellin et al. [2007]).

Due to its complexity and risks, the aerogravity assist has not undergone a lot of research and testing. McRonald and Randolph [1990] and Anderson et al. [1991] developed simple analytical models for the atmospheric flight and vehicles capable of performing the aerogravity assist. Combining these analytical approximations with interplanetary flight was done by Bonfiglio et al. [2000], Sims et al. [2000], and Henning et al. [2014]. Besides the general research done on interplanetary flight, Lohar et al. [1994] and Edelman and Longuski [2017] focused more on finding optimal atmospheric trajectories using several analytical approaches. Additionally, Armellin et al. [2007] developed a method to optimize the vehicle shape together with the atmospheric trajectory of the vehicle. More recently, Lyons et al. [2008] and Casoliva et al. [2008] investigated guidance and control strategies for atmospheric flight during an aerogravity assist. This thesis will use the work of a previous Master thesis performed at the TU Delft Astrodynamics and Space Missions department by Hess [2016] on using genetic algorithms and node control to find optimal atmospheric trajectories for an aerogravity assist at Mars and Jupiter. What is missing from the current state of the art, is the design of a mission planner that uses these accurate, numerically computed, atmospheric trajectories to design possible interplanetary trajectories using the aerogravity assist. This will give more accurate performance measures for the aerogravity assist, and allow more specific research to be done on key problem areas for the aerogravity assist. Furthermore, the investigation of atmospheric trajectories has previously been limited to mainly Mars using limited control and optimization strategies. This research project will build an accurate aerogravity assist mission planner, and do a full investigation on possible atmospheric trajectories at Mars, Earth, and Venus using various optimization strategies.

1.2. Research Goals

This thesis tries to answer a basic question related to the aerogravity assist:

How much does the aerogravity assist improve the performance of interplanetary trajectories compared to a gravity assist?

Answering this question will push the knowledge of this maneuver even further by improving the state of the art on several different levels. To be able to do this, several research goals have been made that, if achieved, can answer the main research question stated before. These research goals are stated here:

1. Build a simulation environment that can simulate the trajectory of a specific vehicle through the atmospheres of several different planets.
2. Build a mission planner that can simulate a specific interplanetary trajectory using both gravity assists and aerogravity assists.
3. Find optimal atmospheric trajectories for an aerogravity assist and use them to find optimal interplanetary trajectories.
4. Compare the optimal interplanetary trajectories using only gravity assists with optimal trajectories that use the aerogravity assist.

Achieving the first goal allows for a tool that can be used in the search for optimal trajectories. Previous research has used several assumptions to create a set of analytical equations that describe the motion of the vehicle through the atmosphere (see e.g. Lohar et al. [1996] and Sims et al. [2000]). The simulator will allow for more realistic models to be implemented. These more accurate models can then be used to compare the results of the simplified equations with. Furthermore, it allows several applications that require a higher accuracy (e.g. sensitivity analyses and guidance algorithm testing) to be performed. Finally, it can be used together with numerical optimization algorithms to find different kinds of optimal trajectories. Part of this goal is designing a realistic vehicle to be used in the simulation. An accurate aerodynamic and heating model can be used to get more information on the feasibility of the aerogravity assist. One sub-goal is to show that using the set-up developed in this thesis, no artificial increase in reference area is needed for the vehicle to successfully find AGA trajectories (as was needed in Hess [2016]). The purpose of goal two is similar to the first goal, as it will allow for the determination of optimal interplanetary trajectories. This mission planner has to be able to use both gravity assists and aerogravity assists as these types of maneuvers need to be compared with each other. The challenge in this goal is to realistically implement the aerogravity assist into the interplanetary trajectory, as this will give insight into the possibilities when using an aerogravity assist. The third and fourth goal will take the tools developed for the first two goals, and use them to answer the main research question.

1.3. Outline

Chapter 2 will describe the flight dynamics of the vehicle, discussing the reference frames needed to express all necessary quantities, the setup of the equations of motion for the vehicle, the relevant models needed to describe the different forces acting on the vehicle, the models detailing the environments through which the vehicle moves, and the simulation of the guidance and control system that is responsible for steering the vehicle through the atmosphere. The aerodynamics of the vehicle when it travels through the atmosphere are one of the most important parts of the aerogravity assist to understand. Chapter 3 discusses the relevant flow regimes in which the aerodynamics need to be modelled, how to model the aerodynamics, which vehicle type can be used in an aerogravity assist, and the heating of the vehicle that exists through the interaction of the airflow with the vehicle. The different numerical methods that are needed to simulate the aerogravity assist are discussed in chapter 4. This chapter goes through the integrators that are needed to solve the equations of motion, different interpolation methods, the least squares fitting procedure that is needed to find a function that approximates a data-set, and the optimization algorithms that will create the optimal trajectories. Chapter 5 goes over how to design the simulator, using everything that has been discussed in the previous chapters. It then also verifies that every module of the simulator works as expected. Chapter 6 discusses the theory of interplanetary flight, how to develop a mission planner that can simulate interplanetary trajectories, and how to use the atmospheric trajectory simulator to incorporate the aerogravity assist in the interplanetary mission planner. Using the theory and setup discussed in the previous chapters, the results for the optimal

atmospheric trajectories are discussed in chapter 7. This chapter first discusses the possible parameters that can be used to construct the optimal trajectories, it compares the performance of the different optimization algorithms, and then discusses the found trajectories. Chapter 8 discusses the results for the implementation of the atmospheric trajectories into the mission planner, and the optimal interplanetary trajectories that are created using both gravity assists and aerogravity assists. Finally, chapter 9 goes over all the goals stated in section 1.2, and discusses the conclusions that can be taken from them using all the previous chapters in this thesis. Afterwards, a few recommendations are given for future research projects on the aerogravity assist.

2

Flight Dynamics

The aerogravity assist (AGA) is a complex maneuver due to the variety of environments the spacecraft experiences and the systems that are required to handle them. First, the spacecraft approaches the planet at an altitude where there are no significant atmospheric effects and thus the gravitational influence of the central body will be the main force acting on the spacecraft. The spacecraft then enters the top layers of the atmosphere, where the air is relatively thin. To model the motion of the spacecraft at these altitudes, a combination of astrodynamics and aerodynamics is required. Gradually the air becomes thicker and the dominant forces acting on the vehicle are aerodynamic of nature. After the spacecraft has flown at the lowest altitude, the spacecraft goes through all of the different environments again until it exits the sphere of influence of the planet. To be able to successfully execute an AGA, one needs to be able to accurately describe all of the dynamics and environments and know where the uncertainties are in these models. This will be the subject of the coming chapter.

First, in section 2.1 the different reference frames that will be used to define the various forces will be discussed. After these frames are defined, the basic equations of motion are set up in section 2.2. The various components of the equations of motion discussed in section 2.2 will then be discussed individually in more detail in section 2.3. In section 2.4, the environment models that are needed to calculate the accelerations acting on the vehicle are discussed, and compared with each other. Finally, section 2.5 describes the method by which the control and guidance system will be simulated.

2.1. Reference Frames

All forces and coordinates are expressed relative to a specific reference frame. These parameters may look different, and have different values, in different reference frames. Thus it is important to understand how these reference frames are defined and how one can switch between the different reference frames. This section will first list all the different reference frames that are used in this research project. Afterwards, the most important reference frame transformations are discussed in 2.1.1. All of the reference frames discussed hereafter are adapted from Mooij [1994].

Ecliptic reference frame This frame has its origin at the barycenter of the Solar System with its x-axis pointing to the position of the mean equinox at J2000 (January 1st, at 12 hrs), its y-axis in Earth's orbital plane perpendicular to the x-axis, and the z-axis completing the right-handed orthogonal frame. This reference frame can be used to determine the heliocentric position of the spacecraft and planets.

Inertial planetocentric frame The origin is defined to be at the center of the central body the spacecraft is orbiting, with its z-axis pointing towards the north of the body aligned with the rotation axis of the body. The x-axis points towards zero longitude at J2000, and the y-axis completes the right-handed orthogonal frame.

Non-inertial/Rotating planetocentric frame This frame is the same as the inertial planetocentric frame, but now the x- and y-axis rotate with the central body. The x-axis points towards zero longitude in the equatorial plane and the y-axis completing the right-handed orthogonal frame. With this frame it is possible to define the state with respect to the surface of the body.

Vertical frame The centre of the frame lies at the centre of mass (com) of the spacecraft, with the z-axis pointing towards the com of the central body, the x-axis towards the north, and the y-axis completing the right-handed orthogonal frame. This reference frame allows us to use more intuitive variables. See figure 2.1.

Body-fixed reference frame The centre of the frame is again at the com of the vehicle, but now with the x-axis in the plane of symmetry of the vehicle, pointing towards the front of the vehicle. The z-axis is also in the plane of symmetry of the vehicle pointing downwards. And the y-axis completes the right-handed orthogonal frame. See figure 2.3.

Aerodynamic reference frame Also with the centre at the com of the vehicle, but now with the x-axis pointing towards the direction of the airspeed, the z-axis in the opposite direction of the lift vector, and the y-axis completing the right-handed orthogonal frame. This frame, in combination with the body-fixed framem, allows us to describe the state with respect to the free-stream flow. See figure 2.2.

Trajectory reference frame The centre of this frame is at the com of the vehicle. The x-axis points towards the direction of the airspeed, the z-axis lies in the vertical plane and points towards the surface, and the y-axis completes the right-handed orthogonal frame. See figure 2.2 and 2.1.

2.1.1. Frame Transformations

In this section the transformation matrices are given that can be used to transform parameters from one frame to another. These matrices are all orthonormal, which leads to the following identity:

$$[C^{A/B}]^{-1} = [C^{A/B}]^T = C^{B/A} \tag{2.1}$$

where $C^{A/B}$ is the transformation matrix of frame B to frame A. Thus, if a transformation matrix is known that can transform parameters from frame B to frame A, the inverse transformation (frame A to frame B) can also be derived by taking the transpose of the known transformation matrix.

Another relation that holds for transformation matrices is the following:

$$C^{A/C} = C^{A/B} C^{B/C} \tag{2.2}$$

This means that any transformation can be done using intermediate transformation matrices.

All of the transformation matrices given in here can be derived using one or more of the following elementary rotation matrices:

$$C_x = \begin{bmatrix} 1 & 0 & 0 \\ 0 & \cos\theta & -\sin\theta \\ 0 & \sin\theta & \cos\theta \end{bmatrix} \tag{2.3}$$

$$C_y = \begin{bmatrix} \cos\theta & 0 & \sin\theta \\ 0 & 1 & 0 \\ -\sin\theta & 0 & \cos\theta \end{bmatrix} \tag{2.4}$$

$$C_z = \begin{bmatrix} \cos\theta & \sin\theta & 0 \\ -\sin\theta & \cos\theta & 0 \\ 0 & 0 & 1 \end{bmatrix} \tag{2.5}$$

where the subscript of each matrix indicates around which axis the rotation takes place (a rotation over an angle of θ). Using successive elementary rotations, the reference frame transformations below can be derived [Mooij, 1994].

Rotating planetocentric to Inertial planetocentric frame For this transformation only the rotation rate of the planet is needed, ω, and the time since the two frames coincided, t. The matrix is given by:

$$C^{I/R} = C_z(-\omega_p t) = \begin{bmatrix} \cos\omega_p t & -\sin\omega_p t & 0 \\ \sin\omega_p t & \cos\omega_p t & 0 \\ 0 & 0 & 1 \end{bmatrix} \tag{2.6}$$

Trajectory to Vertical reference frame For this transformation the flight path angle γ is needed and the heading angle, χ (see figure 2.1):

$$C^{V/T} = C_z(-\chi)C_y(-\gamma) = \begin{bmatrix} \cos\chi\cos\gamma & -\sin\chi & \cos\chi\sin\gamma \\ \sin\chi\cos\gamma & \cos\chi & \sin\chi\sin\gamma \\ -\sin\gamma & 0 & \cos\gamma \end{bmatrix} \tag{2.7}$$

Aerodynamic to Trajectory reference frame For this transformation the bank angle with respect to the airspeed is needed, σ (see figure 2.2):

$$C^{T/A} = C_x(\sigma) = \begin{bmatrix} 1 & 0 & 0 \\ 0 & \cos\sigma & \sin\sigma \\ 0 & -\sin\sigma & \cos\sigma \end{bmatrix} \tag{2.8}$$

Body to Aerodynamic reference frame This transformation matrix uses the two aerodynamic angles: the angle of attack α and the sideslip angle β (see figure 2.3):

$$C^{A/B} = C_z(\beta)C_y(-\alpha) \begin{bmatrix} \cos\alpha\cos\beta & \sin\beta & \sin\alpha\cos\beta \\ -\cos\alpha\sin\beta & \cos\beta & \sin\alpha\sin\beta \\ -\sin\alpha & 0 & \cos\alpha \end{bmatrix} \tag{2.9}$$

More rotation matrices exist that transform between all the various reference frames, the ones mentioned here are the most important ones and if other transformations are needed, they can be found in Mooij [1994].

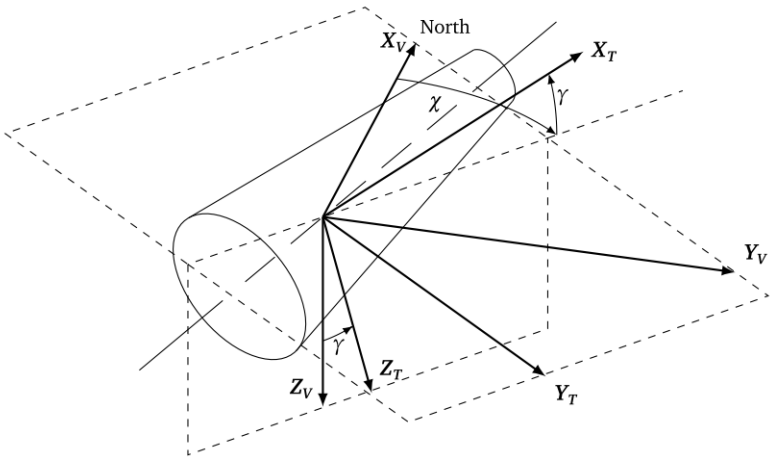

Figure 2.1: The trajectory reference frame (subscript T) and the vertical reference frame (subscript V) with the angles representing rotations between them. Adapted from Mooij [1994].

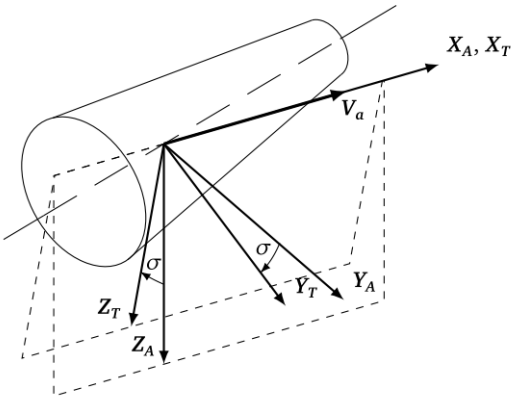

Figure 2.2: The aerodynamic reference frame (subscript A) and the trajectory reference frame (subscript T) with the angles representing rotations between them. Adapted from Mooij [1994].

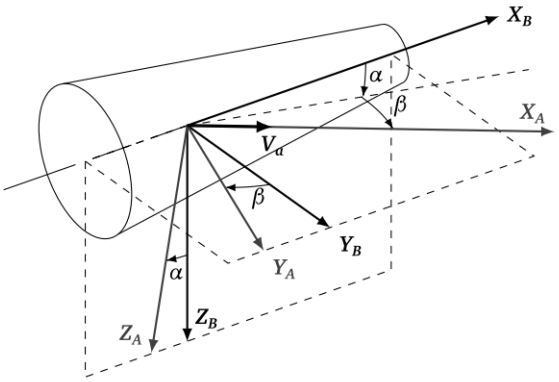

Figure 2.3: The body-fixed reference frame (subscript B) and the aerodynamic reference frame (subscript AV) with the angles representing rotations between them. Adapted from Mooij [1994].

2.2. Equations of Motion

The equations of motion are a set of differential equations that describe the dynamics of the spacecraft as it performs the AGA. The simulator will construct these equations from the user defined settings and solve them using a numerical integrator. This section will describe the set-up of these equations, whereas section 2.3 will discuss the possible acceleration models from which the equations of motion are built. Each simulation can differ from other simulations by selecting different acceleration models that will be part of the equations of motion. The selection of acceleration model can increase the accuracy of the simulation, but also the runtime. Thus depending on the purpose of each simulation, different acceleration models are chosen.

It is important to note that this research project will only consider the translational motion of the spacecraft. The torques acting on the vehicle and the control forces necessary to correct for them are not in the scope of this thesis and will need to be investigated in another report. The way in which several rotational parameters will be implemented into the simulation is discussed in section 2.5.

A simple model can be used to set up a set of analytic equations of motion, this is done in Mooij [1994]

and shown here:

$$\frac{dr}{dt} = V\sin\gamma \tag{2.10}$$

$$\frac{d\Theta}{dt} = \frac{V\cos\gamma\sin\chi}{r\cos\phi} \tag{2.11}$$

$$\frac{d\phi}{dt} = \frac{V\cos\gamma\sin\chi}{r} \tag{2.12}$$

$$\frac{dV}{dt} = -\frac{D(\alpha)}{m} - g\sin\gamma + \omega_p^2 r\cos\phi(\sin\gamma\cos\phi - \cos\gamma\sin\phi\cos\chi) \tag{2.13}$$

$$\frac{d\gamma}{dt} = \frac{1}{V}\left[\frac{L(\alpha)}{m}\cos\sigma - \left(g - \frac{V^2}{r}\right)\cos\gamma\right] + 2\omega_p\cos\phi\sin\chi + \frac{\omega_p^2}{V}r\cos\phi(\cos\gamma\cos\phi + \sin\gamma\sin\phi\cos\chi) \tag{2.14}$$

$$\frac{d\chi}{dt} = \frac{1}{V\cos\gamma}\left[\frac{L(\alpha)}{m}\sin\sigma - \frac{V^2}{r}\cos^2\gamma\cos\chi\tan\phi\right] - 2\omega_p(\tan\gamma\cos\phi\cos\chi - \sin\phi) + \frac{\omega_p^2}{V\cos\gamma}r\cos\phi\sin\phi\sin\chi \tag{2.15}$$

where Θ and ϕ are the longitude and latitude respectively, γ the flight path angle, χ the heading angle, α the angle of attack, σ the bank angle, and ω_p the angular velocity of the planet's rotation. These equations give an insight into the motion of the vehicle and can be used to verify the trajectories produced by the simulator.

To be able to produce more general equations, which can use more accurate models, Newton's second law is used. The forces can be decomposed into three different parts: the gravitational forces, the aerodynamic forces, and the perturbation forces. A general equation of motion can then be set up which can be expanded upon by adding more accurate models to the specific parts of the equation:

$$\boldsymbol{F}^I = m\frac{d^2\boldsymbol{r}^I}{dt^2} = \boldsymbol{F}^I_{grav} + \boldsymbol{F}^I_{aer} + \boldsymbol{F}^I_{pert} \tag{2.16}$$

where the superscript I is added to define the forces in an inertial frame. Using Eq. (2.16), the accelerations acting on the vehicle can be produced. This can be put into the numerical integrator which can propagate the state of the vehicle over time. The state of the vehicle is defined as the position and velocity of the bodies inside the simulation in an inertial reference frame (either the ecliptic or planetocentric reference frame, depending on the application and scope).

The gravitational forces include the force that the central body is exerting on the spacecraft. The gravitational influences of third-bodies will be separated and put under the perturbing forces. More accurate gravitational models require the modelling of the mass distribution inside the central planet, this is thus discussed in section 2.4.1. The aerodynamic forces become important once the vehicle enters the atmosphere of the planet. These forces are discussed in section 2.3.4, and several models for the atmosphere are investigated in section 2.4.3. As the interaction between the airflow and the vehicle is extremely important for the AGA, it is discussed in more detail in chapter 3. The perturbing forces are all remaining forces not mentioned here, and provide a higher accuracy to the equations of motion if implemented. The most important of these perturbation forces are discussed in section 2.3 together with the previously mentioned forces.

2.3. Acceleration Models

The equations of motion discussed in section 2.2 are constructed by the simulation software from the selected acceleration models. Acceleration models define the accelerations of the vehicle from the state of the vehicle and the environment models. The research question and goals stated in chapter 1 mention the performance of the AGA as the main parameter that needs to be measured. Choosing certain acceleration models can increase the accuracy with which an AGA trajectory is modeled. However, if this does not change the achievable performance of the AGA compared to a less accurate model, the gain in choosing a more accurate model is not justified for this research project. Thus a trade-off needs to be made for the choice of acceleration model between the gain in accuracy of the performance of the AGA and the increase in computational effort that specific model requires. This section discusses the possible models that can be used in the simulator. The specific selection of which models will be used is discussed in chapter 5 and 8 where the results for the AGA performance are produced and discussed.

2.3.1. Central Gravity

The simplest model for the gravitational force a body exerts on another body is the central gravity model and is given by Wakker [2015]:

$$\boldsymbol{F}_1 = -\frac{Gm_1m_2}{r_1^3}\boldsymbol{r}_1 \tag{2.17}$$

where G is the universal gravitational constant, m_i is the mass of body i and $r_1 = |\boldsymbol{r}_1|$ is the distance from m_2 to m_1. The subscript of $\boldsymbol{F}$ defines on which body the force is acting. This equation is based on a body that has a spherical symmetric mass distribution and assumes that the bodies don't intersect. If we assume that one of the bodies is much larger ($m_1 << m_2$) and we apply Newton's second law we get:

$$\frac{d^2\boldsymbol{r}_1}{dt^2} = -\frac{\mu}{r_1^3}\boldsymbol{r}_1 \tag{2.18}$$

where μ is the gravitational parameter ($= Gm_2$) which is introduced as this parameter is known with a higher degree of accuracy then the two individual parameters [Wakker, 2015].

This equation works well for bodies with a mass distribution that is radially symmetric; however, for all planets this is not completely the case. The non-uniform mass distribution of planets introduces a perturbation to the body if only equation 2.18 is used [Wakker, 2015]. In section 2.3.2 it is described how this model can be improved for an object with an arbitrary mass distributions.

2.3.2. Spherical Harmonics

To describe the gravitational force of a body with a non-uniform mass distribution, the spherical harmonics series are used [Montenbruck and Gill, 2000]. Spherical harmonics are a set of orthogonal functions that can describe functions on the surface of a sphere. For the gravity of a non-uniform body these functions can be used to describe the concentration of mass beneath a surface element. After a lengthy calculation the gravitational potential of a non-uniform body can be described as follows:

$$U = \frac{\mu}{r}\sum_{n=0}^{\infty}\sum_{m=0}^{n}\frac{R^n}{r^n}P_{nm}(\sin\phi)(C_{nm}\cos(m\Theta) + S_{nm}\sin(m\Theta)) \tag{2.19}$$

where r, ϕ and Θ describe the position with respect to the center of the sphere, the latitude, and the longitude respectively. R is the mean radius of the sphere and $P_n(\sin\phi)$ are the Legendre polynomials. C_{nm} and S_{nm} are constants that depend on the mass distribution of the body. The potential can be related to the acceleration of the smaller body by:

$$\frac{d^2\boldsymbol{r}_1}{dt^2} = \nabla^I U \tag{2.20}$$

The potential rotates together with the planet, thus when calculating this a transformation is needed from the rotating frame to an inertial frame, and the gradient should be taken in the inertial reference frame. How the specific constants C_{nm} and S_{nm} are calculated is discussed in section 2.4.1.

2.3.3. Third-Body Perturbations

Third-body perturbations are gravitational perturbations not due to the gravity of the central body the spacecraft is orbiting, but due to another body that exerts a gravitational force on the spacecraft. These perturbations can have a significant effect on the orbit of the spacecraft over longer periods of time [Montenbruck and Gill, 2000]. Due to the large distances involved in this perturbation, the differences between the central gravity model and the spherical harmonics model are negligible. Thus the simpler central gravity field model can be used to calculate the effect of the third-body perturbation. The equations of motion for a three-body problem can be constructed as follows [Wakker, 2015]:

$$\frac{d^2\boldsymbol{r}_i}{dt^2} = G\frac{m_j}{r_{ij}^3}\boldsymbol{r}_{ij} + G\frac{m_k}{r_{ik}^3}\boldsymbol{r}_{ik} \qquad \{i,j,k\} = \{1,2,3\} \tag{2.21}$$

Where $\boldsymbol{r}_{ij} = \boldsymbol{r}_j - \boldsymbol{r}_i$.

The magnitude of the perturbing force depends on the mass of the perturbing body and inversely on the distance to the perturbing body. For a solar system spacecraft, the largest third-body perturbation is generally the Sun [Wakker, 2015]. However, this perturbation is already much smaller then the second order spherical harmonics perturbation. Just as was said before, if high accuracy is needed for the determination of a trajectory, this perturbation can be included in the simulation.

2.3.4. Aerodynamic forces

To be able to calculate the aerodynamic forces acting on the vehicle when in the atmosphere, several parameters need to be calculated or estimated. The equation for the lift, drag, and side force in the aerodynamic reference frame are as follows:

$$L = \frac{1}{2}\rho V^2 S_{ref} C_L \tag{2.22}$$

$$D = \frac{1}{2}\rho V^2 S_{ref} C_D \tag{2.23}$$

$$S = \frac{1}{2}\rho V^2 S_{ref} C_S \tag{2.24}$$

where ρ is the density of the medium in which the vehicle is moving, V is the velocity with respect to the airflow, S_{ref} is the reference area of the vehicle, and C_L, C_D, and C_S are the lift, drag, and side force coefficients respectively. These coefficients depend on: the shape of the vehicle, the Mach number, airspeed, α, and the flow regime. The density is dependent on the atmosphere and the height of the vehicle above the surface of the body, and S_{ref} needs to be chosen so that it is consistent with the values of the aerodynamic coefficients.

These forces are calculated in the aerodynamic reference frame, thus to include them in the equations of motion they need to be transformed from the aerodynamic reference frame to the inertial reference frame:

$$\boldsymbol{F}^I_{aero} = C^{I/R} C^{R/V} C^{V/T} C^{T/A} [-D - S - L]^T \tag{2.25}$$

The aerodynamic forces are one of the main forces acting on the spacecraft during the AGA, and thus are studied in more detail in chapter 3.

2.3.5. Radiation Pressure

Most of the radiation hitting a spacecraft originates from three different sources: the Sun, radiation being reflected by the planet the satellite is orbiting (due to its albedo), and radiation emitted by the planet itself (due to thermal radiation or other sources like a planets magnetosphere). Another smaller perturbation exists due to the fact that a spacecraft can be heated up one one side more then on the other side. This causes a photon thrust which exerts a small force on that side of the spacecraft. These forces are all relatively small and do not influence the spacecraft over relatively short periods of time compared to the other forces. Thus we shall only consider the largest of these forces here, namely the solar radiation pressure [Montenbruck and Gill, 2000].

The satellite will absorb and reflect photons of the Sun due to the solar flux experienced by the satellite. This solar flux is defined as the amount of solar photons crossing a unit area per unit time. A simple equation can be set up that determines the force that a satellite experiences due to the solar radiation, assuming that the illuminated part of the satellite only has surfaces which are perpendicular to the incoming photons and that the surface of the satellite only reflects and absorbs the photons specular and not diffuse [Montenbruck and Gill, 2000]:

$$\boldsymbol{F}_{rad} = -\frac{\Phi}{c} C_R A \frac{\boldsymbol{r}_\odot}{r_\odot^3} \mathrm{AU}^2 \tag{2.26}$$

where Φ is the solar flux, c is the speed of light in vacuum, A is the illuminated area of the satellite, $r_\odot$ is the distance between the Sun and the satellite, and C_R is the reflectivity coefficient, defined as: $C_R = 1 + \epsilon$, where ϵ is the reflectivity of the satellite.

C_R is the hardest factor to determine and many orbit determination programs put it as a free parameter when calculating the radiation pressure [Montenbruck and Gill, 2000]. When the spacecraft becomes more complicated (e.g. solar panels and scientific instruments on the surface of the spacecraft) equation 2.26 becomes less accurate.

A more accurate method is described in Früh and Jah [2014], where the spacecraft shape is divided into a large number of facets. The radiation is then modelled as rays coming from a specific location and hitting each facet individually. This allows for several effects to be modelled. Firstly, self-shadowing can be modelled as the ray stops when it hits the first facet. Furthermore, as the force is calculated for each individual facet, the torque due to the radiation pressure can be calculated. The main disadvantage of this method is that it requires large computation times as it traces the rays from the source across a large area. This method is mainly used when the solar radiation pressures is one of the largest perturbations, e.g. high area to mass ratio space debris, and might be inefficient for vehicles where the solar radiation pressure is not a large perturbation, or when short periods of time are considered.

Planet	D/O	J_2	σ_{J_2}
Mars	110	$2.0 \cdot 10^{-3}$	$3.1 \cdot 10^{-11}$
Venus	21	$1.997 \cdot 10^{-6}$	$6.915 \cdot 10^{-9}$
Earth	280	$1.1 \cdot 10^{-3}$	$3.5 \cdot 10^{-13}$

Table 2.1: J_2 coefficients for different planets, where D/O stand for the degree and order of the model available. The data is adapted from Dirkx [2015]

2.4. Environment Models

The environment model determines various parameters for the acceleration models mentioned in section 2.3, and thus also influences the accuracy and computation time of the simulation. Just as for the acceleration models, the performance of the AGA is the main driver for the selection of the environment model. If it is expected that the achievable performance changes significantly when a more accurate model is taken, it will be taken into account when selecting the specific environment model.

This section will go through several possible environment models and their respective (dis-)advantages. First the gravity field model is discussed in section 2.4.1, where the determination of the spherical harmonics constants will be mentioned. Afterwards, the ephemeris models of the planets are examined in section 2.4.2. Finally, the atmosphere models are investigated in detail in section 2.4.3.

2.4.1. Gravity Field

Section 2.3.2 discussed the spherical harmonics method for the calculation of the gravity field potential of a body with an arbitrary mass distribution, where Eq. (2.19) shows how the potential is calculated for this model. μ, C_{nm}, and S_{nm} are the main environmental inputs of the model and can be determined using various methods, as discussed in Montenbruck and Gill [2000]. One of those methods is the tracking of a satellite in orbit around the planet and fitting the spherical harmonics model to observations of the position and velocity of the satellite. Another method is called gravimetry, where the gravitational acceleration is calculated using a test mass and observing its inertial reaction. If then r, R and μ are known, the gravitation force can be calculated that is acting on the spacecraft. The further discussion of these methods is out of the scope of this thesis, and readers are referred to e.g. Montenbruck and Gill [2000] or Lissauer and de Pater [2013] for more information.

A widely used notation is that of the J_n, which is defined as:

$$J_n = -C_{n0} \tag{2.27}$$

For $n = 2$ this notation change is used to measure the relative oblateness of a planet. In table 2.1 some planets with their J_2 coefficients (and their respective uncertainties σ) are listed. Some studies on the AGA use the Newtonian gravity model and then add the spherical harmonics expansion with only the J_2 term in the model as a perturbation (see e.g. Hess [2016]) instead of using spherical harmonics as the main gravitational model and using higher order terms in it. Spherical harmonics can be used when a high accuracy is needed for the determination of the gravitational accelerations. However, it also increases the computation time of the simulations as the summation in Eq. (2.19) (containing all the gravitational coefficients) is evaluated at each time-step.

2.4.2. Ephemeris

To be able to determine the position of a spacecraft relative to the position of a planet, not only the position of the spacecraft needs to be known, but also the orbital position of the planet. This is what is called an ephemeris. The ephemeris can be used if a specific mission needs to be analyzed as this requires the position of the planet at the precise moment that this mission is performed. The ephemeris is also needed when interplanetary travel is considered as the relative position of planets is important to find the trajectory of the spacecraft between them.

Analytical expressions for the ephemeris of a planet can be used as this decreases the computation time of the simulation (as the ephemeris tables are usually fairly large), but this will also decrease the accuracy. Thus if accuracy is the main driver of a simulation a database is needed that uses up-to-date ranging data and numerical simulations of the evolution of the orbits of planets.

Geocentric differences	INPOP13c - INPOP10e			INPOP13c - DE430			INPOP10e - DE423		
	α [mas]	δ [mas]	ρ [km]	α [mas]	δ [mas]	ρ [km]	α [mas]	δ [mas]	ρ [km]
Mars	1.19	0.38	0.204	0.35	0.21	0.129	2.1	0.62	0.47
Venus	0.17	0.22	0.023	0.33	0.16	0.017	0.85	0.42	0.045
Jupiter	0.52	0.23	0.60	6.85	9.55	2.98	0.81	0.74	1.11

Table 2.2: The maximum differences in geometric parameters (the declination, δ, the right ascension, α and the range, ρ) between several models and versions. Data adapted from Fienga et al. [2014]

Two of the most widely used ephemeris databases are the Jet Propulsion's Lab Development Ephemeris (JPL-DE) and the French INPOP database [Fienga et al., 2014]. Both of these databases are based on the latest observations of several interplanetary missions like the Venus Express (VEX) and the Mars Express (MEX) missions using the Very Long Baseline Interferometry (VLBI) technique, range and range rate observations, and optical astrometry . The differences between the models and their versions can be seen in table 2.2. These differences show the uncertainty that there is in the location of the planets. The uncertainties in the ephemeris can cause the spacecraft to miss its target, or enter the atmosphere at the wrong location, which then require corrective maneuvers to correct for that increase the propellant needs for a mission.

Both ephemeris databases are available through the SPICE toolkit [Arora and Russell, 2010], which is also used in this research project as it was readily available.

Next to the translational ephemeris discussed above, there is also a need for a rotational ephemeris. The rotational ephemeris defines the rotation matrix of the body-fixed reference frame, and its time derivative, with respect to an inertial reference frame. The rotation of the body has a significant effect on the dynamics of the spacecraft in the atmosphere as can be seen in Eqs. (2.10) - (2.15), thus it is important to get an accurate ephemeris model for the rotational model. The SPICE ephemeris model also includes a rotational ephemeris for several planets, thus this ephemeris shall be used in the simulations for this research project.

2.4.3. Planetary Atmospheres

Planetary atmospheres have a large influence on the dynamics of the vehicle during an AGA. Modelling planetary atmospheres is needed to calculate various aerodynamic forces and heating rates that influence the vehicle and its motion through the atmosphere. For the calculations of these quantities, the density needs to be known to calculate the aerodynamic forces, the temperature and pressure for quantities like the Reynolds number and Mach number, and the composition of the atmosphere for the heating rate and Knudes number (see chapter 3 for more information). Atmospheric models can be divided into two categories: the standard models and the reference models [Mooij, 1994]. The standard models contain a list of values for the quantities mentioned earlier that represent the values for mid-latitudes and averaged over year-round conditions. The reference atmosphere models are more representative for specific geographical locations, certain seasonal conditions, and other effects like geomagnetic variations. It is important to note that for all atmosphere models the accuracy decreases when conditions are needed at high altitudes, as the conditions at these altitudes change rapidly over time due to the Solar activity and are thus hard to predict [Picone et al., 2002]. When performing an AGA the vehicle will go through these higher altitudes twice, but the main gliding flight will take place at lower altitudes.

The selection of the specific atmosphere model depends on its use inside the research project. As was stated before, the goal of this thesis is to measure the performance of the AGA compared to the GA and not simulate a specific mission. Most atmosphere models that offer high accuracy at the cost of computational efficiency are used for specific mission analysis and system design purposes [Duvall et al., 2005] which require a model that allows for the simulation of the precise conditions at a certain moment in time. Thus it is important when selecting the atmosphere model to consider the influence that the accuracy of the atmosphere model has on the performance metrics for the AGA.

This section will go through all the options and describe the differences between the different models. Which atmosphere model for each planet is used to obtain the results is discussed in chapter 5. First the simplest model for an atmosphere is discussed: the exponential atmosphere.

Planet	Scale height [km]
Earth	8.5
Mars	11.0
Venus	16.0
Jupiter	24.0

Table 2.3: Scale height of different planets. The data is taken from Lissauer and de Pater [2013]

Exponential Atmosphere

A simple first-order model for any atmosphere is called the exponential atmosphere [Lissauer and de Pater, 2013]. The exponential atmosphere is based on several assumptions, namely that the atmosphere is a perfect gas which is at rest as the pressure balances out the gravity (hydrostatic equilibrium). Furthermore, the temperature, molecular composition, and the gravitational acceleration ($g = g_0$) is constant for different heights. The assumption of hydrostatic equilibrium can be expressed as follows:

$$dp = -\rho g_0 dh \tag{2.28}$$

where p is the pressure, ρ is the density, g the gravitational constant, and h the height in the atmosphere. This equation can be solved and rewritten using the perfect gas equation, to arrive at:

$$\frac{\rho}{\rho_0} = e^{-\frac{h-h_0}{H}} \tag{2.29}$$

where H is the scale height, given by:

$$H = \frac{RT}{g_0} \tag{2.30}$$

where R is the gas constant and T is the temperature. For the purpose of this thesis, the scale height is assumed to be constant. In table 2.3, different scale heights are given for various planets. The exponential model is not the most accurate model as it is based on several assumptions as was stated before. However, as it can be implemented into the simulation using just one equation, it is computationally efficient and can thus be used for situations where this is the main driver.

As will be shown in chapter 3, the composition of the atmosphere needs to be known to be able to calculate various parameters. The exponential atmosphere model does not take the composition of the atmosphere into account, thus it is important to discuss the assumptions needed to still be able to calculate these parameters. Earth's atmosphere consists of 77 percent N_2, 22 percent O_2, and roughly 1 percent other molecules (e.g. CO_2, O_3, H_2O, etc., see Lissauer and de Pater [2013] for a more detailed compositional analysis of the planetary atmospheres). Thus, for the case of an exponential atmosphere, it is assumed that the Earth's atmosphere consists of 77 percent N_2 and 23 percent O_2, and that this composition is constant as a function of altitude. Both the atmospheres of Venus and Mars consist of roughly 96 percent CO_2, and around 3 percent N_2, thus this shall be taken as the composition of the atmospheres of Venus and Mars.

Mars Atmosphere Model

There are several atmospheric models that are used for missions to Mars. One of the main models is the Mars Global Reference Atmospheric Model, or Mars-GRAM, which is an engineering level model (i.e. applicable for engineering purposes) that was used in various missions [Justus et al., 2002]. This model has been used for various aerobraking missions like the Mars Reconnaissance Orbiter (MRO), Mars Odyssey (MO), and the Mars Global Surveyor (MGS). From the surface to 80 km above the surface the model is based on data of the NASA Ames Mars General Circulation Model (MGCM). From 80 km and above Mars-GRAM is based on the University of Michigan Mars Thermospheric General Circulation Model (MTGCM). One of the main advantages of this model is the ability to do Monte Carlo like analysis as it can introduce various perturbations in the model that reflect real variations in the Martian atmosphere. The latest version of Mars-GRAM is the 2010 version and it has been compared with data from the Thermal Emission Spectrometer (TES) instrument on board the MGS for low altitudes and with data from the MRO, MO, and MGS missions for higher altitudes by Justh et al. [2011]. The observed versus measured density ratios are around 1.0 for equatorial cases and

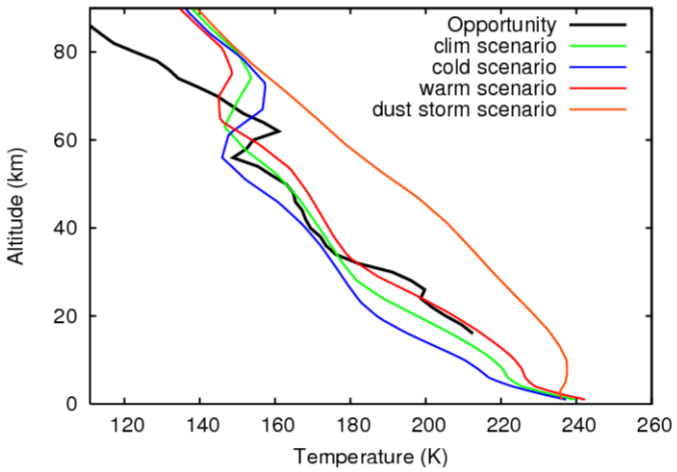

Figure 2.4: Temperature measurements of the landing of Opportunity compared with different scenarios of the MCD, Oppotunity landed during a dust storm. Adapted from Millour et al. [2015].

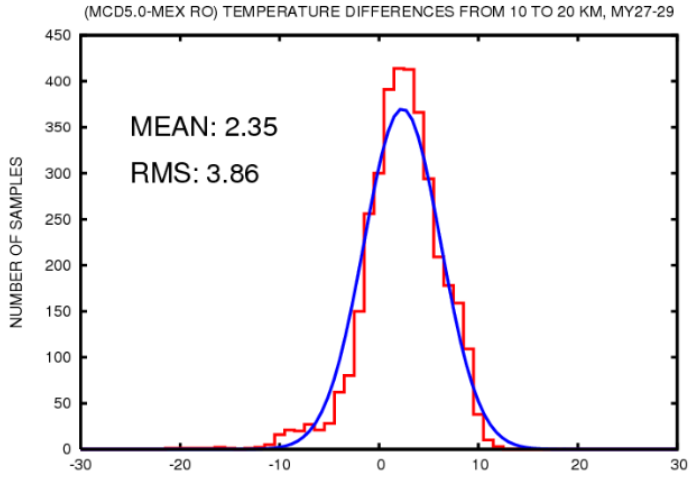

Figure 2.5: Temperature difference between the Mars Express Radio measurements and the MCD. Adapted from Millour et al. [2015].

around 1.1 and 1.2 for higher latitudes and heights. For altitudes above 100 km, the ratios are again around 1.0 for around the equator, but they increase significantly towards the poles. For the MGS mission the average ratio is 1.8 with a maximum of 10.7, for MO the average is 0.99 and a maximum of 8.2 and lastly for the MRO the average is 0.9 with a maximum of 3.6. This shows again the uncertainty there is at higher altitudes; however, it also shows that the most accurate data is at lower latitudes and thus when designing a mission this should be taken into account.

Another widely used Mars atmosphere model is the ESA Mars Climate Database (MCD) [Millour et al., 2015]. This model is made using General Circulation Model numerical simulations and validated by observational data of the Viking, Opportunity, and MGS missions. It can simulate different scenarios like dust storms and cold and warm temperature environments. In figures 2.4 and 2.5, differences between in-situ measurements and the MCD can be seen for the temperature profiles. In figure 2.4, measurements of the Opportunity mission in the landing phase, which was performed during a small dust storm [Millour et al., 2015], are shown. This data shows a relatively large difference between a real dust storm scenario and the opportunity situation. As there aren't many dust storm measurements at higher altitudes from rovers it is expected that this difference is large. In figure 2.5 the difference between certain measurements from Martian orbit are much lower and show a higher correspondence with the EMCD.

The EMCD model was readily available, and contained a large amount of scenarios and conditions that

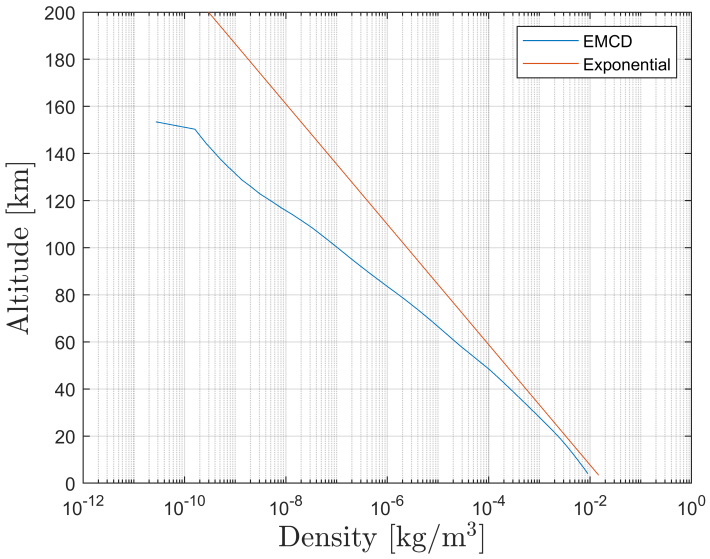

Figure 2.6: Density of the Martian atmosphere as a function of altitude, given both for the exponential atmosphere, and at 0 longitude and latitude for the EMCD.

can be easily accessed by an out-of-the-loop software program. Furthermore, it is relatively accurate and has been validated by several missions. The EMCD was thus chosen as the Mars atmospheric model for high accuracy applications. The exponential atmosphere for Mars and the EMCD for 0 degree latitude and longitude, in a non-perturbed scenario, is shown in figure 2.6. It can be seen that for lower altitudes, the exponential atmosphere and EMCD are relatively close to each other, but for higher altitudes they start to diverge from each other. This is due to the fact that most of the assumptions for the exponential atmosphere do not hold anymore at higher altitudes where the atmosphere is thinner. Moreover, the upper atmosphere is also highly dependent on external processes like the Solar cycle [Lissauer and de Pater, 2013], thus it is more variable and unpredictable over time.

Venus Atmosphere Model

For Venus less information is available about the atmosphere than for Mars. The widely used atmospheric model for Venus is the Global Reference Atmospheric Model (Venus-GRAM). This model is based upon the VIRA model, developed in the 1980's, for altitudes up to 200 km. Above these altitudes the model is extended by taking into account several assumptions [Justh et al., 2006]:

- VIRA conditions and constituents at 250 km are used as lower boundary values.
- Constant (exospheric) temperature is assumed above 250 km (exospheric temperature = local VIRA temperature at 250 km).
- Hydrostatic conditions are computed separately for each constituent (diffusive separation).
- Total pressure is computed from constituent partial pressures.
- Mass density is computed from constituent number densities.

The VIRA model is based only on data of missions in the 1970's, when Venus was extensively studied by the US and the Soviet Union, like the Pioneer Venus Probes and Orbiter (PVO), and the Venera 10, 12, and 13 landers. Later VIRA models included data from the VEGA mission. A more current mission is the Venus Express (VEX) [Svedhem et al., 2007], which flew between 2005 and 2015 around Venus to observe its atmosphere. On board the VEX is the Venus Express Radio Science experiment (VeRa) which uses radio measurements to probe the atmosphere of Venus. The difference between VeRa results and the VIRA model (and the updated VIRA-2 model) are shown in figure 2.7. It can be seen that differences is in the order of 5-10 K for lower altitudes and becomes larger at higher altitudes.

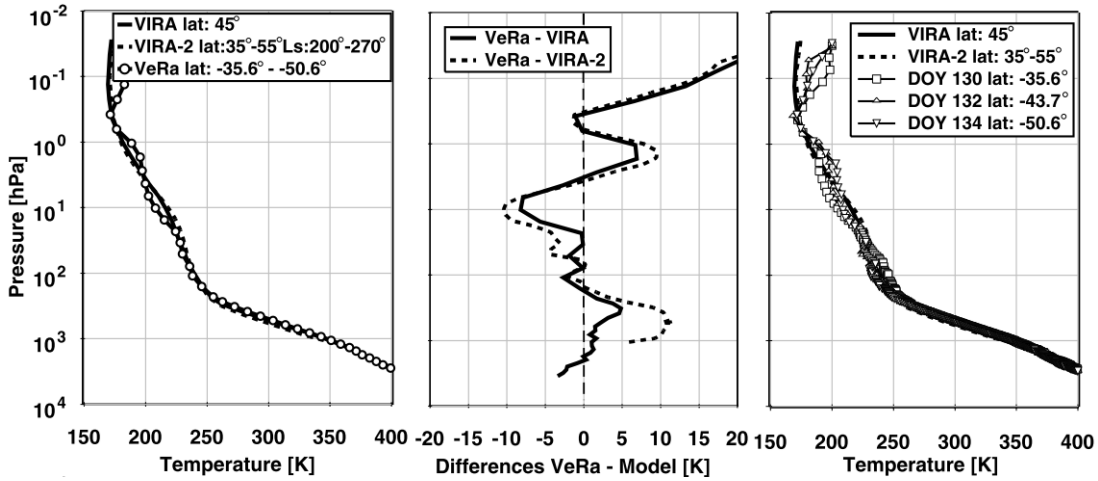

Figure 2.7: Results of VeRa onboard the VEX for mid latitudes (between 35 and 55 degrees) compared to the VIRA and VIRA-2 model. Adapted from Tellmann et al. [2009].

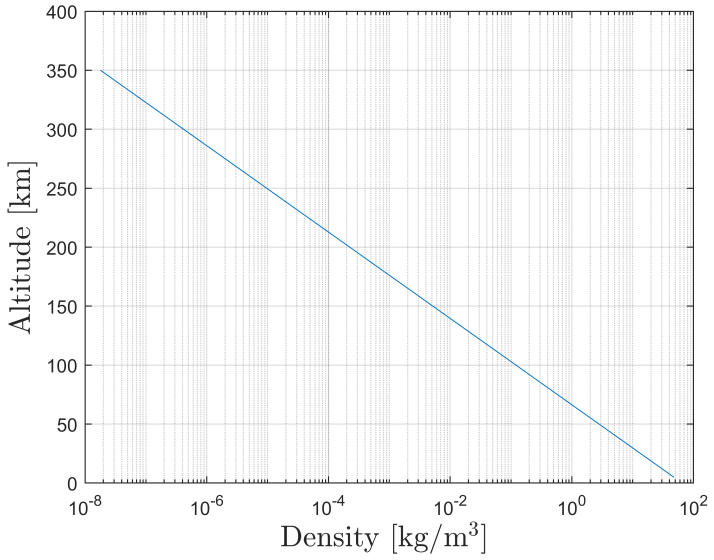

Figure 2.8: Exponential atmosphere for the atmosphere of Venus.

Unfortunately, the implementation of the Venus-GRAM model into the simulation was not possible in the time schedule for this research project. Thus for Venus, only the exponential atmosphere was implemented, which is shown in figure 2.8. If this figure is compared with figure 2.6, it can be seen that the atmosphere of Venus is much denser and also continues up to higher altitudes then the atmosphere of Mars.

Earth Atmosphere Model

There are many models that try to accurately describe the distribution and profile of various quantities of the Earth's atmosphere. As there are more satellites around the Earth then any other planet in the Solar System, and as the Earth's atmosphere is observed by a large variety of instruments, the accuracy by which the atmosphere is known is higher then for other planetary bodies.

One of the older, simpler, models is the 1976 US Standard Atmosphere. This atmosphere model is built up from several sections, in which the temperature profile is treated as a linear function of height. The slope of these linear temperature curves is called the lapse rate and is determined through several measurements of rockets and satellite experiments. The density and pressure are then calculated using the same expressions (and thus with the same assumptions) as for the exponential atmosphere.

Another model is the Earth-GRAM model. This model can reproduce the temperature, density, pressure,

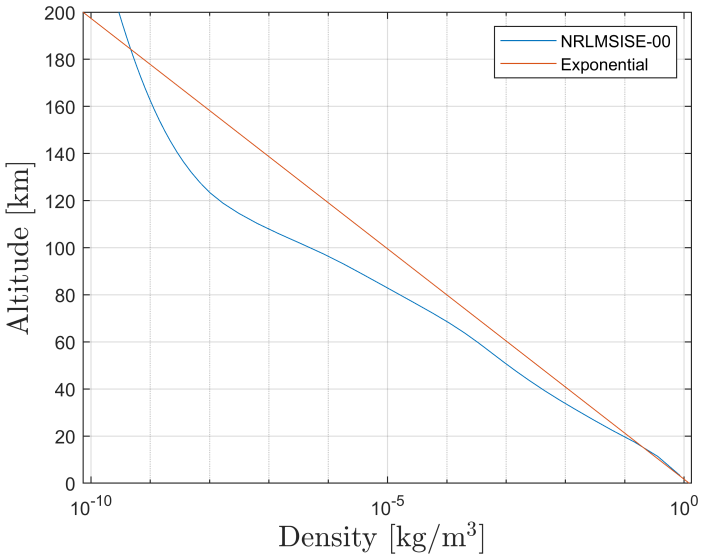

Figure 2.9: The density as a function of altitude for the exponential atmosphere model, and the NRLMSISE-00 model.

winds, and constituents as a function of time, height, and geographical location on Earth [Justus et al., 2004]. The model consists of the National Oceanic and Atmospheric Administration Global Upper Air Climatic Atlas (GUACA) data from the surface up to 27 km. Afterwards it is based on the Middle Atmosphere Program (MAP) data, until 120 km, where after it is based on the NASA Marshall Engineering Thermosphere (MET) model. Justus et al. [2004] compared the Earth-GRAM model with measurements from the Naval Research Laboratory (NRL) and found that the model has a correlation factor of 0.93 with the NRL data. Hess [2016] determined, however, that the Earth-GRAM model is only available to US citizens, and thus cannot be used in this research project.

The NRLMSISE-00 model is another model that is based on empirical data and is often used in trajectory analyses [Picone et al., 2002]. The NRLMSISE-00 model has been a continuation of previous models and contains measurements (taken during the period of 1965-1983) from: the incoherent scatter radar (ISR), mass spectrometers, solar ultraviolet (UV) occultation, pressure gauges, falling spheres, grenade detonations, satellite drag measurements, and satellite-borne accelerometers. The composition, density, temperature, and pressure in the upper atmosphere is highly dependent on the geomagnetic activity, and is thus not completely predictable. The NRLMSISE-00 model takes into account several measurements taken at these altitudes, and averages over them all. Thus when taking data from the model at higher altitudes, the uncertainty will also be higher. Due to its high accuracy, studied in Picone et al. [2002], and the availability of this model, the NRLMSISE-00 model was chosen to be used for high accuracy applications. A comparison between the exponential atmosphere and the NRLMSISE-00 atmosphere is given in figure 2.9.

2.5. Guidance and Control System

To be able to perform a successful AGA, the vehicle will need to be able to follow a certain reference trajectory by controlling (part of) the dynamics of the vehicle. The subsystems responsible are the guidance and control systems.

The guidance system of the vehicle determines the difference between the desired state of the vehicle (from the reference trajectory), and the current state of the vehicle. The current state of the vehicle is the output of the navigation system, which is assumed to be able to produce the state without any uncertainty to the guidance system. From this measurement, the guidance logic will produce a desired command to correct for any existing differences. These guidance commands are then given to the control system. The control system will first transform these guidance commands to control commands, from which they are then issued to the specific control surfaces (or other forms of control systems, e.g. thrusters, reaction wheels, etc.) to be executed. The control commands are vehicle specific as they depend on which control actuators are onboard, and how they relate to the forces and moments acting on the vehicle.

These systems and how they are simulated in this research project are discussed in the following sections.

First in section 2.5.1, the variables that determine the guidance and control commands are discussed. Afterwards, the node control method used in the simulation is discussed in section 2.5.2. Finally, section 2.5.3 will examine the bank reversal algorithm needed for the lateral guidance.

2.5.1. Guidance and Control Variables

In this analysis, only the atmospheric part of the trajectory will be mentioned, the guidance and control during exo-atmospheric flight will not be discussed. Furthermore, it is assumed that the guidance and control systems are ideal. Consequently, there are no uncertainties in these systems and the desired guidance variables will be perfectly translated to the control variables and to the actual state of the vehicle. These assumptions are made as the goal for this thesis is not to determine if the on-board systems are capable of achieving a specific goal. The goal is to determine what the advantage is of an AGA compared to a GA in a general case. Once this is determined, more accurate guidance, navigation, and control systems can be tested in future research to determine their feasibility in achieving the performances determined in this thesis for more specific mission scenarios.

The vehicles state is altered by the forces and moments acting on the vehicle. The forces will influence the translational state of the vehicle, whereas the moments will influence the rotational state of the vehicle. The influence of the different torques on the vehicle are out of the scope of this thesis, thus only the effect of forces on the vehicle are taken into account, and the attitude will only be influenced by the control system of the vehicle. To alter the state of the vehicle and drive it towards the desired state, the direction and magnitude of the forces acting on the vehicle need to be controlled. It is assumed that the vehicle cannot use thrusters during atmospheric flight, controlling the vehicle can only be done using the aerodynamic forces acting on the vehicle. Thus the lift L and drag D force will be used to direct the vehicle to its desired state. As is shown in figure 3.5, L and D can be changed in magnitude using the angle of attack α, which is defined in figure 2.3. α changes the aerodynamic coefficients present in Eq. (2.22) and (2.23), thus it indirectly influences the magnitude of the forces. The sideslip angle β has a smaller influence on the aerodynamics of the vehicle, thus it is assumed that β remains constant and does not change L and D during flight. Another variable that can be used to control the aerodynamic forces is the bank angle σ, which is defined in figure 2.2. σ does not control the magnitude of the aerodynamic forces, but it does change the direction of the lift vector, which changes the normal component of the lift force. However, this also changes the tangential component, and thus induces a lateral movement.

Lyons et al. [2008] listed the differences between using σ as the only guidance variables and keeping α constant, and vice-versa. Using α allows a large range of initial flight path angles, γ_i, to be used. This is due to the fact that the magnitude of the lift force can be altered and thus the region of γ_i that avoids skipping and too steep trajectories can be altered using α. Furthermore, α does not induce a lateral movement, which changes the orbital plane of the outgoing interplanetary trajectory. Changing the orbital plane using an impulsive thrust is expensive [Wakker, 2015], and thus avoiding undesired differences in orbital planes should be avoided. The problem with α control is that changing this angle over larger values may not be feasible at hypersonic velocities. Furthermore, if it is possible, it would require a thermal protection material to be present not only at the nose of the vehicle, but also on all surfaces that are exposed during higher values of α.

σ control allows the vehicle to fly at a pre-determined, constant, α. This can remove the disadvantages of the α control, but it also induces an out-of-plane motion which needs to be accounted for in the guidance system (this is discussed in section 2.5.3). Furthermore, due to the fixed L during entry, γ_i is restricted to a small range of values and thus navigation uncertainties can result in a skip out of the atmosphere, or a entry that is too steep. Hess [2016] and Casoliva et al. [2008] found several AGA trajectories at Mars using σ only control. However, for Hess [2016], it was also required to increase the size of the vehicle by a factor of 10 as the constant lift magnitude was not sufficient for the original design (this is improved upon in this thesis, as will be shown in section 3.2). This shows that selecting only σ as a guidance variable is feasible, but has several problems. Lyons et al. [2008] showed that using α as the single guidance variable can result in successful AGA trajectories, but also argued that the values needed for α would not be feasible during actual flight.

A method of improving upon the disadvantages of both these method is to combine them to use both α and σ as the guidance variables. This method has been used for the Space Shuttle [Harpold and Graves, 1979], and for several mission studies [Papp, 2014]. Both have shown feasible results for entry studies. However, for the AGA there have only been a small amount of studies investigating the effects of using both α and σ as control variables. Armellin et al. [2006] investigated this effect; however, they used the lift coefficient directly as a control variable instead of α. This was done as the lift and drag coefficients as a function of α were not known. This thesis hopes to improve upon this study by using a realistic waverider with its aerodynamic

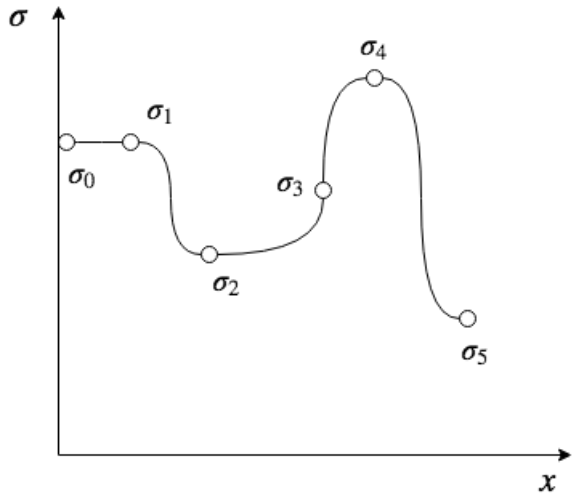

Figure 2.10: An example diagram of how the node control method works for the bank angle σ.

characteristics know for a large range of α to investigate the effect of using both α and σ as control variables.

As was mentioned in the beginning of this section, this study assumes an ideal guidance and control systems. This means that the commanded guidance variables, $(\alpha,\sigma)_C$, are transferred to the control system without any errors, and that the control system is able to immediately drive the current values of (α,σ), to the commanded values. In a non-ideal system, the control algorithm would have needed to transform $(\alpha,\sigma)_C$ to a desired control surface deflection angle, and then the aerodynamic effects of this deflection would need to be simulated to determine if $(\alpha,\sigma)_C$ is reached. As was mentioned earlier, this is out of the scope of this research project, and will thus be left for future research.

In the remainder of this project, α and σ will be referred to as the control variables, as they are the same as the guidance variables.

2.5.2. Node Control

To obtain the control commands for the vehicle, a special method is needed which can produce a continuous control command history along the entire trajectory. A method used before by Dijkstra et al. [2013] and Hess [2016] is called node control. This method places nodes along the trajectory at certain intervals determined by an independent variable, x, and assigns values to the control variables at each node. The control commands at each node are then patched together using an interpolator. The nodes can be grouped together using a guidance matrix Γ:

$$\Gamma = \begin{bmatrix} x_0 & \alpha_0 & \sigma_0 \\ x_1 & \alpha_1 & \sigma_1 \\ \vdots & \vdots & \vdots \\ x_n & \alpha_n & \sigma_n \end{bmatrix} \tag{2.31}$$

Each row in this guidance matrix represents a node $\mathcal{N}_n$, with corresponding values for the α_n and σ_n control variables at independent variable location x_n. A visual example of this method for σ can be seen in figure 2.10.

An optimizer will be used to find the atmospheric trajectory of the vehicle, which will select the values of the second and third columns of Γ. The independent variables x_n are decided beforehand and used as an input to the optimizer as it will then determine the optimal values at each location x_n.

One of the important criteria for the selection of x is if the maximum value of this independent variable is known beforehand. If this is not the case, an estimate must be made for the final value. If this estimate is too low, the optimizer will be limited, and if it is too high, the optimizer will not be efficient as it has too determine values for the dependent variables which will not be reached. Dijkstra et al. [2013] developed a node control algorithm for a re-entry problem using the normalized specific energy, $\hat{E}$, as the independent

variable. $\hat{E}$ was chosen to start at a value of 1, and when it reaches the surface of the Earth (at an altitude and final velocity of 0, thus 0 kinetic and potential energy) the value of $\hat{E}$ is 0. This allows the algorithm to constrain the values of the nodes between 0 and 1. Hess [2016] determined that this would not be a suitable choice for the aerogravity assist as the value of $\hat{E}$ is not known at the end of the trajectory due to the fact that the state at the end of the maneuver is not known beforehand.

A candidate for a bounded independent variable is the atmospheric bending angle. This independent variable gives the angle between the point that the vehicle enters the atmosphere (with a pre-determined value for the start of the atmosphere), and the current location in the atmosphere. This variable can be expressed mathematically as follows:

$$\cos\theta(t) = \frac{\boldsymbol{r}_{\boldsymbol{0}}^{\boldsymbol{I}} \cdot \boldsymbol{r}^{\boldsymbol{I}}(t)}{\left\|\boldsymbol{r}_{\boldsymbol{0}}^{\boldsymbol{I}}\right\| \left\|\boldsymbol{r}^{\boldsymbol{I}}(t)\right\|} \tag{2.32}$$

where $\theta(t)$ is the atmospheric bending angle at time t, $\boldsymbol{r}_{\boldsymbol{0}}^{\boldsymbol{I}}$ is the initial inertial position of the vehicle, and $\boldsymbol{r}^{\boldsymbol{I}}(t)$ is the inertial position of the vehicle at time t. The same problem will arise with the atmospheric bending angle as with the specific energy; however, for the atmospheric bending angle a limit can be set at 180 degrees. This limit can be set because of the fact that if an atmospheric bending angle larger then 180 degrees is chosen, it would be better to enter the atmosphere from the other side. This limit will allow a distribution of nodes between 0 and 180 degrees. If the final bending angle will be smaller then 180 degrees, the nodes between the final value and 180 degrees will still be set but not reached by the vehicle.

The nodes only define the control variables at certain points along the trajectory. To be able to determine a continuous control profile, an interpolator needs to be used to connect the different nodes. This is shown in figure 2.10 and is discussed in more detail in section 4.2.

The final consideration is the number of nodes that will be used in the guidance algorithm. Hess [2016] has performed an analysis of the optimization performance under various amount of nodes. It was found that 10 nodes would result in the quickest convergence and the most robust solutions. Thus this number of nodes will be used in the remainder of this research project.

2.5.3. Lateral Guidance

As was discussed in section 2.5.1, when using a bank angle, σ, that is not equal to 0 degrees or 180 degrees, the vehicle will move in a lateral direction as the lift vector will have a component in that direction. If an orbital plane change is desired, this can be used to control the vehicle to obtain the target final inclination. However, when the orbital plane change is not desired, or the target inclination has not been achieved, an algorithm needs to be designed that can minimize this deviation. One of the methods to do this is the bank reversal. A bank reversal is executed when the predicted final out-going orbital inclination exceeds a certain, pre-defined, tolerance. Once this tolerance is exceeded, the sign of the bank angle will change to reverse the direction of the lateral component of the lift vector. This algorithm has been used on previously flown missions like the space shuttle [Harpold and Graves, 1979], and has been used in other AGA studies [Casoliva et al., 2008]. For the AGA, it was found by Lyons et al. [2008] that for the exit leg of the trajectory, the bank reversal would create unplanned energy losses. Casoliva et al. [2008] has designed algorithms to diminish these effects, but having α as one of the control variables can decrease the needed bank reversals by decreasing the use of σ.

To increase the accuracy of the bank reversal in the simulation, the change in σ should not be instantaneous, but instead follow the following rule:

$$\sigma(t_{i+1}) = \sigma(t_i) + \dot{\sigma} \cdot \Delta t \tag{2.33}$$

where Δt is the time-step of the simulation. The bank angle rate $\dot{\sigma}$ is chosen to be ± 20 degrees per second as this corresponds to space shuttle values [Harpold and Graves, 1979] and was also used in previous waverider studies [Casoliva et al., 2008]. Δt can pose a problem during the simulation, as the time-step size could be variable (see chapter 4 for more information). This could be solved by implementing a fixed guidance algorithm time-step, as was done by Hess [2016]. However, having a constant Δt would decrease the complexity of simulation. Which approach is taken is discussed in section 4.1.

3

Aerothermal Dynamics and Environment

As the vehicle starts to enter the top layers of the atmosphere, the dynamics of the vehicle change as aerodynamic forces start to act on the vehicle. Furthermore, the interaction between the surface of the vehicle and the boundary layer that starts to develop due to the viscous flow generates heat that increases the temperature of the vehicle.

The vehicle will enter the atmosphere at hypersonic speed (defined to be where the Mach number M is greater then 5 [Anderson, 2006]). At hypersonic speeds there are several effects that need to be taken into consideration when designing the vehicle and the mission. The first one is called the thin shock layer effect. The shock wave that exists in hypersonic flow has a smaller angle between the body and the shock wave for larger Mach numbers, thus at hypersonic speeds this angle can be small enough to interact with the viscous boundary layer that has grown from the surface of the body. This can induce complications in the calculation of various aerodynamic and thermodynamic parameters. A second problem with hypersonic flight is the fact that for hypersonic flow the boundary layer will grow very fast, and through this, interact with the outer inviscid flow. This is called the viscous interaction and has a large influence on the pressure distribution on the vehicle and thus on the aerodynamic lift, drag, and side force. The high temperature that the vehicle achieves during the hypersonic flight also brings challenges as these high temperatures affect the composition and chemistry of the flow around the vehicle. This in turn affects the heating of the vehicle. Finally, the rarefied air at high altitudes changes the equations we can use to calculate the aerodynamic forces that act on the vehicle. This is not necessarily a hypersonic effect, but it is an effect that hypersonic vehicles (including the vehicle that will perform the AGA) will undergo. All of these effects make the modeling of the aerothermodynamics of the vehicle complex and thus an in-depth analysis needs to be made of the various methods to calculate the forces and heating rates.

Section 3.1 will discuss the basics of the aerodynamics that need to be considered for this research project. The different flow regimes are considered in this section, together with the different methods available to calculate the aerodynamic coefficients during these different flow regimes. In the following section, section 3.2, the type of vehicle that can be used for the AGA is discussed, and a design analysis is performed to determine the properties of the final vehicle. Then, in section 3.3, the heating phenomena are deliberated upon, which is then linked to the thermal protection system in section 3.4.

3.1. Aerodynamics

The aerodynamics are an important part of the aerogravity assist, as it is used to control the vehicle to increase the bending angle. As was discussed in section 2.3.4 there are three aerodynamic forces that can express the influence of the airflow on the vehicle: the lift force L, the drag force D, and the side force S. Eq. 2.22 and 2.23 give the expressions needed to calculate L and D respectively. The side force S is also important when there is a component of the flow hitting the spacecraft from the side (e.g. winds in the atmosphere). However, only L and D will be used in this thesis as the S component is usually much smaller then the other aerodynamic forces. Looking back at Eq. 2.22, 2.23, and 2.24, there are several quantities that need to be determined to calculate the aerodynamic forces. V and ρ can be determined from the flight conditions, and S_{ref} is a constant parameter that is determined by the selection of vehicle. The complexity lies in the aerodynamic coefficients C_L, C_D, and C_S. These coefficients are dependent on the Mach number M, the shape of the

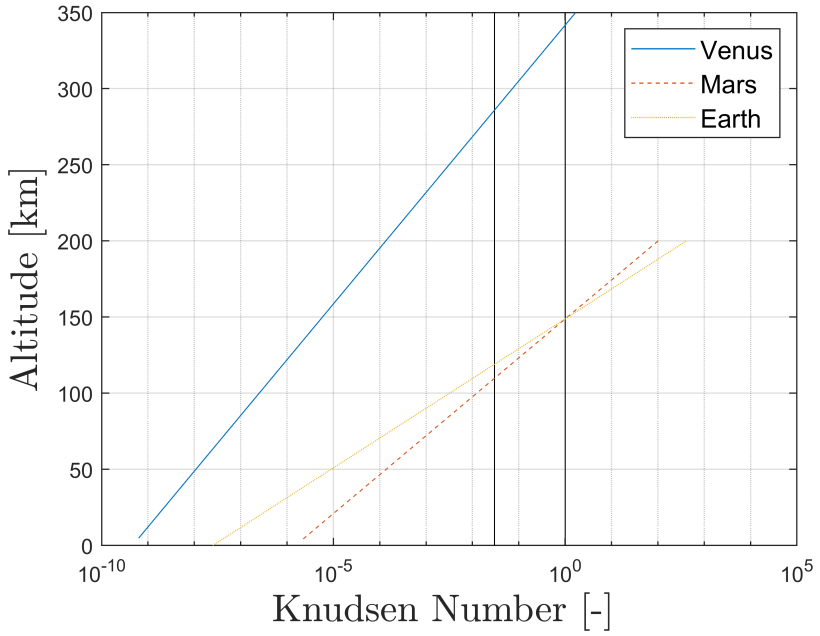

Figure 3.1: The Knudsen number for the three exponential atmosphere models as a function of altitude. The reference length of the vehicle is taken to be 5 meters.

vehicle, the angle-of-attack α, the sideslip angle β (see figure 2.2), the specific flow regime (see section 3.1.1), and several other parameters. There are various analytic and numeric methods that are able to approximately determine these coefficients, which will be discussed in section 3.1.2, section 3.1.3, and section 3.1.4. Which method needs to be used is also determined by the type of flow experienced by the vehicle. Thus, these different flow regimes are first discussed in section 3.1.1.

3.1.1. Flow Regimes

The air in the atmosphere is a combination of various molecules. These molecules remain in the atmosphere mainly due to gravity, but the concentration of these molecules is not homogeneous. At low altitudes the molecules are very close together and the air can be seen as a continuous flow. However, at higher altitudes most of the molecules are spaced far apart and the flow cannot be seen as continuous anymore. This regime is called the free molecular, or rarefied, flow. A number that describes the type of flow is called the Knudsen number [Anderson, 2006]:

$$Kn = \frac{\lambda}{L} = \frac{m_p/(\sqrt{2}\pi\sigma_p^2\rho)}{L} \tag{3.1}$$

where λ is the mean free path length (the mean distance before a molecule hits another particle), L is the characteristic length of the vehicle, m_p the mass of the particle, and σ_p the collisional diameter of the particle. According to Anderson [2006], a continuum flow is considered when $Kn < 0.03$, a transitional flow when $0.03 < Kn < 1.0$ and a free-molecular flow when $Kn > 1.0$. Other authors, e.g. Hess [2016], use a larger transitional flow, from 10^{-3} to 10 for this region, but the exact numbers have no clear theoretical basis and both ranges may be equally valid. Thus the ranges of Anderson [2006] are used in this project. The masses and collisional diameter of the various particles are determined from the molecular composition of the atmosphere models discussed in section 2.4. Figure 3.1 shows the altitudes corresponding to various flow regimes.

3.1.2. Local Surface Inclination Methods

Local inclination methods are a very powerful tool in the calculation of the aerodynamic coefficients of a vehicle. Local inclination methods use equations where the aerodynamic coefficients are only dependent on the angle the surface of the vehicle makes with the incoming flow. The local term comes from the fact that for each vehicle the surface is divided into panels, which are not aerodynamically coupled with each other. It is important to first note that the local inclination methods discussed here provide the pressure coefficient C_p

and in some cases the shear stress coefficient C_τ. To obtain C_L, C_D, and C_S, several steps have to be taken. First the aerodynamic force vector in the body reference frame can be calculated as follows:

$$\boldsymbol{F}^B_{aero} = -q_\infty \sum_{i=1}^{N} (C_{p,i} A_i \boldsymbol{n}_i + C_{\tau,i} A_i \boldsymbol{t}_i) \tag{3.2}$$

where N is the number of panels used to discretize the surface of the vehicle, q_∞ the dynamic pressure, A_i is the surface area of the ith panel, $\boldsymbol{n}_i$ is the normal vector of the ith panel, and $\boldsymbol{t}_i$ is the tangential vector of the ith surface. The minus sign in front is used as the pressure and shear stress act in the opposite direction as the normal and tangential vector. The aerodynamic coefficients can then be calculated as follows:

$$\begin{bmatrix} C_L \\ C_S \\ C_D \end{bmatrix} = \frac{1}{S_{ref} q_\infty} C^{A/B} \boldsymbol{F}^B_{aero} \tag{3.3}$$

where $C^{A/B}$ is the frame transformation matrix from the body frame to the aerodynamic frame. Thus the pressure and shear stress coefficient produced by the local inclination method can be transformed to the aerodynamic coefficients using these transformations.

The methods discussed in this section are the Modified Newtonian method, the tangent wedge/cone method, and the corresponding methods for transitional and rarefied flow. The specific selection of the method(s) that are used to determine the aerodynamic coefficients are discussed in section 3.2.

The Newtonian method is a local surface inclination method that models the flow of air as a so called Newtonian flow. These flows are modelled as a stream of particles that when hitting a wall would transfer all of its momentum to its tangential component. This allows the calculation of the pressure coefficient (which can be used to determine the other aerodynamic coefficients) using the following formula [Anderson, 2006]:

$$C_p = 2\sin^2\theta \tag{3.4}$$

where θ is the angle between the incoming flow and the surface of the vehicle. This formula was first used by Newton in subsonic flows, but quickly discarded due to the lack of real-gas effects and the fact that it could only work for an inviscid flow. However, for high Mach numbers the shock angle is very small and when the flow is deflected by the shock, it travels parallel to the surface downstream. The geometry of a hypersonic flow closely resembles the geometry of a Newtonian flow and it was quickly found that Newton's method of determining the pressure coefficient works very well for high Mach numbers. The predictions made by the Newtonian method can be made more accurate by modifying the physical assumptions underlying it. For the Newtonian method, it was assumed that the shock wave is attached to the surface of the vehicle. However, if this assumption is disregarded, and the loss of total pressure over the shockwave is considered, the Newtonian method can be improved. This method is called the Modified Newtonian method, and is given by the following equation [Anderson, 2006]:

$$C_p = C_{p,max} \sin^2\theta \tag{3.5}$$

$C_{p,max}$ is the value of the pressure coefficient at the stagnation point behind the normal shock wave, given by:

$$C_{p,max} = \frac{2}{\gamma M_\infty^2} \left[\left(\frac{(\gamma+1)^2 M_\infty^2}{4\gamma M_\infty^2 - 2(\gamma-1)} \right)^{\gamma/(\gamma-1)} \left(\frac{1-\gamma+2\gamma M_\infty^2}{\gamma+1} \right) - 1 \right]. \tag{3.6}$$

where γ is the ratio of specific heats, and M_∞ is the free-stream Mach number of the flow.

Another method called the tangent-wedge/tangent-cone method (the wedge is used for two dimensional analyses and the cone for three dimensions) can also be used to determine the aerodynamic coefficients. This method is rather straightforward as it calculates the pressure at a certain point by calculating the pressure downstream of a shockwave with a flow deflection angle that is equivalent to the local angle at that point. The flow deflection angle is the angle that the flow is deflected over after travelling through the shockwave created by the vehicle. This method has less of a theoretical basis compared to Newton's method, but it has been shown by Gillum and Lewis [1997] to yield accurate results for hypersonic vehicles.

Relations that were found by Newton and others have one flaw and that is that they can only be used for inviscid continuum flow [Hart et al., 2014]. When calculating parameters for a continuum flow the Navier-Stokes equation is used, which is a simplification of the Boltzmann equations. The Boltzmann equation

describes a thermodynamic system which is not in equilibrium (e.g. a fluid with a heat gradient). The Navier-Stokes equations, which can explain the characteristics of a viscous flow, are derived from this Boltzmann equation using various simplifications based on a continuous flow. When the flow is rarefied, the Boltzmann equation cannot be simplified to the Navier-Stokes equation anymore and other methods need to be derived. Hart et al. [2014] came up with a method by analyzing the particle-surface interaction during collisions. When a particle (or molecule) hits the surface it can reflect of the surface in two ways: specular reflection and diffuse reflection. In specular reflection the collision is elastic, where the normal momentum component is reversed and the tangential component is preserved. For a diffuse reflection the particle is reflected according to a Maxwellian distribution for a temperature equal to the temperature of the reflected molecule. The reflected molecule can be defined by two parameters: the tangential and the normal momentum accommodation parameters:

$$\sigma_N = \frac{p_i - p_r}{p_1 - p_w} \tag{3.7}$$

$$\sigma_T = \frac{\tau_i - \tau_r}{\tau_i} \tag{3.8}$$

where p is the pressure normal to the surface, τ the shear stress pressure and i, r, and w represent the incident molecule, reflected molecule, and the wall respectively. If $\sigma_N = \sigma_T = 0$ we deal with specular reflection and for $\sigma_N = \sigma_T = 1$ the molecules reflect diffusely. The full derivation of how these assumptions and definitions are used to determine an equation for the pressure and shear stress coefficients is not within the scope of this research project. Thus only the final equation is shown in Eqs. (3.9) and (3.10), and interested readers are referred to Hart et al. [2014] for a more detailed analysis.

$$C_p = \frac{1}{s^2}\left[\left(\frac{2-\sigma_N}{\sqrt{\pi}} s\sin\theta + \frac{\sigma_N}{2}\sqrt{\frac{T_w}{T_\infty}}\right) e^{-(s\sin\theta)^2} + \left((2-\sigma_N)\left((s\sin\theta)^2 + \frac{1}{2}\right) + \sigma_N/2\sqrt{\frac{\pi T_w}{T_\infty}} s\sin\theta\right)(1 + erf(s\sin\theta))\right] \tag{3.9}$$

$$C_\tau = -\frac{-\sigma_T \cos\theta}{s\sqrt{\pi}}\left[e^{-(s\sin\theta)^2} + \sqrt{\pi} s\sin\theta(1 + erf(s\sin\theta))\right] \tag{3.10}$$

$$s = \frac{V_\infty}{\sqrt{2RT_\infty}} \tag{3.11}$$

Here, s is the freestream molecular speed ratio, an analogue for the Mach number, T_∞ the freestream temperature, T_w the wall temperature, R the gas specific constant, and V_∞ the freestream velocity.

The region between the free molecular flow and the continuum flow is called the transitional regime and can be defined to be for a Knudsen number of $0.03 < Kn < 1.0$. To model this region analytically a bridging function was made empirically from Space Shuttle measurements by Blanchard and Buck [1986]:

$$F(Kn) = \sin^2\left[\frac{2 + log_{10}Kn}{8}\pi\right] \tag{3.12}$$

this bridging function can then be used as follows to calculate the force coefficient:

$$\bar{C_x} = \frac{C_x - C_{x_{cont}}}{C_{x_{FM}} - C_{x_{cont}}} = F(Kn) \tag{3.13}$$

where the subscript x is the wanted force coefficient, FM is the coefficient found in the free molecular regime and $cont$ in the continuum regime. This equation was also implemented in numerical simulations by Ronse and Mooij [2014] and Hess [2016] to model the transitional flow regime.

3.1.3. Numerical Methods

The previous section dealt with mainly analytical equations to determine aerodynamic forces. All of these techniques had as an advantage that they only depended on the local angle of the flow with the vehicle. This significantly reduces the computation time as this angle is easily determined. However, for a more accurate description of the aerodynamics of the vehicle, a computational fluid dynamics (CFD) program would be needed. These programs use sophisticated algorithms to solve various equations (e.g. Euler, Navier-Stokes, Boltzmann, etc.) around the vehicle and predict various parameters. However, for hypersonic speeds, CFD analyses are much harder as different effects that were not present during subsonic and supersonic flight now have a major influence on the aerodynamics [Bertin and Cummings, 2006]. These problems include

shock-boundary layer interaction, thin shock layers, entropy layers, viscid/inviscid interaction and real gas effects (for example, dissociation and for high temperatures ionization), which are discussed in more detail at the beginning of the chapter. Another problem that many hypersonic vehicles face is the fact that they fly through rarefied air (i.e. the free molecular regime). As was discussed earlier, this does not allow for the use of simplified equations, e.g. Navier-Stokes, anymore. Thus the full Boltzmann equation needs to be solved, which is computationally intensive [Hart et al., 2014]. There have been several probabilistic methods that are able to approximate the solution to the Boltzmann equation [Bird, 1994]. One of the most widely used methods is called the Direct Simulation Monte Carlo Simulation (DSMC), which will be discussed in the following section.

Direct Simulation Monte Carlo

The DSMC method was developed by Bird [1994], and is based on three stages for every time step (which is a user chosen discretization of the time inside the simulation). In the first stage the equations of motion of the particles in the flow are solved, including external force terms like the gravity. The only exception for forces that are not included in the solving of the equations of motion are the inter-molecular collisions. The equations of motion are solved numerically by a numerical solver, which can be chosen depending on the use of the simulator. After the molecules are propagated to their new state, the physical space of the simulated volume is divided up in cells. If in one of these cells there are multiple molecules, the simulator will make pairs of these molecules. Using statistical tools and kinetic theory, a probabilistic value is assigned to each pair. This probabilistic value can be calculated several ways, but it still has to adhere to physical conditions, including the distribution given by the Boltzmann equation. If the probabilistic value is larger then a certain pre-determined value, the two molecules will collide and their momentum vectors are updated to the post-collision values. The final stage of the simulation is the application of boundary conditions. One of these boundary conditions is checking if some molecules have hit the vehicle or checking if new molecules can enter the simulated volume from outside the boundaries. These boundary conditions can be set by the simulator, but as said earlier, they have to adhere to physical limits. The force acting on the vehicle is then obtained from the particles that have hit the surface of the vehicle, which is also located in the simulated volume.

The advantage of this method is the fact that the propagation of the state of the particle and the calculation of the collision of particles are separated. This requires much less computation time as if this was not separated, every molecule had to be checked for a collision. The only requirements that the DSMC method has is that the time step needs to be much smaller then the mean molecular collision time and that the gas is in the free molecular regime, as in this regime only molecular collisions dominate and no other long distance inter-molecular forces are present. The DSMC works best at high Knudsen numbers as the computation time would increase significantly with lower Knudsen numbers. This simulation method has already been used in missions by Moss et al. [1999] to calculate re-entry aerodynamics. Furthermore, Boyd [2015] has tested the DSMC against other models and wind tunnel tests, for which the results are shown in figure 3.2. The results show that compared to the modified Newtonian method the DSMC agrees much more with experimental data from the wind tunnel. Thus for higher Knudsen numbers (free molecular flow), the DSMC method is superior. For lower Knudsen numbers (partly the transitional flow and continuum flow), the DSMC method will be computationally expensive, and thus not practical to use for this research project.

3.1.4. Selection of Methods

Dirkx and Mooij [2011] performed an analysis of which method for the continuum flow is appropriate for which type of vehicle shape. It was determined that for high inclination 'flat' vehicle shapes, at hypersonic conditions, the modified Newtonian method works best. As will be discussed in section 3.2, the vehicle used for the AGA has a low inclination 'flat' shape, and thus the modified Newtonian method is selected to be used as the preferred method. Gillum and Lewis [1997] determined that the modified Newtonian method corresponds well to wind tunnel tests, and Dirkx and Mooij [2011] validated the Newtonian method further using aerodynamic data of the Space Shuttle and the Apollo capsule. This method was readily available to use due to the work done by Ronse and Mooij [2014].

For the free molecular flow, the options are between the analytical equations given in section 3.1.2, and the DSMC numerical method given in section 3.1.3. A comparison between these two methods was performed by Hess [2016], and it was found that there are several differences between the results from these two methods. First, it was found that the local inclination methods for the free molecular flow would lead to a discontinuity in the drag and shear stress coefficient profile as several panels would be in the shadow zone

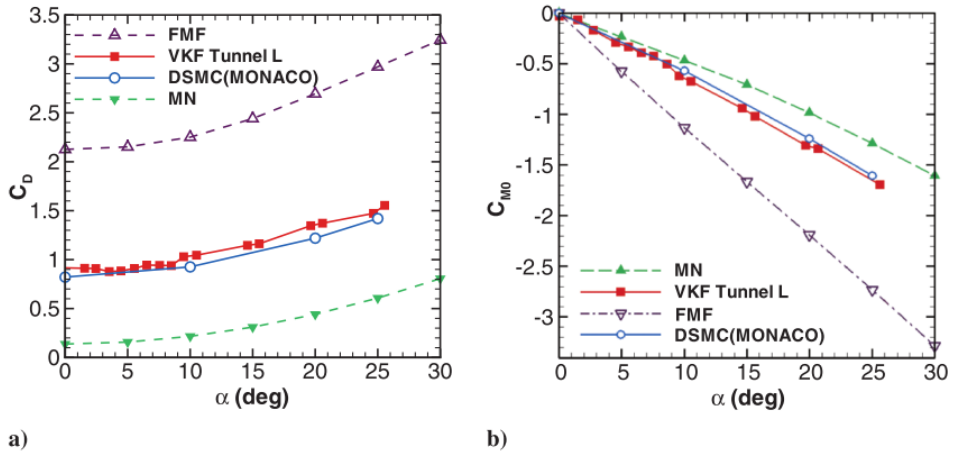

Figure 3.2: Aerodynamics as calculated by the DSMC method (the simulator is called MONACO, the modified Newtonian method (MN), analytic equations from free molecular theory (FMF) and from wind tunnel data ($M_\infty = 10.0$ and $Kn = 0.065$). Figure a) shows the results for the drag coefficient, and figure b) shows the results for the pitch moment coefficient. Adapted from Boyd [2015].

(the zone shielded from the incoming flow). For a local inclination method, θ would first be very close to zero (thus close to a maximum for $\cos\theta$, thus also for C_D and C_τ) before the panels would get into the shadow zone. When the angle of attack (α) then changes to get these panels completely into the shadow zone, the maximum will then suddenly jump to zero. The DSMC method has shown that it can avoid this behaviour, and thus increase the accuracy of the aerodynamic coefficients. Furthermore, previous studies used these (free molecular flow) local inclination methods on blunter bodies [Ronse and Mooij, 2014]. These blunt bodies do not have sharp edges, contrary to waveriders, and are thus more suitable for these methods. It was thus chosen that for the free molecular flow aerodynamic modelling, the DSMC method will be used. Specifically using the SPARTA[1] software package, created at the Sandia National Laboratories.

Finally, the transitional flow will be modelled according to a weighted average between the continuum and free molecular flow, given by Eq. 3.12.

3.2. Hypersonic Waveriders

In chapter 2 it was already mentioned that the dynamics of the vehicle during the AGA are dependent, separately, on the lift and drag force experienced by the vehicle. However, according to McRonald and Randolph [1990], the L/D ratio is more important for the dynamics of the vehicle. If the L/D ratio is high, the losses due to drag will be minimized and the spacecraft will fly more efficiently. This in contrast with other hypersonic vehicles as their primary goal is to reduce speed and minimize heating by using atmospheric drag and blunted noses (e.g. the Apollo vehicles returning to Earth). Early on in the development of the AGA, various authors (see e.g. McRonald and Randolph [1990] and Anderson et al. [1991]) already found that the hypersonic waverider class of vehicles were the best option for the execution of an AGA due to their aerodynamic design, see figure 3.3. Hypersonic waveriders have a slender design which generates an attached shock wave all along its leading edge during hypersonic flight. A high pressure zone is generated behind the shock wave on the side of the vehicle that is facing the incoming flow. This pressure zone cannot "leak" to the other side of the waverider as it is shielded by the attached shock wave. Thus, the pressure zone generates a high amount of lift. In combination with a slender body reducing the drag, the vehicle can generate high values for the L/D ratio.

Starkey and Lewis [1999] parameterized the shape of a hypersonic waverider using five parameters: l, w, m, θ, δ and n. The equations that describe the design of the waverider are as follows:

$$y_p = Ax^n \tag{3.14}$$

$$y_l = C(x\tan\theta - z)^m \tag{3.15}$$

$$z_u = (y_u/B)^{1/n} \tag{3.16}$$

[1] https://sparta.sandia.gov/

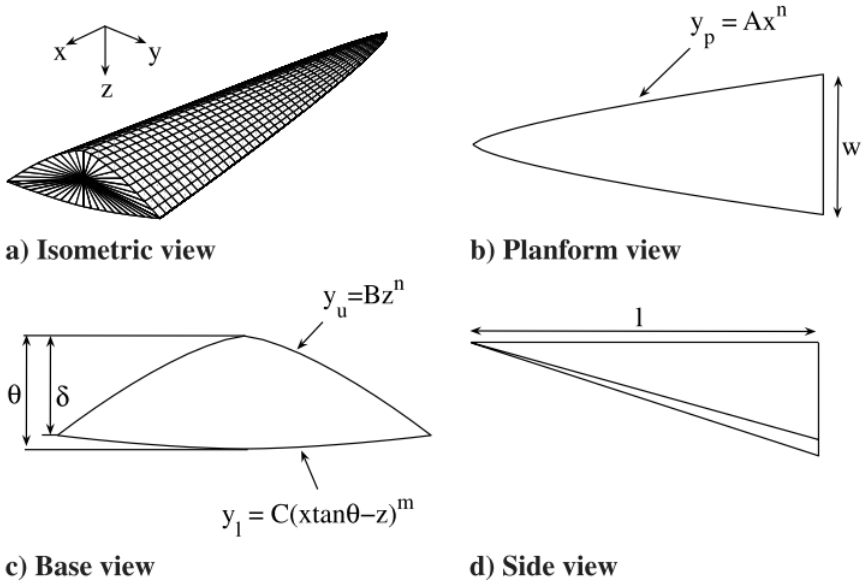

Figure 3.3: The shape of a waverider with the equations describing the geometry. Adapted from Armellin et al. [2007].

$$z_l = x\tan\theta - \left(\frac{2yl_l^n}{wx^{n-m}}\right)^{1/m}(\tan\theta - \tan\delta) \tag{3.17}$$

where y_p describes the planform view, y_l the lower base surface, z_u and z_l describe the lower surfaces, and A, B, and C are constants. In figure 3.3 the waverider is shown with the equations describing them.

3.2.1. Mission Heritage

The hypersonic waverider is a relatively new vehicle which was first proposed by Nonweiler [1959]. Most of the research and development on this vehicle since then has been theoretical. However, recently there have been some developments as waverider like vehicles have undergone more practical tests.

A hypersonic wind tunnel test has been performed on a blunted waverider at Mach 14 by Gillum and Lewis [1997]. These blunted edges were added to analyze the losses in flow "spillage" between the upper and lower area, as the theoretical infinitely sharp edges for hypersonic waveriders are not feasible (due to heating and mechanical loads). It was found that the losses due to the spillage are minimal, however the drag induced due to the blunted edges was higher and could diminish the aerodynamic efficiency.

Variations on the waverider design have been flight tested. The Hyper-x project performed several test flight to investigate the use of hypersonic vehicles with air-breathing propulsion systems [McClinton et al., 2005]. The X43-a is one of these vehicles which flew successfully at a Mach number of 7 for around one minute [McClinton et al., 2005]. It was launched from a B-52 aircraft, where an attached booster brought it to the desired velocity after separation from the aircraft. Once the desired velocity was reached, the test vehicle detached from the booster and turned on its engine to perform the test flight. During this time it gathered aerodynamic data to be used in future validation and wind tunnel tests.

Another vehicle that has been flight tested is the Hypersonic Test Vehicle 2 or the HTV-2. This vehicle has a more waverider like shape, but as it is developed by DARPA and the Air Force, data on the aerodynamics was not available. What is known is that it was launched on a ballistic missile and it reached a peak Mach number of about 20 [Walker, 2008].

3.2.2. Waverider Design and Modelling

The waverider can be designed to optimize one or more different objectives, e.g. the L/D ratio, peak heat flux, total heat load, the drag coefficient, the total volume, etc. The shape of the waverider can be designed according to the parametrization showed in figure 3.3, and the aerodynamic properties can be derived according to the methods discussion in section 3.1.4.

The vehicle design analysis was previously performed by Hess [2016] to determine a suitable waverider shape for a different AGA study. It was decided that the waverider selected from this analysis will also be used

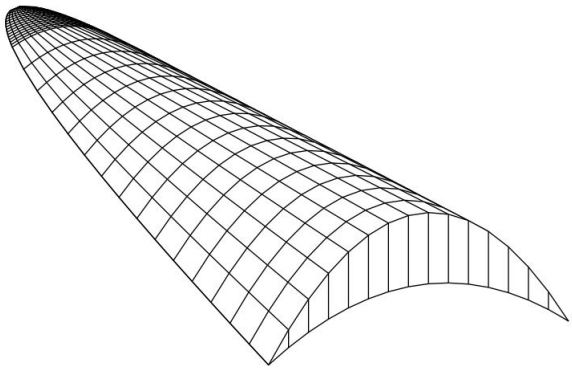

Figure 3.4: The selected hypersonic waverider shape.

w [m]	l [m]	n [-]	θ [deg]	δ [deg]	mass [kg]	S_{ref} [m^2]	V [m^3]
2.0	5.0	0.5	5.0	9.0	800.0	6.67	1.17

Table 3.1: The properties of the selected waverider.

for this research project, as this will allow comparisons to be made between the studies, and to build upon the previously done research of that research project. The shape of this waverider is shown in figure 3.4, and the properties of this vehicle are shown in table 3.1. The specific waverider shape was selected due to its high aerodynamic efficiency (high L/D) and its relatively low C_D compared to other designs. Hess [2016] found that the reference area (S_{ref}) of table 3.1 was not large enough to be able to generate a sufficient amount of lift force at Mars to perform a successful AGA. To counteract this, the S_{ref} was increased by a factor of 10. This resulted in a vehicle size that is beyond current launch capabilities. One of the goals of this research project is to find AGA trajectories that can be performed successfully using the setup of table 3.1.

Figure 3.5 shows the L/D profile as a function of the angle-of-attack α of the vehicle. It can be seen that the L/D profile of the free molecular flow is significantly lower then the L/D profile of the continuum flow. If the L/D profile of the free molecular flow could be increased, the vehicle could remain in the less dense part of the atmosphere for a longer period of time, and thus experience less drag and heating. This could significantly increase the performance of the AGA. However, the design of this type of vehicle is beyond the scope of this research project, and is thus left for future research.

3.3. Aerodynamic Heating

Heating of a body during atmospheric entry happens as the surface of the vehicle interacts with the flow around the body. The heating of the vehicle can be divided into three forms: convection, radiation, and catalytic recombination. Convection happens when a temperature gradient exists at the wall. The heat is transported through the boundary layer formed at the surface of the vehicle, in the direction of decreasing temperature, which in most cases is towards the wall of the vehicle. Radiation heating happens when a substance becomes hot enough to emit large amounts of thermal radiation, in this case the shock layer, where this radiation can then heat up the body of the vehicle. The last mechanism is catalytic recombination, which is heating due to the formation of molecules at the surface of the body. The latent heat of these reactions happening at the wall can then heat up the body. Authors like Armellin et al. [2007] and Casoliva et al. [2008] have already shown that convective heating and radiative heating dominate the heating of a body during the AGA and that catalytic recombination can be ignored. In the next sections we will deal with the models that predict the heating on the spacecraft during the atmospheric phase.

3.3.1. Convection

As mentioned in section 3.1.3, numerical methods like CFD programs are able to model the flow around a vehicle and with it predict the heating of the vehicle. However, these programs are time consuming and in some cases unreliable. Thus, an analytic model is needed that is based on the fundamental principles of

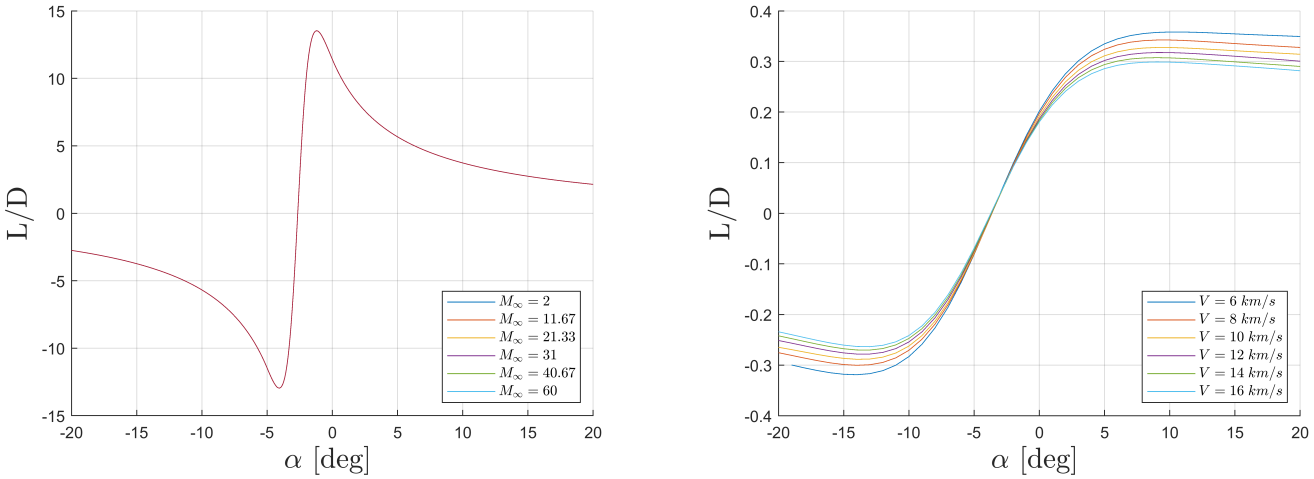

(a) L/D ratio continuum flow.

(b) L/D ratio for the free molecular flow.

Figure 3.5: The waveriders L/D ratio for the two different flow regimes.

heating. The Fourier equation for convective heat conduction is given by Anderson [2006]:

$$q_w = \left[k \frac{\partial T}{\partial y} \right]_w \tag{3.18}$$

where q_w is the heating rate at the wall and k is the thermal conductivity of the material transporting the heat. This equation shows that to have a convective heat flux, a temperature gradient is needed. This equation can be used as a basis to derive the analytic equations for the convective heat flux. Sutton and Graves [1971] found an expression for the heating at the stagnation-point for a fully catalytic cold wall and an arbitrary atmospheric composition:

$$q_{c,0} = K \sqrt{\frac{p_s}{R_N}} (h_s - h_w) \tag{3.19}$$

where $q_{c,0}$ is the heat flux in MW/m^2, p_s is the stagnation point pressure in atmospheres, R_N the nose radius of the vehicle, h_s is the total enthalpy, h_w is the wall enthalpy, and K is a constant dependent on the constitution of the atmosphere, given by:

$$K = \frac{9.8297 \cdot 10^{-5}}{Pr^{0.6}} \left(\sum \frac{c_{0,i}}{M_{0,i} \gamma_{0,i}} \right)^{-1/2} \tag{3.20}$$

where Pr is the Prandtl number, $c_{0,i}$ the mass fraction of species i, $M_{0,i}$ the molecular mass of species i, and $\gamma_{0,i}$ the transport parameter, for which the exact definition can be found in Sutton and Graves [1971]. The units of this constant is kg/s $\cdot$ m$^{-3/2}$ $\cdot$ atm$^{-1/2}$. Important to note is the fact that Eq. (3.19) is dependent on the stagnation pressure, and inversely on the nose radius. At hypersonic speeds, the stagnation point pressure increases significantly compared to (sub-)sonic speeds. Furthermore, the nose radius of waveriders is very low as will be discussed in section 3.3.3. These two effects result in relatively high heat fluxes during the AGA.

Eq. (3.19) is accurate; however it is also difficult to estimate the required enthalpies. Using the assumption that the vehicle wall is fully catalytic can simplify the equation. A fully catalytic wall assumes that all atoms at the wall are recombined, irrespective of the mass fraction of this atom. It was shown by Tauber et al. [1989] that for these walls, the heating rate is higher then for partially catalytic walls. Thus using this assumption may result in higher estimates for the heat flux (this can be an advantage as it will naturally give a buffer to the thermal protection system design). Furthermore, another assumption that can be used is the cold-wall model ($h_w << h_\infty$). Using these assumptions, the equation can be simplified to:

$$q_{c,0} = k_h \sqrt{\frac{\rho}{R_N}} V^3 \tag{3.21}$$

where $q_{c,0}$ is now given in W/m^2, ρ is the density in kg/m^3, V is the airspeed in m/s, and k_h is now a dimensionless constant, given by:

$$k_h = K \cdot \left[\frac{1}{4}\sqrt{2}(101325)^{-1/2} \right] \tag{3.22}$$

Using Eq. (3.21) is a more conservative approach, as Dirkx and Mooij [2014] showed that the heating rate will be overestimated by around 10% using Eq. (3.21). Furthermore, this form is also used in various other studies, e.g. Casoliva et al. [2008] and Edelman and Longuski [2017]. Thus, for this research project, Eq. (3.21) will be used to determine the convective heat flux. The value for k_h for several atmospheric compositions are given in table 3.2.

Composition	$k_h(\cdot 10^{-4})$
CO_2	1.903
N_2	1.749
O_2	1.889
0.85 CO_2, 0.15 N_2	1.845
0.23 O_2, 0.77 N_2	1.751

Table 3.2: Convective heating constants for various atmospheric compositions. The data is adapted from Sutton and Graves [1971].

3.3.2. Radiation

During atmospheric flight the gas surrounding the vehicle will increase in temperature significantly, which in turn leads to the gas emitting increasingly higher energetic radiation. This radiation will heat up the vehicle and can cause increased temperatures on the body.

As said before in sections 3.1.3 and 3.3.1, some CFD programs are able to model this effect. However, these programs can be quite computationally intensive. An analytic model would decrease the computing time and give a first-order approximation of the heating. However, to model the radiative heating an assumption has to be made. The assumption is that thermochemical equilibrium exists, which means that the flow is in thermodynamical equilibrium (no heat exchange between two systems) and that it is in chemical equilibrium (a system where both the reactants and products are present, but there is no change in mass fraction of the respective species). This assumption has been verified by various measurements of Mars missions to be reasonably accurate [Tauber et al., 1989]. From this, an equation can be made for radiative heating in the atmosphere of Earth and Mars [Tauber and Sutton, 1991]:

$$q_r = C R_N^a \rho^b f(V) \tag{3.23}$$

where C is a constant, R_N the nose radius, ρ the atmospheric density and $f(V)$ tabulated values depending on the velocity with respect to the atmosphere (values for different atmospheres can be found in Tauber and Sutton [1991]). C, a, and b are constants depending on the atmosphere of the target planet. This equation is again dependent on the velocity, density, and nose radius of the vehicle. However, in contrast to convective heating, a larger nose radius does not mean less heating. Thus, this value needs to be balanced to get a reasonable value for the total heat load. Tauber and Sutton [1991] found that the equations for radiative heating for Mars and Earth are accurate to around 10 percent against numerically computed data. For Mars the specific constants in Eq. (3.23) are:

$$C = 2.35 \cdot 10^8$$

$$a = 0.526$$

$$b = 1.19$$

For Earth they are:

$$C = 4.736 \cdot 10^8$$

$$a = 1.072 \cdot 10^{-6} \cdot V^{-1.88} \cdot \rho^{-0.328}$$

$$b = 1.22$$

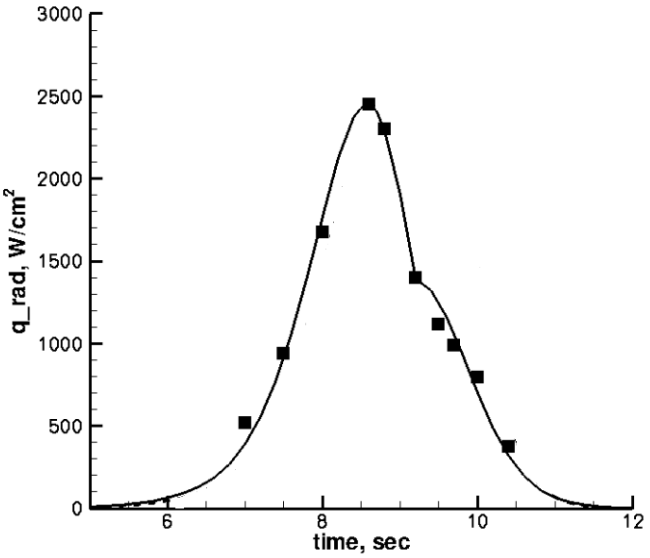

Figure 3.6: Data from the Pioneer-Venus large probe (squares) against predictions from equations 3.24 and 3.25 (solid line). Adapted from Tauber et al. [2012].

For Venus a different equation was made by Tauber et al. [2012]:

$$q_r = 9.497 \cdot 10^{-63} V^{18} \rho^{1.2} R_N^{0.49} \tag{3.24}$$

where this equation is valid for velocities between 10,028 m/s and 12,000 m/s. For velocities below 10,028 m/s:

$$q_r = 2.195 \cdot 10^{-22} V^{7.9} \rho^{1.2} R_N^{0.49} \tag{3.25}$$

The verification of these equations for Venus can be found in figure 3.6. It shows good compliance with data from the Pioneer-Venus large probe.

3.3.3. Leading Edge Design

Both the conductive and radiative heating equations presented in section 3.3.1 and 3.3.2 show that the nose radius is an important parameter that determines a part of the heat flux experienced by the waverider.

The waverider shown in figure 3.4 has a sharp leading edge, which results in an infinitely small nose radius. This results in a theoretical infinite heat flux, meaning the equations previously presented cannot be used. Furthermore, in a practical sense, this type of nose would also be undesirable as the heating rates would be extremely high and the thermal protection system would not work well with sharp leading edges. Designing blunt leading edges decreases the heating of the vehicle. However, this would also detach the shockwave from the leading edge, and thus increase the flow spillage. This reduces the aerodynamic performance of the vehicle by reducing the L/D.

Several authors (see e.g. Blosser et al. [1995] and Gillum and Lewis [1997]) have investigated the influence of blunted edges on the aerodynamic performance of waveriders. Blosser et al. [1995] found that the L/D was reduced by 7 to 10 percent if the leading edge of the vehicle was reduced by 4 percent to allow for blunted edges. Furthermore, Gillum and Lewis [1997] performed a wind tunnel test to compare a sharp leading edge waverider with a blunt leading edge waverider. It was found that using a worst case scenario blunted nose, the maximum L/D of the vehicle was reduced from 4.61 to 3.7. It was noted by Gillum and Lewis [1997] that this is an unlikely scenario, and that a more realistic blunt nose would decrease the flow spillage.

The nose radius used for this study is derived from previous AGA studies [Lohar et al., 1994] [Casoliva et al., 2008] [Edelman and Longuski, 2017] to be able to compare the heating results with the results from these studies. The nose radius taken is 1 meter.

3.4. Thermal Protection System

The thermal protection system (TPS) of a spacecraft protects the payload and other subsystems on board the spacecraft against the high heat flux and heat loads experienced during atmospheric entry. There are several

different types of TPS that all have different working mechanisms.

One category of these methods is the reusable TPS. Reusable TPS experiences no change in its properties after the heating exposure. It has a material with a high emissivity, which helps in radiating out the heat in the material. Furthermore, it has a low catalycity as this reduces the convective heating. The heat that enters the material then gets insulated or dissipated through various techniques. Reusable TPS is often used for missions that have multiple heating periods and for lower heating environments. Ceramic structures are often used as reusable TPS, for example in the X-38 vehicle [Ortelt et al., 2012]. This vehicle was used for tests on manned re-entry and has performed several sub-orbital test flights. The TPS material used was a ceramic composite of Carbon and Silicon (SiC) and for the X-38 it could withstand heat loads of up to around 74 W/cm^2. However, in Edelman and Longuski [2017] it was found that the heat load for an AGA is >100 W/cm^2, thus the ceramics on the X-38 have not been tested up to this level of heating. An advantage of this material is that it is relatively light compared to metallic TPS and it has a high technological readiness level (TRL) [Ortelt et al., 2012].

Another form of reusable TPS is active-cooling. This form of TPS can be used together with other materials like the SiC ceramics. The main principle of this technique is to pump a cooling fluid along the surface of the vehicle that can absorb heat and transport it away. One of the most promising active cooling techniques is variable transpiration cooling (VTC), described by Gulli et al. [2012]. In VTC, the cooling fluid gets injected into the boundary layer through a porous material on the surface. This cooling fluid is made to decrease the temperature gradient at the wall and thus decrease the heating. Gulli et al. [2012] showed that for various flow rates the heating could be decrease by around 60 percent for a laminar flat plate case. However, this methods requires a significant increase in mass for the storage of cooling fluids and also the material on the surface needs to specially made to allow a specific flow rate for the cooling fluid.

Another category of TPS is the non-reusable TPS, from which the ablative TPS is the most commonly used. An ablative TPS is used more in cases of extremely high heating or if re-usability is not a design consideration. It is comprised out of several layers which all have a different purpose. One of the layers pyrolysis (changes chemical state and phase) into several gasses. Part of these gasses get injected into the boundary layer and reduces the convective heating. Resin from the pyrolysis gets left on the surface of the body, “char”, which can also have an effect on the heating of the vehicle. Ablative TPS can handle higher thermal loads, but is also much more complex in its effect on the boundary layer and the heating. This form of TPS has been used on many different missions at various planets, and is thus also tested extensively [Venkatapathy et al., 2010].

Various studies already did uncertainty analyses on the ablative TPS thickness needed for several different missions (see e.g. Wright et al. [2007], Mazzaracchio and Marchetti [2010], and Turchi et al. [2017]). They used a Monte Carlo approach to model how different uncertainties in the TPS affect the final TPS thickness needed (for an ablative TPS). It was found that uncertainties in the char properties have the most influence on the final thickness uncertainty. Mainly the char conductivity has a large influence on how uncertain the TPS thickness is. Uncertainties in the working of the TPS can have influences on the aerodynamic properties of the vehicle, which need to be researched for an AGA. However, this is out of the scope of this thesis and will be left for future research.

Ablative TPS have been used in most missions where higher heat loads were expected. Table 3.3 shows some details from previously flown missions that have used ablative TPS, and table 3.4 shows some currently used materials and their properties. The three Mars entry missions listed here (Pathfinder, Viking, and MER) all use the SLA-561V TPS, a silicate based honeycomb structure which is filled with cork [Edquist et al., 2007]. This TPS material was effective as all these three missions were successful. However, for the Mars Science Laboratory it was found that SLA-561V could fail under a certain combination of conditions [Venkatapathy et al., 2010]. Thus the Phenolic Impregnated Carbon Ablator (PICA) material (see table 3.4) was chosen to replace SLA-561V on the MSL. The advanced Carbon-Carbon (ACC) TPS material was developed by industry to improve the Space Shuttle Carbon-Carbon TPS material. This material was then also used for the Genesis mission, which returned a sample of solar dust to the Earth. The Avcoat TPS material was used on the Apollo missions, and has thus been tested successfully under tight constraints. Since then there has been some research in the Avcoat material to be able to use it for the Orion crew return vehicles [Meseguer et al., 2012]. The Heritage Carbon Phenolic TPS is only used for missions with high heat fluxes and heat loads. It has as a property that it is denser then other TPS materials, and thus has bad insulating capabilities. However, it is a good ablator and thus effective for missions where the vehicle experiences both high stagnation pressure and high peak heat flux. For the missions discussed in this research project, the maximum heat fluxes experienced for Mars are around 500 W/cm^2. Thus a material like PICA would be suitable, as it has good peak heat flux capabilities and has been flight tested. For both Earth and Venus, higher heat fluxes of around 2000

W/cm^2 are experienced, thus the Heritage Carbon Phenolic could be a good choice due to its heritage and capabilities. However, it is a heavy material and thus it could be replaced by e.g. ACC if the mass would be a problem. However, it is shown in Laub and Venkatapathy [2003] that the mass is mostly determined by the heat load and not the peak heat flux, thus this will mostly be the driver for the mass of the TPS. To be able to give an estimate of the TPS mass fraction, figure 3.7 can be used. The line is fitted through the data points of previous missions and gives a rough estimate of the TPS mass fraction needed for a specific heat load. The equation of the fitted line is as follows:

$$m_{frac,TPS} = 0.091 Q^{0.51575} \tag{3.26}$$

Mission	TPS material	Peak q_{stag} [W/cm^2]	Heat load Q [J/cm^2]	TPS mass fraction
Apollo	Avcoat	500	$3 \cdot 10^4$	15%
Galileo (Jupiter)	Heritage Carbon Phenolic	30,000	$2 \cdot 10^5$	50%
Gemini	DC-325	50	-	-
Genesis	ACC	600	$1.7 \cdot 10^4$	20%
Mars Pathfinder	SLA-561V	100	$4 \cdot 10^3$	8%
Mars Viking	SLA-561V	20	$1 \cdot 10^3$	3%
MER	SLA-561V	50	$5 \cdot 10^3$	12%
Pioneer (Venus)	Heritage Carbon Phenolic	10,000	$1 \cdot 10^4$	13%

Table 3.3: Summary of several previous missions that used ablative TPS. The data is adapted from Laub and Venkatapathy [2003].

TPS material	Peak q_{stag} [W/cm^2]	Flight Qualification/TRL	V capabilities	
			< 13 km/s	> 13 km/s
PICA	~ 1200	Stardust	++	~
Avcoat	~ 1000	Apollo	++	-
ACC	>2000	Genesis	~	~
BPA	~ 1000	TRL 3-4	~	-
PhenCarb family	1000 – 4000	TRL 5-6	~	~
3DQP	~ 5000	TRL 4	+	+
Heritage Carbon Phenolic	10,000 – 30,000	Pioneer, Galileo	+	+

Table 3.4: List of a selected group of available TPS materials. ++: capable; +: capable, but heavy; ~: needs testing; -: not capable. The data is adapted from Venkatapathy et al. [2010].

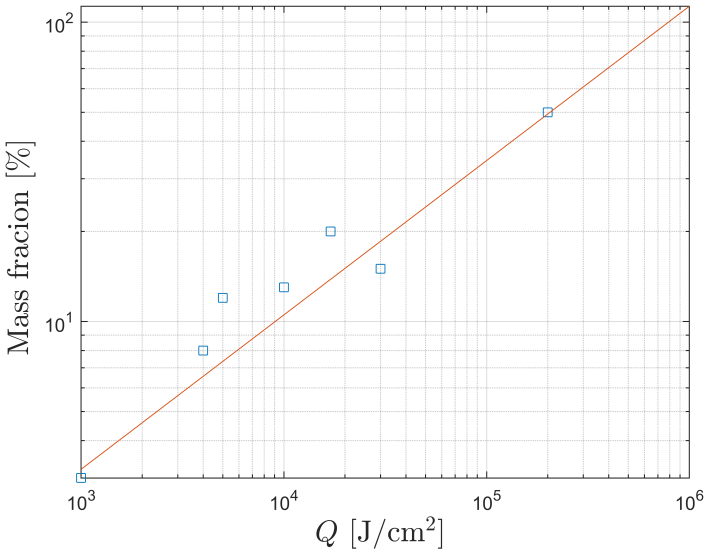

Figure 3.7: The TPS mass fractions of previous missions compared to the total heat load Q. The solid line is an estimate that can be used to give a first order approximation of the expected TPS mass fraction.

4

Numerical Methods

The simulation of the AGA is done by taking the state of the spacecraft (the x, y, and z coordinates and the corresponding velocities) and for each time step propagating them forward to the next time step using the equations of motion mentioned in section 2.2. The task of propagating the state of the spacecraft is non-trivial and various authors have already discussed ways of tackling this problem [Press et al., 1992]. In section 4.1 the various methods to propagate the state will be discussed and with it the advantages and disadvantages of them. Then in section 4.2 several methods of interpolation are mentioned, which are needed to produce a continuous history of states between the time steps. Section 4.3 then explains the least squares method, which is needed to fit models through data. Finally, in section 4.4, the different numerical optimization schemes that can be used to optimize the atmospheric and interplanetary trajectories will be discussed.

4.1. Integrators

A propagator is a formulation of the equations of motion and dynamics of the system to be solved. The integrator is the method by which the governing differential equations needs to be solved [Press et al., 1992]. For an AGA, the integrator will propagate the equations of motion which are discussed in section 2.2. An integrator is characterized by several parameters, including: the step size (often this can be varied by the user or the algorithm), the truncation error (the error made when doing a single integration step), the efficiency (the number of evaluations for a given accuracy), the sensitivity to initial conditions, and the error accumulation. The key drivers for the selection of the integrator are the accuracy and the efficiency of the integrator. Important here is that the integrator error should be lower then the model errors. This section will discuss the options available for the integrators that can be used in the simulation software to integrate the equations of motion.

The first integrators considered are fixed step-size integrators, namely the Euler-method and the Runge-Kutta 4 integrator (RK4). The Euler-method is the most simple method available and is mostly used as a example method as even for simple problems, it will quickly lead to large accumulated errors and low efficiency. It propagates the state as follows:

$$\boldsymbol{y}(t_{i+1}) = \boldsymbol{y}(t_i) + \Delta t \dot{\boldsymbol{y}}(t_i) \tag{4.1}$$

where $\boldsymbol{y}$ is the state vector and Δt is the time step. This method has as advantages that it is very easy to understand and very quick, but it is also very inaccurate and inefficient [Press et al., 1992]. Thus, this method will not be further considered. The RK4 integrator uses the same principle as the Euler-method, but between two steps it evaluates the equations two more times. Thus, for every step it evaluates the function a total of 4 times, see figure 4.1. This method increases the accuracy significantly compared to the Euler-method because of the reduction of the truncation error. The accuracy of the integrator can be increased by just adding more evaluations between two points, but this would also keep on increasing the computation time of the integrator.

Another type of integrator is the variable step-size integrator. This integrator changes the step-size according to various algorithms. A Runge-Kutta-Fehlberg RKF method uses two different sets of function evaluations to determine the required step size. For example, a RKF45 integrator first uses a RK4 method to

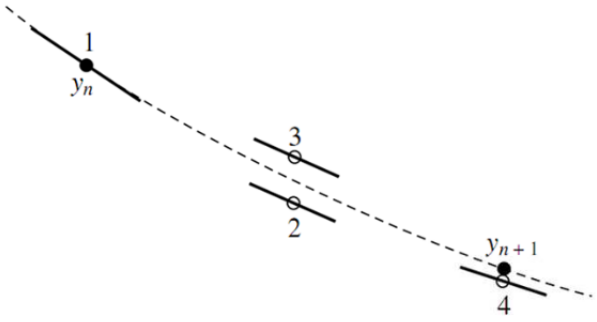

Figure 4.1: Example of how an RK4 integrator works, where the numbers represent at which point the integrator evaluates the equations. Adapted from Noomen [2016].

determine a solution: y_{k+1}. Next, a RK5 method is used to determine a second solution: z_{k+1}. The integration is first done with an initial step size Δt, the new step size will then become $s \cdot \Delta t$, where s is calculated using the following formula [Press et al., 1992]:

$$s = \left(\frac{\text{tol}\,\Delta t}{2|z_{k+1} - y_{k+1}|} \right)^{1/4} \tag{4.2}$$

where tol Δt is a user defined tolerance. The same principle holds for the higher order RKF methods, but then the solutions calculated are of a higher order.

The goal of this thesis is to determine the performance increase of an AGA compared to a GA. If the goal was to simulate with a high accuracy a specific AGA trajectory that can be used during a mission, a variable step-size integrator would be taken over a fixed step-size integrator. However, as was shown in section 2.4.3 and will be shown in section 5.2, the model errors are larger then the integrator errors and the error on the performance metrics are not influenced significantly by the integrator. Furthermore, as the complexity of the guidance algorithm would be significantly reduced if a fixed step-size integrator is used, an RK4 integrator with a 1 second time-step will be used for the remainder of this thesis. A quantitative validation of this selection is given in section 5.3.

4.2. Interpolation

As was discussed in section 2.5.2, the control profile of the atmospheric trajectory is determined using the node control method. The nodes resulting from this method need to be connected to determine a continuous control profile. This is done using interpolation. Interpolation is the process where between two or more points a function is fitted that is able to give a functional value for points where the simulator has not calculated a value. In this section three interpolation methods will be discussed briefly: linear interpolation, cubic spline interpolation, and Hermite spline interpolation.

Linear Interpolation

Linear interpolation is the most simple interpolation scheme available. Between the two points, (x_0, y_0) and (x_1, y_1), a line is fitted with start and end values corresponding to the two points that are used for interpolation. The formula for the line can be given by [Press et al., 1992]:

$$y = y_0 + (x - x_0)\frac{y_1 - y_0}{x_1 - x_0} \tag{4.3}$$

where the subscript 0 corresponds to the value of the first point and 1 to the value of the second point. The problem with this method is that it is not continuous in the first derivative across the whole trajectory. This is not accurate compared to real world examples where quantities cannot jump from one value to another instantaneously. Furthermore, if a derivative needs to be taken, this method will lead to singularities.

Cubic Spline

With a cubic spline the interpolation between two points is not done by a first-order polynomial as in the linear interpolation, but with a cubic polynomial. Each function between two points is called a segment. The

equation for one of these segments is given by:

$$S_i(x) = a_i(x-x_i)^3 + b_i(x-x_i)^2 + c_i(x-x_i) + d_i \tag{4.4}$$

This function has 4 constants that need to be determined. Thus for every segment, there needs to be 4 pieces of information to determine all of these constants. These four conditions are:

$$S_i(x_i) = y_i \tag{4.5}$$
$$S_i(x_{i+1}) = y_{i+1} \tag{4.6}$$
$$S'_{i-1}(x_i) = S'_i(x_i) \tag{4.7}$$
$$S''_{i-1}(x_i) = S''_i(x_i) \tag{4.8}$$
$$\tag{4.9}$$

These four conditions make sure that the segments between points are smooth in the first derivative, and continuous in the second derivative. However, they can overshoot the points when the application is sensitive to higher order derivatives, as can be seen in figure 4.2.

Hermite Spline

A Hermite spline uses the same principle of a cubic spline. However, instead of defining a cubic polynomial between each point, the Hermite spline is defined by the location and tangent vectors at each data point. This means that instead of computing the first derivative from the boundary conditions given by Eq. (4.7), the first derivative is imposed. The tangent vectors are determined such that there is no overshoot in the data values. First, it is determined if the slope before and after a specific data point changes in sign. If it does, the point is a local maximum or minimum, thus the first derivative is zero. If there is no sign change, the derivative d_i is determined by the weighted harmonic mean:

$$\frac{w_1 + w_2}{d_i} = \frac{w_1}{\delta_{i-1}} + \frac{w_2}{\delta_i} \tag{4.10}$$

where $w_1 = 2h_i + h_{i-1}$, $w_2 = h_i + 2h_{i-1}$, $h_i = x_{i+1} - x_i$, and $\delta = (y_{i+1} - y_i)/h_i$. The derivatives at the ends of the data points are given by a three-point-formula, given in Hess [2016].

An example of the three interpolation techniques is shown in figure 4.2. It can be seen that the cubic spline overshoots the data points before or after it reaches the data points. The Hermite spline, however, follows the data points more closely and does not have jumps at the data points in the function and its derivatives. Thus the Hermite spline is will be the choice for interpolation in this research project.

4.3. Least Squares Fitting

Fitting is the process of finding a model that tries to represent a data-set. This is needed in this research project to link the atmospheric trajectories to the interplanetary trajectories, as will be explained in chapter 6. The method that will be used is the least squares method.

Assume a linear model that is used to approximate a data-set containing N data points $(\boldsymbol{x}_i, y_i)$, given by: $y(\boldsymbol{x}|\boldsymbol{a})$ where $\boldsymbol{x}$ is the vector of quantities from which data is available, and $\boldsymbol{a}$ is a vector containing model parameters. The goal of the least squares algorithm is to find $\boldsymbol{a}$, which minimizes the error between the data and the model, given by the following formula [Press et al., 1992]:

$$S = \sum_{i=1}^{N} (y_i - y(\boldsymbol{x}_i|\boldsymbol{a}))^2 = \sum_{i=1}^{N} r^2 \tag{4.11}$$

The model in Eq.(4.11) can be written downs as follows (assuming a linear model): $\boldsymbol{y}(\boldsymbol{x}|\boldsymbol{a}) = A\boldsymbol{a}$, where A is a matrix, and each entry of $\boldsymbol{y}$ is the result of entering data point $\boldsymbol{x}_i$ in the model. Furthermore, the sum from Eq. (4.11) can be removed completely by making a vector $\boldsymbol{y}$ containing all the data points y_i as entries. Together, the least squares fitting problem can be written as:

$$S = (\boldsymbol{y} - A\boldsymbol{a})^T W (\boldsymbol{y} - A\boldsymbol{a}) \tag{4.12}$$

where W is a weight matrix, often given by the inverse of the covariance matrix V. This then needs to be minimized using the following equation:

$$\frac{1}{2}\frac{\partial S}{\partial \boldsymbol{a}} = (-A^T W \boldsymbol{y} + (A^T W A)\hat{\boldsymbol{a}}) = 0 \tag{4.13}$$

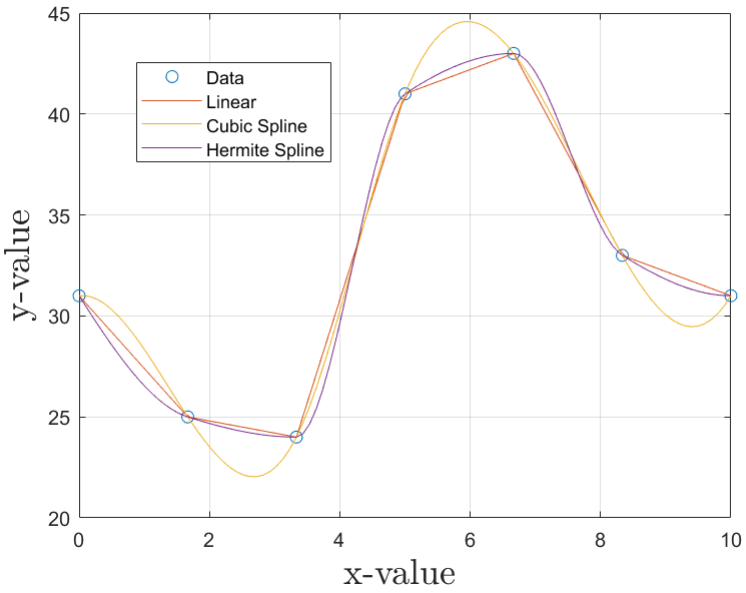

Figure 4.2: The three different interpolation methods.

This can be re-written to find the best guess $\hat{\boldsymbol{a}}$:

$$\hat{\boldsymbol{a}} = (A^T W A)^{-1} A^T W \boldsymbol{y} = B\boldsymbol{y} \tag{4.14}$$

The covariance matrix of $\hat{\boldsymbol{a}}$ can be found as follows [Press et al., 1992]:

$$V(\hat{\boldsymbol{a}}) = BV(\boldsymbol{y})B^T \tag{4.15}$$

Eq. (4.14) thus allows to calculate the best estimate for the model parameters considering the data-set.

4.4. Optimization Algorithms

The work in this thesis consists of two separate optimizations: the optimization of the atmospheric trajectory of the AGA and the optimization of the interplanetary trajectory.

The problem a general multi-objective optimization algorithm has to solve is formulated as follows:

$$\begin{aligned} \underset{\boldsymbol{x}}{\text{minimize}} \quad & \boldsymbol{f}(\boldsymbol{x}) = [f_1(\boldsymbol{x}), ..., f_m(\boldsymbol{x})]^T \\ \text{subject to} \quad & \boldsymbol{g}(\boldsymbol{x}) \leq \boldsymbol{c}_{in} \\ & \boldsymbol{h}(\boldsymbol{x}) = \boldsymbol{c}_{eq} \\ & \boldsymbol{lb} \leq \boldsymbol{x} \leq \boldsymbol{ub} \end{aligned} \tag{4.16}$$

where $\boldsymbol{x}$ is the vector of decision variables, $\boldsymbol{f}$ is the fitness vector (a scalar for single-objective problems, and a vector for multi-objective problems), m the number of objectives, $\boldsymbol{g}$ and $\boldsymbol{h}$ are the functions to be constrained, $\boldsymbol{c}_{in}$ are the inequality constraints, $\boldsymbol{c}_{eq}$ are the equality constraints, and $\boldsymbol{lb}$ and $\boldsymbol{ub}$ are the lower and upper bounds for the decision variables respectively. The objectives and decision variables used in this thesis are discussed in section 7.1 and 8.2. The implementation and selection of constraints is discussed in section 4.4.3.

The definition of an optimal solution in a multi-objective optimization problem is not the same as for a single-objective optimization problem. Several definitions need to be given before the specific algorithms that are discussed here can be understood.

Take two feasible solutions of the optimization problem: $\boldsymbol{x}_1$ and $\boldsymbol{x}_2$. $\boldsymbol{x}_2$ dominates $\boldsymbol{x}_1$ when the following conditions hold:

$$\forall i: \; f_i(\boldsymbol{x}_1) \geq f_i(\boldsymbol{x}_2) \tag{4.17}$$

$$\exists j: \; f_j(\boldsymbol{x}_1) > f_j(\boldsymbol{x}_2) \tag{4.18}$$

in other words, solution $\boldsymbol{x}_2$ is equal or better then $\boldsymbol{x}_1$ in each individual optimization objective, and for at least one optimization objective, it must be better then solution $\boldsymbol{x}_1$. A collection of non-dominated solutions is called a Pareto front, and an individual is called Pareto optimal when it is part of a Pareto front. The goal of a multi-objective optimization algorithm is thus to find Pareto optimal solutions and improve the Pareto front.

There are several software packages readily available that have several single- and multi-objective optimization algorithms available. The software package that will be used in this research project is PaGMO 2, developed by Biscani et al. [2018]. This software package was chosen because it contained a large selection of algorithms, and it was readily available for use with the simulator. A list of available algorithms can be found on their website[1].

For most problems concerning the generation of atmospheric trajectories for the AGA, and finding optimal interplanetary trajectories, a multi-objective optimization algorithm is needed (see section 7.4 and 8.2). Thus, the focus of the remainder of this section will be on multi-objective optimization algorithms. Sections 4.4.1 and 4.4.2, and will discuss two of the available multi-objective optimization algorithms in PaGMO 2: NSGA-II and MOEA/D. Afterwards, section 4.4.3 discussed the implementation of constraints into the optimization algorithms and 4.4.4 goes through the methods to determine the performance of the results from multi-objective optimization algorithms.

4.4.1. NSGA-II

The non-dominated sorting genetic algorithm (NSGA-II) was developed by Deb et al. [2002]. It is an evolutionary algorithm (from which genetic algorithms are a subset of) based on crowding distance sorting and dominance of individual solutions. NSGA-II has been used previously by Gang et al. [2005] to optimize atmospheric trajectories for re-entry problems. The NSGA-II algorithm has several steps it takes in each generation. First it selects the best individuals from the off-spring (Q) of the previous generation, and from the individuals from the previous generation (the parents, P). From this newly constructed population (of size $2 \cdot n_{pop}$), the individuals are ranked according to their dominance over other individuals. All non-dominated individuals are placed in rank 1 ($\mathscr{F}_1$), and then they are removed from the population. Afterwards, all non-dominated individuals from the new population (without $\mathscr{F}_1$ individuals) are assigned to $\mathscr{F}_2$ and removed from the population. This process is repeated until all individuals are ranked. After this process is done, each rank will be sorted according to their crowding distance. The crowding-distance is a measure for how many individuals are "close" to each other. The larger the crowding-distance, the less individuals are closer to you, the better the solution. Each rank is sorted according to the crowding-distance and then added to the parents of the next generation. As the size of each $\mathscr{F}_i$ is smaller or equal to the population size, the process of crowding-distance sorting and adding $\mathscr{F}_i$ to the parents is repeated until the parents are the size of n_{pop}. Due to the fact that each $\mathscr{F}_i$ is sorted according to the crowding-distance, even the individuals from the last rank added to the new parents are better then all other individuals not taken into the new parents. After this is done, the off-spring of the new parents is created using the evolutionary operators: selection, reproduction, and mutation. The pseudo-code for this algorithm can be found in algorithm 4.1. A graphical representation of the optimization procedure is given in figure 4.3.

Algorithm 4.1 NSGA-II algorithm.

$R_t = P_t \cup Q_t$ ▷ Combine parents and off-spring to create new population.
$\mathscr{F}$ = non-dominated-sort(R_t) ▷ $\mathscr{F} = [\mathscr{F}_1, \mathscr{F}_2, ...]$
$P_{t+1} = \emptyset$, $i = 1$
while $|P_{t+1}| + |\mathscr{F}_i| \leq n_{pop}$ **do** ▷ Until new generation is full.
    Crowding-distance-sort($\mathscr{F}_i$)
    $P_{t+1} = P_{t+1} \cup \mathscr{F}_i$ ▷ Add crowding-distances sorted rank to new population.
    i = i + 1
end while
Crowding-distance-sort($\mathscr{F}_i$)
$P_{t+1} = P_{t+1} \cup \mathscr{F}_i[1 : n_{pop} - |\mathscr{F}_i|]$ ▷ Add the best $n_{pop} - |\mathscr{F}_i|$ of the final rank to the new generation.
Q_{i+1} = create-new-population(P_{t+1}) ▷ Use evolutionary operators to create off-spring.
$t = t + 1$ ▷ Go to next generation and repeat until convergence.

[1] `https://esa.github.io/pagmo2/docs/algorithm_list.html`, PaGMO 2, accessed: September 21, 2018

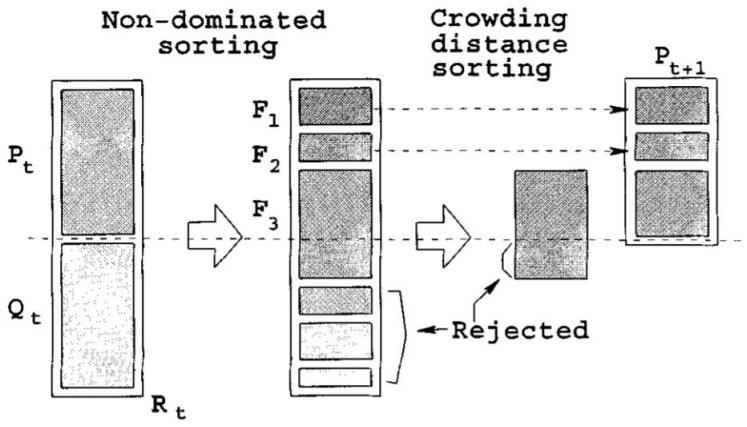

Figure 4.3: A graphical representation of the NSGA-II optimization algorithm, taken from Deb et al. [2002].

4.4.2. MOEA/D

Multi-Objective Evolutionary Algorithm based on Decomposition (MOEA/D) was developed by Qingfu Zhang and Hui Li [2007], and works on the principle of decomposing the multi-objective problem into several scalar single-objective problems.

This algorithm uses a weight vector $\boldsymbol{\lambda}$, with $\lambda_i \geq 0$ for all $i = 1, ..., m$, and $\sum_{i=1}^{m} \lambda_i = 1$. The scalar optimization problem is then formulated as follows:

$$\underset{\boldsymbol{x}}{\text{minimize}} \quad g(\boldsymbol{x}|\boldsymbol{\lambda}, \boldsymbol{z}^*) = \max_{1 \leq i \leq m} \{\lambda_i | f_i(\boldsymbol{x}) - z_i^*|\} \tag{4.19}$$

where $\boldsymbol{z}^*$ is a reference point given by:

$$z_i^* = \min\{f_i(\boldsymbol{x}) | x \in \Omega\} \tag{4.20}$$

where Ω is the bounded population space. The principle on which the algorithm can then optimize the problem is the fact that for each Pareto optimal point $\boldsymbol{x}^*$ (see section 4.4.1), there exists a weight vector $\boldsymbol{\lambda}$ such that $\boldsymbol{x}^*$ is an optimal solution of eq. (4.19). Furthermore, each optimal solution of eq. (4.19) is a Pareto optimal solution of eq. (4.16). This means that by altering the weight vector, it is possible to obtain different Pareto optimal solutions.

The MOEA/D optimization framework can then be set up as follows. First a set of N weight vectors $\boldsymbol{\lambda}^1, ..., \boldsymbol{\lambda}^N$ are generated using either a random or a grid generation process (see Qingfu Zhang and Hui Li [2007] for a more detailed explanation of these processes), and a reference point $\boldsymbol{z}^*$ is generated. The problem can then be decomposed into N scalar optimization problems, using the so called Tchebycheff approach:

$$g(\boldsymbol{x}|\boldsymbol{\lambda}^j, \boldsymbol{z}^*) = \max_{1 \leq i \leq m} \{\lambda_i^j | f_i(\boldsymbol{x}) - z_i^*|\} \tag{4.21}$$

these N problems are then simultaneously optimized using an evolutionary algorithm. The advantage of this algorithm is that $g(\boldsymbol{x}|\boldsymbol{\lambda}^j, \boldsymbol{z}^*)$ is continuous in λ^j. Which means that a solution to problem k can give information on problem j, if $\boldsymbol{\lambda}^k$ is close to $\boldsymbol{\lambda}^j$.

The specific steps taken can be seen in algorithm 4.2.

4.4.3. Constraints

The handling of constraints in an optimization algorithm can be done in several ways. One option is to optimize the constraint variables separately. An example of this is shown in Edelman and Longuski [2017], where the combined radiative and convective heat flux was minimized given a pre-determined trajectory. This allows for a good determination of the optimal constraint value; however, it is also possible to diminish the objective variables when optimizing the constraint value. Another option is to discard the trajectories which exceed the constraints during the optimization runs (see e.g. Hess [2016]). This will guarantee that no trajectory can exceed the constraints, however it also results in information being lost in the optimization process, which can lead to possible sub-optimal solutions as these trajectories might be close to a feasible solution which is then discarded. This option will discard trajectories which might only exceed the constraints

Algorithm 4.2 MOEA/D algorithm.

EP= $\emptyset$ ▷ Used for storing optimal solutions.
Select n_b closest weight vectors to each $\boldsymbol{\lambda}^j$, using Euclidian distances, and store the indices in variable $B(i)$.
Generate initial population $\boldsymbol{x}^1, ..., \boldsymbol{x}^N$, and set $FV(i) = \boldsymbol{F}(\boldsymbol{x}^i)$.
Initialize $\boldsymbol{z}^*$. ▷ Done in PaGMO 2 using evolutionary algorithm tactics.
while Convergence criterion is not met. **do**
    $i = 0$
    while $i < N$ **do** ▷ Until all weight vectors are handled.
        Select two indices, k and l from $B(i)$.
        Generate new solution $\boldsymbol{y}$ from $\boldsymbol{x}^k$ and $\boldsymbol{x}^l$ using genetic operators.
        For each $j = 1, ..., m$, if $z_j < f_j(\boldsymbol{y})$, set $z_j = f_j(\boldsymbol{y})$. ▷ Update of $\boldsymbol{z}^*$.
        For each $j \in B(i)$, if $g(\boldsymbol{y}|\boldsymbol{\lambda}^j, \boldsymbol{z}^*) \leq g(\boldsymbol{x}^j|\boldsymbol{\lambda}^j, \boldsymbol{z}^*)$, set $\boldsymbol{x}^j = \boldsymbol{y}$ and $FV(j) = F(\boldsymbol{y})$. ▷ update neighbouring solutions.
        Add $F(\boldsymbol{y})$ to EP if $F(\boldsymbol{y})$ if no vectors in EP dominate $F(\boldsymbol{y})$, and remove all dominated vectors from EP.
        i = i + 1
    end while
end while

by a small fraction, but otherwise have good values for the objectives. This can be solved by introducing a penalty on the fitness function instead of discarding the whole trajectory. The fitness function is defined as the function that takes the output of the simulation and determines how well the objectives are met. Using a penalty to include the constraints, the fitness function will be calculated as follows:

$$\boldsymbol{f}(\boldsymbol{x}) = \boldsymbol{f}_{obj}(\boldsymbol{x}) + \boldsymbol{f}_{pen}(\boldsymbol{c}_{sim}) \tag{4.22}$$

where $\boldsymbol{f}$ is the final fitness value, $\boldsymbol{f}_{obj}$ is the fitness determined by the objective value, and $\boldsymbol{f}_{pen}$ is the penalty function given by:

$$\boldsymbol{f}_{pen}(\boldsymbol{c}_{sim}) = \sum_{i=1}^{N_{con}} w_i \frac{c_{sim,i}}{c_i} \tag{4.23}$$

where N_{con} are the number of constraints, w_i is the weight corresponding to the ith constraint, $c_{sim,i}$ is the resulting values for the ith constraint variable (determined for a single trajectory), and c_i is the ith constraint. The weight is set to zero if the constraint is not violated to not allow it to influence the objective fitness function. Using this method will allow the most information to be stored during the optimization process, but it will also allow trajectories with broken constraints to be found as optimal. Thus it is important to always check if these constraints are not exceeded in the final trajectory.

4.4.4. Performance Metrics

Having a single-objective optimization problem, or a multi-objective optimization problem where one of the variables is more important as a performance metric (see chapter 7), allows the result from an optimization run to be evaluated using just the value found for this objective variable. Having a multi-objective optimization problem where multiple objective variables are important to evaluate the performance of the results, complicates the evaluation of a single Pareto front. A Pareto front should be evaluated on several criteria:

- Minimal distance between the Pareto front and the theoretical optimal Pareto front.
- A uniform distribution of the Pareto front.
- A wide spread of solutions for each objective.

Zitzler et al. [2000] showed that there are two performance metrics that can be used together to evaluate the performance of a Pareto front compared to another.

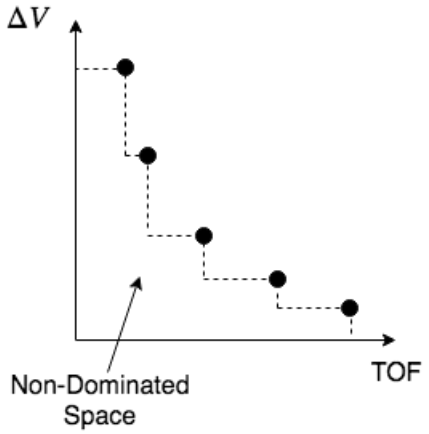

Figure 4.4: The non-dominated space of a Pareto front. The smaller this space is, the better the Pareto front.

The first performance metric is called the non-dominated space S, and is shown in figure 4.4. This performance metric determines the space between the Pareto front, and the theoretical optimal-Pareto front of the objectives. If S is lower for one Pareto front, there are fewer trajectories that can dominate the Pareto front and thus the performance of that Pareto front is better. S covers all three criteria for the evaluation of the Pareto front, thus it cannot evaluate differences between these criteria for different Pareto fronts. A performance metric that can be used in combination with S is the coverage of two different Pareto fronts. Take two Pareto fronts: A and B. The function $C(A,B)$ maps the combination (A,B) to $[0,1]$, and is given as follows:

$$C(A,B) = \frac{\{b \in B;\, \exists a \in A : a \succ b\}}{|B|} \tag{4.24}$$

where $a \succ b$ means that solution a dominates solution b. This performance metric thus determines the fraction of Pareto front B that is dominated by A. If $C(A,B) = 0$, no individual in B is dominated by A, and if $C(A,B) = 1$, all individuals in B are dominated by A. It is important to note that $C(A,B)$ is not necessarily equal to $C(B,A) - 1$. The combination of these two metrics allow Pareto fronts to be evaluated and compared for all three criteria.

5

Simulator Design and Verification

The previous chapters all discussed the various models and tools needed for the simulation of the atmospheric trajectory of an AGA. These tools and models now need to be combined into a software package that is able to simulate the AGA and use it for further research.

This chapter discusses how the simulation environment is built, and performs a verification of the simulator. Section 5.1 will first go through how the simulation environment, and the dynamics simulator inside, are set-up. Then, section 5.2 discusses the process of verifying that each module of the simulator works as expected. This process includes the verification of the implementation of previously done work into the simulator (e.g. vehicle aerodynamics of Hess [2016]) and the newly designed modules (e.g. the node control module). After the modules are all verified separately, the full simulator is verified. Finally, the models that will be used for the generation of optimal atmospheric trajectories are chosen in section 5.3.

5.1. Atmospheric Trajectory Simulator

The simulation environment was built using the TU Delft Astrodynamics Toolbox, or Tudat[1]. Tudat was built by the Astrodynamics and Space Missions section at the TU Delft, and is publicly available.

The atmospheric trajectory simulator consists of several parts. How the environment of the simulator is built up is shown in figure 5.1. The main module is the dynamics simulator, shown in more detail in figure 5.2, which takes as an input the integrator and propagation settings. The integrator and its settings were discussed in section 4.1, and need as an input: the type of integrator, (if a fixed time-step integrator is used) the time-step size, and the initial time from which the simulation is started. The propagation settings describe the equations of motion of the system (using the user defined acceleration models, defined inside the acceleration list), the different bodies that are used in the simulation, the initial state of the system, for which condition(s) the simulation is terminated, and which variables are outputted by the simulator.

The vehicle module inside the simulation environment is built up from different sub-modules. The aerodynamic interface consists of two tables of aerodynamic coefficients: the table for the continuum flow coefficients and the table for the free molecular flow (FMF) coefficients. How these coefficients are determined, and on which variables they are dependent on, is discussed in chapter 3. The aerodynamic interface is responsible for selecting the correct coefficients from the flight conditions during the simulation, and determining the transitional flow coefficients using Eq. (3.12). The vehicle properties sub-module contains all the different properties of the vehicle that are used to determine several other parameters during the simulation (e.g. heating from the nose radius, Knudsen number using the reference length , etc.). Finally, the guidance sub-module is needed to define the desired control variables needed during the simulation. This is discussed in more detail in section 2.5.2.

The planets and other Solar System bodies that are used in the simulation are developed in another module. This module produces a list of bodies with all of their properties and environment models. The chosen environment models are: the atmosphere model, the rotational model, the ephemeris, and the gravitational field model. All of these models are discussed in more detail in section 2.4. After each planetary body has the selected environment models incorporated, they are combined with the waverider model to a larger list of all bodies included in the simulation.

[1] `Tudat:http://tudat.tudelft.nl/`, TU Delft Astrodynamics Toolbox, accessed: October 22, 2018

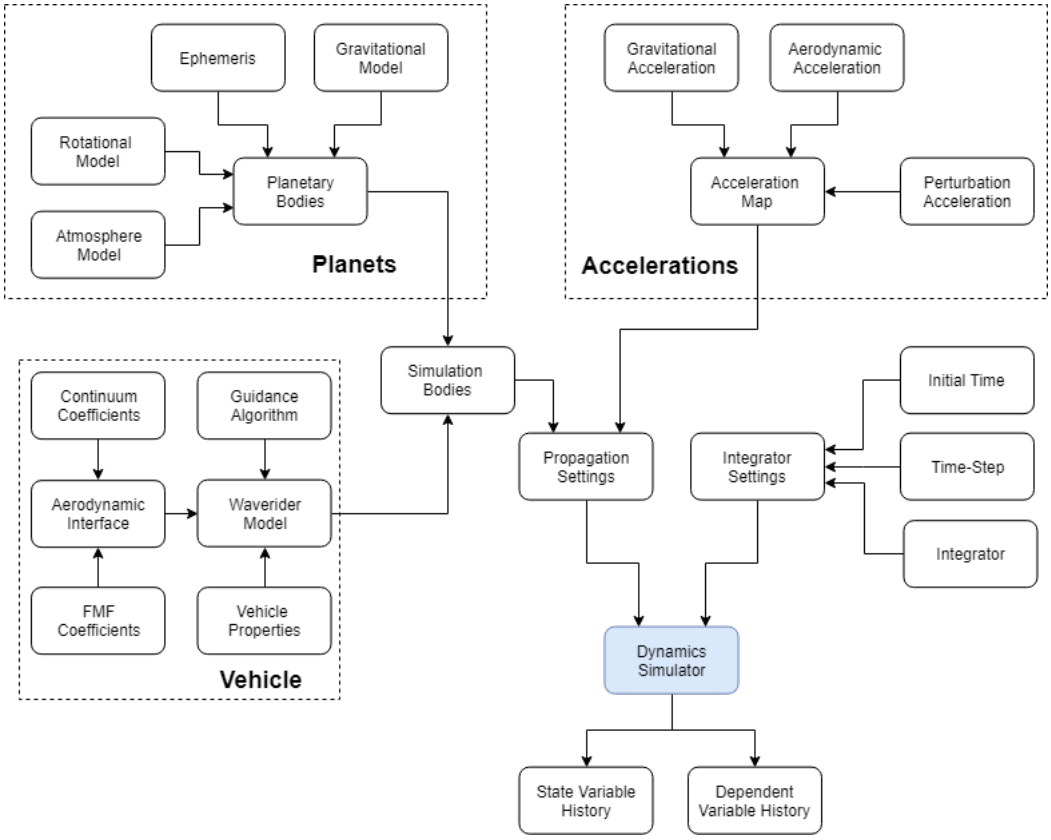

Figure 5.1: The set-up of the simulation environment.

The third module is the accelerations module. In the accelerations module, a list is made which links the bodies chosen in the simulation bodies list to (multiple) acceleration model(s) and to the body exerting this acceleration. Thus, for example, a gravitational acceleration model can be implemented, which is exerted by Mars on the waverider. The acceleration models are divided into three sub-modules, which correspond to the three different components of the equations of motion defined in section 2.2: the gravitational acceleration models, the aerodynamic acceleration models, and the perturbation acceleration models. The specific acceleration models that can be selected are discussed in more detail in section 2.3.

Both the simulation bodies list and the acceleration model list are then added to the propagation settings, which are then used as an input to the dynamics simulator module together with the integrator settings. The dynamics simulator then performs the simulation and outputs the state variable history and the dependent variable history for analysis.

The set-up of the dynamics simulator is shown in figure 5.2. The dynamics simulator module is responsible for taking all the settings from the propagator and integrator and using them to simulate the system in question. The main module is the dynamics modules, shown in blue in figure 5.2. This module collects all the information of the acceleration models and the current state and control variables, and combines them to determine the equations of motion of the whole system. The state of all the bodies is then propagated to the next point in time using these equations of motion and the integrator settings selected by the user. The state at that point in time is then given to the vehicle system module, the flight conditions module, the guidance algorithm module, and back to the dynamics module. The vehicle systems module uses the state and the flight conditions at the current point in time to determine the aerodynamic coefficients of the waverider. It also gives several parameters (the mass, length, and nose radius of the vehicle) to the flight conditions module. The flight conditions module uses these vehicle parameters, and the current state of the vehicle, to calculate several parameters that are needed in the rest of the dynamics simulator. These parameters include: the local density, the local pressure, the local temperature, the airspeed, the Mach number, the Knudsen number, the g-load, the convective and radiative heating, the location with respect to the other bodies, and the atmospheric composition at that location. The flight conditions are then given to the acceleration and environment models, which together can determine the accelerations acting on all the vehicles in the simulation.

Input	Output
List of Bodies with corresponding acceleration and environment models	State history
Vehicle parameters	Dependent variable history (e.g. flight conditions, control profile, etc.)
Aerodynamic database	
Guidance matrix: Γ	
Initial state	
Integrator settings	

Table 5.1: Inputs and outputs of the atmospheric trajectory simulator.

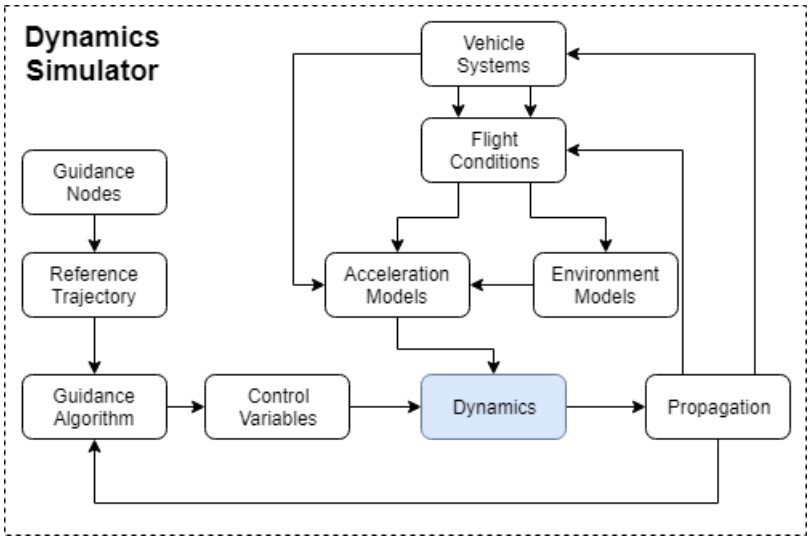

Figure 5.2: The set-up of the dynamics simulator inside the simulation environment.

This information is then given back to the dynamics simulator. Looking back at the propagated state, this is given back to the dynamics module and the guidance algorithm. The guidance algorithm takes the reference trajectory, and calculates the current atmospheric bending angle to determine the desired control variables (this process is discussed in more detail in section 2.5.2). These control variables are then finally used as an input to the dynamics module.

This loop is repeated until the dynamics module notices that one of the termination conditions is met. The simulation will then be terminated and the history of the state of each body, combined with the history of the dependent variables saved mostly in the flight conditions module, will then be given back to the user.

The inputs and outputs of the simulation can be seen in table 5.1.

5.2. Simulator Verification

After the simulation is built, the different modules inside the simulator need to be verified. This is done by either testing it to see if the simulator output is the same as the predicted output, or compare it to other sources. Once these modules are all verified, the simulator can be used further in this research project.

5.2.1. Modules Verification

Each separate module of the simulator first needs to be verified. A part of the simulation modules does not need to be verified separately as these modules are already part of the Tudat libraries and are verified using unit tests present in Tudat. These modules are listed below.

- **Planet Ephemerides.** The translational and rotational ephemerides of the planets are taken from the SPICE[2] software package, developed at the Jet Propulsion Laboratory. The implementation of these ephemerides are tested in the unit tests by comparing the Tudat outputted values with the actual values from SPICE.

- **Exponential Atmosphere.** The exponential atmosphere model is readily available in Tudat and is verified by taking hand calculated values and values from the US standard atmosphere and comparing them with the output of the exponential atmosphere.

- **NRLMSISE00 Atmosphere.** The NRLMSISE00 atmosphere model has already been implemented in Tudat and a unit test to verify the implementation has also been developed. This unit test compared the output values with hard coded values obtained directly from the model.

- **Gravity Models.** Both the point mass gravity model and the spherical harmonics gravity model are present in Tudat. The point mass model is verified using hand calculated values, whereas the spherical harmonics model is checked using values from the National Geospatial-Intelligence Agency (NGA), retrieved from Matlab[3].

- **Astrodynamics.** Tudat contains several functions for astrodynamical purposes that are used in the simulator. These functions are mainly to convert between coordinate frames and calculate several properties of orbits. The coordinate transformations are checked by comparing the coordinate values to hand calculated values, and the basic functions are tested in the same manner.

- **Flight Dynamics.** The flight dynamics module in Tudat takes the acceleration and environment modules and integrates the created equations of motion. This is tested using various unit tests in different modules by comparing the integrated values with expected, hand calculated values.

All of these unit tests were performed before the simulation was built to ensure a correct usage of these modules. All of the unit tests passed the verification and can thus be used in the simulator.

The building of the other modules in the simulator was discussed in the previous chapters. These modules need to be verified before the research can be continued. Below are the modules listed that need to be verified.

- **Guidance Algorithm.** The guidance algorithm consists of two parts that need to be verified. The first part is the node control algorithm. This module is tested by inputting a set of α nodes and observing if the outputted α corresponds to the expected output. As can be seen in figure 5.3, the α flown by the vehicle in the simulator reaches each node, except for the final two nodes. These final two nodes are not reached as the simulation stops due to the vehicle leaving the atmosphere before reaching these nodes. The α profile of figure 5.3 also shows that the connection of nodes is done in a smooth manner, without any overshoot or discontinuities. This shows the correct implementation of the Hermite spline interpolator.

  The other part of the guidance algorithm is the bank reversal. This part of the algorithm changes the sign of the bank angle when a certain inclination is reached. This inclination can be set using the inclination tolerance, i_{tol}. i_{tol} will be set at 3 degrees from the initial inclination and the bank angle rate at 20 degrees per second. If the algorithm is correct, the inclination will go over the tolerance value for a trajectory where σ is used, and a bank reversal is initialized. The results are shown in figure 5.4. It can be seen that when the inclination exceeds the tolerance, the bank reversal is engaged and the inclination changes direction. This verifies that the bank reversal algorithm functions as designed.

- **EMCD atmosphere model.** The ESA Mars Climate Database is used in this research project by the simulation to obtain the density, temperature, pressure, and ratio of specific heats, as a function of altitude. The implementation of this model is done off-line and is independent of longitude, latitude, and time. Thus to verify if the model is correctly implemented (assuming that the model itself is verified, which was done by comparing them with measurements of several missions by Justh et al. [2011]), the values from the model were compared with values from the simulation. It was verified that all values (temperature, density, pressure and atmospheric composition) given by the simulation are equal to the values given by the EMCD.

[2] `https://naif.jpl.nasa.gov/naif/spiceconcept.html`, accessed 12 April 2018
[3] `https://nl.mathworks.com/help/aeroblks/sphericalharmonicgravitymodel.html`, accessed 12 April 2018

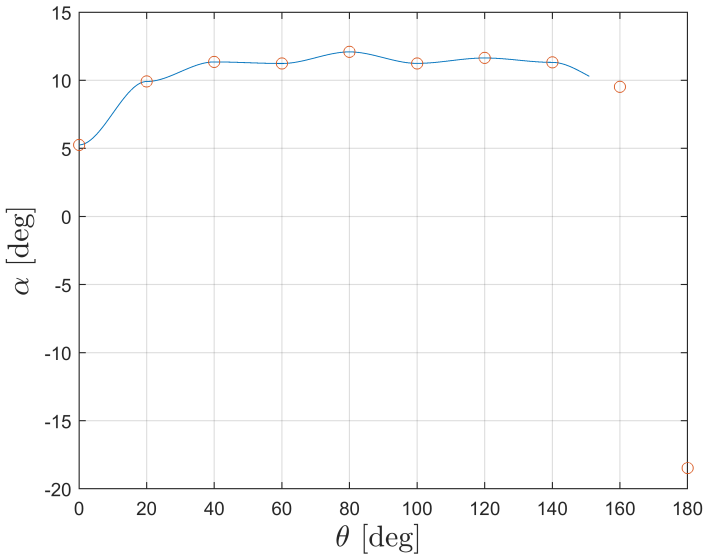

Figure 5.3: The angle of attack as a function of the atmospheric bending angle, where the continuous line is the output of the simulation, and the rings are the input angle of attack nodes.

- **Aerodynamics.** The aerodynamic database used in this simulation is retrieved from Hess [2016]. The database contained the aerodynamic coefficients of the vehicle as a function of the Mach number, angle of attack, sideslip angle, airspeed, and Knudsen number. The values of the aerodynamic coefficients, outputted by the simulation, are compared to the values in the database and it was found that these values are equal. The verification of the generated aerodynamic coefficients was performed by Hess [2016], and it is thus assumed here that these aerodynamic coefficients are correct.

- **Heating.** Tudat calculates the heat flux using the Fay-Riddell method. For the purpose of this research, two new methods, the Sutton-Graves convective heat flux and the Tauber-Sutton radiative heat flux, were implemented (see section 3.3). Heat fluxes outputted by the simulator were compared to hand calculated values and shown to be equal. The specific equations used here are verified using mission data, as is shown in section 3.3.

5.2.2. Full Simulator Verification

Besides the verification of the different individual modules of the simulation, it is also important to verify that they are incorporated into the simulation well and that the interfaces function correctly. This is done by verifying the complete simulator.

This verification is done using the analytical equations of motion given by Eqs. (2.10) - (2.15). All of the parameters present in these equations are outputted by the simulator either though the state history or through the dependent variable history. These variables can be differentiated numerically using the central differencing technique [Press et al., 1992]. If the numerically differentiated variables are then compared to the analytically computed ones using the flight conditions of the simulation, the simulator can be verified. The results are shown in figure 5.5. It can be seen that the numerical and analytical results coincide, and thus the simulator behaves as expected.

5.3. Model Selection

The simulator discussed in this thesis is capable of performing various tasks. For example, sensitivity analyses can be done to investigate the sensitivity of the atmospheric trajectory to perturbations. Or guidance, navigation, and control algorithms can be tested and validated for a specific AGA mission trajectory. These tasks have in common that they require acceleration and environment models with a high accuracy. Furthermore, numerical inaccuracies (e.g. truncation errors due to the numerical integrator) have to be minimized to allow for a high fidelity simulation of a specific trajectory. This thesis will use the simulator to determine the achievable performance of an AGA compared to a GA, which is done by optimizing the atmospheric tra-

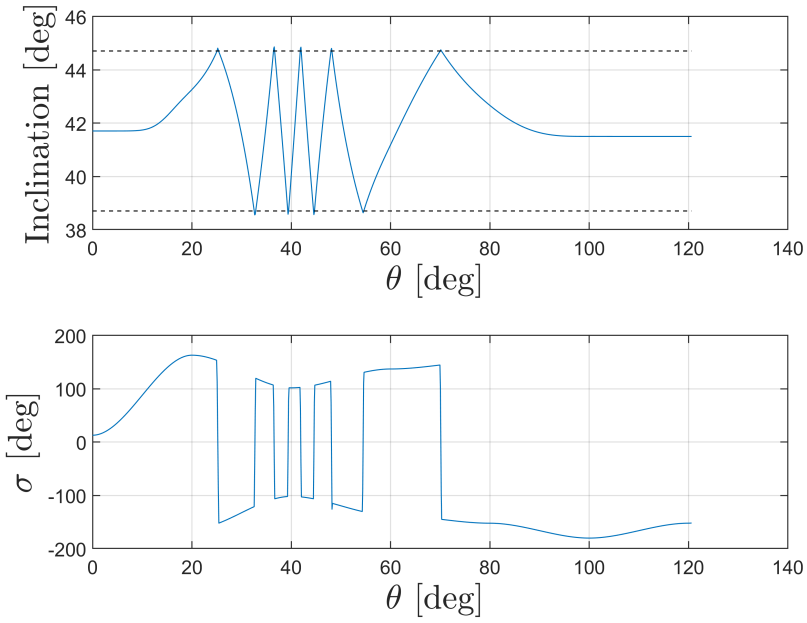

Figure 5.4: Above: the inclination as a function of the atmospheric bending angle. The tolerance is shown by the dotted lines. Below: the bank angle as a function of atmospheric bending angle.

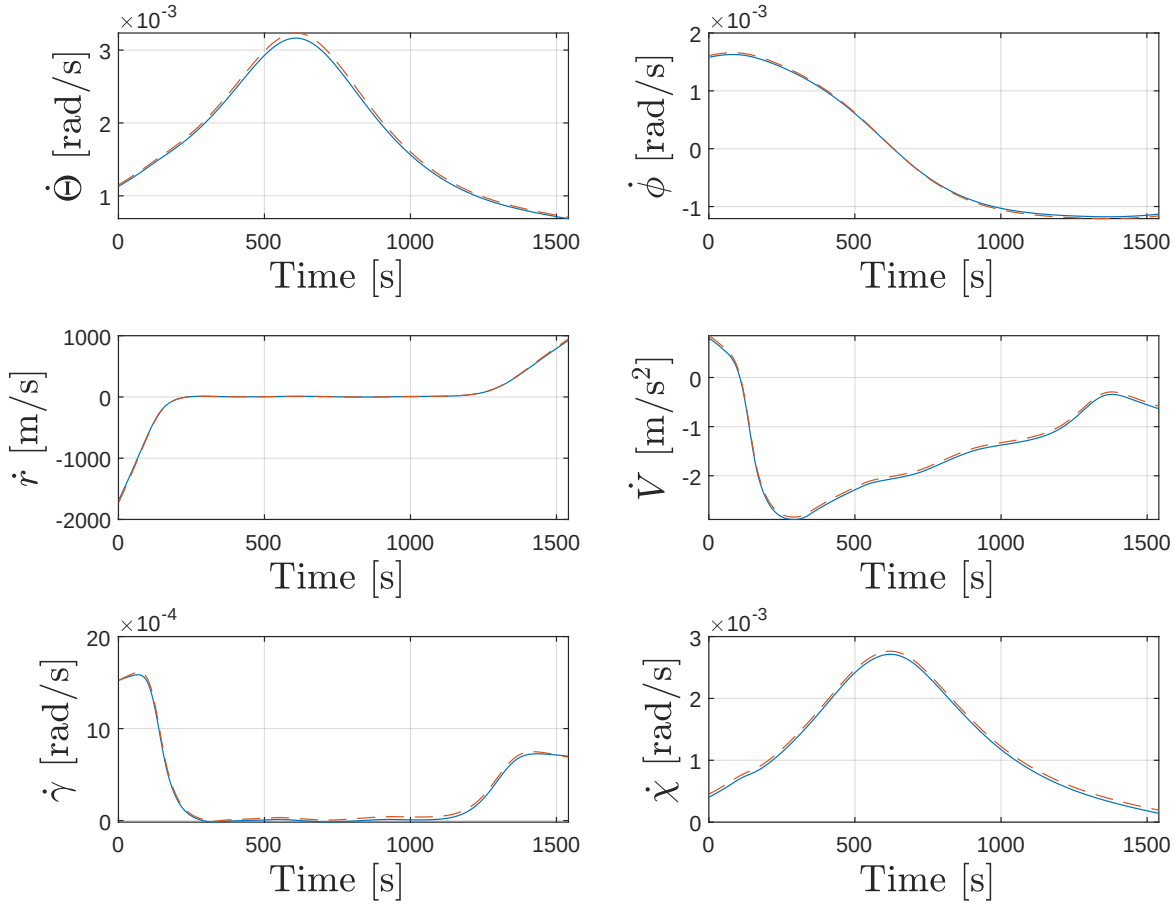

Figure 5.5: The verification of the complete simulator, where the dashed line is the analytic equations of motion and the solid line the numerical solution.

jectory of the AGA. The optimization process, which is discussed in section 4.4, requires a large amount of simulations to be run as this will allow the algorithm to find the optimal trajectory. Thus for this thesis it is important to make a trade-off between accuracy and computational efficiency. In general, a specific model is selected on the basis that an increase in accuracy of a model does not change the achievable performance of the AGA significantly compared to a less accurate model which has a significantly lower run-time. The following discussion goes through the different models and gives a qualitative discussion on which model is going to be used to develop the results given in chapter 7 and 8.

The exponential atmosphere will be taken as the atmosphere model for each planet. This model is computationally efficient as it can be evaluated using a simple equation and, as was shown in section 2.4, the exponential model follows the higher fidelity models reasonably well. In general, the flight of the vehicle through the atmosphere can be separated into three sections: atmospheric entry, equilibrium gliding flight, and atmospheric exit. As will be shown in section 7.4, the section that influences the performance the most is the gliding flight. In general, the gliding flight takes place at a certain density of the atmosphere selected by the optimization algorithm. This density of the gliding flight does not change when a different atmosphere model is taken, however the altitude does change slightly as the density-altitude profile is different between models. Thus it is expected that although the specific trajectory that is flown can differ slightly between the two models, the resulting performance will not change significantly.

All the different aerodynamic regimes (free molecular regime, transitional regime, and continuum regime) will be implemented into the simulation as the aerodynamic forces dominate most of the simulation. The central gravity field model will be used, as higher order gravitational coefficients are expected to not have a large effect due to the shorter flight time and the much higher aerodynamic accelerations. Gravitational models like the spherical harmonics model also require higher computation times compared to the central gravity model due to the large number of coefficients present in the equation. The perturbation accelerations will also not be implemented as they are not as important during the atmospheric flight compared to the exo-atmospheric flight. This also implies that only a constant ephemeris setting is needed for the central body as only the relative position between the central body and the spacecraft is needed. This also decreases the computation time as the ephemeris for the bodies that exert a third-body perturbation do not need to be implemented. The rotational model is, however, important for the dynamics of the atmospheric flight (see Eqs.(2.10) and (2.15), and thus a rotational model is taken using the SPICE toolkit. A more quantitative validation for the use of all of the models given here compared to higher fidelity models is given in section 7.4.2 and appendix B.

Section 4.1 discussed the numerical integration options and chose the RK4 integrator with a 1 second time-step to be used in this thesis. This selection is discussed and validated in more detail here. The accuracy of the RK4 integrator for the integration of the EOM for an AGA has been tested using several integrators with different time-step sizes. The specific AGA that is used is performed at Earth using the models discussed before. These trajectories are compared with a baseline trajectory (which reached a final atmospheric bending angle of 60 degrees), simulated using an RK4 integrator with a time-step size of 0.01 seconds. The other time-step size were selected between 0.05 seconds and 10 seconds. Furthermore, to diminish the effects of non-numerical errors on the analysis, the time-step sizes were selected to be integer ratios of each other. This makes sure that all the different integrators are at least evaluated at the same points in time as the other integrators, the difference being how many times the integrators are evaluated between those times. The results are shown in figure 5.6. Both the errors in final location and atmospheric bending angle with respect to the baseline trajectory are shown. The error in location reaches a maximum of 7.5 km for a time-step of 10 seconds, however the error in atmospheric angle is only 0.09 degrees. As will be shown in chapter 7, the atmospheric angle will be used as an important parameter in this research project. Thus when the goal of the trajectory generated is to determine this angle, a RK4 integrator with a relatively large time-step can be used as this will allow relatively quick computation times and less complexity in several simulation components (compared to variable step-size integrators), while still giving a reliable results. However, for more accurate purposes, e.g. sensitivity analyses or guidance algorithm testing, a more efficient integrator should be used.

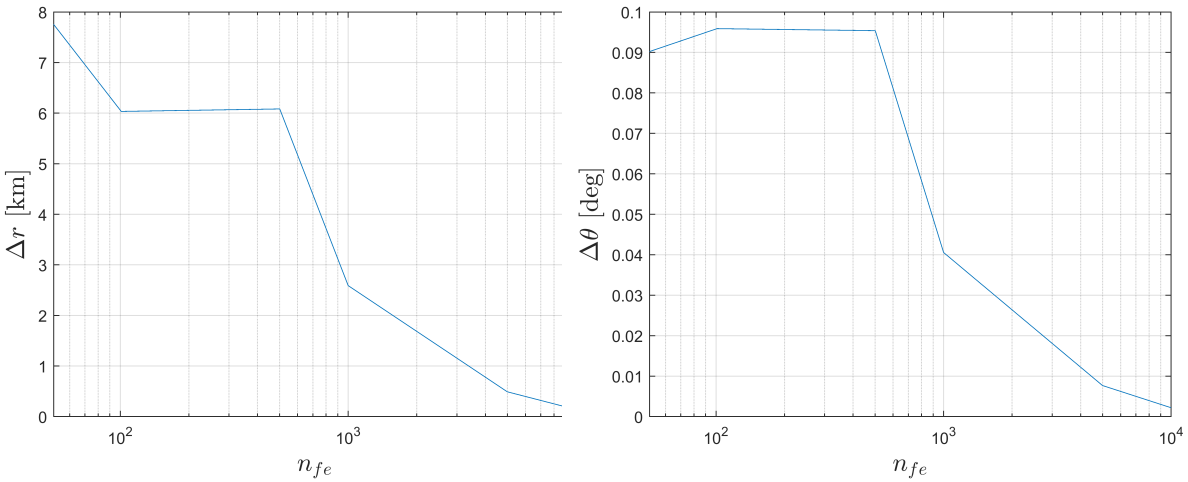

(a) Error in the final position.

(b) Error in the final atmospheric angle.

Figure 5.6: The accuracy of the RK4 integrator as a function of the number of evaluations of the EOM. The baseline trajectory is made with a RK4 inegrator with a 0.01 second time step.

6

Interplanetary Mission Planner

The simulator discussed in chapter 5 covers the aerogravity assist from the entry of the atmosphere to the vehicle exiting the atmosphere again at the end of the trajectory. This simulator can determine the performance of the AGA and show the specific trajectory it needs to take through the atmosphere to reach its goals. However, to complete the analysis of the AGA, the atmospheric trajectory needs to be linked to the interplanetary trajectory to determine its benefits compared to the GA. To be able to do this an interplanetary mission planner needs to be built that can simulate the whole trajectory, including: departure from the initial planet, interplanetary travel, gravity assists, aerogravity assists, and capture at the target body. Part of this mission planner was previously developed by Musegaas [2012], whose mission planner will be used as a basis for the mission planner developed in this thesis. Musegaas [2012] developed a planner that could calculate the total ΔV and time-of-flight (TOF) of a pre-defined trajectory using only gravity assists at the intermediate planets. The mission planner assumptions are that patched conics is used, no perturbations are considered, and the mission planner uses only single revolution transfers to build the transfers between planets. This thesis will focus on adding the aerogravity assist to this planner and seeing how this can make a difference compared to a gravity assist at the same location.

Section 6.1 will discuss the different mission segments of the interplanetary mission planner, and how the atmospheric trajectory simulator of chapter 5 will be used to develop the aerogravity assist mission segment. In the next section, section 6.2, the design of the mission planner and its verification are discussed.

6.1. Mission Segments

The interplanetary mission planner consists of various trajectory models (discussed in section 6.2) for each leg of the mission. These trajectory models are built up from mission segments, which are astrodynamics functions that are used to determine various parameters of the trajectory. Each separate trajectory model uses different mission segments, or uses them in a different order, compared to other models. This section will discuss the different mission segments and what they can be used for in the mission planner.

Section 6.1.1 discusses the Lambert targeter, which can be used to determine a Keplerian trajectory between two points in space for a given time-of-flight. Then, section 6.1.2 explains how a gravity assist works, and how it can be used in the mission planner. How the aerogravity assist will be used inside the mission planner will then be discussed in section 6.1.3. Finally, the capture of the spacecraft around the target planet is the focus of section 6.1.4.

6.1.1. Lambert Targeter

A Lambert targeter is an algorithm that can solve Lambert's orbital boundary-value problem. Lambert's problem can be stated as follows[Gooding, 1990]: find an unperturbed orbit connecting two points in space, $P(t_0)$ and $P(t_f)$, around a central body, C, given a specific time-of-flight (TOF): $\Delta t = t_f - t_0$. There will always be at least one solution, which depend on the geometry of the triangle connecting the central body, $P(t_0)$,and $P(t_f)$ and on the specified TOF Δt. The geometry of this problem is shown in figure 6.1.

Observing figure 6.1, there must always be two different solutions: the one covering the ellipse over an angle ϕ, or the one over an angle $2\pi - \phi$. However, as interplanetary trajectories are considered and all planets move in a counter-clockwise direction around the Sun, the clockwise solution can be neglected.

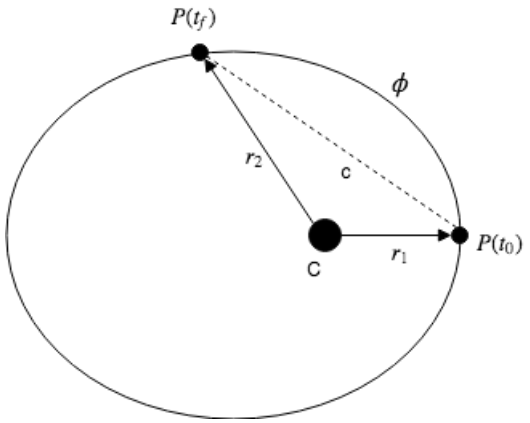

Figure 6.1: The geometry of the Lambert problem.

It was shown by Lambert that the solution to this problem only depends on the semi-major axis a, the sum of the distances r_1 and r_2, and the chord c, which is summarized in Lambert's Theorem [Wakker, 2015]:

$$\sqrt{\mu}(t_f - t_0) = f(a, r_1 + r_2, c) \tag{6.1}$$

Since the TOF, r_1, r_2, and c are known, the problem becomes finding the appropriate a for the orbit linking $P(t_0)$ and $P(t_f)$.

There are various methods to solve this problem efficiently. The explanation and discussion of these methods is out of the scope of this thesis and readers are referred to either Gooding [1990] or Secretin [2012] for a more detailed explanation of the various methods to solve Lambert's problem. This mission planner uses Izzo's method [Izzo and Dario, 2014] to solve Lambert's problem. It was found by Musegaas [2012] that this method is relatively efficient and accurate, and thus it was chosen to be used in this research project. It is also noted that for the mission planner not only the ellipse section connecting the two points is necessary, but also the initial and final velocity along the ellipse are needed. The method to obtain these velocities is discussed in Secretin [2012] and will be used in the mission planner.

6.1.2. Gravity Assist

Chapter 1 already gave an introduction on what the gravity assist (GA) is and the working principle behind it. This section will go into more detail behind the GA, discuss the mathematical framework behind it, and how it is implemented in the mission planner.

The principle behind the GA is the exchange of momentum between the spacecraft and planet during the fly-by. Using the conservation of momentum, the following equation can be set-up:

$$m_s \boldsymbol{V}_s^{I,-} + m_p \boldsymbol{V}_t^{I,-} = m_s \boldsymbol{V}_s^{I,+} + m_t \boldsymbol{V}_t^{I,+} \tag{6.2}$$

where the subscript s stands for the spacecraft, the subscript t for the target planet, the superscript $-$ stands for the incoming leg, and the superscript $+$ stands for the outgoing leg. The velocities in this equation are taken in the inertial (ecliptic) reference frame. This equation can be rewritten to:

$$\Delta \boldsymbol{V}_s = \boldsymbol{V}_s^{I,+} - \boldsymbol{V}_s^{I,-} = \frac{m_t}{m_s}(\boldsymbol{V}_t^{I,-} - \boldsymbol{V}_t^{I,+}) \tag{6.3}$$

As the mass of a planet is significantly larger then the mass of the spacecraft the velocity of the planet remains unchanged, whereas the velocity of the spacecraft does change significantly.

A detailed 2D geometry of the complete maneuver is given in figure 6.2 and a diagram representing the velocity vectors is given in figure 6.3. $\boldsymbol{V}_t'$ gives the component of $\boldsymbol{V}_t$ in the plane spanned by the incoming and outgoing hyperbolic excess velocities: V_∞^- and V_∞^+. V_∞ is defined as follows:

$$(V_\infty^P)^2 = (V_s^P)^2 - (V_{esc}^P)^2 \tag{6.4}$$

where V_{esc} is the escape velocity of the target planet. Due to energy conservation, the magnitude of V_∞^- and V_∞^+ is equal. However, these velocities are bent over an angle δ which results in a gain in the inertial velocity of

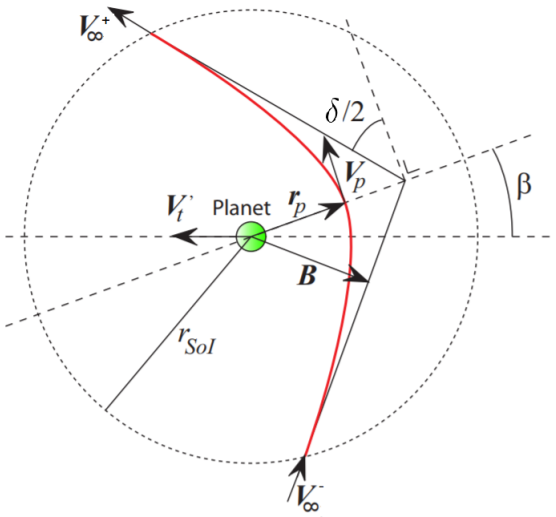

Figure 6.2: The geometry of the gravity assist. Adapted from Melman [2007].

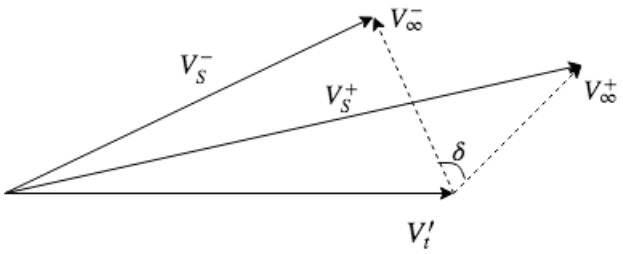

Figure 6.3: A velocity vector diagram for the gravity assist.

Planet	h_{min} [km]	Mission
Mercury	200	Messenger
Venus	284	Cassini
Earth	306	Galileo
Mars	257	Rosetta
Jupiter	42895	Pioneer 11
Saturn	20612	Pioneer 11
Uranus	81533	Voyager 2
Neptune	4482	Voyager 2
Pluto	9600	New Horizons

Table 6.1: The minimal height for an GA for all the planets achieved during several different missions. Data adapted from Melman [2007].

the spacecraft after the GA. This principle is sketched in figure 6.3. If the spacecraft passes behind the planet (as in figure 6.2), V_∞^+ gets aligned more with $\boldsymbol{V}_t'$ and thus $\boldsymbol{V}_s^{I,+}$ is increased. If the spacecraft would be pass in front of the target planet, $\boldsymbol{V}_s^{I,+}$ would be decreased.

Looking at figure 6.2, some important relations can be derived for the GA. Using the conservation of momentum, the following relation can be stated:

$$BV_\infty = r_p V_p \tag{6.5}$$

where B is the impact parameter (defined in figure 6.2) and the subscript p is used to determine quantities at the pericenter (the superscript of $\boldsymbol{V}_\infty$ is omitted as for a GA it remains constant). Wakker [2015] gives an equation for r_p:

$$r_p = -\frac{\mu}{V_\infty^2} + \sqrt{\frac{\mu^2}{V_\infty^4} + B^2} \tag{6.6}$$

Using this equation, and equations describing the geometry of an hyperbola, the following relation for the velocity bending angle can be found:

$$\sin\frac{\delta}{2} = \frac{1}{e} = \frac{1}{1 + \frac{r_p (V^{P,-})^2}{\mu}} = \frac{1}{\sqrt{1 + \frac{B^2 V_\infty^4}{\mu^2}}} \tag{6.7}$$

This equation shows that the velocity bending angle δ can be increased if: B is decreased, V_∞ is decreased, or if the planet is heavier. The performance of the GA is constrained by the radius of the planet, as if r_p is too small the spacecraft could impact on the surface of the planet. This constraints can be expressed as follows in an equation using the expression for the escape velocity given in Wakker [2015]:

$$B \leq R_t \sqrt{1 + \frac{V_{esc}^2}{V_\infty^2}} \tag{6.8}$$

This is a theoretical limit that needs to be taken into account when designing an GA. However, there are more parameters that also need to be taken into account. Harsh radiation environments close to the planet could harm the spacecraft subsystems, or the atmospheric drag close to a planet could slow down the spacecraft if an AGA is not used. A summary of the minimal heights above the planets used by previous missions is given in table 6.1. These heights will be used in the mission planner when calculating the GA.

The previous discussion was focused on the theoretical basis of the GA, the following section will use this theoretical basis to derive a method of implementing the GA into the mission planner. The mission planner allows the GA to be powered, i.e. an impulsive thrust maneuver can be applied at the pericenter, to obtain the optimal trajectory [Musegaas, 2012]. The method starts with the planetocentric velocity vectors:

$$\boldsymbol{V}_s^{P,\pm} = \boldsymbol{V}_s^{I,\pm} - \boldsymbol{V}_t^I \tag{6.9}$$

where the superscript P is the vector represented in the planetocentric reference frame, and I in the ecliptic, inertial, reference frame. The angle between $\boldsymbol{V}_s^{P,-}$ and $\boldsymbol{V}_s^{P,+}$ gives the desired velocity bending angle δ. Adding the bending angle before and after the impulsive thrust at the pericenter gives a relation between r_p and δ:

$$\delta = \delta^- + \delta^+ = \arcsin\frac{1}{1+\frac{r_p|\boldsymbol{V}_s^{P,-}|^2}{\mu}} + \arcsin\frac{1}{1+\frac{r_p|\boldsymbol{V}_s^{P,+}|^2}{\mu}} \tag{6.10}$$

This equation allows the maximum possible δ to be found by setting r_p to the minimum value (from table 6.1). The additional ΔV needed, and the method to calculate it, depends on if the maximum δ is sufficient for the desired δ or not. If the desired δ can be met, Eq.(6.10) will be used to solve for r_p. r_p can then be used to find the incoming and outgoing pericenter velocities. The difference between the pericenter velocities is the ΔV needed for the GA. To solve Eq. (6.10), a root-finding scheme needs to be employed. Musegaas [2012] discusses two different options for how to solve Eq.(6.10) using a Newton-Raphson scheme (using either the pericenter radius or the eccentricity), which will not be repeated here for brevity. If the maximum δ is not sufficient for the desired δ, an extra impulsive thrust needs to be performed [Wakker, 2015]:

$$\Delta V_{bend} = 2V_\infty \sin\frac{\Delta\delta}{2} \tag{6.11}$$

Thus, the spacecraft will approach at $r_{p,min}$, apply an impulsive thrust to patch the pericenter velocities, and, as discussed in Wakker [2015], will perform the impulsive thrust calculated by Eq.(6.11) to patch the bending angle once it leaves the SOI.

6.1.3. Aerogravity Assist

The basic principle of the aerogravity assist (AGA) has already been discussed in chapter 1, and more detail was provided on the different sections and subsystems of this maneuver in the previous chapters. This section will summarize the basic principle of the AGA, give some useful relations between the different parameters of the AGA, and discuss how the AGA will be used in the mission planner.

The AGA works on the same principle as the GA, that the exchange of momentum between the central body and the spacecraft increases the heliocentric velocity (i.e. the velocity in the ecliptic reference frame) of the spacecraft as was shown in Eq. (6.3). The geometry of the AGA is shown in figure 6.4. The difference with the GA is the fact that using the lift of the vehicle inside the atmosphere, the centrifugal force is counteracted and the vehicle can bend more around the central body compared to the GA. The gain of a longer velocity bending angle δ is shown in figure 6.5, where it can be seen that even though $\boldsymbol{V}_{\infty,AGA}^+$ is reduced compared to $\boldsymbol{V}_{\infty,GA}^+$ due to the atmospheric drag, the larger δ_{AGA} increases the heliocentric velocity $V_{s,AGA}^+$ significantly compared to $V_{s,GA}^+$. However, if a vehicle is used that is not aerodynamically efficient, or the vehicle stays in the atmosphere too long, $\boldsymbol{V}_{\infty,AGA}^+$ will not be large enough to increase $V_{s,AGA}^+$ compared to $V_{s,GA}^+$.

As was mentioned in section 6.1.2, the mission planner starts with the incoming and outgoing heliocentric velocities (i.e. taken in the ecliptic reference frame). From these velocities, the planetocentric velocity can be calculated using Eq. (6.9). At the start and end of the AGA mission segment, when the spacecraft enters and exits the SOI of the central body, the following assumption can be made: $\boldsymbol{V}_\infty^\pm = \boldsymbol{V}_s^{P,\pm}$. The mission planner thus receives the desired $\boldsymbol{V}_\infty^-$ and $\boldsymbol{V}_\infty^+$ from the Lambert targeter of section 6.1.1 and from the previously mentioned assumption, and from this it can calculate the desired bending angle for the AGA. This is similar to the GA; however, as the vehicle needs to enter the atmosphere, the initial velocity at the edge of the atmosphere needs to be calculated (at this point the simulation, discussed in chapter 5, will start). This can be done using the conservation of energy:

$$V_{atm} = \sqrt{|\boldsymbol{V}_\infty|^2 + \frac{2\mu}{r_{atm}}} \tag{6.12}$$

where r_{atm} will be defined in chapter 7. Once the vehicle enters the atmosphere, it will travel through it over an angle called the atmospheric bending angle θ. The relation between the achieved velocity bending angle $\delta(t_f)$ and θ can be found from figure 6.4 [Casoliva et al., 2008]:

$$\delta(t_f) = \frac{1}{2}\delta_{GA}(t_i) + \theta_p(t_i) + \frac{1}{2}\delta_{GA}(t_f) - \theta_p(t_f) + \theta(t_f) \tag{6.13}$$

where δ_{GA} can be taken from Eq.(6.7) using $e(t_i)$ and $e(t_f)$, and θ_p is defined as follows (where j can be either the initial or final value):

$$\theta_p(t_j) = \arctan\left(\frac{v(t_j)^2 \sin\gamma(t_j)\cos\gamma(t_j)}{v(t_j)^2\cos^2\gamma(t_j) - 1}\right) \tag{6.14}$$

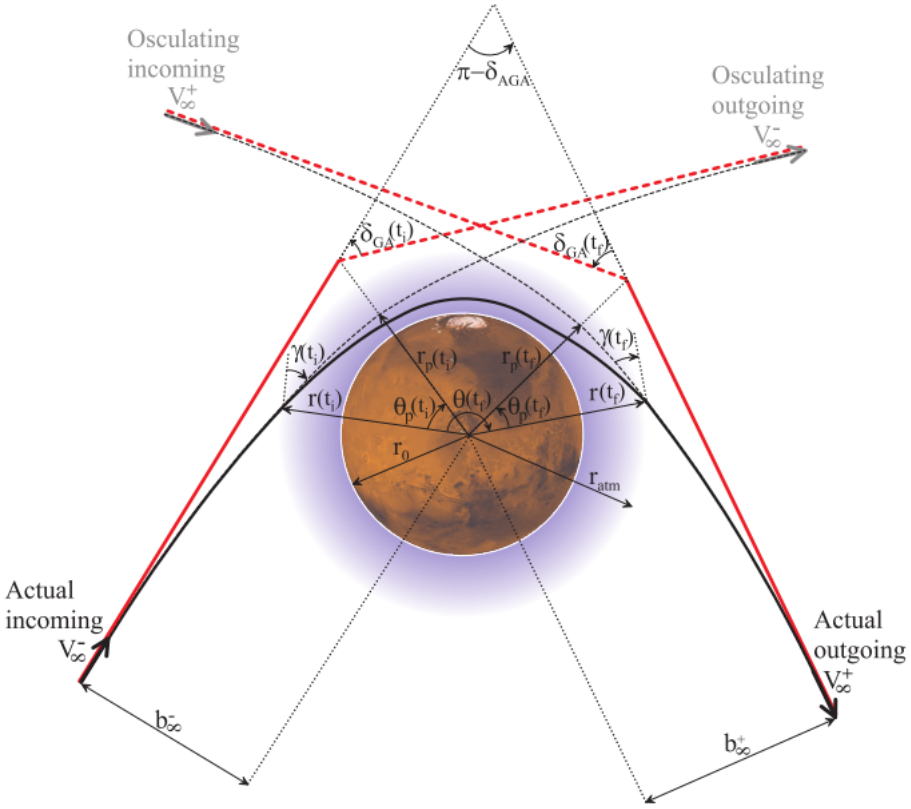

Figure 6.4: Geometry of the aerogravity assist. Adapted from Casoliva et al. [2008].

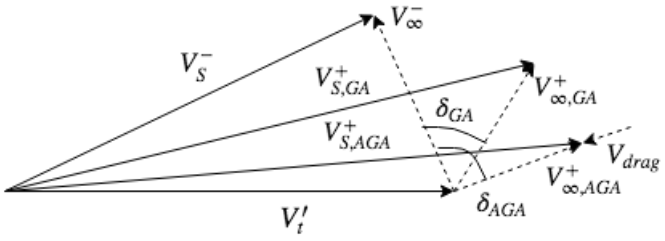

Figure 6.5: A velocity vector diagram for the aerogravity assist.

where γ is the flight path angle, and ν the normalized velocity defined by:

$$\nu(t_j) = \frac{V(t_j)}{\sqrt{\frac{\mu}{r(t_j)}}} \tag{6.15}$$

The only unknown variable in Eq. (6.13) is now θ, which can be determined by several different methods.

Henning et al. [2014] implemented a method to combine the atmospheric and interplanetary sections of the AGA into a mission planner. The interplanetary section uses a similar set-up as the mission planner of Musegaas [2012], where the V_∞ before and after an (A)GA is determined using a Lambert targeter. From this, the minimal needed L/D for that mission is determined using a two-point boundary value problem for the atmospheric section. This set-up uses several assumptions that this thesis improves upon. First, the aerodynamics of the waverider in Henning et al. [2014] are approximated using an user chosen maximum lift coefficient and a parabolic drag polar to determine its drag coefficient. Furthermore, the lift coefficient C_L is directly used as the control parameter (in contrast to α and/or β) and is allowed to vary freely between 0 and its maximum. Additionally, no heating constrains were added to the atmospheric optimization and the motion of the vehicle in the atmosphere was limited to 2 dimensions. This approach gives a good first indication of the possibilities of an AGA, but lacks accuracy in the possible atmospheric trajectories and will be improved upon in this thesis.

There are two approaches that can be used to implemented the AGA into the mission planner: in-the-loop atmospheric optimization (as is done Henning et al. [2014] using analytic optimization) and out-of-the-loop atmospheric optimization. The first option takes as an input the conditions at the start of the atmosphere from the mission planner and optimizes the atmospheric trajectory to find the optimal θ. If needed, the ΔV needed to reach the desired values of $V^+_{\infty,f}$ and δ_f will also be calculated. The problem with this approach is the computation time of one interplanetary trajectory. As will be discussed in chapter 7, the time it takes to run an optimization of the AGA with 3 seeds is around 15 hours (3.50 GhZ AMD A10 Radeon R7 processor with 10 cores, and 8 GB RAM). For an optimization of the whole interplanetary trajectory, the atmospheric trajectory will then be optimized around 600 times, which makes the total run time in-feasible.

The out-of-the-loop atmospheric optimization significantly decreases the run time as this method optimizes the atmospheric trajectories before the interplanetary trajectory is optimized. This is done by finding optimal atmospheric trajectories for a range of V^-_∞, where θ and V^+_∞ are maximized. Then, θ is used in Eq. (6.13) to calculate $\delta(t_f)$ and form a Pareto front together with V^+_∞, which is shown in figure 6.6. Through the Pareto front in 3D-space ($V^-_\infty(t_f)$, $V^+_\infty(t_f)$, and $\delta(t_f)$), a function is fitted that acts as a limiting surface for the mission planner. The mission planner will now input the desired parameters: $V^-_{\infty,f}$, $V^+_{\infty,f}$, and δ_f, and calculate the performance metrics defined as:

$$\Delta V_\infty = V^+_{\infty,f} - V^+_\infty(t_f) \tag{6.16}$$

$$\Delta\delta = \delta_f - \delta(t_f) \tag{6.17}$$

if the performance metrics are negative, the parameters will be seen as reachable and $\Delta V_{AGA} = 0$. If the performance metrics are positive, as in figure 6.6, a ΔV will be added to the interplanetary trajectory. There are three different options for the correctional burn: ΔV_{ν_∞}, ΔV_δ, and ΔV_c. ΔV_{ν_∞} is a burn to correct for the deficiency in V^+_∞ and is equal to Eq. (6.16). ΔV_δ is used when there is a deficiency in the final bending angle δ and is corrected using Eq.(6.11). Finally, ΔV_c is used when there is a deficiency in both V^+_∞ and δ, and is calculated according to the following equation [Casoliva et al., 2008]:

$$\Delta V_c = \sqrt{|\boldsymbol{V}^+_{\infty,f}|^2 + |\boldsymbol{V}^+_\infty(t_f)|^2 - 2|\boldsymbol{V}^+_{\infty,f}||\boldsymbol{V}^+_\infty(t_f)|\cos\Delta\delta} \tag{6.18}$$

where it is assumed that no extra ΔV is needed to correct for out-of-plane corrections. The method with the smallest ΔV is the one that is used.

The out-of-the-loop atmospheric optimization method is significantly better then the in-the-loop method from a computational efficiency standpoint, as the atmospheric trajectory only needs to be optimized for a pre-defined range of V^-_∞ instead of for each individual in an interplanetary trajectory optimization run. However, the gaps between the V^-_∞ that are not optimized are assumed to also have optimal trajectories, which is not guaranteed. This requires that if an AGA trajectory is found, the atmospheric trajectory should always be checked afterwards to exist. Due to its advantages over the in-the-loop method, the out-of-the-loop atmospheric optimization method is selected to be used for the AGA mission segment.

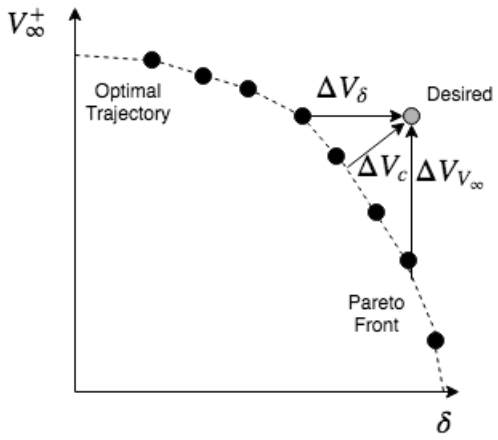

Figure 6.6: A diagram that shows how the ΔV for the out-of-the-loop aerogravity assist is calculated. The black dots are previously optimized trajectories and the grey dot is the desired output of the mission planner.

6.1.4. Departure and Capture

At the start and end of a trajectory there always needs to be a departure and capture maneuver respectively. The departure maneuver is a maneuver from a parking orbit around the departure planet to achieve a specific V_∞, and a capture maneuver is used to decelerate from a hyperbolic orbit with a specific V_∞ to a parking orbit around the target body. Both of these ΔV can be calculated using the following equation [Wakker, 2015]:

$$\Delta V = \sqrt{\frac{2\mu}{a(1-e)} + V_\infty^2} - \sqrt{\frac{2\mu}{a(1-e)} - \frac{\mu}{a}} \tag{6.19}$$

where a and e are the parking orbit parameters. These maneuvers are always implemented at the end and start of an interplanetary trajectory, and thus the parameters of these final orbits always needs to be given.

6.2. Mission Planner Design

Each interplanetary trajectory is made up from several mission segments, all calculated in a specific order. However, to be able to build a range of different interplanetary trajectories, a more general set-up needs to be made for the mission planner. This section will discuss how the mission planner is designed and how it is able to calculate the different parameters needed to be able to do an analysis for a specific interplanetary trajectory. The design of the mission planner using only GAs is performed by Musegaas [2012], the incorporation of the AGA is novel to this thesis.

6.2.1. Software Architecture

The complete interplanetary trajectory is built up from different legs. For this specific model, there are three different types of legs: departure leg, swing-by leg, and capture leg. Each leg is made up of different mission segments. However, the initial and final conditions are the same for each type of leg. The three types of legs can be seen in figure 6.7 and are explained in more detail below:

- **Departure Leg** This leg starts from a parking orbit around the departure planet and ends at the SOI of the next planet. This leg requires information of the parking orbit, namely a and e, together with the required hyperbolic excess velocity to be able to determine the required ΔV for this the departure maneuver. The departure leg is built by first using a Lambert targeter between the departure and target planet, and then using the departure velocity to calculate the departure ΔV.

- **Swing-by Leg** This leg starts when the vehicle enters the SOI of the swing-by planet, where it performs either a GA or an AGA, and ends when it reaches the SOI of the target planet. Multiple of these legs can be stringed together. The leg starts with a Lambert targeter between the swing-by body and the target body. The departure velocity found by this Lambert targeter is then used together with the arrival velocity given from the previous leg to calculate the GA or AGA ΔV.

Input	Output
Planetary sequence	Total mission ΔV
Leg type sequence	$\boldsymbol{r}(t)$ and $\boldsymbol{V}(t)$ along the whole trajectory
Departure time	Location and magnitude of ΔV maneuvers
TOF of each leg	Planetary trajectories
a and e of parking orbits	
Ephemeris of planets	

Table 6.2: Inputs and outputs of the mission planner.

- **Capture Leg** The capture leg also starts at the entrance of the SOI of the capture planet. This leg only consists of the maneuver to enter the parking orbit around the capture planet. The capture leg uses the arrival velocity from the previous leg and calculates the capture ΔV using this velocity.

The basic idea of the mission planner is that depending on the input, it adds different types of legs together to form a complete interplanetary trajectory. The order of the types of legs cannot be selected freely, as a departure leg always has to be put at the beginning of the trajectory or after a capture leg, the swing-by leg can only come after a departure leg or another swing-by leg, and the capture leg can only come after a swing-by leg or a departure leg.

The mission planner uses several assumptions to build the final interplanetary trajectory [Musegaas, 2012]:

- The patched-conics approximation is used, which assumes that the trajectory is built up from Keplerian orbits without any perturbations. Inside the SOI of a planet, the central body to calculate the orbit is the planet itself, and outside the SOI the Sun acts as the central body for the Keplerian orbit.
- The sequence of the planets in the trajectory is selected beforehand.
- No deep space maneuvers (DSM). The only times an impulsive maneuver is allowed, is at the departure planet, capture planet, or swing-by planet.
- Each transfer is in a counter-clockwise direction and consists of only one revolution.

The use of a DSM is incorporated into mission planner of Musegaas [2012], and was shown to be able to improve some interplanetary trajectories compared to the GA only trajectories. However, as is discussed in Musegaas [2012], the incorporation of a DSM complicates the optimization of the interplanetary trajectory significantly, and is thus left for future research. Using these assumptions, the mission planner will build the interplanetary trajectories using the input parameters and produces several output parameters to be able to analyze the trajectory. The specific inputs and outputs of the mission planner are shown in table 6.2. An example of how the interplanetary mission planner builds an interplanetary trajectory is shown in figure 6.7.

6.2.2. Verification

A detailed verification process was employed by Musegaas [2012] to test each individual leg against legs from the Cassini-1 mission. This test was only done for the GA assist case and not for the AGA case as the AGA has not yet been flight-tested. The Cassini-1 mission used a EVVEJS trajectory, where the GA was employed at VVEJ. The results for each individual leg can be found in Musegaas [2012]. The full model verification will be looked at closer here.

The best, putative, results can be found using ESA's Global Trajectory Optimization Problems[1] (GTOP) database, which contains the full Cassini-1 trajectory. GTOP finds that the ΔV for this trajectory is 4930.7268 m/s. To be able to compare this the same ephemeris needs to be used as else the ΔV could change significantly. If, for example, the by Tudat used JPL approximate planet position ephemeris[2] is used in the mission planner, the ΔV would be 5635.9550 m/s. However, if the GTOP ephemeris is used, the ΔV is 4930.7284 m/s.

[1] GTOP: `https://www.esa.int/gsp/ACT/projects/gtop/gtop.html`. Accessed October 22, 2018

[2] Approximate Planet Positions: `https://ssd.jpl.nasa.gov/txt/aprx_pos_planets.pdf`. Accessed October 22, 2018

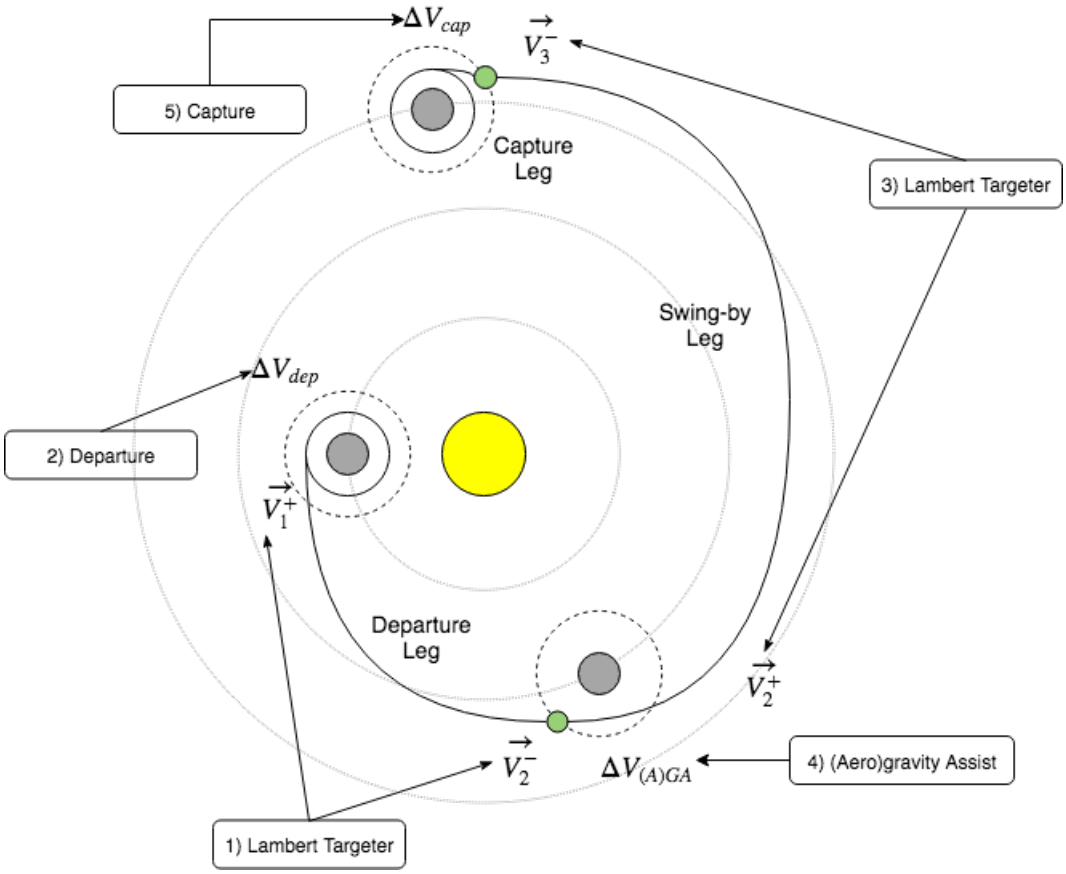

Figure 6.7: The set-up of the trajectory model and the mission planner.

This shows both that: the results are incredibly sensitive to the ephemeris database, and that the mission planner is able to reproduce the results from an already verified software program. This means that the mission planner works correctly, and that if an accurate interplanetary trajectory needs to be found an accurate ephemeris model needs to be used. However, for a comparative analysis, like is done in this research project, a less accurate (quicker) ephemeris model could be used if it is used for each interplanetary trajectory. The fact that the mission planner is this sensitive to the ephemeris database could be explained by the sensitivity of the Lambert targeter. Musegaas [2012] found that the main difference between the ephemerides was the location of Venus in the z-plane, and that thus a large part of the extra ΔV came from the Venus-Venus leg.

Several other trajectories, beside the Cassini-1 trajectory, were also used to verify the mission planner to be able to show that it works for multiple types of trajectories. These trajectories include the Messenger and Cassini-2 trajectories, and are shown to correspond with expected results in Musegaas [2012].

Verifying an interplanetary trajectory with an AGA is harder, as there are no baseline trajectories to compare with. Authors including Bonfiglio et al. [2000] and Henning et al. [2014] both describe interplanetary trajectories using an AGA that can be used as validation. However, the assumptions made in terms of waverider aerodynamics and atmospheric trajectories are not compatible with the set-up used in this thesis (as was described in section 6.1.3) which uses more accurate models. As the same input and output variables are used as in the GA model, the only part that needs to be verified is if the output of the AGA software model is the same as is expected from a hand-calculated value. This was done by taking an incoming and outgoing velocity for a GA at Mars, Venus, and Earth, calculating the desired δ, seeing where this trajectory would end up in the limiting surface for the respective planets (shown in chapter 8), and comparing the hand-calculated ΔV with the mission planner ΔV output. It was found that for all three planets the values correspond, thus it can be assumed that the AGA works as expected within the mission planner.

7

Atmospheric Trajectory Optimization

This chapter will focus on using the simulator described in chapter 5 to find optimal atmospheric trajectories for an aerogravity assist at Earth, Mars, and Venus. These optimal trajectories are generated using the optimization algorithms discussed in section 4.4, and thus the set-up and settings of these algorithms are discussed in this chapter, next to the trajectories they will produce.

First, section 7.1 will discuss the choice of variables that can be used by the optimizer to generate a specific trajectory, and the variables that are used as objectives by the optimizer will be discussed. Furthermore, a Monte Carlo analysis will be used to investigate these different variables in more detail. Afterwards, using the information from the Monte Carlo analysis, the full set-up of the optimizer will be discussed in section 7.2. Then, section 7.3 will use what is discussed before to decide on which specific algorithm is to be used to generate the optimal atmospheric trajectories. Finally, these trajectories will then be shown and discussed in section 7.4.

7.1. Decision and Objective Variables

To optimize the atmospheric trajectory for the AGA, a selection must be made between the decision variables that are used to find an optimum and the objective variables which are used to define what the optimum is. Depending on the specific problem and what needs to be analyzed, the selection of which variables will be used changes. Thus, it is important that a large selection of variables are analyzed to get a better idea of the relations between them and how they can be used in the optimization algorithm.

The inputs and outputs of the atmospheric simulator, shown in table 5.1, determine the possible decision and objective variables. A selection of these input and output variables are used in a Monte Carlo analysis to determine their properties when trying to find optimal atmospheric trajectories. However, before the Monte Carlo analysis is performed, the selected variables are listed below:

- σ_i, the bank angle nodes of the trajectory. See figure 2.2 for a definition of the bank angle. A change in the bank angle will also change the direction of the lift vector, thus it can affect the trajectory of the waverider. In total, 10 nodes will be set spaced evenly over θ.
- α_i, the angle of attack nodes of the trajectory. See figure 2.3 for a definition of the angle of attack. As was shown in section 3.2.2, α has a large influence over the L/D ratio, and thus also on the trajectory itself. In total, 10 nodes will be set spaced evenly over θ.
- γ_i, the initial flight path angle. See figure 2.1 for a definition of the flight path angle. This variable determines how steep the waverider will enter the atmosphere.
- V_∞^-, the incoming hyperbolic excess velocity, which in term determines the velocity at which the waverider enters the atmosphere.

The objective variables are the quantities that are optimized by the optimization algorithm. The objective variables cannot be influenced directly by the optimizer, but they are a result of a specific selection of decision variables. Selecting different objective variables can result in a completely different trajectory being found, and thus it is important to understand the specifics of each of these possible variables. An important note is

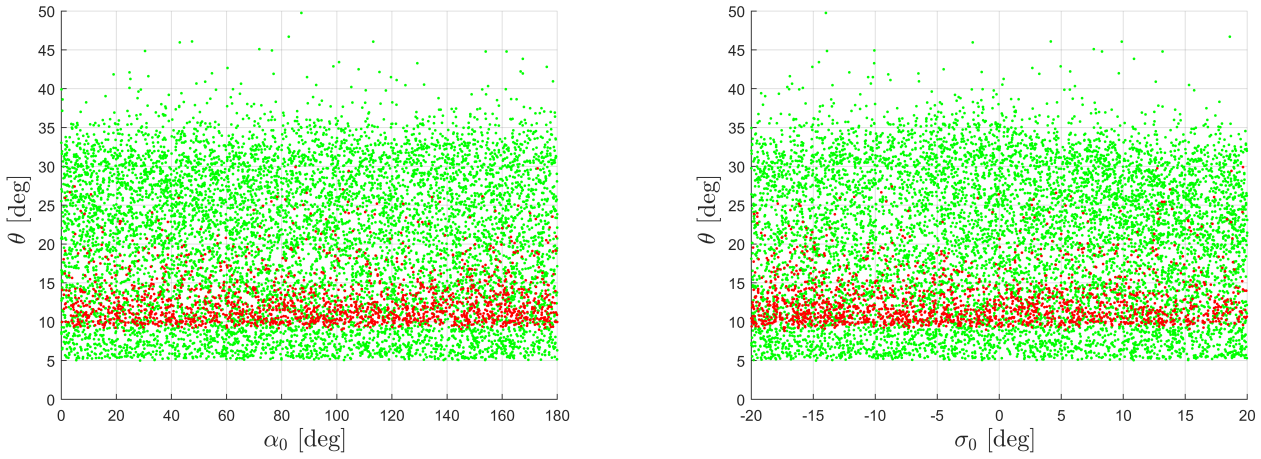

(a) First α node.

(b) First σ node.

Figure 7.1: The results for the Monte Carlo analysis for the first control nodes as a function of θ. The red dots represent trajectories with final altitudes below zero kilometres, the green dots represent trajectories which leave the atmosphere again.

that it is possible to interchange an objective variable with a constraint. Whether a variable is chosen to be used as an objective variable or a constraint variable is discussed in section 7.2. A list of objective variables is given here:

- θ, the final atmospheric angle. This variable shows how long the vehicle stays in the atmosphere, which, as was shown in chapter 6, directly relates to the heliocentric velocity gain.
- Δi, the change between in-going and out-going orbital inclination. This change shows how well the AGA can perform a certain plane change, or reduce the unwanted out-of-plane motion.
- $\Delta\delta$, the difference between a target velocity bending angle and the true value found at the end of the trajectory.
- $\Delta RAAN$, the change between in-going and out-going right ascension of the ascending node.
- CA, the control action. This is a measure for how much the vehicle needs to exert control effort during a trajectory. It is calculated by integrating the sum of $\dot{\sigma}^2$ and $\dot{\alpha}^2$ over the whole trajectory.
- Q_{stag}, the heat-load experienced at the stagnation point of the vehicle. A measure of the mass needed for the TPS system.
- q_{conv}, the maximum convective heat flux experienced by the vehicle.
- q_{rad}, the maximum radiative heat flux experienced by the vehicle.
- g_{load}, the maximum g-load experienced by the vehicle. This is a measure for the aerodynamic forces acting on the vehicle.

Section 7.1.1 will analyze the decision and objective variables listed above in more detail using a Monte Carlo analysis.

7.1.1. Monte Carlo Analysis

To determine what the effect is of the decision variables on the objectives, a Monte Carlo analysis was performed. Monte Carlo analyses try to understand the distribution of certain values by running a large number of simulations and changing certain values by a random amount for each run. A vector containing all possible decision variables is made for each simulation run. The values of the variables in this vector are drawn from a uniform distribution and are thus slightly different each run. A specific combination of decision variables will result in certain values for all the objectives. If a large number of runs are performed, the dependencies between the decision and objective variables can be analyzed. For this analysis, all the decision and objective

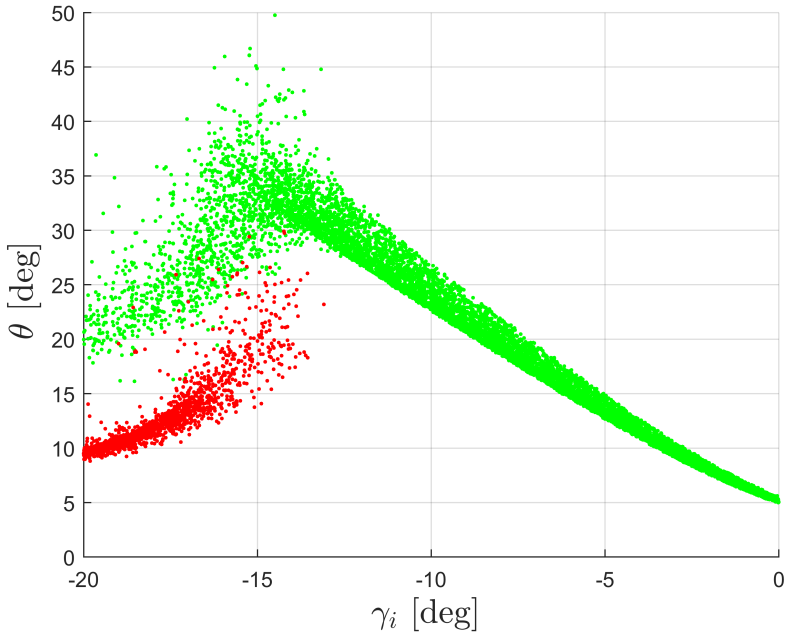

Figure 7.2: Monte Carlo analysis results for the initial flight path angle γ as a function of the final atmospheric bending angle θ. The red dots represent trajectories with final altitudes below zero kilometres, the green dots represent trajectories which leave the atmosphere again.

variables discussed in the first part of section 7.1 are taken, and 10,000 runs are performed at Mars (the conclusions taken from the results of the Monte Carlo analysis at Mars are similar to those for Earth and Venus, thus only Mars is discussed here). The results from this Monte Carlo analysis are used in section 7.2 to help select the decision, objective, and constraint variables.

First, the two control variables are analyzed: the angle of attack α and the bank angle σ. The results for θ and the first control nodes are shown in figure 7.1 and the complete results can be found in appendix A. All 10 nodes are varied for each trajectory and trajectories which end in the vehicle reaching an altitude of below zero kilometres and trajectories that end with the vehicle leaving the atmosphere again are separated by red and green dots respectively. Only the first control nodes as a function of θ are shown here, as the results for all other nodes and objective variables are similar and have the same conclusion. Furthermore, as the for most trajectories $\theta < 50°$, the nodes spaced at higher values of θ do not influence the trajectory significantly. Figure 7.1 shows that there is no discernible relation between a single control node and the atmospheric bending angle achieved. Furthermore, the maximum bending angle found is around 50 degrees, which is not close to the optimal values that can be found as will be described in section 7.4. This shows how sensitive the performance of the AGA is to the different control variables. It was found that for this Monte Carlo analysis, only 1 in 50,000 trajectories produced an atmospheric bending angle larger then 90 degrees. This shows the need for a robust global optimization algorithm to optimize θ.

In figure 7.2, the Monte Carlo results are shown for the initial flight path angle γ_i against the final atmospheric bending angle θ. Contrary to the results for α and σ, a clear shape can be observed in this relationship. There seems to be a region of γ_i between -16 degrees and -13 degrees for which θ is optimal. For larger γ_i (on the right side of the figure) there are only green trajectories, which mean that the vehicle quickly skips out of the atmosphere again after entering it. For smaller γ, the vehicle will either enter the atmosphere and reach an altitude of below zero kilometres (red dots), or it will leave the atmosphere again after entering it (green dots). It can also be seen that the spread in dots for a single value of γ_i is larger for trajectories where the vehicle enters the atmosphere then for trajectories where the vehicle immediately skips out. For these steeper trajectories, the vehicle enters the atmosphere to lower altitudes, thus experiencing more aerodynamic forces. These aerodynamic forces are controlled by α and σ, and thus for the same γ_i there are several possible θ, corresponding to different values of α and σ. From this analysis, it can be concluded that for an optimal AGA atmospheric trajectory, γ_i should be optimized as well. γ_i is set by the incoming hyperbolic orbit, thus to achieve the desired angle, an impulsive maneuver should be performed.

In Hess [2016], the same behaviour of γ_i was observed as was discussed before. In his work, only σ was used as a control variable for the atmospheric trajectory of the AGA. This required the extra constraint that γ_i should be small enough to allow the vehicle to enter the atmosphere, and not skip out. This was needed as optimal AGA trajectories start with $\sigma = 180\,\text{deg}$ (lift down), which means that if any uncertainty in the initial conditions would result in the vehicle skipping of the atmosphere the vehicle will not be able to add downward force to correct for this. In this research project, α is added to the control variable to be able to correct for this deficiency in σ only control. As in the case of α and σ control, α could be altered to add a larger downward force.

Figure 7.3 shows the distribution of all the objective variables discussed in the beginning of section 7.1. Each subplot in the figure shows the dependency between the two corresponding objective variables. The red dots (trajectories which reach an altitude of below 0 km) are not shown for Δi, $\Delta\delta$, and $\Delta RAAN$, as these quantities require the vehicle to exit the atmosphere at the end of flight. This figure can tell if there are correlations between different objective variables and thus which could be important to use in the optimization algorithm.

The first important results to observe is that, as expected, all the heating variables have a positive correlation, i.e. if either the radiative or convective heating is high the other heat flux will also be high. This relationship can still be observed in the heat load Q; however, in this case it is much less strong. This can be explained by the fact that for trajectories with high peak heat fluxes, it is possible that the length of the trajectory is not as long as for trajectories with lower peak heat fluxes. This could results higher heat loads for the longer trajectories with lower peak heating. $\Delta\delta$ also has a dependency on the heating variables. For $\Delta\delta$ this can be explained by the fact that for high heat fluxes θ is generally also lower (see figure 7.3), thus the atmospheric section, which can alter the path of the vehicle significantly, is much shorter.

Another important observation is the relation between $\Delta RAAN$ and Δi. Hess [2016] discussed the option of having $\Delta RAAN$ also minimized together with Δi in the optimization algorithm. This would ensure that the target orbital plane is reached. However, in figure 7.3 it is shown that if Δi is minimized, $\Delta RAAN$ will also be minimal. Thus having both as objective variables would be redundant. A physical explanation can be given using Gauss' variation-of-parameters equations for $\dot{RAAN}$ and $\dot{i}$ [Wakker, 2015]:

$$\frac{d\,RAAN}{dt} = \sqrt{\frac{a(1-e^2}{\mu}}\frac{N\sin u}{\sin i(1+e\cos\phi)} \tag{7.1}$$

$$\frac{d\,i}{dt} = \sqrt{\frac{a(1-e^2}{\mu}}\frac{N\cos u}{(1+e\cos\phi)} \tag{7.2}$$

where u is the argument of latitude (sum of latitude and argument of perigee) and N is the out-of-plane acceleration. These equations show that when i changes over time, the $RAAN$ will follow as most of the terms in both equations are equal. This corresponds to what was found in the Monte Carlo analysis.

Comparing the control action CA with the other objective variables, it can be seen that all the red trajectories, which do not leave the atmosphere, have a significantly lower CA then the green trajectories. This can be explained, partly, by the fact that red trajectories are shorter then green trajectories, thus there is less CA exerted. However, it is also partly due to the control effort required to return the waverider to the exit of the atmosphere.

Finally, looking at θ it can be seen that higher values of the g-load correspond to red trajectories and generally lower values of θ. The same holds for the peak convective and radiative heat flux. However, the heat load shows a slight increase when higher θ are reached as these trajectories stay longer in the atmosphere and are thus subject to more heating.

Using the results of the Monte Carlo analysis, the set-up of the final optimization can be determined. This is done in the following section.

7.2. Optimization Set-up

This section uses the Monte Carlo analysis done in section 7.1.1 to determine which variables should be used as decision variables, objective variables, and constraints. At the end of this section, a final set-up for the optimization is presented.

For the atmospheric trajectories of the AGA there are several constraints that need to be included. The two constraints that will be added to the fitness calculation are the maximum heat flux (radiative and convective combined) and the maximum g-load. These are chosen as the goal of this thesis is to find atmospheric trajectories that can be flown using current technology. Thus it is more important to find trajectories that are within

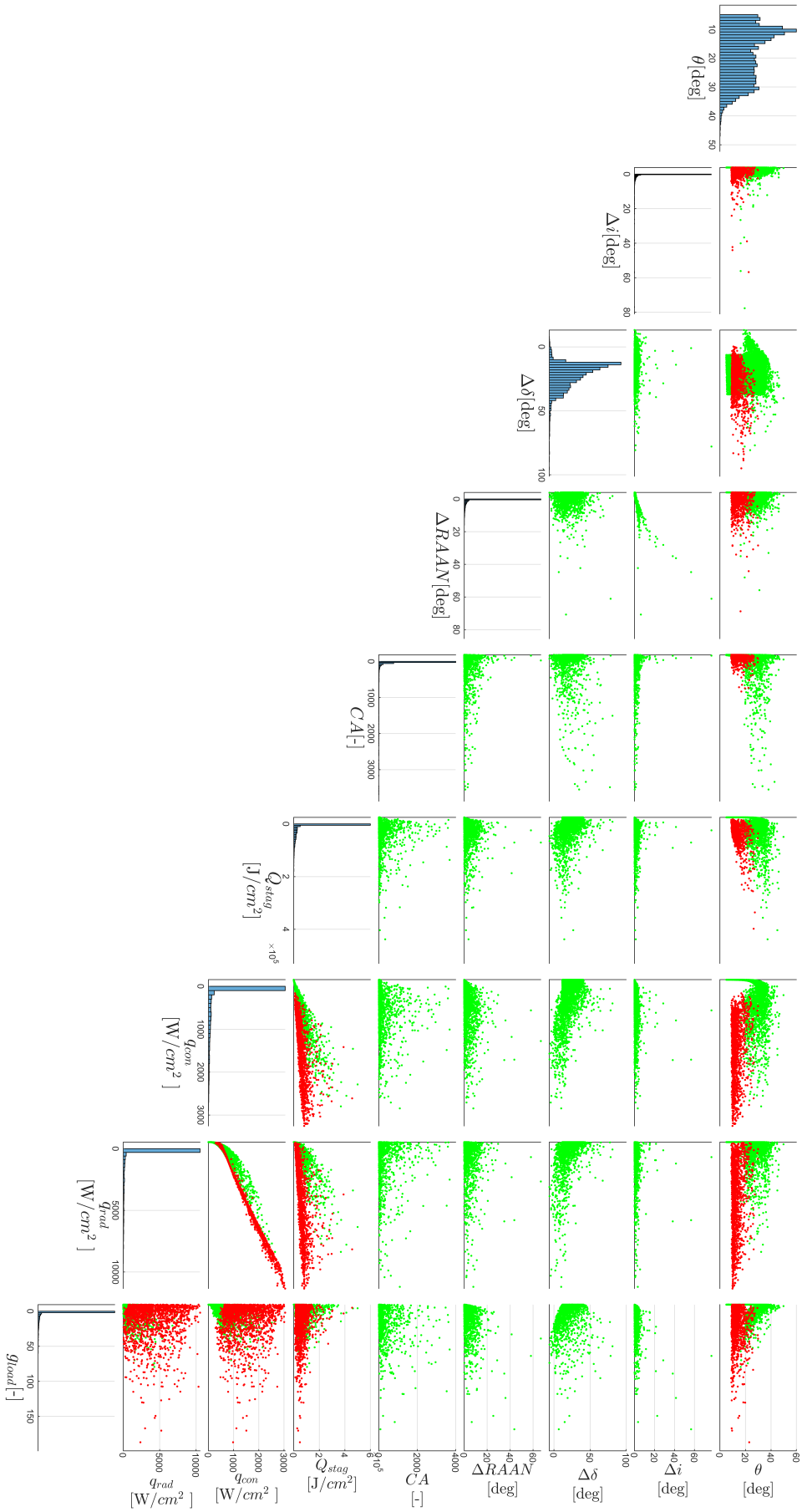

Figure 7.3: The results of the Monte Carlo analysis for all possible objectives. The histograms show the distribution of the respective objective variable.

the allowable ranges of current TPS technology, then to find heating and mechanical load optimal trajectories. As was shown in section 7.1.1, the heat load Q can be minimized to reduce the peak heat flux. However, this does not guarantee that the peak heat flux is under the maximum allowable vehicle constraint as Q could be small due to low heating over the whole trajectory, with a short peak heat flux which is over the constraint. Thus, for Mars, a heat flux constraint of 500 W/cm^2 is used, which is adapted from the study of a similar vehicle in Dijkstra et al. [2013]. The maximum g-load will be chosen to be 15 g, which is adapted from another aerogravity assist study [Casoliva et al., 2008]. Due to the atmospheres of Earth and Venus being much denser and the velocities much higher due to their higher gravitational influence, the heat flux constraint of 500 W/cm^2 cannot be met for these planets. After several test optimization runs, it was found that for both atmospheres a maximum peak heat flux of 2000 W/cm^2 still provided decent results while not exceeding the heating constraints. The g-load constraint is selected from previous studies (see e.g. Casoliva et al. [2008] and Hess [2016]) to be 15 g for all planets. Two other constraints that will not be included in the fitness function are the necessity of the outgoing orbit to be hyperbolic (final eccentricity larger then 1) and the vehicle to leave the atmosphere at the end of the trajectory (final altitude larger then zero). These constraints will not be added to the penalty function, but used as conditions for the trajectory. This means that if the constraints are violated, that trajectory is discarded. This is done for several reasons. The altitude and eccentricity are important in the classification of the maneuver. If the altitude reaches 0 km at some point, it is considered to be an entry. If the eccentricity is smaller then 1 at exit, it is considered to be an aerocapture. Thus using this approach allows the optimizer to only optimize AGA trajectories. Furthermore, as more terms are added to the penalty fitness function, the optimizer will have more trouble with converging on the global optimum as there are an increasing amount of parameters influencing the fitness value. As the optimization algorithm cannot distinguish between the individual terms, improving the fitness value will become harder. Thus it was chosen to not incorporate these variables into the fitness function.

From the variables discussed at the beginning of section 7.1, several possible options for objective variables can be selected. The goal of the atmospheric trajectory optimization is to find the maximum achievable performance of the AGA. As was discussed in section 6.1.3, one of the main parameters that can be used as a performance metric is θ. This directly relates to the velocity bending angle δ, which in term directly relates to the increase in heliocentric velocity and possible mission profiles. Due to this discussion, and the fact that this variable has been used in previous research (e.g. Casoliva et al. [2008], Henning et al. [2014], and Hess [2016]), the final atmospheric bending angle is chosen to be one of the objective variables. $\Delta\delta$ would require a pre-determined target value to determine. The goal in this thesis is not the find an atmospheric trajectory for a specific mission, but to find the maximum capabilities of an AGA. Thus $\Delta\delta$ is not used as an objective variable here. As discussed in section 2.5, the bank angle σ is used as a control variable and thus an out-of-plane motion is induced during atmospheric flight. Two of the parameters that characterize the orbital plane are i and $RAAN$. As unwanted orbital plane changes can be costly to correct, it is important to minimize the change in these variables. Section 7.1.1 showed that these two variables are connected, and that minimizing one of these variables would likely also minimize the other. As Hess [2016] used the change in i as an objective variable, this will also be the selected variable here instead of the $RAAN$. The remaining two variables are the heat load Q and the control action CA. The heat load was shown to be influenced by θ in the Monte Carlo simulation as lower values of θ lead to shorter heating periods and thus lower Q. CA has shown similar attributes as longer atmospheric flight times require more use of the control systems. Both these variables are important for the increased complexity of several vehicle systems (e.g. the TPS and control system) compared to the GA. However, they do not influence the maximum achievable heliocentric velocity gain, which is the main goal for the optimization of the atmospheric trajectory. These variables can be used to improve specific trajectory parameters after the maximum performance is obtained to decrease the complexity of the vehicle design, as will be shown in section 7.4.

The decision variables that will be used for the trajectory optimization are based partly on the Monte Carlo analysis done in section 7.1.1 and the control system discussed in section 2.5. Both α_i and σ_i for all ten nodes are selected to be decision variables for the atmospheric trajectory optimization. Even though the Monte Carlo analysis showed no direct relationship between θ and the control nodes, it is expected that this is not due to the fact that there is no dependency between the two parameters. As was discussed in section 7.1.1, this is likely due to the fact that a random selection of control nodes yields a small chance of finding the right combination of nodes to achieve higher bending angles. Furthermore, figure 7.2 shows that for trajectories which skip out of the atmosphere quickly there is less of a spread in achieved θ then for trajectories which entered the atmosphere. These trajectories thus experience more aerodynamic accelerations. This showed that α and σ do have an influence on the trajectory, and are thus important to control the trajectory to achieve

optimized objective variables. Additionally, as was already discussed in section 7.1.1, γ_i will be used next to the control nodes as a decision variable.

Now that the settings of the optimization have been discussed, a summary of the optimization is given below:

- **Objective Variables**
  - -$\theta(t_f)$
  - Δi
- **Decision Variables**
  - $\alpha_0, \ldots, \alpha_9$
  - $\sigma_0, \ldots, \sigma_9$
  - γ_{init}
- **Constraints**
  - $q_{max,M} \leq 500$ W/cm^2; $q_{max,E} \leq 2000$ W/cm^2; $q_{max,V} \leq 2000$ W/cm^2
  - $g_{load,max} \leq 15$
  - $h(t) > 0$
  - $e_f > 1$
  - $-20° \leq \alpha_i \leq 20°$
  - $|\sigma_i| \leq 180°$

A negative sign is put before θ as the optimization algorithms can only minimize the objective functions. The constraints for α_i were chosen because of the limits of the aerodynamic database. The bank angle σ is constrained to be only positive, as the sign of the bank angle is given by the lateral guidance algorithm discussed in section 2.5.3.

The optimization algorithm uses a fitness function to determine the optimal solution. As was discussed in section 4.4.3, the fitness function will not only include the objective variables, but also the constraints. As these constraints are normalized, the objectives should also be normalized to make the units compatible. The fitness functions are thus developed as follows:

$$f_\theta = -\frac{\theta(t_f)}{\pi} + w_g \frac{g_{load}}{g_{load,max}} + w_q \frac{q_{conv} + q_{rad}}{q_{max}} \tag{7.3}$$

$$f_{\Delta i} = \frac{\Delta i}{\pi} + w_g \frac{g_{load}}{g_{load,max}} + w_q \frac{q_{conv} + q_{rad}}{q_{max}} \tag{7.4}$$

$$\boldsymbol{f} = \begin{bmatrix} f_\theta \\ f_{\Delta i} \end{bmatrix} \tag{7.5}$$

The weights in the penalty function of equation (7.5) also have to be determined before the optimization is performed. Only three different weights could be examined: 0.1, 1, and 10. These were selected as each part of Eq. (7.5) is normalized, and thus the three chosen weight represent the influence of different orders of magnitude on each part of Eq. (7.5). For each combination of heat flux and g-load weights, three different optimization runs at different seeds were performed for Mars. The objective of this optimization was to maximize the final atmospheric bending angle. It was quickly determined that if a value of 0.1 was used the optimal trajectories would have a large chance of exceeding the constraints. Thus, this value was dismissed. Combinations of the other two values are shown in figure 7.4. The first conclusion that can be made is the fact that the $g_{load,max}$ constraint does not influence the results of the optimizer. This shows that the $g_{load,max}$ never gets higher then the constraint value and is thus never activated. Comparing the values for the q_{max} constraint shows that the higher weight of 10 increases the likelihood of the optimization converging on better solutions. Furthermore, the convergence also happens earlier compared to the lower weight value. The (10, 10) weights were thus chosen to be used. It is possible to test more values for the weights inside and outside the tested range to see if improvements can be made. However, as will be shown in section 7.3, there are other parameters whose influence on the performance is much larger then that of the constraint weights. Thus this is left for future research.

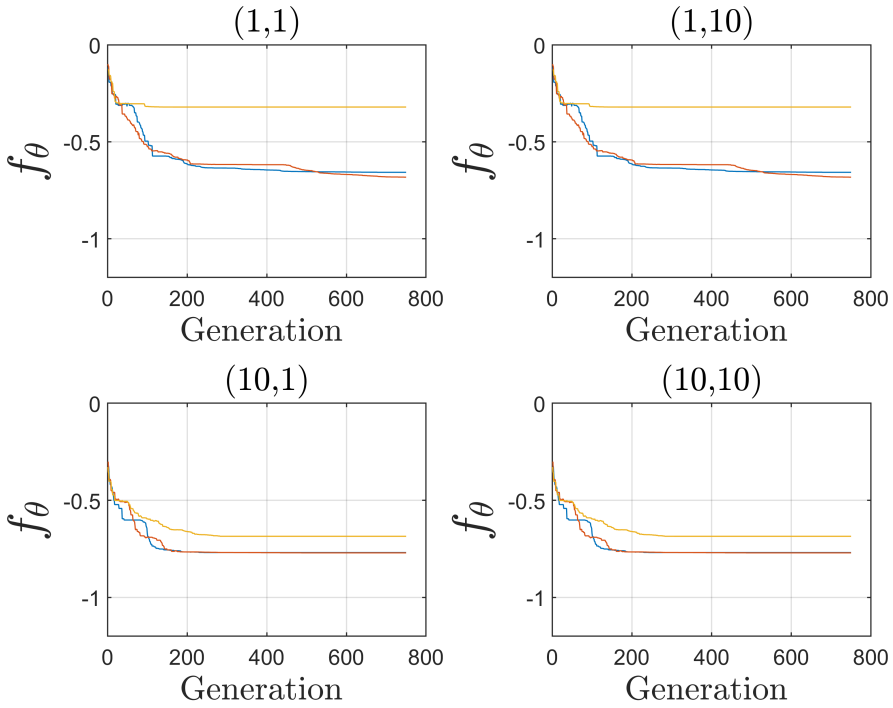

Figure 7.4: The optimization runs for 4 different combinations of weights on the maximum heat flux and maximum g-load. From top-left clockwise, the values are (where it is shown as (w_q, w_g)): (1,1), (1,10), (10,1), and (10,10).

7.3. Optimization Algorithm Comparison

To decide on which optimization algorithm to use, the algorithms that were discussed in section 4.4 are now compared by trying to optimize an atmospheric trajectory of Mars using the two different algorithms.

This section will compare the two algorithms and discuss the effect the tuning parameters have on the performance of the algorithm. Due to the fact that one optimization run requires a large amount of time to complete (5 hours for 750 generations, using a 3.50 GhZ AMD A10 Radeon R7 processor with 4 cores, and 8 GB RAM), it was not possible to perform an extensive tuning of the algorithms to be able to select the most efficient and robust algorithm-parameter combination. Thus, this will be left for future research.

Figure 7.5 shows the performance of the other two algorithms for the θ objective for three different seeds. Three different seeds are used to eliminate some of the random nature of the algorithms in the analysis. A larger amount of different seeds would increase the reliability of the analysis. As was stated earlier, this would take a large amount of time to perform and will be left for future research. The MOEA/D algorithm performs much better then the NSGA-II algorithm. The MOEA/D algorithm converges to more optimal solutions compared to NSGA-II, and it does this also for all three seeds. The NSGA-II converges much quicker then the MOEA/D algorithm, which means that a more exploratory method is desirable as it would not converge prematurely. The performance of the NSGA-II could be increased by changing several tuning parameters to increase the exploration of the solution space. However, tuning both algorithms and determining the best combination of tuning parameters and algorithm requires a large amount of time and is thus left for future research. For the remainder of this thesis, the MOEA/D algorithm will be used to optimize the atmospheric trajectory.

There are several parameters that can be used to change the performance of the MOEA/D algorithm. The first one is the population size n_p. The population size influences the exploration of the search space, as a larger population size will increase the exploration. However, this also increases the computation time of the optimization run if the same number of generations is taken. Thus, the population size selection is a trade off between exploration and computational efficiency. From previous research (e.g. Hess [2016]), and several test runs performed at: n_p = 60, 80, 100, 120, a population size of 100 was selected as these yield the best results while remaining computationally efficient.

When the off-spring is made from the current generation, there are two parameters that have an influence

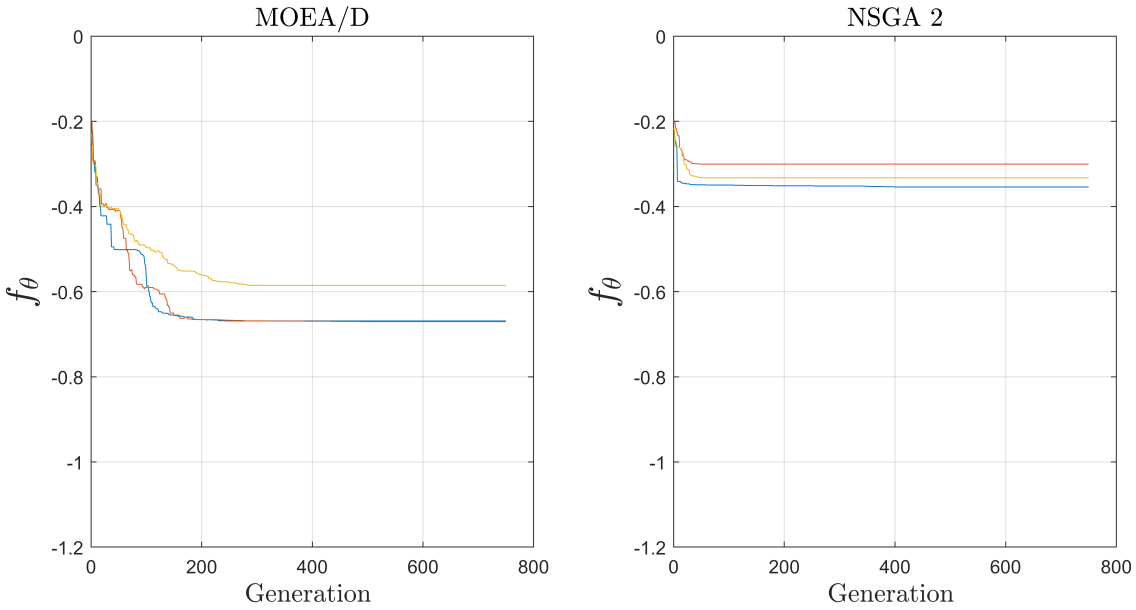

Figure 7.5: The results for an optimization run at Mars for the two different multi-objective algorithms.

on the new generation. The crossover rate C_r is used to define the chance of two individuals in the population crossing over and generating a new off-spring. C_r can determine how fast a local optima is exploited by the algorithm. This can help the optimization find optima quicker, but also result in premature convergence. The other parameter is the differential weight F. This parameter determines how much an individual is crossed over with (how much of the other individuals chromosomes are used in the off-spring). This can increase the exploration, but also decrease the chance of the population converging to an optima. There are no general rules on optimal values for these parameter, thus a small comparison was made using different values for these parameters to observe their influence on the performance of the algorithm. Using MOEA/D, the same problem as for the algorithm selection was optimized. Each optimization run had a different combination of tuning parameters with all the other settings kept equal. The parameter values used are: $F = [0.5, 1.0]$ and $Cr = [0.3, 0.5, 0.7, 1.0]$. The results for one seed are shown in figure 7.6. The results are distributed fairly randomly and no conclusion can be made on if increasing or decreasing one of the parameters will improve the performance of the algorithm. However, it does tell that the AGA problem is extremely sensitive to any changes in the optimization algorithm and that if sub-optimal results are found, the first strategy to improve the results could be to alter F and C_r.

The last parameter that will be inspected is the neighbourhood size n_b. This parameter is mentioned in algorithm 4.2 and determines the amount of weight vectors in the neighbourhood of $\boldsymbol{\lambda}$. A higher value of n_b can increase exploration, but also decrease the chance of converging on the global optimum. Ishibuchi et al. [2013] showed that n_b should be somewhere between 2 and 10 percent of n_p, but Hess [2016] found it to be 20 percent. For the best parameters found before ($n_p = 100$, $F = 0.5$, $C_r = 0.5$), 5 n_b values were chosen: $n_b = 5$, 10, 15, 20, 30. Figure 7.7 shows the results of this analysis. Again, it is noted that the spread of results is high, thus n_b also has a large influence on the performance of the algorithm. $n_b = 5$ was found to perform the best as it was the only setting that was able to reach an optimum near the theoretical minimum.

This section was meant to demonstrate the sensitivity of the problem to the chosen optimization algorithm and the parameters of that optimization algorithm. Due to the fact that only a small number of optimization runs at different seeds were performed, and the search space of the different parameters was not detailed enough, no general conclusion can be given on the optimal combination of algorithm and parameters. In the remainder of this research project, the MOEA/D optimizer will be chosen to optimize the atmospheric trajectories. The algorithm parameters will be set as follows: $N_p = 100$, $F = 0.5$, $C_r = 0.5$, $n_b = 5$, as this combination of parameters has shown to be capable of (near) optimal θ.

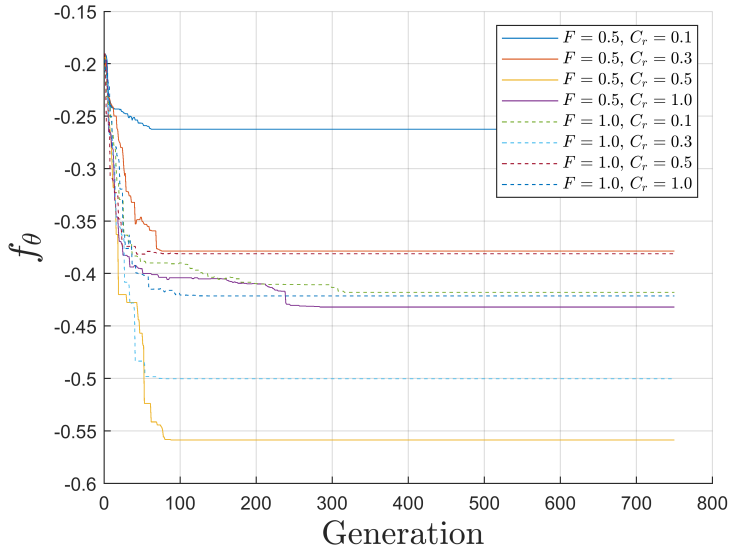

Figure 7.6: The results for different values of C_r and F for the MOEA/D algorithm.

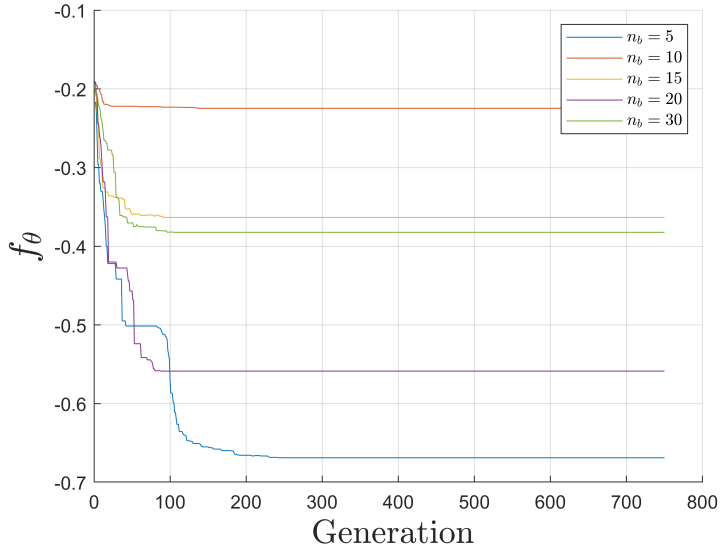

Figure 7.7: The results for different values of n_b for the MOEA/D algorithm.

Parameter	Value
h_i	Mars: 163 km Earth: 200 km Venus: 350 km
V_∞^-	5.0 km/s
Latitude	17.19°
Longitude	68.75°
χ	34.38°

Table 7.1: Initial conditions for the simulation runs.

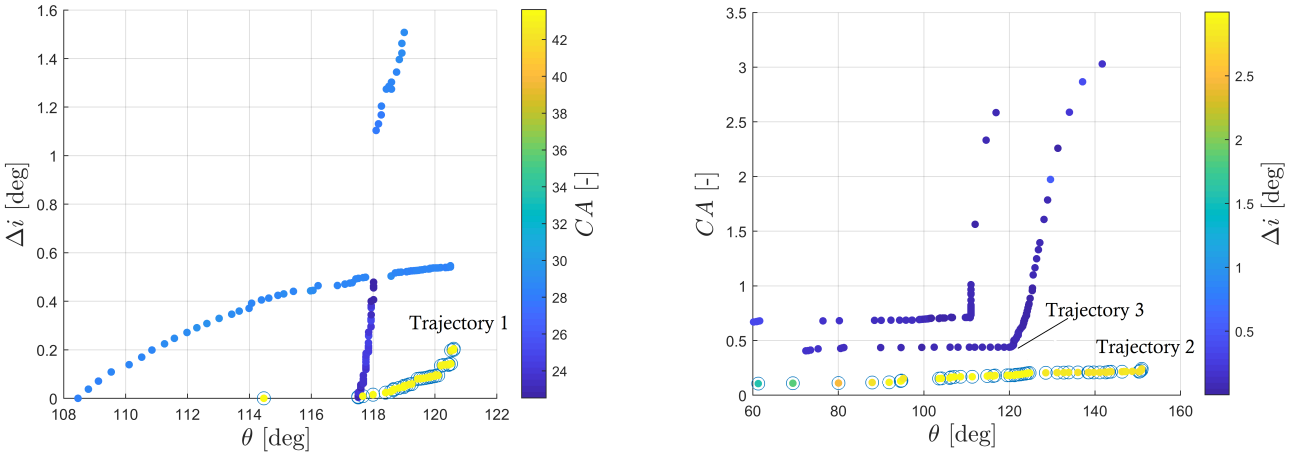

(a) Δi optimization run.

(b) CA optimization run.

Figure 7.8: The two final populations (for all seeds) for the Mars atmospheric trajectory optimization runs. The left figure contains the results for the optimization using Δi as objective variable, and the right figure the results for CA as objective variable. The circled dots are individuals that are not dominated by any other individual, and thus form a Pareto front.

7.4. Results

This section will explore the atmospheric trajectories that can be produced for an AGA at Mars, Earth, and Venus.

The MOEA/D algorithm will run the simulation at three independent seeds (seed 1: 12345677890, seed 2: 9876543210, and seed 3: 123454321) each producing a fitness value using Eq. (7.5). The initial conditions of these simulations are shown in table 7.1. The results for the different planets are shown and discussed separately in the next sections. A summary and comparative discussion of all the results is given in section 7.4.4.

7.4.1. Mars

The final population of the optimization at Mars for all seeds are shown in figure 7.8a. The individuals that are a part of the Pareto front spanned by all the different seeds combined are encircled. It can be seen that the Pareto front covers a small region of the objective space where the θ are spanned between 114 degrees and 121 degrees, and the Δi is limited to between 0 and 0.25 degrees. This shows that the combination of σ and α as control variables is capable of achieving relatively high atmospheric bending angles, while still maintaining a low Δi. Figure 7.8a shows that there are a lot of individuals (mostly from other seeds) that do not reach the putative optimal Pareto front. This shows that the convergence behaviour is poor for this problem and that it is possible that the found Pareto front could be improved upon for different combinations of seeds and settings.

To investigate the atmospheric trajectory in more detail, a trajectory from the Pareto front was selected. This specific trajectory can be seen in figure 7.8a with the label "trajectory 1". The trajectory is shown in more detail in figure 7.9, where trajectory 1 is represented by the solid line.

As was shown in figure 2.6, the atmosphere of Mars is relatively thin. This results in less drag experienced by the waverider as it travels through the atmosphere. Furthermore, lower velocities compared to other planets are needed to travel through the atmosphere and escape again as the gravitational influence of Mars is not as significant. This also reduces the drag experienced by the vehicle and the heating rate of the vehicle. As the waverider needs to exit the atmosphere on a hyperbolic orbit to escape the gravity field of Mars again, it cannot experience too much drag as this could slow down the waverider until it is captured by the gravity field of Mars. Figure 7.9 shows that the velocity at the end of the trajectory is just larger then the escape velocity of Mars (dotted line), which means that the optimal trajectory stays inside the atmosphere for as long as possible until it reaches the maximum θ when the velocity is just high enough to exit the atmosphere again on a hyperbolic trajectory.

The influence of adding α as a control variable can be seen through several parameters. The L/D of the vehicle does not remain constant at the highest L/D value as it would be for a σ only trajectory. In this case, the L/D changes significantly over the whole trajectory. Over the first and final couple of degrees that the vehicle travels through the atmosphere, the L/D of the vehicle changes as the vehicle travels through the different flow regimes. This is thus not necessarily due to changes in α. Afterwards, the L/D does not reach the maximum value until halfway through the trajectory, where it immediately turns negative afterwards. This is peculiar as previous research (see e.g. McRonald and Randolph [1990]) has shown that having the vehicle at high values of L/D increases the performance of the AGA. The fact that the optimization algorithm has not found a trajectory where L/D is at a maximum for the whole trajectory shows that either using α decreases the performance of the AGA, or that there are other factors that keep the L/D from being maximum over the whole trajectory. As high values of θ are still found, which also do not differ significantly from previous research (see e.g. Hess [2016]) that has used only σ as a control variable, shows that the performance has not been decreased due to α. A possible reason can be that, as can be seen in figure 3.5, the peak in the L/D profile is steep and even changing the value of α slightly will result in the L/D being changed significantly. This makes finding a maximum L/D profile harder for the optimizer (as well as giving the guidance algorithm hard constraints for deviations in α from the nominal trajectory). An advantage of the smaller values for L/D is the fact that the g-load is also significantly lower, as can be seen in figure 7.9. Observing the control variables shows that α changes significantly during the trajectory. At some points the value of α induces a negative L, which acts as a large bank reversal as the lift vector is turned 180 degrees. However, the bank angle profile still contains 5 bank reversals, which will increase the complexity of the on-board guidance and control systems. Furthermore, the trajectory through the atmosphere is not smooth, which translates to multiple heat flux peaks in the heating profile. This complicates the design of the TPS system as the heat load increases significantly.

To improve the control variable profiles, a different strategy to the optimization is needed. Instead of Δi being optimized, the control action, CA, will be optimized. CA is defined as follows:

$$CA = \int_{t_0}^{t_f} \dot{\alpha}^2 + \dot{\sigma}^2 \, dt \tag{7.6}$$

Using CA as a objective variable will decrease the change in value of the control variables during the trajectory, and thus decrease the bumps induced by the variable lift and drag coefficients. The final population of the CA optimization is shown in figure 7.8b. As before, the circled individuals are part of the Pareto front. The color of the individuals in figure 7.8 show the value of the other optimization's run second objective variable. As can be seen, the CA is improved significantly compared to the Δi trajectories while the Δi still remains relatively low (around 3 degrees). Two trajectories have been selected to be shown in more detail. One of these trajectories (trajectory 3) has a similar performance in θ as the maximum found θ for the Δi optimal trajectory (this trajectory is not part of the Pareto front to show how one of the off-Pareto trajectories differ from the Pareto front trajectories). The other trajectory (trajectory 2) has a θ that has been increased by around 30 degrees. This shows that CA trajectories are also capable of achieving higher performances for the AGA. The two CA optimal trajectories that have been labelled in figure 7.8 are shown in figure 7.9 as the dashed line (trajectory 2) and the dashed-dotted line (trajectory 3).

The use of CA has shown to be able to remove the bumps completely from the trajectory, which reduces the amount of q peaks to only 1. Furthermore, as was discussed in section 2.5.1, changing α over large amounts during hypersonic flight is often not possible or desired. Using CA as an objective variable has

significantly reduced the changes needed for α, as for most of the trajectory α stays constant, except for the start of the trajectory. The σ profile is also improved as no bank reversals are needed. This reduces the complexity of the on-board guidance and control systems significantly. Thus a CA optimal trajectory increases the feasibility of an AGA trajectory at Mars.

It is important to note that the reason that the Δi optimal trajectories are not as smooth as the CA optimal trajectory is not, necessarily, a physical reason. As there were no influences on the fitness function of the CA or any other parameters that measure the "smoothness" of the trajectory, the optimizer did not take this factor into account and found the trajectories shown in figure 7.8 instead. If one of these factors would be incorporated in the fitness value, the final trajectory could have been smoother. Furthermore, if trajectory 2 was part of the Δi final individuals seen in figure 7.8a, it would also be part of the Pareto front found there as $\theta(t_f)$ is larger then the largest $\theta(t_f)$ found in that optimization run. Thus, under different settings and a different seed, the optimizer could have also found that trajectory as part of the Δi optimal individuals.

Figure 7.10 shows the results of figure 7.8, with different parameters being shown as the color of the individuals. The γ_i of all individuals are shown in figures 7.10a and 7.10b. They all lie close together (between 13.6 and 14.15 degrees) and thus show that there is a small region of γ_i which result in optimal trajectories. Looking at figures 7.10c and 7.10d, the final hyperbolic excess velocities for the higher θ are all close to 0. This, as was discussed before, is due to the fact that the vehicle needs to escape the gravitational influence of the planet once it exits the atmosphere of the planet. Lower θ trajectories have more velocity left at the end of the trajectory as they experience less drag due to the early exit. However, comparing figures 7.10c and 7.10d shows that for similar θ the exit hyperbolic excess velocity is much greater for CA optimal trajectories. Thus, the drag experienced during these trajectories is much less. This could be due to the different control profiles or due to the different densities which are flown through as can be seen in figure 7.9. Finally, the peak heat fluxes are shown in figures 7.10e and 7.10f. This figure shows that the trajectories within each seed all have similar peak heat fluxes. However, the three different seeds all have different peak heat fluxes. The Pareto fronts (the circled individuals) both lie close to the constraint value, which shows that if this peak heat flux constraint is increased the Pareto front might have been improved. As for similar θ different peak heat fluxes are observed for trajectories that have higher Δi or CA, it can be argued that it might be beneficial to select e.g. trajectory 3 over trajectory 1 as it has similar θ and Δi with a decrease in q_{max} of around 200 W/cm^2. However, this depends on the context and objectives of the mission.

7.4.2. Earth

Figure 7.11a shows the results for the final population of each seed for the trajectory optimization at Earth. Compared to Mars, Earth has a thick atmosphere and thus larger aerodynamic forces are experienced by the waverider during its trajectory. Additionally, the gravitational influence of Earth is larger then that of Mars. Thus, a vehicle in a hyperbolic orbit around Earth has a much larger velocity then around Mars, which results in higher velocities inside the atmosphere and thus more drag experienced by the vehicle. This results in a lower $\theta(t_f)$ being reached compared to Mars. The Δi of the trajectories in the Pareto front are close to 0. This is due to the fact that σ has not yet had a large influence on the out-of-plane movement during the shorter trajectory compared to Mars. To investigate the atmospheric trajectory around Earth in more detail, a trajectory marked as "trajectory 1" in figure 7.11a from the Pareto front is shown in more detail in figure 7.12.

It can be seen that compared to figure 7.9, the velocities experienced at Mars are much higher as the escape velocity is about 6 km/s higher. This results in higher amounts of drag, and thus a lower $\theta(t_f)$ as the vehicle has to leave the atmosphere quicker before the velocity is below the escape velocity. Having the lowest altitude of the waverider higher in the atmosphere could help, as the density of the atmosphere is not as high there and thus the drag would also be lower. However, the aerodynamic forces would also not be high enough to sufficiently control the waverider, and thus the waverider would either leave the atmosphere or go deeper into the atmosphere again where it would encounter higher drag forces.

As discussed in chapter 2, Earth has various acceleration and environment models that can be used to improve the accuracy of the simulation. For the simulations used in the optimization of the AGA, lower fidelity models are used (e.g. the exponential atmosphere and central gravity) as this significantly reduces the computational time of the optimization algorithm. To ensure that these lower fidelity optimal trajectories are representative for trajectories where more accurate models are used, an optimization was run using higher fidelity models. The NRLMSISE-00 model was used instead of the exponential model to increase the accuracy of all the atmospheric parameters. The difference between the exponential model and the NRLMSISE-00 model is mainly experienced at higher altitude as the NRLMSISE-00 model incorporates certain solar weather data. The original simulation used only the gravity of the Earth. For this simulation both the gravity of the

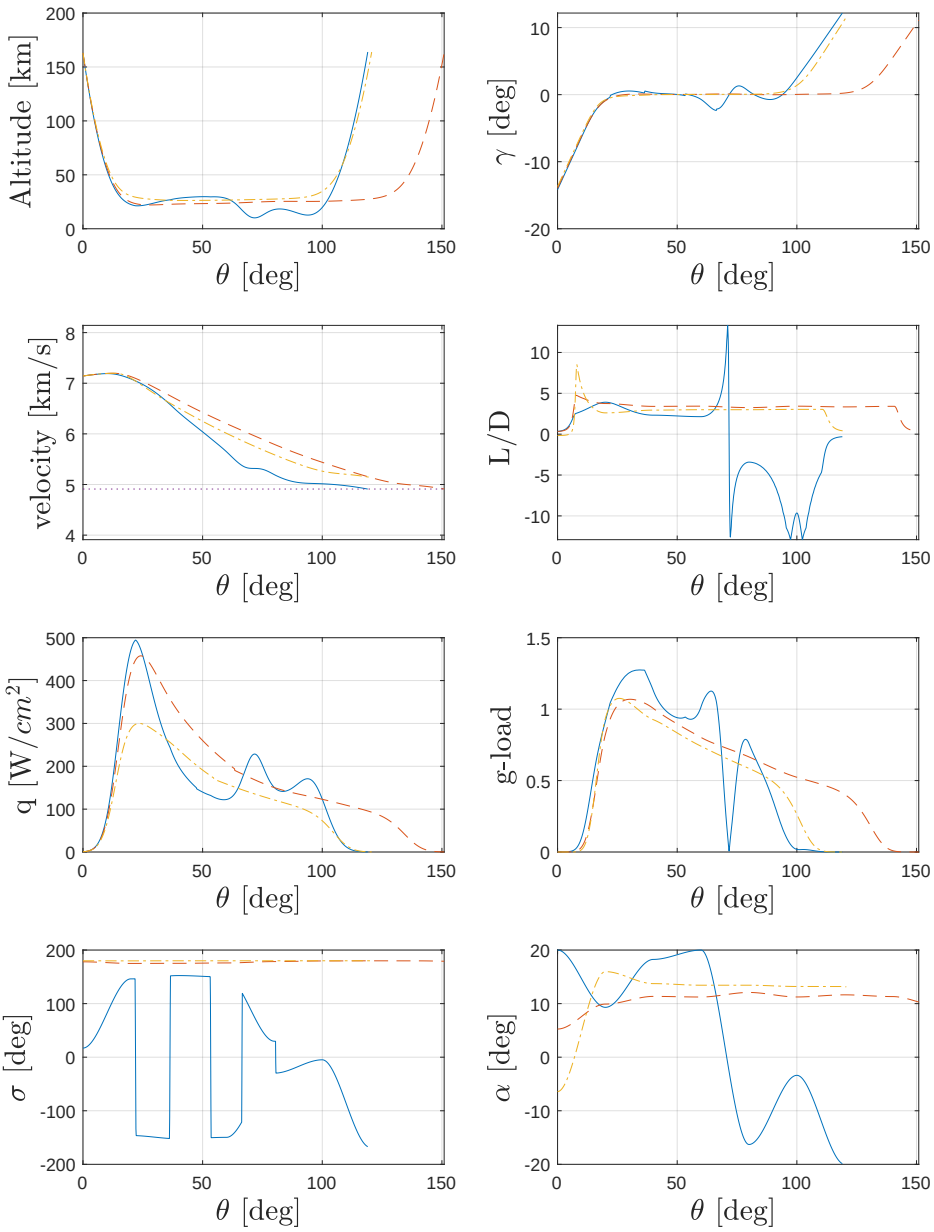

Figure 7.9: Optimal atmospheric trajectories for an AGA at Mars. The solid line represents trajectory 1 from figure 7.8, the dashed and dashed-dotted line represent trajectory 2 and 3 respectively from figure 7.8. The light dotted line in the velocity figure represents the escape velocity at the exit altitude.

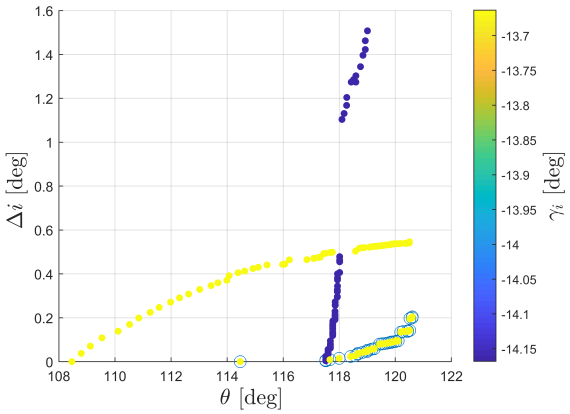

(a) Δi optimization, γ decision variable.

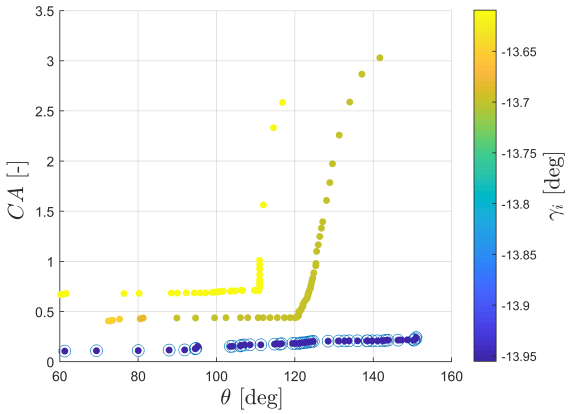

(b) CA optimization, γ decision variable.

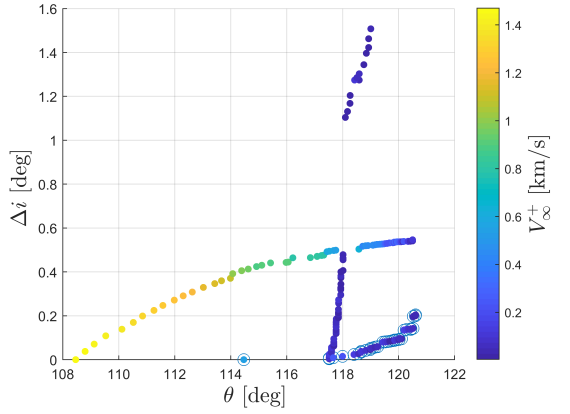

(c) Δi optimization, V_∞^+ variable.

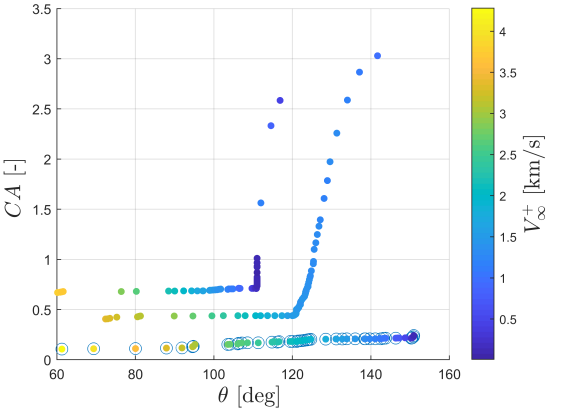

(d) CA optimization, V_∞^+ variable.

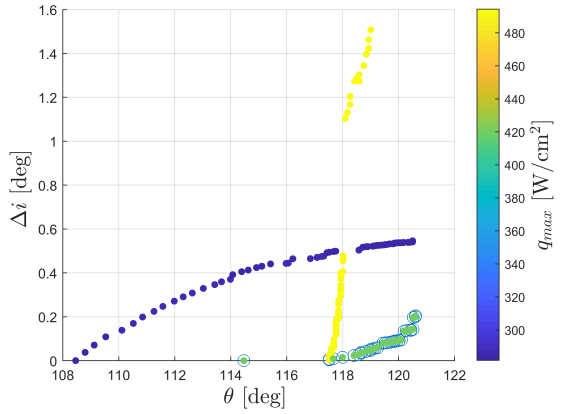

(e) Δi optimization, q_{max} decision variable.

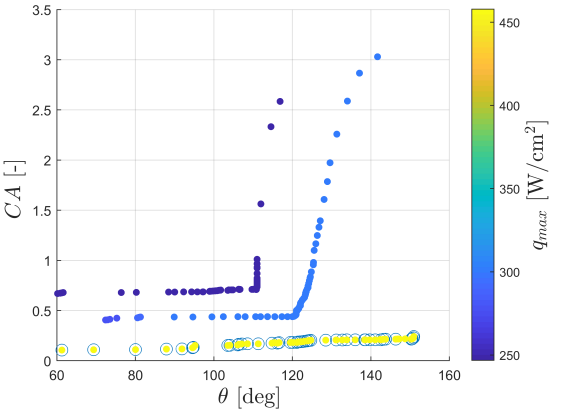

(f) CA optimization, q_{max} decision variable.

Figure 7.10: The final individuals for the Mars optimization runs with three different variables shown using the color of the markers in the figures.

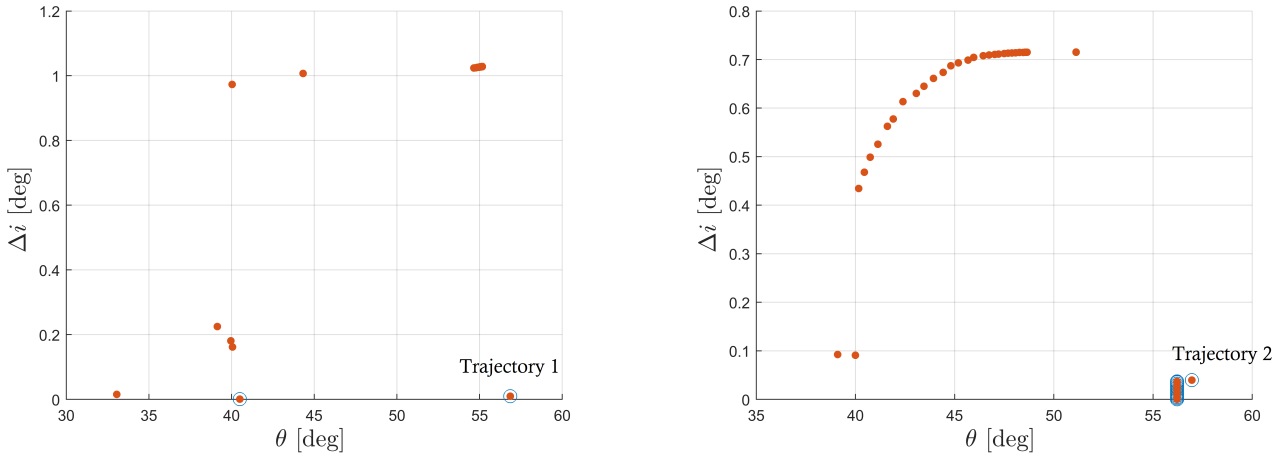

(a) Δi optimization run with low fidelity models.

(b) Δi optimization run with high fidelity models.

Figure 7.11: The two final populations (for all seeds) for the Earth atmospheric trajectory optimization runs. The left figure contains the results for the optimization using low fidelity models and the right figure the results for the high fidelity models. The circled dots are individuals that are not dominated by any other individual, and thus form a Pareto front.

Sun and the Moon are also included, using the SPICE ephemeris model for their relative location. These third-body perturbations can have small effects on the accelerations of the vehicle. However, they are expected to be much lower then the central body gravitational acceleration and the aerodynamic accelerations. For the gravity of Earth, the central gravity model was replaced by a spherical harmonics model with degree and order of 4. This model allows for several aspects of the mass distribution of the Earth (e.g. the oblateness of the Earth) to be modelled in the gravitational acceleration. These analyses have also been done for Mars and Venus and are shown in appendix B for brevity. The results for the final population for the three seeds are shown in figure 7.11b. The final population does have a different distribution as for the low fidelity model optimization. However, when the Pareto front of the high fidelity optimization is observed, it can be seen that the obtained values for both θ and Δi are similar to those of the low fidelity optimization. The difference in distribution over the objective space shows the sensitivity of the optimizer to changes in the model. As the goal is to determine the maximum possible performance of the AGA, this difference in distribution is allowable as long as the performance metrics are similar. Again, one trajectory is chosen from the Pareto front, here labeled as "trajectory 2", and shown in more detail in figure 7.12 as the dashed line. As can be seen, the difference between the two trajectories are not large. One of the main differences that can be observed is the fact that the lowest point is around 10 km lower for trajectory 2. This was observed to be due to the fact that the density at this point is the same for both trajectories. However, this does not correspond to the same altitude for both atmosphere models and thus the equilibrium gliding altitude is different. Additionally, the L/D profile is slightly lower for trajectory 2 along the whole trajectory. The α profile could be the reason, as it slightly differs from each other, mainly at the start and end of the trajectory. This could be due to the larger difference between the exponential atmosphere model and the NRLMSISE-00 model at higher altitudes as is shown in figure 2.9. Another observation that can be made is the fact that σ remains close to 180 degrees for the whole trajectory. Only at the start of the trajectory a small out-of-plane motion is induced by σ deviating slightly from 180 degrees. However, no bank reversal was needed as this motion did not induce a large change in the inclination.

Figure 7.13 shows more information on all the optimized individuals. Figures 7.13a and 7.13b show again that most individuals have similar γ_i. Thus a small range of γ_i show to be optimal, as was the case for Mars. The difference with Mars is that Earth trajectories have a less steep γ_i. Thus the peak for the optimal γ_i can differ significantly between planets. The exit hyperbolic excess velocity is shown in figures 7.13c and 7.13d. Similar results as for Mars are seen for Earth, except for the fact that V_∞^+ decreases quicker as a function of θ, which results in the lower $\theta(t_f)$ compared to Mars. Figures 7.13e and 7.13f show the peak heat flux reached for each individual. Compared to the AGA at Mars, most of the individuals show similar peak heat fluxes near the constraint value of 2000 W/cm^2. There are, however, several trajectories which have exceeded the constraint by about 1500 W/cm^2 for the low fidelity model optimization. This can also be seen in figures 7.13a and 7.13b where the trajectories seem to enter the atmosphere at a slightly steeper angle. The fact

that these trajectories with a higher heat flux do not improve on the Pareto front individuals is likely due to the optimization algorithm looking for trajectories that decrease the peak heat flux to minimize the penalty instead of using that heat flux penalty and increasing the θ. As the Pareto fronts show that their peak heat flux is near the constraint value, the performance would likely be increased if the heat flux constraint would be increased.

7.4.3. Venus

The final population for each seed is shown in figure 7.14a. The θ that is reached by the individuals in the Pareto front, shown as the encircled dots, is larger then those of Earth as the escape velocity at the exit altitude of Venus is slightly lower (about 1 km/s). This results in lower velocities inside the atmosphere, and thus less drag experienced by the vehicle. For the Δi objective variable, it can be seen that most of the non-dominated individuals are between 1 degree and 1.5 degree inclination change. There is one individual that is able to reach a much lower Δi as the other individuals, while still obtaining a relatively large $\theta(t_f)$. This individual also dominates a large part of the other individuals due to its low Δi. The individual with the largest $\theta(t_f)$ was taken to be inspected in more detail. This trajectory is labeled "trajectory 1"in figure 7.14a, and is shown as the solid line in figure 7.15.

From the three planets discussed in this thesis, Venus has the most dense atmosphere with a relatively high scale height. Due to this fact, the AGA starts at an altitude of 350 km and only reaches a lowest altitude of around 160 km. The atmospheric angle that is reached is still lower then that of Mars as the dense atmosphere of Venus and high velocities required slows down the waverider significantly. A difference between the other planets is that a second dip is found after the flight path angle reaches 0 for the first time. This allows the waverider to stay longer in the atmosphere, but it also generates a second heat flux peak next to the first one generated during the first part of the trajectory. This second heat flux peak is around 1000 W/cm^2 higher then the first peak and hits the heat flux constraint set by the optimization algorithm. This second heat flux peak increases the TPS mass required to be able to execute this trajectory as the heating period is also extended for a longer period of time. Furthermore, the σ profile of this trajectory is not ideal, as at the start of the trajectory an out-of-plane lift force is present due to the fact that σ is not equal to 0 or 180 degrees. This is corrected later in the trajectory by a bank reversal, which ensures a relatively low Δi. However, as can be seen in figure 7.14a, there are trajectories with an even lower Δi (also with a lower $\theta(t_f)$).

To be able to reduce the influence of the heating during the trajectory of the waverider, a different optimization strategy was applied to the problem. Instead of the inclination difference being optimized, the heat load Q (the integrated heat flux over the whole trajectory) was also optimized. The population of the final generation for all the seeds of this optimization is shown in figure 7.14b. It can be seen that for this optimization most of the final population is part of the Pareto front. As can be seen from the colors of the dots in both figure 7.14a and figure 7.14b, the performance of Δi is relatively similar for both optimization runs; however, the heat load Q is significantly reduced. The only disadvantage is that the maximum possible $\theta(t_f)$ is smaller for the Q optimal trajectories. The trajectory with the highest $\theta(t_f)$ is again selected to be studied in more detail, and is labelled in figure 7.14b as "trajectory 2". Trajectory 2 is shown completely in figure 7.15 as the dashed line. The Q optimal trajectory significantly reduces the peak heat flux reached together with the total heat load of the trajectory. This is done by removing the second dip in the atmosphere. However, this also reduces $\theta(t_f)$ of the trajectory as the second dip also serves to keep the waverider in the atmosphere for a longer period of time. Thus a trade-off needs to be made where the gain in ΔV (thus decrease in propellant mass) due to the larger atmospheric angle is compared with the gain in TPS material due to the larger heat load of the trajectory.

Additional results on the Pareto fronts of the AGA at Venus are shown in figure 7.16. The γ_i shown in figures 7.16a and 7.16b show again the small region of γ_i for which optimal trajectories exist. These trajectories also show more similarity in γ_i compared to Earth, which shows that AGA trajectories at these planets have similarities in their optimal trajectories. What can also be observed is the relation between γ_i, θ, and Q. When γ_i becomes steeper, θ and Q become higher. V_∞^+ shown in figures 7.16c and 7.16d show similar behaviour as AGA trajectories at other planets, where V_∞^+ decreases as θ increases due to the longer periods of high drag experienced. Figure 7.16e shows that for different seeds the peak heat fluxes are different, and within the seeds the peak heat fluxes are similar for each trajectory. These heat fluxes are also all close to the maximum allowed heat flux of 2000 W/cm^2. If this is compared with figure 7.16f, it can be seen that the peak heat fluxes are decreased significantly. This shows that for similar θ there are trajectories that can significantly reduce the heat fluxes experienced. However, these trajectories are not found for the highest θ found in figure 7.16e.

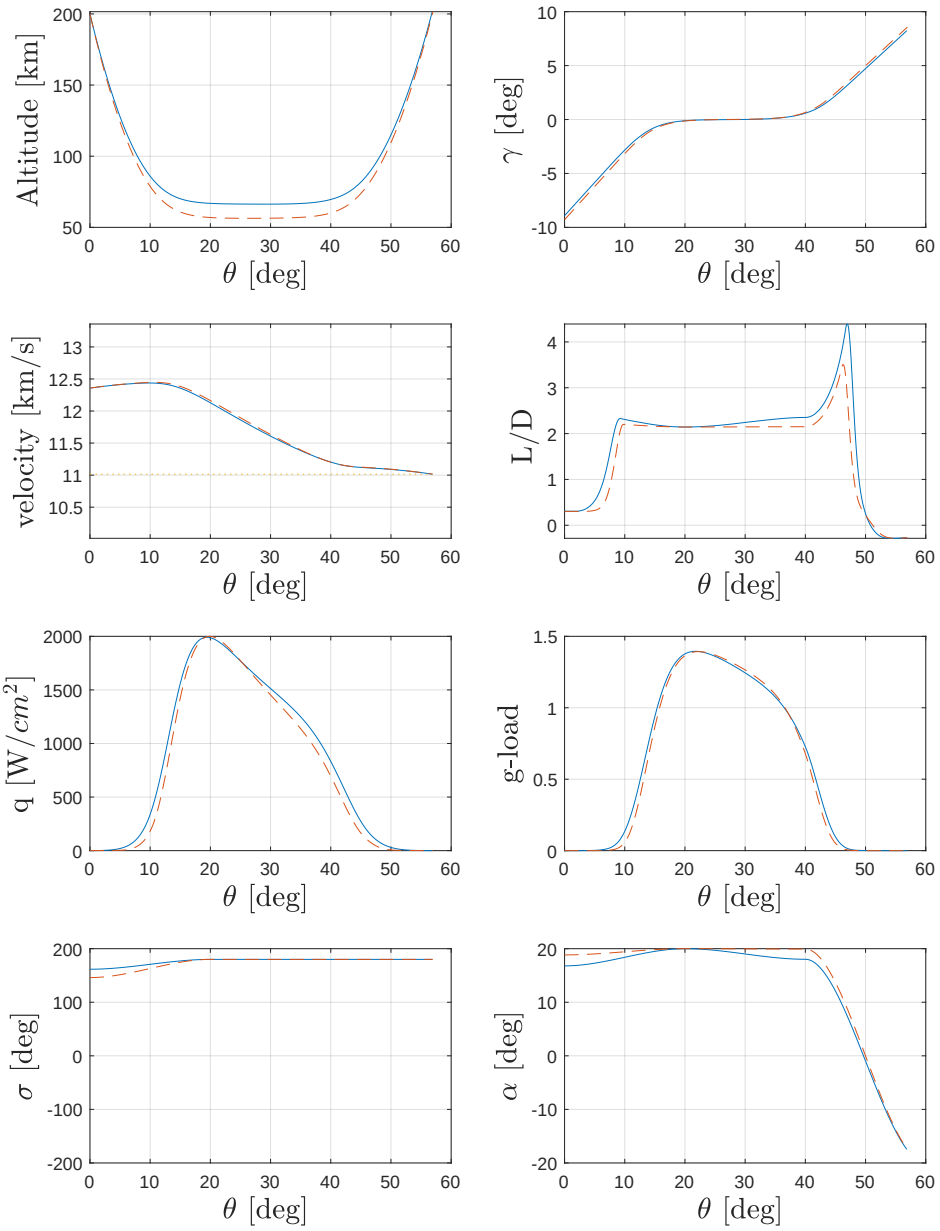

Figure 7.12: Optimal atmospheric trajectories for an AGA at Earth. The solid line represents trajectory 1 from figure 7.11, and the dashed line represents trajectory 2. The light dotted line in the velocity figure represents the escape velocity at the exit altitude.

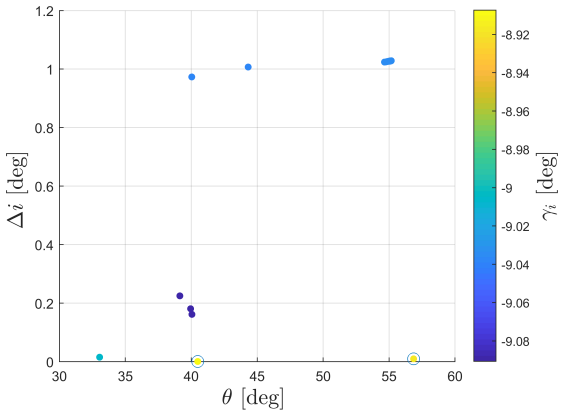

(a) Low fidelity models optimization, γ decision variable.

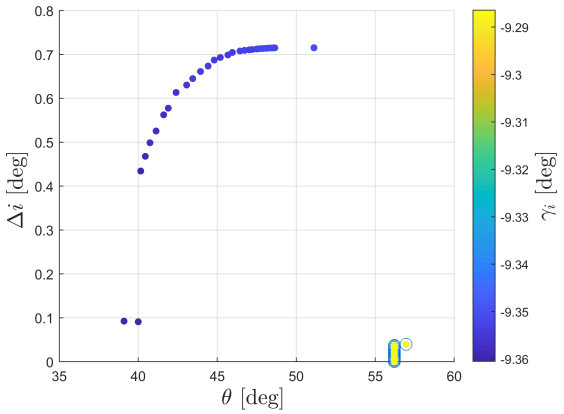

(b) High fidelity models optimization, γ decision variable.

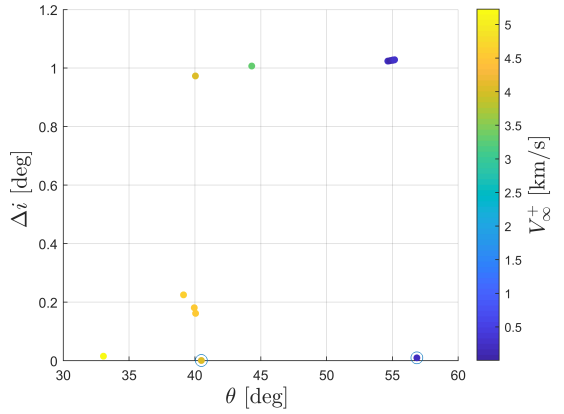

(c) Low fidelity models optimization, V_∞^+ variable.

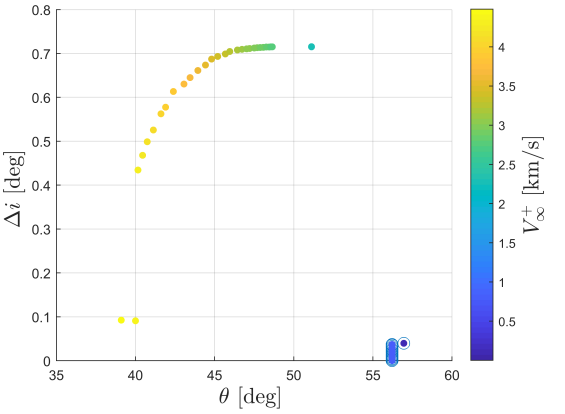

(d) High fidelity models optimization V_∞^+ variable.

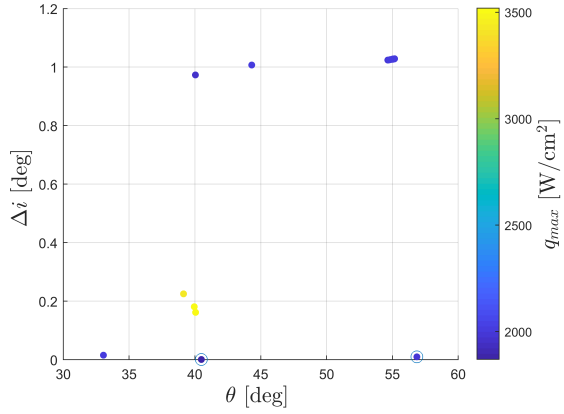

(e) Low fidelity models optimization, q_{max} decision variable.

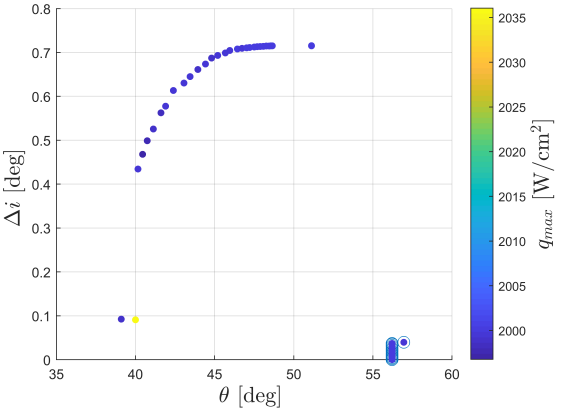

(f) High fidelity models optimization, q_{max} decision variable.

Figure 7.13: The final individuals for the Earth optimization runs with three different variables shown using the color of the markers in the figures.

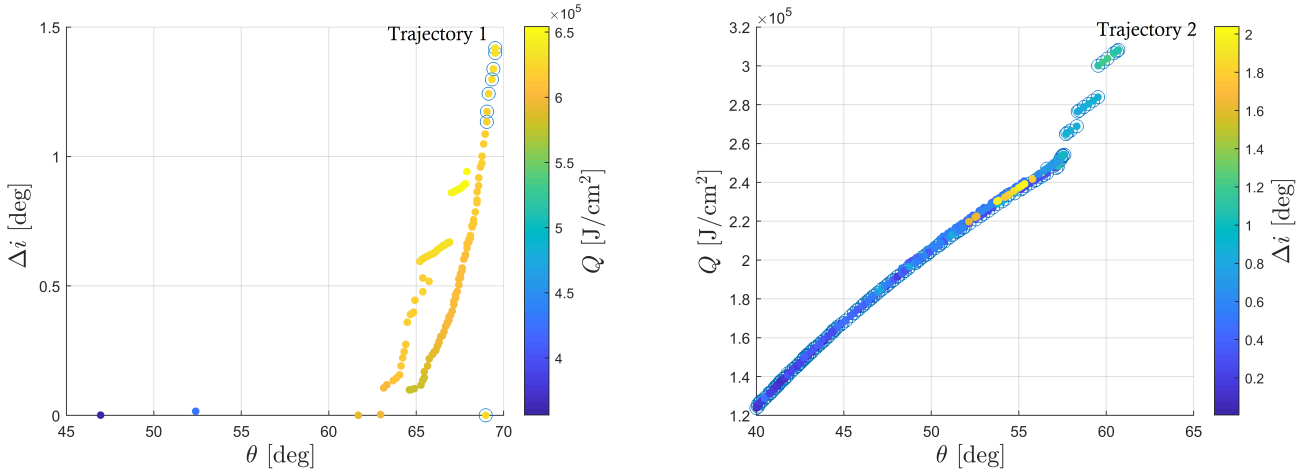

(a) Δi optimization run.

(b) Q optimization run.

Figure 7.14: The two final populations (for all seeds) for the Venus atmospheric trajectory optimization runs. The left figure contains the results for the optimization using Δi as objective variable, and the right figure the results for Q as objective variable. The circled dots are individuals that are not dominated by any other individual, and thus form a Pareto front.

7.4.4. Comparative Discussion

Previous sections have discussed the results of the AGA trajectories at Mars, Earth, and Venus separately. Furthermore, they have touched upon the similarities and differences between the trajectories at each planets and discussed the reasons of these differences. This section will summarize these results together and compare the results with each other and with previous research.

The AGA trajectories at Mars significantly outperformed trajectories at other planets for the maximum achievable θ. Using Δi as the second objective variable resulted in a maximum $\theta(t_f) = 120.5°$, and using CA instead of Δi resulted in $\theta(t_f) = 151.2°$. Maximum heat fluxes close to the heat flux constraint of 500 W/cm^2 were found for the Pareto optimal solutions. However, if similar θ trajectories are taken which have a degradation of the performance in the second objective variable, the maximum heat flux peak could be reduced by around 100 W/cm^2. Several studies have tried to optimize an AGA at Mars with a pre-defined $\theta(t_f)$ to inspect the trajectory. Henning et al. [2014] showed trajectories which reached a $\theta(t_f)$ of around 100 degrees using initial velocities of around 10 km/s, not considering heating of the vehicle. This value falls well within the maximum performance achieved in this thesis. Lohar et al. [1996] maximized AGA trajectories for their outgoing heliocentric velocities considering heating and found trajectories with $\theta(t_f) = 81.36°$, with a peak heat flux of 392 W/cm^2. The outgoing hyperbolic excess velocity was found to be 6 km/s, which as can be seen from figure 7.10c is higher then the velocity found here. This is likely due to the fact that in their work, the outgoing velocity was maximized and thus a different trajectory was found that achieved higher exit velocities. Hess [2016] performed a similar study as was done in this thesis. The differences are mainly in the fact that Hess [2016] only used σ as a control variable and that the S_{ref} of the waverider was increased by a factor of 10. Hess [2016] found for an initial velocity of 8.0 km/s a $\theta(t_f) = 153°$. This $\theta(t_f)$ is reached by trajectories found in this thesis using CA as the second objective variable using α and σ as control variables. As for this trajectory the S_{ref} did not need to be increased to allow for this $\theta(t_f)$, the benefit of α as an extra control variable is clearly shown.

The AGA trajectories at Venus and Earth have shown to achieve lesser $\theta(t_f)$ then the AGA trajectories at Mars. This is mainly due to the e constraint which requires to be above 1.0 to leave the planet again on a hyperbolic trajectory (see figures 7.13c, 7.13d, 7.16c, and 7.16d). The velocities at these planets are much higher then at Mars, thus more energy is lost due to drag which results in the vehicle leaving the atmosphere at lower values of θ. The heat flux constraints at these planets also limit the achievable $\theta(t_f)$ as most of the optimization solutions are close to the heat flux constraint of 2000 W/cm^2. Most of the previous studies on atmospheric trajectories use Mars due to the reasons listed above. This means that there are only a limited number of studies that can be used as a comparison for Earth and Venus. Lohar et al. [1994] performed a study of an AGA at Venus maximizing the heliocentric exit velocity. Similar assumptions as Henning et al. [2014] are taken where the control variables is the lift coefficient, which can be changed between its maximum and 0 freely during the trajectory. It was found that a maximum of 63 degrees for $\theta(t_f)$ is achievable. Heating

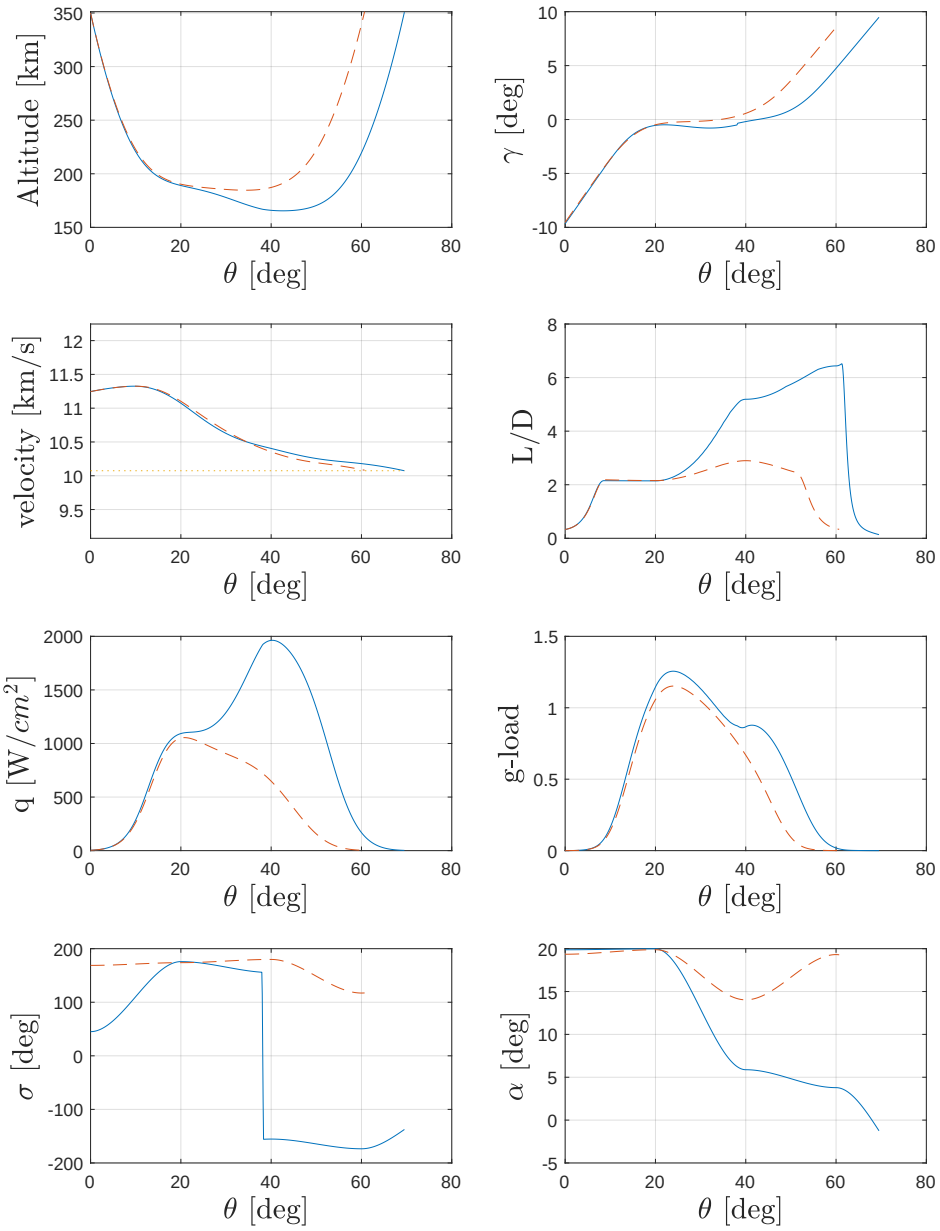

Figure 7.15: Optimal atmospheric trajectories for an AGA at Venus. The solid line represents trajectory 1 from figure 7.14, and the dashed line represents trajectory 2. The light dotted line in the velocity figure represents the escape velocity at the exit altitude.

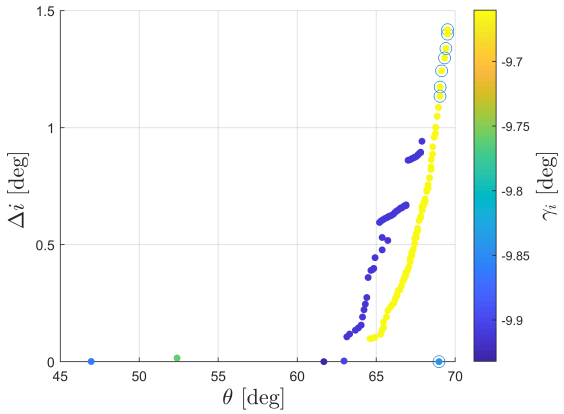

(a) Δi optimization, γ decision variable.

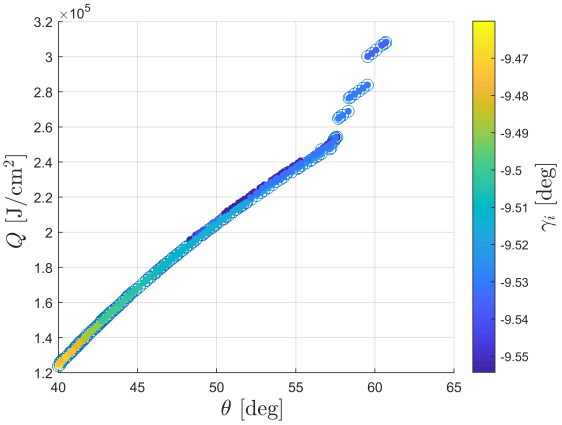

(b) Q optimization, γ decision variable.

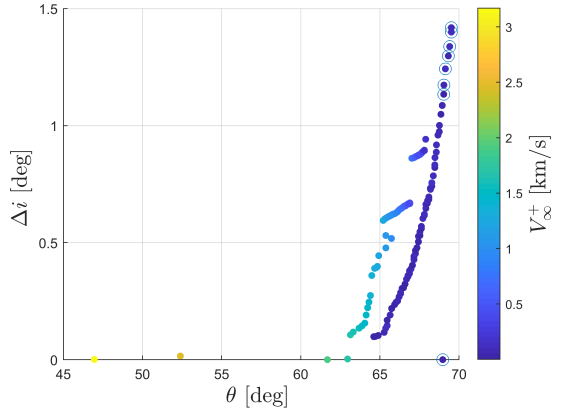

(c) Q optimization, V_∞^+ variable.

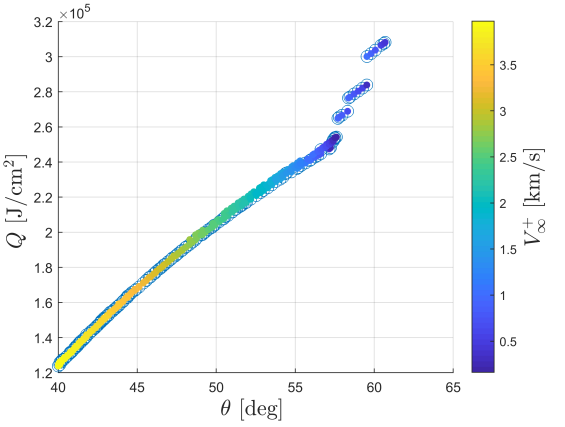

(d) Q optimization, V_∞^+ variable.

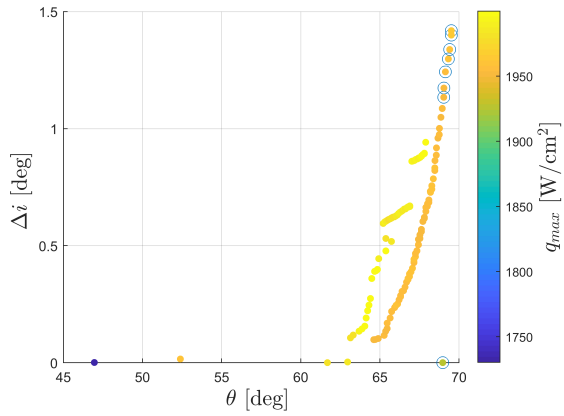

(e) Δi optimization, q_{max} decision variable.

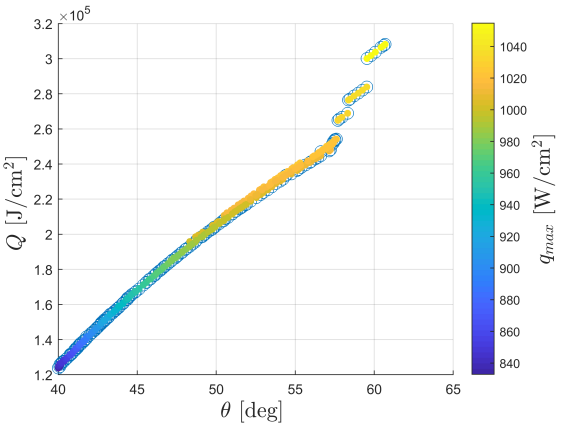

(f) Q optimization, q_{max} decision variable.

Figure 7.16: The final individuals for the Venus optimization runs with three different variables shown using the color of the markers in the figures.

rates were found to be much less then in this thesis. However, this is due to the fact that the maximum lift coefficient taken in Lohar et al. [1994] is much higher then what is achievable for the waverider in this thesis. Mars is able to achieve better performances for the atmospheric trajectories, however having studies also focused on Earth and Venus allows for different mission geometries to be considered for the AGA and is thus important to investigate.

Figures 7.8, 7.11, and 7.14 show that the convergence behaviour of this problem is poor as there are a significant amount of optimized individuals who have not converged to the putative Pareto front. Thus, it is possible that the putative solution found in this thesis is also not the true optimal solution, and thus the performance of the AGA could be improved. This can be shown to be true if an in-depth analysis is performed of the optimization algorithm combined with the optimization settings of this problem. This analysis can result in an optimal setup of the optimizer and thus in improvements in the putative solutions found here.

8

Interplanetary Trajectory Optimization

Chapter 7 discussed the atmospheric trajectory of the AGA. This chapter will take the trajectories of chapter 7 and connect them with the interplanetary phase of a mission. This will show if the AGA can improve the performance of interplanetary trajectories compared with a GA only mission and how it is able to do this. As the theory behind the mission planner is given in chapter 6, and the theory behind the optimization is given in chapter 4, this chapter will mainly focus on the problems that are discussed here and the results for the interplanetary trajectories.

First, in section 8.1, the connection between the atmospheric trajectories and the interplanetary trajectories using Pareto fronts is discussed. The specific Pareto fronts for Mars, Earth, and Venus are all shown and discussed separately. Afterwards, section 8.2 goes through the interplanetary trajectories that will be tested, how they are going to be tested, and the results for each trajectory are shown. Finally, section 8.3 takes some of the previous sections results and investigates them in more detail.

8.1. Aerogravity Assist Pareto Front

Section 6.1.3 discussed how the AGA mission segment was implemented into the interplanetary mission planner. This mission segment required a Pareto front for each planet that would limit the possible AGA trajectories. Before the interplanetary trajectories can be found, these Pareto fronts need to be generated and put into the mission planner.

To generate these Pareto fronts, a swing-by leg is set-up as was discussed in chapter 6. The incoming velocity at the SOI of the planet is taken first and using a Lambert targeter the outgoing velocity at the exit of the SOI is then found. These velocities were then used to find the required δ, and together they are used as an input for the GA mission segment. Thus, for the AGA a Pareto front is needed with the incoming velocity, the outgoing velocity, and δ contained in it. This results in the following optimization scheme:

- **Objective Variables**
  - -θ_f
  - -$|V_\infty^+| = -V_\infty^+$
- **Decision Variables**
  - $\alpha_0, \ldots, \alpha_9$
  - $\sigma_0, \ldots, \sigma_9$
  - γ_{init}
- **Constraints**
  - $q_{max,M} \leq 500$ W/cm^2; $q_{max,E} \leq 2000$ W/cm^2; $q_{max,V} \leq 2000$ W/cm^2
  - $g_{load,max} \leq 15$
  - $h(t) > 0$

- $e_f > 1$
- $-20° \leq \alpha_i \leq 20°$
- $|\sigma_i| \leq 180°$

which is almost the same as in chapter 7. However the Δi objective is changed to the -V_∞^+ objective and instead of only using 1 value for V_∞^-, a range of values was taken separated in increments of 1 km/s. The Δi is controlled here using solely the lateral guidance algorithm discussed in section 2.5.3, which has shown to work in reducing orbital plane changes even though Δi is not optimized in section 7.4. During initial testing, it was found that after optimizing the trajectories using the before mentioned set-up, the trajectories would all converge to an optimum where $\theta(t_f)$ was low and V_∞^+ almost equal to V_∞^-. The reason for this could be the fact that these trajectories were much easier to find by the optimization algorithm, thus the optimization would converge quickly to these solutions. As a Pareto front that is more spread across $\theta(t_f)$ is more desirable, a different approach was taken. The new method takes trajectories where $\theta(t_f)$ is small, and penalizes V_∞^+ according to the value of $\theta(t_f)$ and a pre-defined penalty value θ_{pen}. The fitness function for the velocity objective thus looks as follows:

$$f_{V_\infty^+} = -\frac{V_\infty^+}{V_\infty^-} + w_g \frac{g_{load}}{g_{load,max}} + w_q \frac{q_{conv} + q_{rad}}{q_{max}} + f_{v,pen}(\theta) \tag{8.1}$$

where V_∞^- was used to normalize the objective as it is not possible to have $V_\infty^+ > V_\infty^-$ as this would mean that the vehicle has gained energy in the atmosphere without using an impulsive thrust. The θ penalty function penalizes the fitness with a value of $\theta_{pen}/\theta(t_f)$ if $\theta(t_f) < \theta_{pen}$, and be equal to 0 if it is larger then the penalty function. Each optimization (for each V_∞^-) was performed for three different seeds to minimize random effects on the optimization results. If for a specific V_∞^- trajectories were found that would exceed one of the constraints, they will not be included in the Pareto front.

The optimization gives a range of points in 3D-space that each represent a trajectory found by the optimizer. To obtain a surface that can be evaluated at any point in this space, a polynomial needs to be fit through all of these optimal trajectories. This is done using the least squares fitting method discussed in section 4.3. Comparing the residuals between data and model, it was found that a polynomial of the first order in V_∞^- and of the third order in δ would result in the best fits. The equation for this polynomial is thus as follows:

$$V_\infty^+ = p_{00} + p_{10}V_\infty^- + p_{01}\delta + p_{11}V_\infty^-\delta + p_{02}\delta^2 + p_{12}V_\infty^-\delta^2 + p_{03}\delta^3 \tag{8.2}$$

This method assumes that in between the optimal trajectories, there also exists optimal trajectories. As these regions have not been explored by the atmospheric optimizer, there is no 100 percent certainty that there exist optimal trajectories in these regions. However, using trajectories that are distributed evenly over the whole space increases the accuracy, which is done by selecting a wide range of V_∞^-. Furthermore, larger regions on the Pareto fronts that contain no trajectories are identified after the Pareto front is generated, and removed from the final Pareto front. These empty regions, together with other regions of the space that are not covered by the Pareto front will have a flag that will be given to the mission planner algorithm. If this flag is found, a GA trajectory will be used instead of an AGA trajectory.

For each of the three planets discussed in chapter 7, a Pareto front is created. Each one will be discussed separately in the following sections.

Planet	p_{00}	p_{10}	p_{01}	p_{11}	p_{02}	p_{12}	p_{03}
Mars	2380.0	0.85	-1048	-0.3385	641.6	0.03174	-160.4
Earth	11070.0	0.5121	-6379	-0.312	2059	0.02376	-385.2
Venus	1636.0	0.8908	263.9	0.008134	-20.19	-0.1481	-15.19

Table 8.1: Pareto front parameters for each planet.

8.1.1. Mars

The Pareto front, or the limiting surface, of Mars is shown in figure 8.1. The distribution of the residuals, which shows the difference between the actual Pareto front and the fitted surface, is shown in figure 8.2. Most

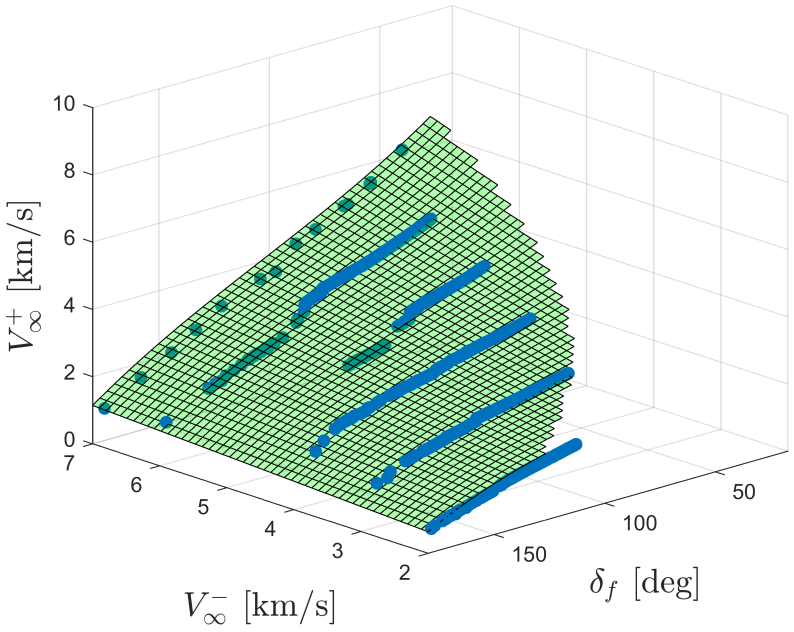

Figure 8.1: The limiting surface for the AGA at Mars, where the dots are the optimal trajectories.

of the absolute residuals are below 300 m/s, and only a small amount of trajectories show higher deviations compared to the surface. The standard deviation found for the residuals was found to be 184,85 m/s, this value can thus be taken as the uncertainty in the final value of the found velocity. As was discussed in chapter 7, an AGA at Mars can achieve large atmospheric bending angles and thus also large δ are reached in the Pareto front. Initial velocities smaller then 2 km/s showed bad performances, as the initial velocity was not high enough to generate high bending angles. Thus, these trajectories were not added to the Pareto front of Mars. Furthermore, higher initial velocities, those above 7 km/s, could not find optimal trajectories that did not exceed the peak heat flux constraint, thus they were also removed from the Pareto front. Another constraint that is put into each Pareto front is the fact that $V_\infty^- \geq V_\infty^+$. This limits one side of the Pareto front as can be seen in figure 8.1. Furthermore, the Pareto front cannot go below $V_\infty^+ = 0$, as this means the vehicle is captured in an orbit around the planet instead of leaving it on a hyperbolic orbit. Furthermore, δ larger then 180 degrees are also not included as this means that it would be better to enter the atmosphere from the other side. Outside of the constraints on the Pareto front mentioned before, the optimal trajectories are evenly spread across the surface and no regions of the Pareto front need to be discarded as a result. For an incoming velocity of 5 km/s, there is a region of larger δ that is not filled with trajectories. This region could be removed from the Pareto front; however, as for both larger and smaller V_∞^- there are optimal trajectories in this region, it is assumed that the lack of optimal trajectories there is due to the seeds used and not due to any physical reason. Thus it was chosen to leave this section in the final limiting surface.

8.1.2. Earth

As was discussed in chapter 7, Earth's atmosphere is relatively thick and the gravitational influence is relatively high. Thus, when entering the atmosphere the vehicle experiences a large amount of drag. This drag slows the vehicle down quickly, and thus the vehicle has to leave the atmosphere again before it doesn't have enough velocity anymore to escape the gravity field of Earth. As was shown in Eq. (6.13), θ is important for the total velocity bending angle. However, the GA contribution also adds to the total velocity bending angle of the AGA, which for Earth is relatively high. This results in relatively high δ found for the Pareto front of Earth, which can be seen in figure 8.3, even though the θ is relatively low for Earth AGA's. The thicker atmosphere does have other disadvantages that can be seen in the Pareto front. First of all, just as for Mars, the lower V_∞^- are removed as the velocity of the vehicle is not high enough to results in reasonable results. However, for Earth this happens for velocities lower then 3 km/s, whereas for Mars this was at 2 km/s. Second, for higher velocities, the maximum δ becomes lower as the drag and heating becomes significantly higher. Thus

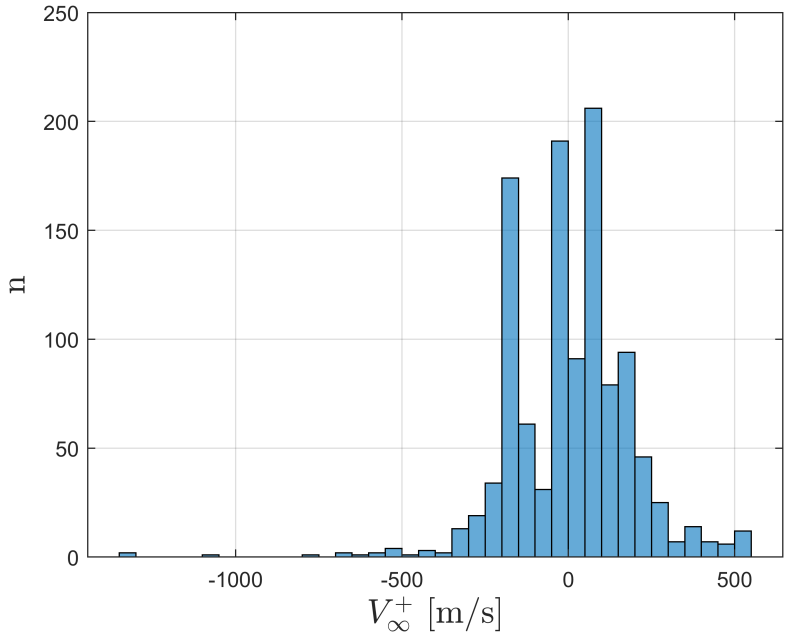

Figure 8.2: The distribution of the residuals of the Mars Pareto front compared to the fitted surface.

for these higher incoming velocities, parts of the Pareto front are missing for higher δ. Finally, the range of δ covered by the AGA Pareto front is much smaller then that of Mars, as the V_∞^+ decreases much quicker as a function of δ. All of these facts combined result in a much smaller region which is covered by the AGA Pareto front compared to the Pareto front of Mars. This will make it harder for the optimizer to find a good AGA trajectory at Earth that fits in the larger interplanetary trajectory. The distribution of the residuals of the fitted surface are shown in figure 8.4. These residuals are more closely distributed around 0.0 m/s compared to Mars and Earth. This results in a more accurate representation of the found Pareto front for Earth of the limiting surface. The found standard deviation of the residuals is equal to 21.06 m/s.

8.1.3. Venus

The Pareto front for Venus can be seen in figure 8.5, and the residuals for the fitted surface are shown in figure 8.6. The residuals of Venus show the same order of magnitude values as Mars; however, compared to Mars there are no large outliers present over 1 km/s. The standard deviation of the residuals was found to be 202.27 m/s, which is similar to that of the Mars limiting surface. Venus has the thickest atmosphere of all the planets and also has a similar gravitational influence as Earth. Thus it suffers from the same problems as Earth. For Venus, the drag experience by the vehicle is also high, and thus V_∞^+ also decreases fast as δ becomes higher. Low V_∞^- are also not present in the Pareto front as those trajectories are do not have sufficient velocity to achieve reasonable δ. One of the bigger differences between Venus and Earth is the fact that there are several trajectories found above a V_∞^- of 6.5 km/s. For Earth, these trajectories were not found as the heating constraints were violated. The fact that these trajectories are there for Venus and not Earth could be due to the fact that the composition of the atmospheres are different, and thus different heating functions are used. Or it could be due to the fact that the optimizer could not find these for Earth with this specific combination of seeds and tuning parameters. Due to time constraints, it was not possible to test which of these might be the origin of the difference.

8.2. Interplanetary Trajectories

There are several differences between the method of finding optimal interplanetary trajectories and finding optimal atmospheric trajectories. First of all, the objective and decision variables are limited due to the design of the mission planner. As the planetary sequence is fixed, the only possible decision variables will be the departure time and the time-of-flight, TOF, of each leg. The objective variables are also limited to the possible output of the mission planner. From the state of the vehicle along the trajectory, there are several parameters

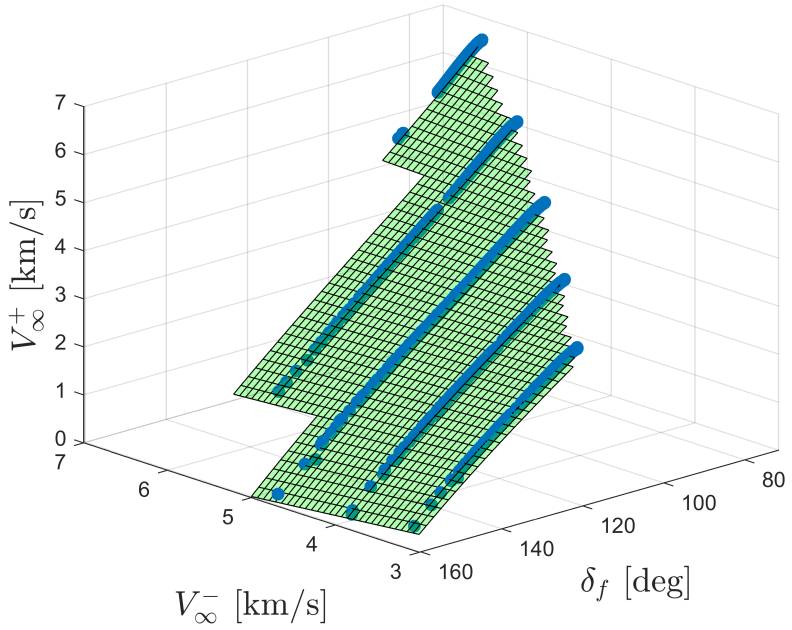

Figure 8.3: The limiting surface for the AGA at Earth, where the dots are the optimal trajectories.

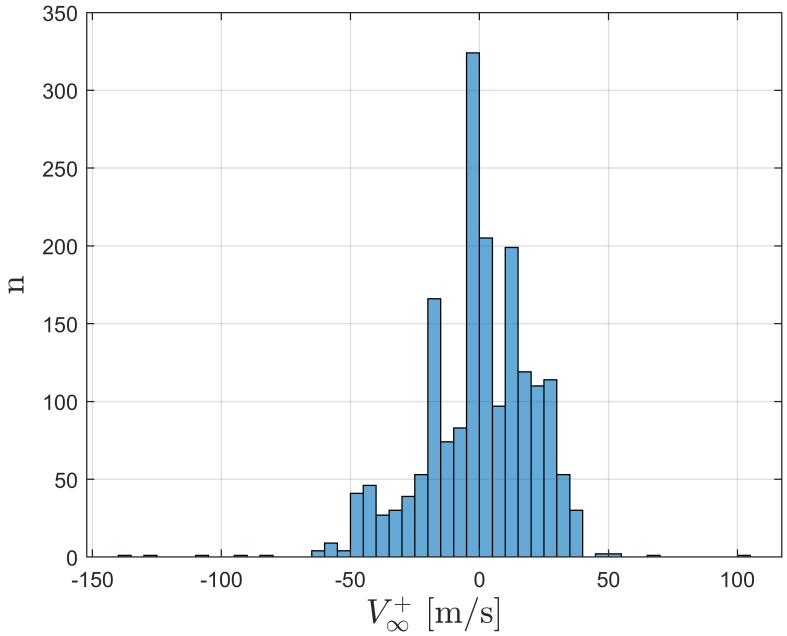

Figure 8.4: The distribution of the residuals of the Earth Pareto front compared to the fitted surface.

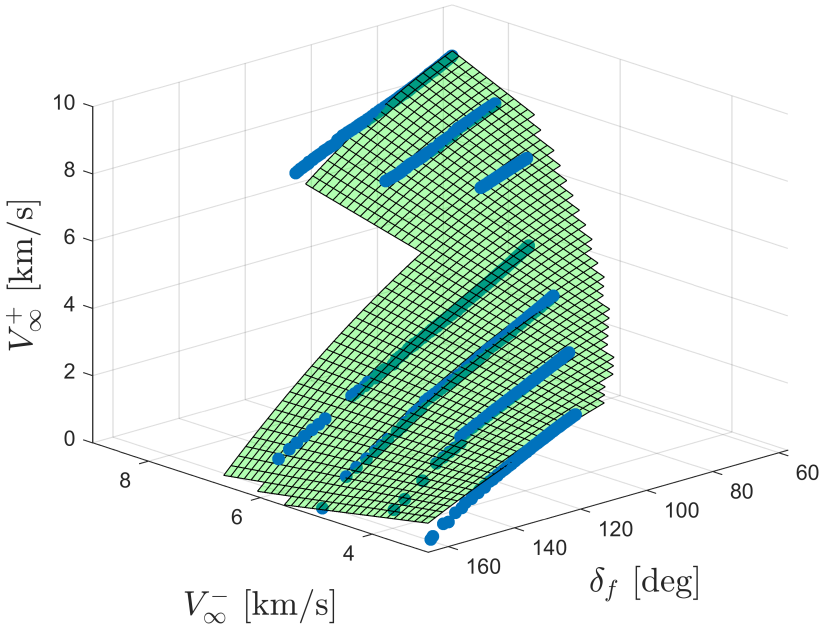

Figure 8.5: The limiting surface for the AGA at Venus, where the dots are the optimal trajectories.

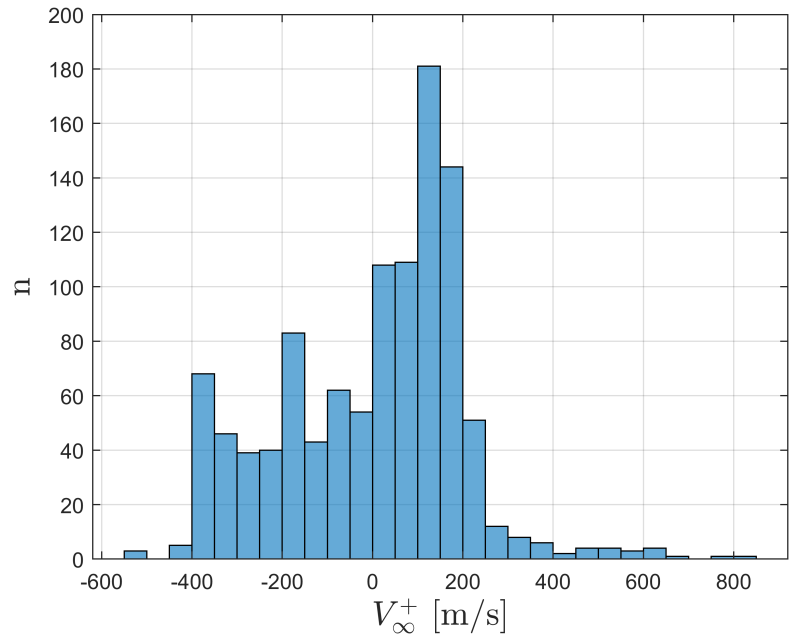

Figure 8.6: The distribution of the residuals of the Venus Pareto front compared to the fitted surface.

	t_0 [MJD2000]		TOF_1 [days]		TOF_2 [days]		TOF_3 [days]		TOF_4 [days]	
	LB	UB	LB	UB	LB	UB	LB	UB	LB	UB
EMJS	3650	7300	80	400	600	2000	600	2000	-	-
EVEJS	3650	7300	80	400	80	400	600	2000	60	2000
EVEJ	3650	7300	80	400	80	400	600	2000	-	-
EVVEJ	3650	7300	80	400	80	400	80	400	600	2000
EVEEJ	3650	7300	80	400	80	400	80	400	600	2000

Table 8.2: The bounds for all the interplanetary trajectories. These bounds are based on the bounds used in Vasile and Pascale [2006].

that can be deduced. There are two of these parameters that are the most important performance measures for these types of interplanetary trajectories. The total ΔV needed to execute an interplanetary trajectory can give a indication of the mass needed for a specific mission and thus it is also gives a good indication of the cost of the mission. The other objective parameter is the TOF of the complete mission. If the TOF is shorter, the spacecraft will be exposed less to the harsh environment of interplanetary space, and a longer section of the mission lifetime could be spent at the target instead of during interplanetary flight. Previous research has also used either one, or both, of these variables (see e.g. Musegaas [2012], Vasile and Pascale [2006], Secretin [2012]), and thus the trajectories that were found can be used to give an indication of typical performances.

An advantage of the optimization process of interplanetary trajectories compared to the atmospheric trajectories is the fact that no numerical integration is used in the mission planner. This significantly reduces the computation time of one trajectory evaluation. This allows the use of a large amount of different seeds and combination of tuning parameters to be used to find the optimal trajectories. This gives a higher chance of finding the global optimum compared to the atmospheric trajectory optimization.

Due to the large amount of optimization runs that will be performed, and that the objective of this chapter is to observe the differences between GA and AGA optimal trajectories, different performance metrics will be used to determine the performance of the Pareto front that the optimizer will produce for a specific optimization run. The specific metrics that will be used is explained in section 4.4.4.

In section 8.2.1, the trajectories that will be optimized, and the approach to find the optimal trajectories, are discussed. Section 8.2.2 will then go over the results for these different interplanetary trajectories.

8.2.1. Problem Description

The interplanetary trajectory problems that will be optimized are shown in table 8.2 together with the search space for all the decision variables. The abbreviations for each trajectory represent the sequence of planets, where the first letter is the departure planet (in all cases this is Earth) and the final letter is the capture planet (either Saturn or Jupiter). Each trajectory problem will have a optimization run using only a GA, and for each planet where it is possible an AGA. Thus, for example, for EMJS there will be one optimization run using a GA at Mars and Jupiter, and there will be an optimization run using an AGA at Mars and a GA at Jupiter. Whereas for EVEJS, there will be a GA run, an AGA at Venus run, and an AGA at Earth run. There will be no runs where an AGA at two different planets are used, as the design of a vehicle that can perform an AGA at two different planets is currently not feasible.

An optimization run for an interplanetary trajectory problem consists of 500 individual optimizations of the problem, called trials, which are performed at different seeds. For each trial, the settings for the optimization algorithm remain the same. Once the 500 trials have been performed, the final population of each trial is saved and the optimization algorithm will change settings and do another 500 trials. Only F and Cr will be changed, and n_p and n_b will remain the same. These two parameters were selected as Musegaas [2012] showed that the influence of the other tuning parameters is relatively low. There will be 15 different combinations of tuning parameters. F will be varied between: $[0.2, 0.4, 0.6, 0.8, 1.0]$, and Cr will be varied between $[0.4, 0.6, 0.8]$. This will give a reasonably large exploration of the objective space, and thus a large chance of finding the global optimum. The final problem that will be optimized for each trial is given below:

- **Objective Variables**
  - ΔV

		$S_{best} \cdot 10^7$ [-]	ΔV_{best} [m/s]	TOF_{best} [days]
EMJS	GA	3.08	9898.35	1280
	Mars AGA	2.39	5831.29	1280
EVEJS	GA	2.38	5520.47	1360
	Venus AGA	2.07	5588.79	1360
	Earth AGA	2.38	5520.47	1360
EVEJ	GA	1.08	5554.53	760
	Venus AGA	0.966	5569.84	760
	Earth AGA	1.08	5554.53	760
EVVEJ	GA	1.53	5209.49	840
	Venus 1 AGA	1.50	5600.66	840
	Venus 2 AGA	1.53	5209.49	840
	Earth AGA	1.53	5209.49	840
EVEEJ	GA	2.04	9773.71	840
	Venus AGA	2.15	9953.17	840
	Earth 1 AGA	2.00	9773.71	840
	Earth 2 AGA	2.04	9773.71	840

Table 8.3: Interplanetary trajectory results.

  - TOF_{tot}

- **Decision Variables**
  - t_0
  - $TOF_1, \ldots, TOF_{n_l}$
- **Constraints**
  - see table 8.2

8.2.2. Results

After all the interplanetary trajectories have gone through the analysis discussed in section 8.2.1, the best trajectories for each of the following three metrics are found: S, ΔV, and TOF. The values found for each metric do not necessarily correspond to the same trajectories or Pareto fronts in each row, they are the best values found for all the different seeds, for each algorithm setting. The results are shown in table 8.3.

The first observation that can be made is the fact that for all the trajectories, the minimum TOF can be met. This is expected as, if the ΔV is not limited, the ideal TOF can be met using large impulsive maneuvers to get any desired TOF optimal trajectory. For the ΔV it is harder to get optimal trajectories.

The EMJS trajectory shows a big improvement in both the ΔV and the non-dominated size S, compared to the GA trajectory. An increase of 4067.06 m/s was found in the optimal ΔV trajectory, and a decrease of 7 percent was found in the optimal non-dominated space for the best Pareto front. A more detailed summary of the results for the EMJS trajectory is given in figure 8.7. These figures show the results of all the different algorithm settings for the three different metrics of table 8.3, and it shows the mean coverage C of each of the different S-optimal Pareto fronts found for each setting, where it takes the mean of all the calculated C compared to the other algorithm settings. For both the GA and the AGA, the optimal TOF of all the different settings are relatively the same and are all close to the minimum possible TOF. For the ΔV, the AGA improves upon the GA for all settings, and within the AGA the optimal ΔV trajectories for each setting only differ by a

maximum of 5 m/s. This shows that an AGA ΔV optimal trajectory is relatively easy to find, and that there are multiple options for an AGA trajectory that will improve upon the GA trajectory as for each setting a different trajectory was found. The non-dominated space S shows that, compared to the ΔV, not all the AGA settings will improve upon all the GA settings results. However, if comparing the same settings, each result for the AGA does improve upon the results for the same setting of the GA. What has to be mentioned is that the setting with the best S does not have the best mean C, which means that it gets dominated, on average, by several individuals of the other settings' Pareto fronts. This means that the best non-dominated space Pareto front might not be the best overall Pareto front, and another front with a lower value for C could be selected as the best overall Pareto front.

Several of the Pareto fronts from figure 8.7 are shown in figure 8.8. The Pareto fronts that are selected, for both the GA and AGA, are: the Pareto fronts containing the best ΔV (GA: $F = 0.6$, $C_r = 0.8$, AGA: $F = 0.4$, $C_r = 0.4$), the Pareto fronts with the best non-dominated size S (GA: $F = 0.2$, $C_r = 0.4$, AGA: $F = 0.2$, $C_r = 0.4$), and the Pareto fronts with the best combined non-dominated size S and mean coverage C (GA: $F = 0.4$, $C_r = 0.6$, AGA: $F = 0.4$, $C_r = 0.4$). The non-dominated size is a measure for the area in which new solution can dominate the ones part of the Pareto front. The mean C measures the average fraction of the Pareto front which is dominated by other Pareto fronts. It is imported to note that the AGA Pareto front that has the best ΔV is not the same as the Pareto front that has the best combined S and C, even though the values for the algorithm parameters are the same. Figure 8.8 shows that the Pareto fronts for the GA and AGA are located around the same values for the TOF, and are significantly different in their ΔV requirements. It can also be seen that for the trajectories with the minimal ΔV a TOF of roughly 9 years is expected, which can be minimized by also increasing the ΔV cost. However, this is the same for both the AGA and the GA, thus this is not a disadvantage of the AGA alone. The difference between the optimal S Pareto fronts and the combined S and C optimal Pareto fronts can be seen in the difference in spread of the Pareto fronts. The S Pareto front is more concentrated around a small area, which thus reduces the S of that Pareto front. However, this might not be optimal as only a small part of the solutions are given by that Pareto front. The combined S and C Pareto front has an increase in spread compared to the S optimal Pareto front, which leads to a slightly higher S, but also a better C is found as it spreads more across the Pareto front and thus dominates more of the other Pareto fronts.

Figure 8.9 shows the same Pareto front as in figure 8.8; however, the color of the markers now define the value of one of the decision variables. For both the AGA and GA Pareto fronts, the departure date is relatively similar for individuals that have similar total TOF. This could mean that for all individuals a similar solution was explored, where small differences in the departure date resulted in different TOF and ΔV. Furthermore, the change in departure date shows to have less influence on the ΔV then the TOF. If the TOF of the different legs are inspected, it can be seen that the most changes between Pareto fronts and individuals are for the final two legs: MJ and JS. For the best ΔV Pareto fronts, it can be seen that for ΔV higher then 14 km/s there are several individuals with a low total TOF and a low TOF for the MJ leg, as is expected. However, for the AGA Pareto front there are individuals that have similar total TOF, with lower TOF for the MJ leg. Furthermore, this is compensated for the JS leg, where the inverse has happened and the AGA JS legs are longer then the GA JS legs for the ΔV optimal Pareto fronts. This shows that mission profiles for the AGA are different after the AGA has been performed, and that the approach to the GA including departure date does not have a large influence for these specific Pareto fronts. The optimal S and combined S and C Pareto fronts show similar behaviour for the departure date, where this date is similar for all individuals found in each Pareto front. For the TOF of each leg, it can be seen that each leg has a significantly lower TOF then the ΔV Pareto fronts. Which is expected as the total TOF of both the S and combined S and C Pareto fronts are significantly lower for most of the individuals. Between the AGA and GA Pareto fronts there are less differences. Which results in similar mission profiles, where the main difference is the significant decrease in required ΔV.

Looking at table 8.3, other then the EMJS trajectory there are no AGA interplanetary trajectories among the trajectories that are considered here that improve upon the GA trajectories in ΔV. There are several trajectories that slightly improve S compared to the GA trajectory, but these are only a couple of percents and cannot be weighed against the increased complexity of an AGA. The fact that there is no improvement is most likely due to the fact that either Earth or Venus is used for an AGA in these trajectories. As was shown in section 8.1, the Pareto fronts for Earth and Venus cover significantly less of the search space then the Pareto front of Mars. Furthermore, the area that is covered by the Pareto front is not optimal as V_∞^+ decrease quickly as a function of δ due to the drag experienced in these thicker atmospheres. Thus, trajectories that require long bending angles, which is the main reason of the increase in performance of the AGA, also decrease the velocity significantly. This could cause large ΔV requirements for certain trajectories. This point is eluded upon

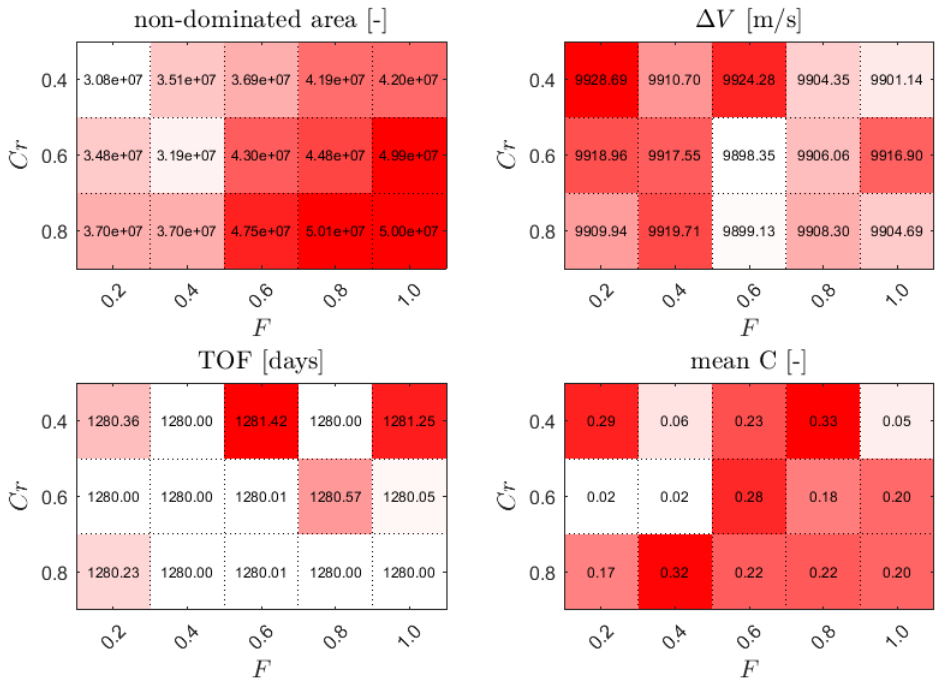

(a) Mars GA.

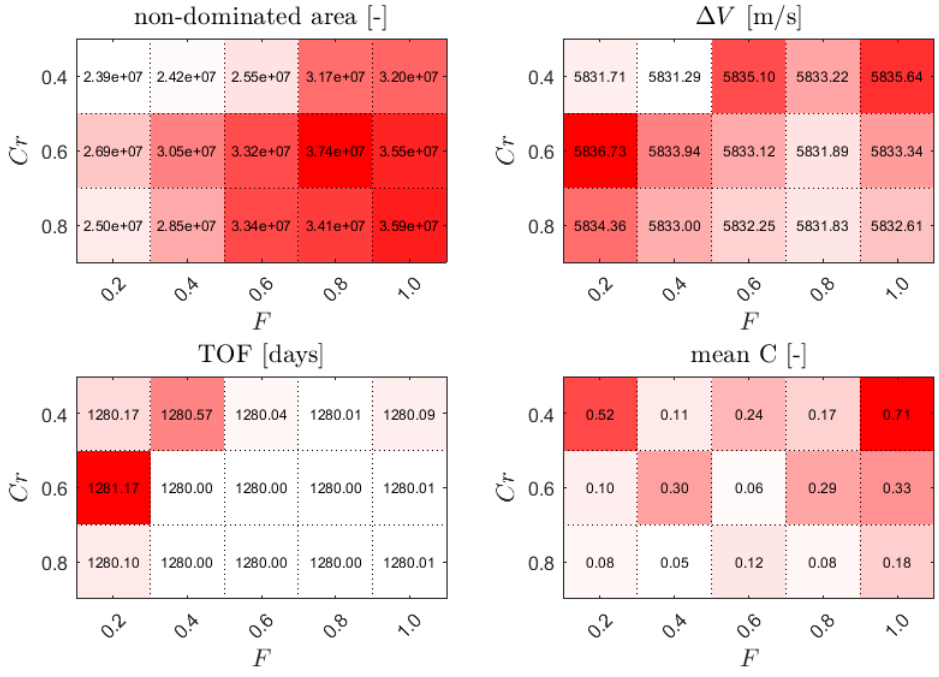

(b) Mars AGA.

Figure 8.7: The statistics of the results for both the GA and AGA of the EMJS trajectory.

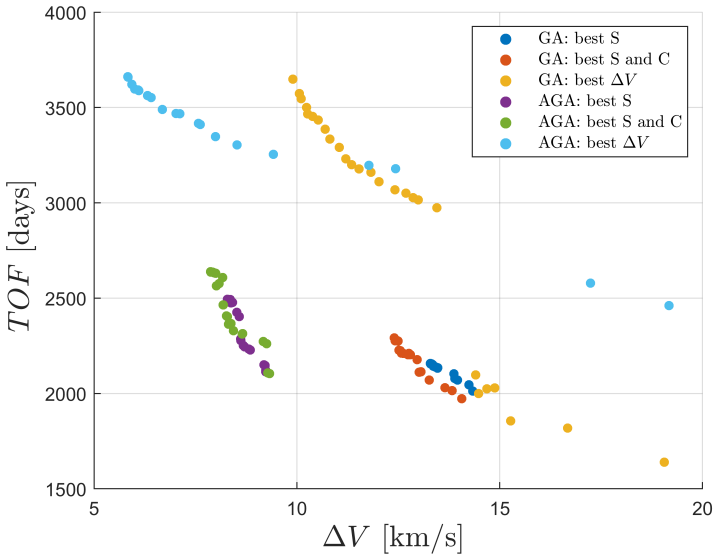

Figure 8.8: Several different Pareto fronts for the EMJS trajectory. The specific fronts are taken from figure 8.7.

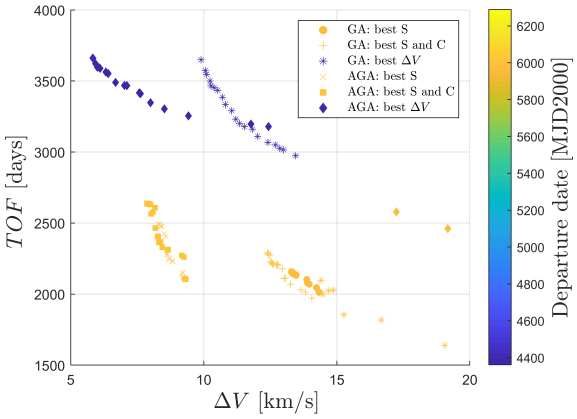

(a) Departure date.

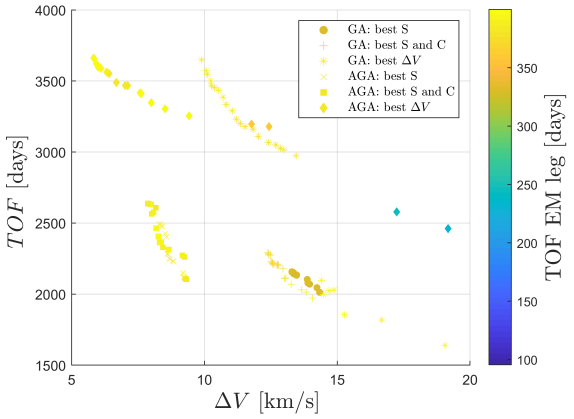

(b) TOF EM leg.

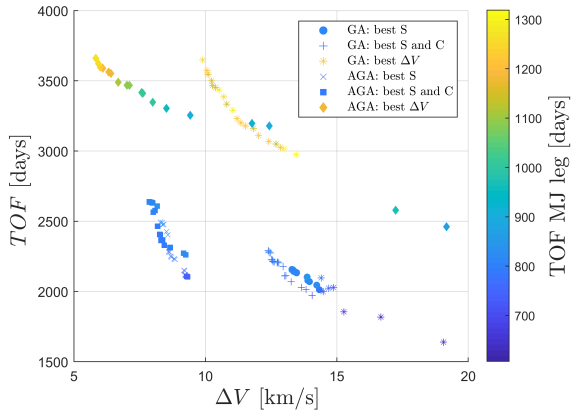

(c) TOF MJ leg

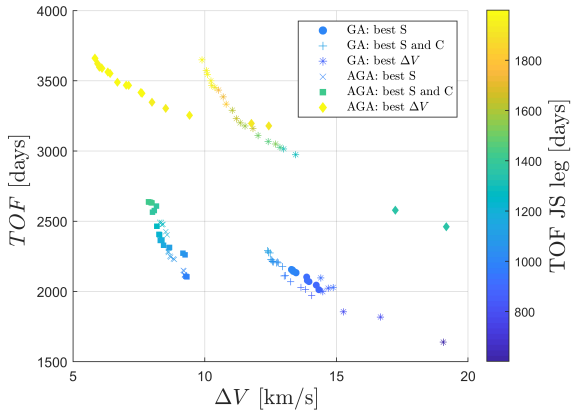

(d) TOF JS leg

Figure 8.9: The values of the decision variables for the different Pareto fronts shown in figure 8.8.

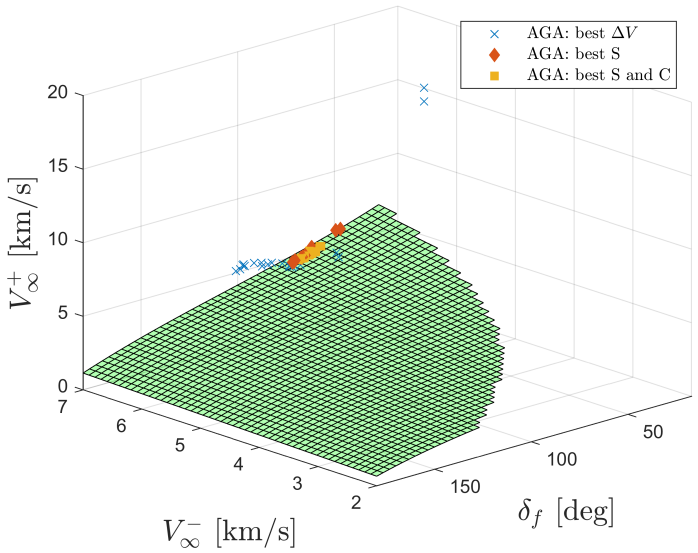

Figure 8.10: The location of the population of several different AGA Pareto fronts for EMJS on the limiting surface of Mars shown in figure 8.1.

more in section 7.4.4.

The EMJS trajectory shows the best promise for an AGA as it increases the performance significantly compared to the GA, and thus this trajectory will be studied in more detail in the next section.

8.3. EMJS Trajectory

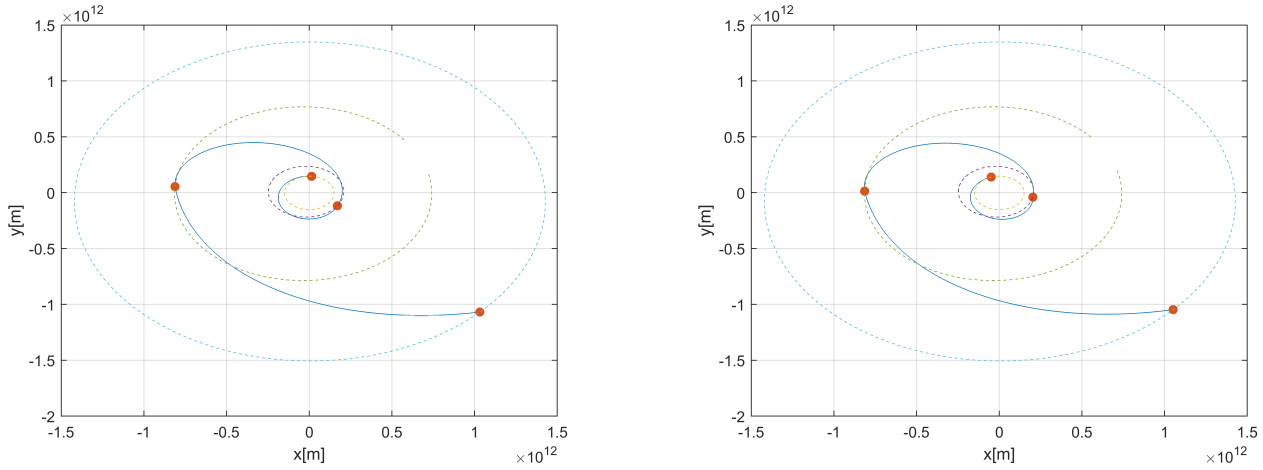

(a) Mars GA.

(b) Mars AGA.

Figure 8.11: The interplanetary trajectory of the EMJS, for both the GA and the AGA at Mars.

The three different AGA Pareto fronts showed in figures 8.8 and 8.9 are now shown in the Mars Pareto front in figure 8.10. Except for two individuals located around V_∞^+, most of the individuals are concentrated around the same region. This location is around the edge of the possible V_∞^- and in a region of lower δ_f. Thus the optimal trajectories for an AGA at Mars in the EMJS trajectories require a high initial velocity and V_∞^+ to not be reduced by drag significantly. Thus, it is likely that the performance of the interplanetary trajectory can be improved by the atmospheric trajectory if the Pareto front is extended beyond its maximum V_∞^- and reduces the slope of V_∞^+ less to allow higher bending angles. The edge can be extended by allowing the heat flux constraint to be increased, or by changing the aerodynamic performance of the waverider to allow flight at

		t_{dep} [MJD2000]	TOF [days]	ΔV [m/s]
Earth departure	GA	4367.238	388.202	3273.18
	AGA	4391.988	399.99	3365.46
Mars swing-by	GA	4755.44	1262.407	5764.64
	AGA	4791.987	1263.669	1609.14
Jupiter swing-by	GA	6017.847	1999.142	0.411876
	AGA	6055.647	1998.439	18.033
Saturn capture	GA	8016.989	-	860.116
	AGA	8054.086	-	838.66

Table 8.4: EMJS trajectory.

	V_∞^- [m/s]	V_∞^+ [m/s]	δ [deg]
GA	5618.85	7157.6	74.47
AGA	6811.43	5773.87	97.23

Table 8.5: Mars swing-by parameters.

less dense altitudes. This can also decrease the drag losses and reduce the slope of V_∞^+. Testing how this can be done and if it improves the interplanetary trajectory performance is left for future research as it is out of the scope of this thesis.

Figure 8.11 shows both the optimal ΔV trajectories of the GA and AGA EMJS problem. Table 8.4 gives the start time of each leg, the TOF of each leg, and the ΔV required for each leg. The trajectories are relatively similar, from both figure 8.11 and table 8.4 it can be seen that the start date of the trajectory only differ by about 24 days, and thus the configuration of planets is also relatively similar. Looking at the departure times, TOF, and ΔV for the Earth departure leg, the Jupiter swing-by leg, and the capture leg at Saturn, it can be seen that the differences are minimal. The Mars swing-by leg also doesn't show significant differences in the departure time and TOF of the leg; however, the ΔV is improved by 4155 m/s. The specific differences of the two maneuvers are shown in table 8.5.

The increased performance of the AGA compared to the GA can be attributed to two parts. The first is the fact that the velocity bending angle is increased by around 23 degrees. This increase in bending angle can increase the heliocentric velocity of the spacecraft compared to the GA maneuver, and thus require less ΔV. The second part is the ΔV required to perform the maneuver. For the GA, a bending angle of 74.47 degrees, and an exit hyperbolic excess velocity of 7157.6 m/s are not possible through an un-powered GA. Thus, to reach these parameters a large impulsive maneuver is used, which costs a significant amount of ΔV. For the AGA, this ΔV cost is significantly less. As can be seen in figure 8.1, when the required δ of 97.23 degrees is reached, the V_∞^+ has not been decreased significantly. This is due to the fact that Mars has a lower gravitational influence then Earth or Mars. This reduces the required velocities to remain in a hyperbolic orbit and thus reduce the gravity losses while in the atmosphere. Thus after travelling over larger θ, less ΔV is needed to correct for the drag losses.

Now that the merit of the Mars AGA is shown, and the parameters for this trajectory are found, it is important to check if the atmospheric trajectory is feasible and what the resulting trajectory looks like.

To find this trajectory, another optimization has to be performed. For this trajectory, it is important not to maximize the bending angle or the exit velocity, but to minimize the difference between the desired and final values of these parameters. As these differences have to be optimized for δ, V_∞^+, and i, and, as was seen in chapter 7, there are other variables (e.g. CA or Q) that can be optimized to improve the trajectory, it is important to find an objective variable that can combine these parameters. Eq. (6.18) gives the ΔV needed to correct for the difference between the desired bending angle δ_f and the actual bending angle $\delta(t_f)$, and for the difference between the desired hyperbolic exit velocity $V_{\infty,f}^+$ and the actual hyperbolic exit velocity

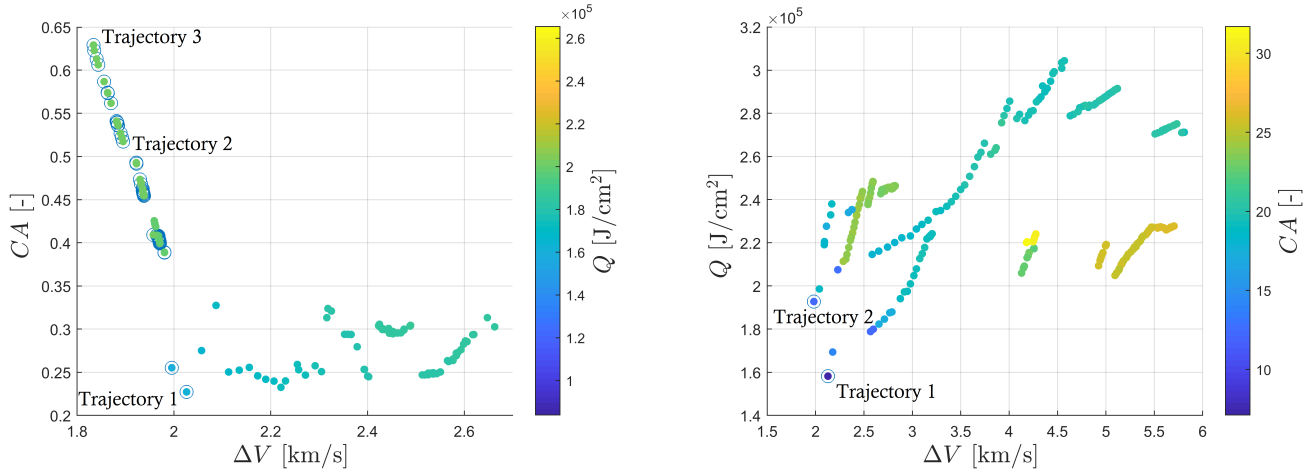

(a) CA optimization run.

(b) Q optimization run.

Figure 8.12: Pareto fronts for the ΔV optimization runs. The whole population for the three seeds are shown, the individuals that are circled are not dominated by any other individuals and are thus part of the Pareto front.

$V_\infty^+(t_f)$. This equation assumes that there is no inclination off-set, but it can be adapted to include this. The equation then looks as follows [Casoliva et al., 2008]:

$$\Delta V_\infty^\perp = V_\infty^+(t_f)\sin(|\Delta i|) \tag{8.3}$$

$$\Delta V_\infty^\parallel = \sqrt{|\boldsymbol{V}_{\infty,f}^+|^2 + |\boldsymbol{V}_\infty^+(t_f)|^2\cos^2(|\Delta i|) - 2|\boldsymbol{V}_{\infty,f}^+||\boldsymbol{V}_\infty^+(t_f)|\cos\Delta\delta\cos(|\Delta i|)} \tag{8.4}$$

$$\Delta V_\infty = \sqrt{(\Delta V_\infty^\perp)^2 + (\Delta V_\infty^\parallel)^2} \tag{8.5}$$

This can be used as an objective variable together with either CA or Q to generate trajectories that minimize the propellant mass needed to correct for the differences between the desired and final values of the AGA. The final trajectories ΔV_∞ should be close to, or below, the value found in table 8.4 (1609 m/s), to verify that the mission planner is able to find feasible AGA trajectories.

The setup of the optimization is the same as in section 7.4. However, the objective variables are now changed to ΔV_∞ and to either CA or Q. CA is used to smoothen the atmospheric trajectory and decrease the change in α over the whole trajectory. Q is used to minimize the TPS mass fraction needed for the AGA. If this mass fraction is larger then the propellant mass decrease due to the lower ΔV of the AGA, the AGA would not be found beneficial compared to the GA. The initial conditions of the simulation are kept the same as in section 7.4, except for the V_∞^-, which is taken from table 8.5. Both of these optimizations are performed for three different seeds and the combined final population is shown in figure 8.12.

For both optimization runs, there are several individuals that are not dominated by any other individual in the population and are thus part of the Pareto front. These individuals are encircled in figure 8.12. For the CA optimization, the individual with the lowest $\Delta V = 1829$ m/s is found to differ with the expected $\Delta V = 1609$ m/s by 210 m/s. When compared to the residuals shown in figure 8.2, the difference of 210 m/s falls within a large part of the residuals of the Pareto front of Mars. Furthermore, comparing the 210 m/s with the increase in ΔV for the gravity assist at Mars shows that this difference does not affect the conclusion that can be drawn with respect to the performance increase of the AGA. The difference between the estimated ΔV and the true ΔV is likely due to the uncertainty in the surface fitted through the Pareto front for the Mars AGA, and the inclusion of Δi into the ΔV calculation. Furthermore, as was shown in section 7.4, the convergence behaviour of the atmospheric trajectory optimization is rather poor, thus differences in the solution for which the two different optimizations are performed is expected. The difference of 210 m/s should be investigated further in future research to improve the accuracy of the interplanetary mission planner.

To inspect the atmospheric trajectories, several trajectories are selected from both Pareto fronts. For the CA Pareto front three trajectories were selected that are spaced evenly over the Pareto front. These trajectories are highlighted in figure 8.12a and shown in detail in figure 8.13. For the Q trajectory, there are only two individuals that are part of the Pareto front, thus these ones are also selected to be shown in more detail. These trajectories are also highlighted in figure 8.12b and shown in detail in figure 8.14.

	M_{wet} [kg]	M_{prop} [kg]	M_{TPS} [kg]	M_{res} [kg]
GA	800	680	0	120
AGA	800	456	151	193

Table 8.6: Masses for the two different missions.

The three CA trajectories all have a similar θ of between 80 and 90 degrees. This shows that the desired δ is reachable by all three trajectories. Furthermore, due to the fact that Δi is part of the ΔV objective variable, and the fact that CA is used as the second objective variable, the bank angle σ remains close to constant at an angle of 180 degrees for the whole trajectory. This minimized the out-of-plane movement and thus the offset in inclination. The largest source of ΔV is thus the V_∞^+ difference. The velocity of the vehicle does not go down to just above the escape velocity as in section 7.4, as this is done to minimize the velocity difference. However, as it is not possible to completely reach the target value of V_∞^+ due to the drag losses when reaching the desired δ, there is still a ΔV maneuver required to increase the velocity when exiting the atmosphere. Observing the heat profile, it can be seen that both trajectory 2 and 3 have two heat flux peaks. This is not beneficial as the heat load is increased and thus also the TPS mass. This can be solved by minimizing the heat load Q.

The Q optimization trajectories show similar results as the CA trajectories for the reached θ and the final velocities. However, for these trajectories the heat load is significantly lowered (even though there still exists a second, smaller heat flux peak for one of the trajectories). The downside is that for these trajectories, the bank angle does not stay constant and an out-of-plane movement is thus present, which requires an increase in ΔV. Taking the heat load for trajectory 1 ($1.6 \cdot 10^5$ J/cm^2) and inferring the TPS mass fraction using the data from previous missions given in table 3.3 and Eq. (3.26), it can be estimated that the mass fraction needed is roughly 44 percent of the dry mass of the spacecraft. Figure 3.7 shows that Eq.(3.26) has a rather large uncertainty compared to the data, especially between $Q = 3 \cdot 10^4$ and $Q = 2 \cdot 10^5$. Thus the TPS mass fraction given here is a rough estimate. This mass fraction can be compared with the decrease in propellant mass from the ΔV decrease due to the use of the AGA. As for the departure maneuver a part of the rocket can be used to depart from the parking orbit, this maneuver is not taken into account for the mass calculation. Using Tsiolkovsky's rocket equation where I_{sp} is the specific impulse of the rocket:

$$\Delta V = -I_{sp} g_0 \ln \frac{M_{dry}}{M_{wet}} \tag{8.6}$$

and the following fact for the propellant mass fraction:

$$\frac{M_{prop}}{M_{wet}} = 1 - \frac{M_{dry}}{M_{wet}} \tag{8.7}$$

the propellant mass can be calculated using the following equation:

$$\frac{M_{prop}}{M_{wet}} = 1 - \exp\left(-\frac{\Delta V}{I_{sp} g_0}\right) \tag{8.8}$$

Filling in the ΔV of the GA at Mars from table 8.4 and the ΔV from trajectory 1 of figure 8.14 in Eq.(8.8) using $I_{sp} = 350$ s gives the distribution of masses for the mission vehicles of the GA and the AGA in table 8.6. As can be seen, the increase in available mass for this mission is 60 percent larger when an AGA is used then for the GA mission profile. This mass can either be reduced to minimize the launch costs from Earth, or it can be used towards the payload or other subsystems of the vehicle to increase the value of the mission.

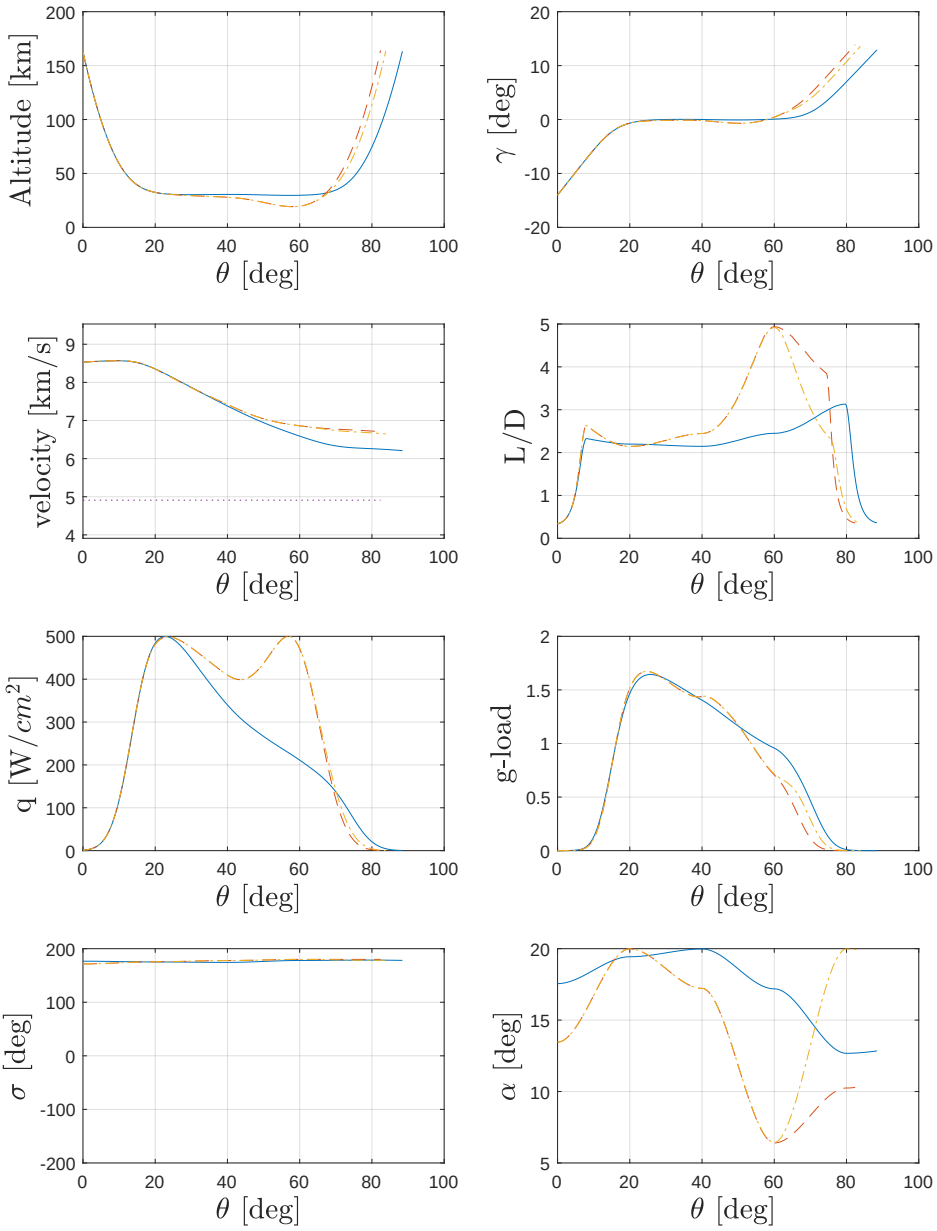

Figure 8.13: Three selected trajectories from the ΔV and CA optimization results seen in figure 8.12. Trajectory 1 is the solid line, trajectory 2 the dashed line, and trajectory 3 the dashed-dotted line.

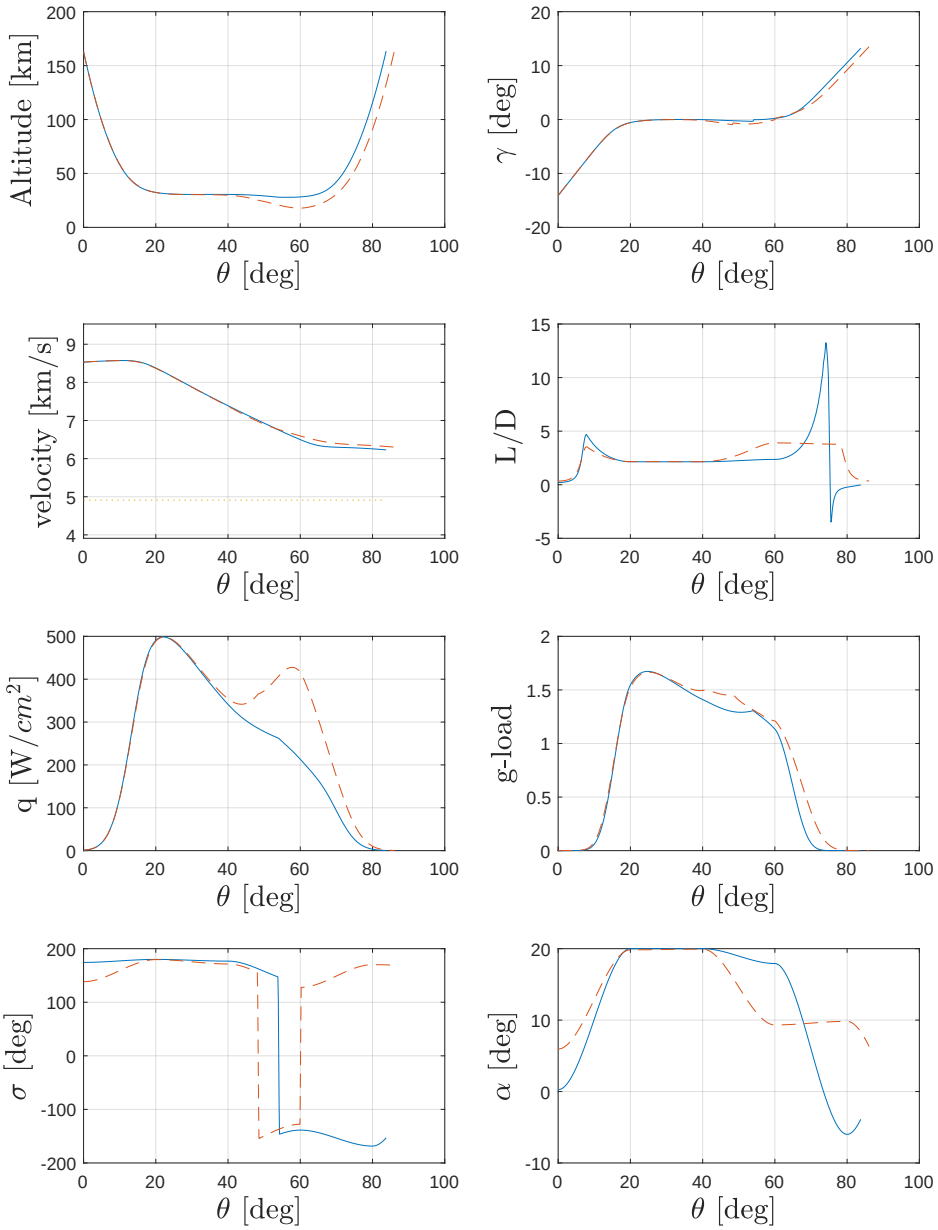

Figure 8.14: Three selected trajectories from the ΔV and Q optimization results seen in figure 8.12. Trajectory 1 is the solid line, and trajectory 2 is the dashed line.

9

Conclusion and Recommendations

9.1. Conclusion

In chapter 1, several goals were stated that needed to be achieved during this research project:

1. Build a simulation environment that can simulate the trajectory of a specific vehicle through the atmospheres of several different planets.
2. Build a mission planner that can simulate a specific interplanetary trajectory using both gravity assists and aerogravity assists.
3. Find optimal atmospheric trajectories for an aerogravity assist and use them to find optimal interplanetary trajectories.
4. Compare the optimal interplanetary trajectories using only gravity assists with optimal trajectories that use the aerogravity assist.

Together, these goals should allow for an answer to the main research question of this thesis:

How much does the aerogravity assist improve the performance of interplanetary trajectories compared to a gravity assist?

This section will go through these goals and discuss the main conclusions that can be made about them. At the end of this section, an answer will then be given for the main research question based on the conclusions of the research goals.

The Simulation Environment

The simulation environment was built using the TU Delft Astrodynamics Toolbox. The complete set-up of the simulator is discussed in section 5.1 and the selection of the specific models used in the generation of atmospheric trajectories is discussed in 5.3. The models used are based on the fact that the goal of this thesis is to show the feasibility of AGA trajectories and determine the achievable performance characteristics.

The development of the guidance and control system is discussed in section 2.5. This system was assumed to be perfect, thus meaning that the desired control variables are directly translated to the vehicles state. This assumption is made as the main goal is not to test what systems are needed to fly a specific AGA trajectory, but to find feasible trajectories and determine the gain of an AGA compared to a GA. Previous research (see e.g. Casoliva et al. [2008], Lyons et al. [2008], and Hess [2016]) used either the bank angle σ or the angle-of-attack α as the only control variable, and kept the other variable constant during flight. Section 2.5.1 lists the advantages and disadvantages of using each separate control strategy. It was decided to use both α and σ as control variables to combine the advantages of both control variables, and diminish the disadvantages of each of them. Hess [2016] found that using σ only control, an aerogravity assist for a vehicle with a reference area of 6.67 m^2 was not possible at Mars and increased the surface area by a factor of 10. For the same vehicle, using both σ and α as control variables, it was found that an aerogravity assist could be performed using the same reference area as before. Furthermore, no constraints needed to be set on γ_i as using α allows for more controllability during atmospheric entry.

The aerodynamics of the vehicle are one of the most important aspects of an AGA, thus this is discussed in detail in chapter 3. A waverider designed by Hess [2016] is used in this thesis where the aerodynamic characteristics of this vehicle are determined in the three different aerodynamic regimes discussed in section 3.1.1. It was found that the L/D of this vehicle is 10 times larger for the continuum flow then for the free molecular flow.

Both the convective and radiative heating is simulated during the AGA. To protect the vehicle, an analysis was done of possible thermal protection systems (TPS). A maximum heat flux of 500 W/cm^2 at Mars and 2000 W/cm^2 at Earth and Venus was put as a constraint for the atmospheric trajectories, and thus from this a material can be selected. For Mars, it was determined that PICA would be suitable for the TPS, and for Venus and Earth, the Heritage Carbon Phenolic material was deemed as suitable.

Mission Planner

The mission planner architecture was based on the work done by Melman [2007] and Musegaas [2012] and is discussed in detail in section 6. The mission planner assumed single revolution Keplerian transfer with no external perturbations and using no deep space maneuvers.

A key contribution of this thesis is the implementation of the numerically found AGA atmospheric trajectories into the interplanetary mission planner. Henning et al. [2014] developed a similar method to find interplanetary AGA trajectories using optimal control theory and a simplified dynamical model for the atmospheric trajectories. This thesis developed a novel method and improves on Henning et al. [2014] by moving the calculation of atmospheric trajectories out of the interplanetary optimization loop and implementing heating constraints, improved and more accurate control strategies, and a realistic dynamical model. The mission planner designed in this thesis allows for more realistic interplanetary trajectories to be found and increasing the accuracy of the AGA and GA trajectory comparisons.

Atmospheric Trajectory

An optimization algorithm was used to find atmospheric trajectories for the aerogravity assist. To investigate the search space of the optimization problem and the dependencies between the possible decision and objective variables, a Monte Carlo analysis was performed. This analyses resulted in the conclusion that the optimal solutions for the atmospheric trajectory are located in a small volume inside the search space and that to find this solution, a global optimization algorithm is needed. The Monte Carlo analysis also helped in the determination of the optimal optimization set-up, discussed in section 7.2.

The performance of two optimization algorithms, MOEA/D and NSGA-II, are determined in section 7.3. It was found that the performance of the MOEA/D is more desirable then that of the NSGA-II algorithm. The effect of the algorithm settings was also investigated and it was shown that changing one of these settings can already have a large effect on the solution found by the optimization algorithm. The fact that a large amount of local minima were found in this analysis, in combination with the poor convergence behaviour shown by several of the results in section 7.4, shows that future research should be focused on tuning the optimization algorithm to be able to find the global optimum for the atmospheric trajectory.

The atmospheric trajectory for an aerogravity assist at Mars, Earth, and Venus were optimized, where θ and Δi were chosen as the objective variables. It was found that the trajectories part of the Pareto front at Mars were able to reach the largest bending angles of all the planets investigated: $\theta = (114°, 121°)$, with $\Delta i = (0°, 0.25°)$. However, the trajectory was also found to not be smooth due to the changes in the L/D induced by α. This was solved by minimizing the control action (CA) instead of Δi which minimizes the changes in α and σ during the trajectory. Using CA resulted in a smoother, more desirable, trajectory for Mars. Furthermore, the maximum θ found was increased by 30 degrees. Both Earth and Venus trajectories showed smaller θ then Mars, as their atmospheres are much thicker and thus the velocity was reduced quicker due to the drag losses. Furthermore, due to the higher gravitational influence of the two planets, the velocities to remain in a hyperbolic orbit are much higher and thus the drag experienced is also higher. The Pareto front of Earth trajectories were comprised of trajectories for which $\theta = (40°, 56°)$. The Pareto front at Venus performed slightly better with: $\theta = (68°, 70°)$. The trajectory at Venus experiences two heat flux peaks, which is undesirable as the TPS mass fraction would need to be high. This was solved by optimizing the total heat load Q instead of Δi. The results not only showed that the second heat flux peak was removed, the maximum heat flux was also diminished by 1000 W/cm^2. However, θ was significantly reduced for this trajectory. For Earth, it was also tested if the accuracy of the environment and acceleration models used influences the found trajectory. The achieved performance of the two different optimizations were found to be equal. The flown trajectories were different due to the fact that the gliding equilibrium flight took place at different altitudes. It

was found that the density at which the trajectories performed the gliding equilibrium flight was equal, thus the difference in trajectory is mainly due to the difference in density profiles of the atmosphere models.

Interplanetary Trajectory

The implementation of the AGA into the mission planner can be found in section 6.1.3 and the limiting surfaces of the three different planets are found in section 8.1. It was found that the different V_∞^- were limited to between: 2 and 7 km/s for Mars, 3 and 6.5 km/s for Earth, and 3 and 8.5 km/s for Venus. These limits are present due to the fact that either the vehicle does not have a high enough velocity to exit the gravitational field again after the AGA, and because of the fact that for higher initial velocities, the maximum heat flux is exceeded. It was found that the Pareto front of Earth and Venus cover a smaller space then that of Mars. Furthermore, the V_∞^+ drops off much quicker for Earth and Venus compared to Mars, due to the larger drag losses. The misfits between the optimized atmospheric trajectories and the fitted surface were found to be generally around 200 m/s for Mars and Venus, whereas the misfits for Earth are more in the area of 20 m/s.

The different interplanetary trajectories that are optimized can be found in section 8.2. From the results of 5 different planetary sequences, it was observed that only an aerogravity assist at Mars could significantly increase the performance of the interplanetary trajectory compared to a gravity assist. The lowest found non-dominated space was decreased by 7 percent for the aerogravity assist, and the ΔV was decreased by 4067 m/s. For each trajectory that used an aerogravity assist at Venus or Earth, the performance was not increased compared to the gravity assist. It was determined that at Earth and Venus the velocities during atmospheric flight are much higher due to the larger gravitational influence. Furthermore, the atmospheres at these planets are much thicker then at Mars. These physical effects increase the drag loss and heating experienced by the vehicle, which in turn decreases the possible V_∞^- range, decreases the possible δ, and increases the drop in V_∞^+ as a function of δ.

The Mars aerogravity assist was investigated in more detail, and it was found that the parameters for the gravity assist and aerogravity assist for the ΔV optimal trajectory are relatively similar. The main differences were the increase of 23 degrees in δ, and the fact that for the aerogravity assist 4155 m/s less ΔV was required to perform the swing-by maneuver. To observe the atmospheric trajectory of this Mars aerogravity assist, and verify that the ΔV found by the mission planner is accurate, an optimization was performed for the atmospheric trajectory, where the objective variable is the ΔV needed to achieve the desired trajectory. Two different optimization runs were performed, where one run used CA as the second objective variable, and the other one used Q as the second objective variable. It was found that for the CA trajectory, the ΔV is increased by 210 m/s compared to what was expected. This increase corresponds to the standard deviation of the misfits and is not significant enough to make the performance of the aerogravity assist less then that of the gravity assist. Furthermore, σ was kept almost constant at 180 degrees for the complete trajectory and no bank reversals were performed. This decreases the complexity of the guidance and control system significantly. The Q optimal trajectories show trajectories that decrease the heat load compared to the CA trajectory. However, the optimal ΔV of the Q trajectory is slightly higher then that of the CA trajectory. It was found that, taking the parameters of the Q optimal trajectory, the difference between the propellant mass needed for the extra ΔV of a gravity assist trajectory and the TPS mass needed for the aerogravity assist is 60 percent. This 60 percent could thus be used for extra mass towards the payload, or other important subsystems of the spacecraft. There is a large uncertainty in the TPS mass fraction, and thus this number is a rough approximation. However, it shows a promising result for the use of an AGA in an interplanetary mission.

9.2. Recommendations

There are several sections of the AGA that can be investigated in more detail, which are listed below.

Optimal Solution Search

It was already shown in this thesis that the optimization process for this problem is complex. The behaviour of the decision and objective space was not predictable, and the convergence behaviour of the solutions found in section 7.4 was not optimal. Increasing the computational time of the optimization algorithm using either large clusters of processors, or using more efficient algorithms could significantly help the search for optimal trajectories. This would allow a more extensive tuning operation to be done for the generation of optimal atmospheric trajectories. Having the optimal setup of the optimization algorithm could increase the likelihood of finding optimal trajectories, and even possibly find better trajectories then are currently found.

The optimal setup can furthermore be found by performing a dedicated study on the decision and objective space of this problem. This thesis had performed a preliminary analysis using a Monte Carlo analysis, which can be improved upon in future research. Musegaas [2012] gives various methods by which this can be done, and provides several ways of implementing the results of this analysis into the set-up and tuning process of the optimization algorithm.

Increasing Technological Readiness Level

The main research of this thesis was focused on finding interplanetary and atmospheric trajectories for the aerogravity assist. A logical next step would be to focus more on individual vehicle systems and find if current technology allows for these trajectories to be performed. A disadvantage of using α for control was that changing α over large amount of degrees might not be possible at hypersonic speeds. Studying if the trajectories found here have this problem, and if so, how it could be solved, could give more insight in what the optimal control strategy is for an aerogravity assist. Furthermore, in this thesis, it was assumed that there were no perturbations in the environment compared to the expected conditions, and that there are no uncertainties in the control and navigation systems. Performing a sensitivity analysis gives information on how these uncertainties and perturbations might affect the trajectory of the vehicle. Combining this with the development of a guidance algorithm that corrects for these uncertainties and perturbations, might give more insight into the feasibility of the aerogravity assist.

A rough estimate was used to determine the mass of the TPS. As the heating of the vehicle is one of the main drawbacks of the AGA, a more in depth analysis of the heating effects and the design of the TPS is needed to determine more accurate heating constraints for trajectory optimization, and determine the effects of the TPS on the dynamics of the vehicle.

Vehicle Dynamics

Due to the low performance of the waverider at higher altitudes, it could be of interest to investigate if the aerodynamic performance at high Knudsen numbers could be increased. This was especially a problem at Earth and Venus as the higher velocities increased the drag experienced by the waverider at these planets. The development of a vehicle that performs better at higher Knudsen numbers could allow for the waverider to fly at higher altitudes and thus experience less drag. This could increase the performance at Venus and Earth, and thus also increase the amount of optimal interplanetary trajectories. Furthermore, flight and wind tunnel tests of waverider type vehicles have not been performed extensively. These types of research could give more insight in the feasibility and properties of these types of vehicles.

The mission planner in this thesis could be expanded to increase the amount of situations it can simulate. Currently, the mission planner allows only single revolution trajectories to be found, and no deep space maneuvers were considered. Adding multiple revolutions allow for more possible trajectories to be found by the optimization algorithm. Deep space maneuvers could be beneficial for aerogravity assists as they can alter the state of the spacecraft before entering the atmosphere to prepare for an aerogravity assist, or correct for the drag losses experienced during atmospheric flight. This increase in ΔV for the deep space maneuver could be offset by a decrease in the ΔV needed for an aerogravity assist compared to a gravity assist.

The investigation of trajectories was limited to only 5 different combinations of swing-by bodies. To increase the accuracy of the conclusions made about aerogravity assists, extra trajectories need to be considered. Trajectories that go further then Saturn, and trajectories towards the inner Solar System have not been considered yet, and might give different results. Furthermore, this thesis was not concerned with the amount of possible launch dates for aerogravity assist trajectories. Investigating this could show more advantages to using an aerogravity assist compared to a gravity assist.

A

Monte Carlo Results

The results for the Monte Carlo analysis for both the angle-of-attack nodes (figure A.1) and the bank angle nodes (figure A.2) are shown in this appendix. The Monte Carlo analysis was performed using 10,000 different runs, where for each run the value at each control node is altered. Each objective variable is explained in more detail in section 7.1. All 10 nodes are varied for each trajectory and trajectories which end in the vehicle reaching an altitude of below zero kilometres and trajectories that end with the vehicle leaving the atmosphere again are separated by red and green dots respectively. For Δi, $\Delta\delta$, and $\Delta RAAN$, the red trajectories are not shown, as these quantities are not valid for trajectories that do no leave the atmosphere.

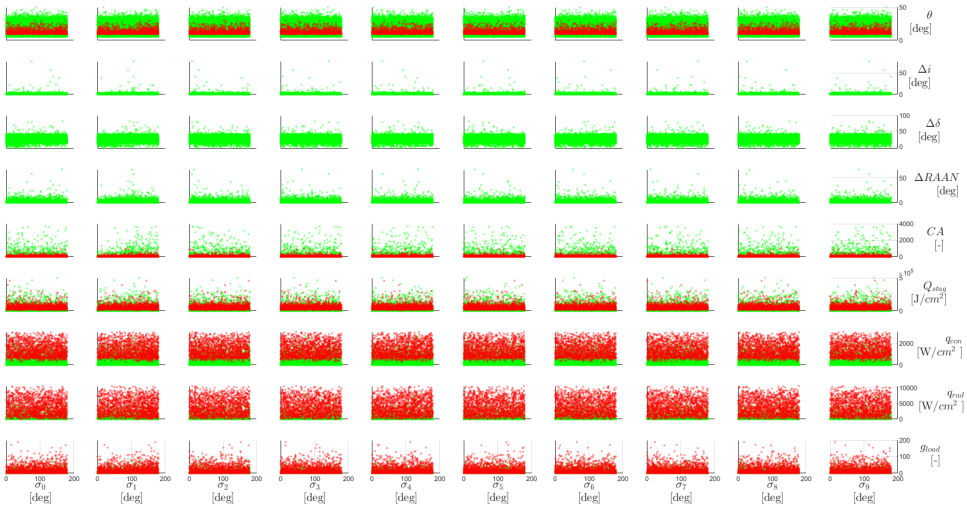

Figure A.1: The Monte Carlo results with 10,000 runs for the angle-of-attack control nodes. The red dots represent trajectories where the vehicle reaches zero kilometres altitude, and the green dots represent trajectories where the vehicle leaves the atmosphere again.

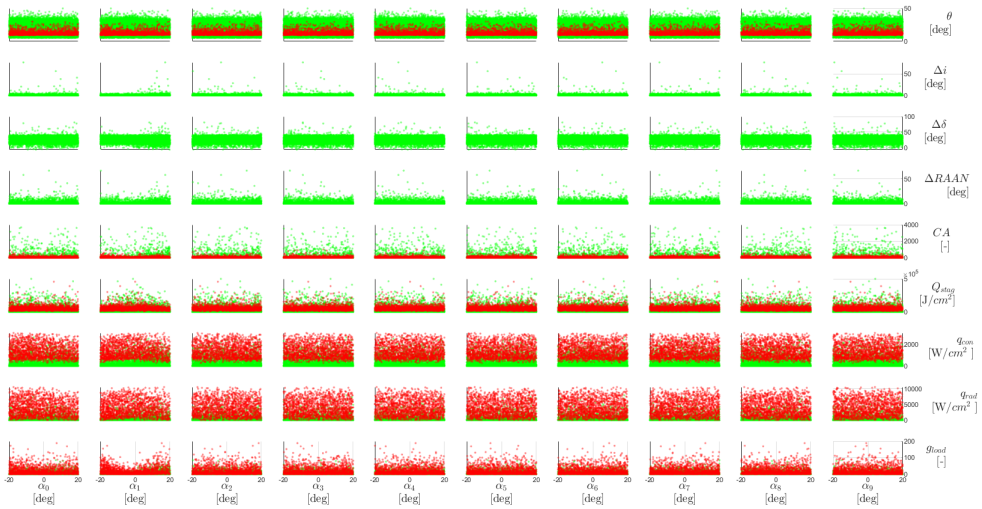

Figure A.2: The Monte Carlo results with 10,000 runs for the angle-of-attack control nodes. The red dots represent trajectories where the vehicle reaches zero kilometres altitude, and the green dots represent trajectories where the vehicle leaves the atmosphere again.

B

Model Selection Validation

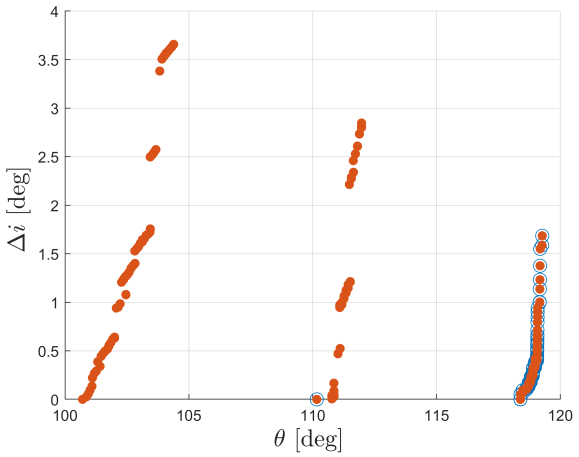

(a) Mars high fidelity optimization run.

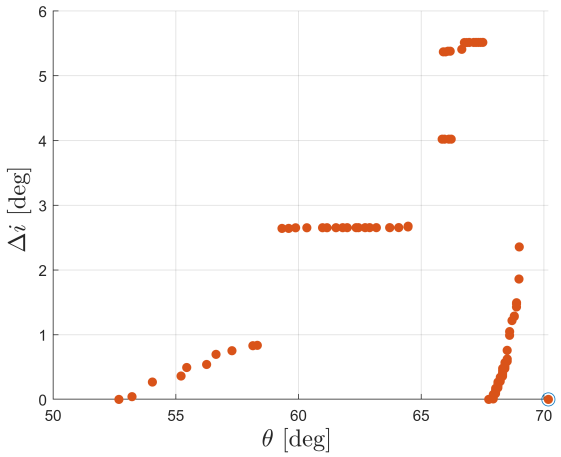

(b) Venus high fidelity optimization run.

Figure B.1: Pareto fronts for the high fidelity optimization runs. The whole population for the three seeds are shown, the individuals that are circled are not dominated by any other individuals and are thus part of the Pareto front.

Figure B.1 shows the final population for the optimization runs at Mars and Venus using high fidelity models. For Mars the EMCD atmosphere model, 4th degree spherical harmonics gravity field, and third body perturbation of the Sun was used. Venus also uses the 4th degree spherical harmonics gravity field and third body perturbation of the Sun, however due to time constraints a higher fidelity atmosphere model was not available. It can be seen that the performance of the Pareto fronts found for this optimization set-up is similar to the ones found in section 7.4. The distribution of the individuals is different, which means that the specific trajectories might not be similar. The goal of this thesis is not to simulate trajectories that need to be flown, but to generate feasible AGA trajectories and determine their achievable performance. Thus as the performance is similar for high and low fidelity models, it is valid to use the low fidelity models to generate the trajectories for this thesis.

Bibliography

Altwegg, K., Balsiger, H., Bar-Nun, A., Berthelier, J. J., Bieler, A., Bochsler, P., Briois, C., Calmonte, U., Combi, M., De Keyser, J., Eberhardt, P., Fiethe, B., Fuselier, S., Gasc, S., Gombosi, T. I., Hansen, K. C., Hassig, M., Jackel, A., Kopp, E., Korth, A., LeRoy, L., Mall, U., Marty, B., Mousis, O., Neefs, E., Owen, T., Reme, H., Rubin, M., Semon, T., Tzou, C.-Y., Waite, H., and Wurz, P. (2015). 67P/Churyumov-Gerasimenko, a Jupiter family comet with a high D/H ratio. *Science*, 347(6220):1261952–1261952.

Anderson, J. D. (2006). *Hypersonic and High-Temperature Gas Dynamics*. American Institute of Aeronautics and Astronautics, 1801 Alexander Bell Drive, Reston, Virginia 20191-4344, second edition.

Anderson, J. D., Lewis, M. J., Kothari, A. P., and Corda, S. (1991). Hypersonic waveriders for planetary atmospheres. *Journal of Spacecraft and Rockets*, 28(4):401–410.

Armellin, R., Lavagna, M., and Ercoli-Finzi, A. (2006). Aero-gravity assist maneuvers: controlled dynamics modeling and optimization. *Celestial Mechanics and Dynamical Astronomy*, 95(1-4):391–405.

Armellin, R., Lavagna, M., Starkey, R. P., and Lewis, M. J. (2007). Aerogravity Assist Maneuvers: Coupled Trajectory and Vehicle Shape Optimization. *Journal of Spacecraft and Rockets*, 44(5):1051–1059.

Arora, N. and Russell, R. P. (2010). A fast, accurate, and smooth planetary ephemeris retrieval system. *Celestial Mechanics and Dynamical Astronomy*, 108(2):107–124.

Battin, R. H. (1959). The Determination of Round-Trip Planetary Reconnaissance Trajectories. *Journal of the Aerospace Sciences*, 26(9):545–567.

Bertin, J. J. and Cummings, R. M. (2006). Critical Hypersonic Aerothermodynamic Phenomena. *Annual Review of Fluid Mechanics*, 38(1):129–157.

Bird, G. (1994). *Molecular Gas Dynamics and the Direct Simulation of Gas Flows*. Oxford University Press, Walton Street, Oxford, OX2 6DP, first edition.

Biscani, F., Izzo, D., and Märtens, M. (2018). esa/pagmo2: pagmo 2.7.

Blanchard, R. C. and Buck, G. M. (1986). Rarefied-flow aerodynamics and thermosphere structure from Shuttle flight measurements. *Journal of Spacecraft and Rockets*, 23(1):18–24.

Blosser, M. L., Blankson, I. M., Schwoerke, S., Brunson, D., and Hagseth, P. (1995). Wing leading-edge design concepts for airbreathing hypersonic waveriders. *Journal of Aircraft*, 32(2):307–312.

Bonfiglio, E. P., Longuski, J. M., and Vinh, N. X. (2000). Automated Design of Aerogravity-Assist Trajectories. *Journal of Spacecraft and Rockets*, 37(6):768–775.

Boyd, I. D. (2015). Computation of Hypersonic Flows Using the Direct Simulation Monte Carlo Method. *Journal of Spacecraft and Rockets*, 52(1):38–53.

Breakwell, J. V. and Rauch, H. E. (1966). Optimum Guidance for a Low Thrust Interplanetary Vehicle. *AIAA*, 4(4):693–704.

Casoliva, J., Lyons, D., Wolf, A., and Mease, K. (2008). Robust Guidance via a Predictor-Corrector Algorithm with Drag Tracking for Aero-Gravity Assist Maneuvers. In *AIAA Guidance, Navigation and Control Conference and Exhibit*, Reston, Virigina. American Institute of Aeronautics and Astronautics.

Deb, K., Pratap, A., Agarwal, S., and Meyarivan, T. (2002). A Fast and Elitist Multiobjective Genetic Algorithm: NSGA-II. *IEEE Transactions on Evolutionary Computation*, 6(2).

Dijkstra, M., Mooij, E., and Sudmeijer, K. (2013). Trajectory Optimization to Support the Study of Hypersonic Aerothermodynamic Phenomena. In *AIAA Atmospheric Flight Mechanics (AFM) Conference*, Reston, Virginia. American Institute of Aeronautics and Astronautics.

Dirkx, D. (2015). *Interplanetary Laser Ranging*. PhD thesis, Delft University of Technology.

Dirkx, D. and Mooij, E. (2011). Continuous Aerodynamic Modelling of Entry Shapes. In *AIAA Atmospheric Flight Mechanics Conference*, Reston, Virigina. American Institute of Aeronautics and Astronautics.

Dirkx, D. and Mooij, E. (2014). Optimization of entry-vehicle shapes during conceptual design. *Acta Astronautica*, 94(1):198–214.

Duvall, A., Justus, C., and Keller, V. (2005). Global Reference Atmospheric Model (GRAM) Series for Aeroassist Applications. In *43rd AIAA Aerospace Sciences Meeting and Exhibit*, Reston, Virigina. American Institute of Aeronautics and Astronautics.

Edelman, P. J. and Longuski, J. M. (2017). Optimal Aerogravity-Assist Trajectories Minimizing Total Heat Load. *Journal of Guidance, Control, and Dynamics*, pages 1–5.

Edquist, K. T., Hollis, B. R., Dyakonov, A. A., Laub, B., Wright, M. J., Rivellini, T. P., Slimko, E. M., and Willcockson, W. H. (2007). Mars Science Laboratory Entry Capsule Aerothermodynamics and Thermal Protection System. In *2007 IEEE Aerospace Conference*, pages 1–13. IEEE.

Ehrenfreund, P. and Charnley, S. B. (2000). Organic Molecules in the Interstellar Medium, Comets, and Meteorites: A Voyage from Dark Clouds to the Early Earth. *Annual Review of Astronomy and Astrophysics*, 38(1):427–483.

Fienga, A., Manche, H., Laskar, J., Gastineau, M., and Verma, A. (2014). INPOP new release: INPOP13b. *ArXiv e-prints*.

Flandro, G. (1966). Fast reconnaissance missions to the outer solar system utilizing energy derived from the gravitational field of Jupiter. *Acta Astronautica*, 12:329–337.

Früh, C. and Jah, M. K. (2014). Coupled orbit–attitude motion of high area-to-mass ratio (HAMR) objects including efficient self-shadowing. *Acta Astronautica*, 95:227–241.

Gang, C., Min, X., Zi-ming, W., and Si-lu, C. (2005). RLV Reentry Trajectory Multi-Objective Optimization Design Based on NSGA2 Algorithm. In *AIAA Atmospheric Flight Mechanics Conference and Exhibit*, Reston, Virigina. American Institute of Aeronautics and Astronautics.

Gillum, M. J. and Lewis, M. J. (1997). Experimental Results on a Mach 14 Waverider with Blunt Leading Edges. *Journal of Aircraft*, 34(3):296–303.

Gooding, R. H. (1990). A procedure for the solution of Lambert's orbital boundary-value problem. *Celestial Mechanics and Dynamical Astronomy*, 48(2):145–165.

Gulli, S., Maddalena, L., and Hosder, S. (2012). Variable Transpiration Cooling: A New Solution for the Thermal Management of Hypersonic Vehicles. In *50th AIAA Aerospace Sciences Meeting including the New Horizons Forum and Aerospace Exposition*, Reston, Virigina. American Institute of Aeronautics and Astronautics.

Harpold, J. C. and Graves, C. A. (1979). Shuttle Entry Guidance. *Journal of the Astronautical Sciences*, 27(3):239–268.

Hart, K. A., Dutta, S., Simonis, K., Steinfeldt, B. A., and Braun, R. D. (2014). Analytically-derived Aerodynamic Force and Moment Coefficients of Resident Space Objects in Free-Molecular Flow. In *AIAA Atmospheric Flight Mechanics Conference*, Reston, Virginia. American Institute of Aeronautics and Astronautics.

Henning, G. A., Edelman, P. J., and Longuski, J. M. (2014). Design and Optimization of Interplanetary Aerogravity-Assist Tours. *Journal of Spacecraft and Rockets*, 51(6):1849–1856.

Hess, J. (2016). Aerogravity assists: Hypersonic maneuvering to improve planetary gravity assists. Master's thesis, Delft University of Technology, the Netherlands.

Huang, W., Ma, L., Wang, Z.-g., Pourkashanian, M., Ingham, D. B., Luo, S.-b., and Lei, J. (2011). A parametric study on the aerodynamic characteristics of a hypersonic waverider vehicle. *Acta Astronautica*, 69(3-4):135–140.

Ishibuchi, H., Akedo, N., and Nojima, Y. (2013). Relation between Neighborhood Size and MOEA/D Performance on Many-Objective Problems. In *EMO 2013: Evolutionary Multi-Criterion Optimization*, pages 459–474. Springer, Berlin, Heidelberg.

Izzo, D. and Dario (2014). Revisiting Lambert's Problem. *Celestial Mechanics and Dynamical Astronomy, Volume 121, Issue 1, pp.1-15*, 121:1–15.

Justh, H. L., Justus, C. G., Keller, V. W., Justus, C. G., and Kelle, V. W. (2006). Global Reference Atmospheric Models, including thermospheres, for Mars, Venus and Earth. In *Collection of Technical Papers - AIAA/AAS Astrodynamics Specialist Conference, 2006*, volume 2, pages 988–992, Keystone, CO.

Justh, H. L., Justus, C. G., and Ramey, H. S. (2011). The Next Generation of Mars-GRAM and Its Role in the Autonomous Aerobraking Development Plan. In *2011 AAS/AIAA Astrodynamics Specialists Conference*, Girdwood, AK. NASA Marshall Space Flight Center; Huntsville, AL, United States.

Justus, C., Duvall, A., and Johnson, D. (2004). Earth global reference atmospheric model (GRAM-99) and trace constituents. *Advances in Space Research*, 34(8):1731–1735.

Justus, C., James, B., Bougher, S., Bridger, A., Haberle, R., Murphy, J., and Engel, S. (2002). Mars-GRAM 2000: A Mars atmospheric model for engineering applications. *Advances in Space Research*, 29(2):193–202.

Laub, B. and Venkatapathy, E. (2003). Thermal Protection System Technology and Facility Needs for Demanding Future Planetary Missions. Technical report.

Leipold, M., Eiden, M., Garner, C., Herbeck, L., Kassing, D., Niederstadt, T., Krüger, T., Pagel, G., Rezazad, M., Rozemeijer, H., Seboldt, W., Schöppinger, C., Sickinger, C., and Unckenbold, W. (2003). Solar sail technology development and demonstration. *Acta Astronautica*, 52(2-6):317–326.

Lissauer, J. and de Pater, I. (2013). *Fundamental Planetary Science*. Cambridge University Press, 32 Avenue of the Americas, New York, NY 10013-2473, USA.

Lohar, F., Mateescu, D., and Misra, A. (1994). Optimal atmospheric trajectory for aero-gravity assist. *Acta Astronautica*, 32(2):89–96.

Lohar, F. A., Misra, A. K., and Mateescu, D. (1996). Optimal aero-gravity assist with heliocentric plane change. *Acta Astronautica*, 38(4-8):445–456.

Lyons, D., Sklyanskiy, E., Casoliva, J., and Wolf, A. (2008). Parametric Optimization and Guidance for an Aerogravity Assisted Atmospheric Sample Return From Mars and Venus. In *AIAA/AAS Astrodynamics Specialist Conference and Exhibit*, Reston, Virigina. American Institute of Aeronautics and Astronautics.

Mazzaracchio, A. and Marchetti, M. (2010). A probabilistic sizing tool and Monte Carlo analysis for entry vehicle ablative thermal protection systems. *Acta Astronautica*, 66(5-6):821–835.

McClinton, C. R., Rausch, V. L., Shaw, R. J., Metha, U., and Naftel, C. (2005). Hyper-X: Foundation for future hypersonic launch vehicles. *Acta Astronautica*, 57(2-8):614–622.

McRonald, A. and Randolph, J. (1990). Hypersonic maneuvering to provide planetary gravity assist. In *28th Aerospace Sciences Meeting*, Reston, Virigina. American Institute of Aeronautics and Astronautics.

Melman, J. (2007). Trajectory optimization for a mission to neptune and triton. Master's thesis, Delft University of Technology, the Netherlands.

Meseguer, J., Pérez-Grande, I., and Sanz-Andrés, A. (2012). Thermal protection systems. *Spacecraft Thermal Control*, pages 305–325.

Millour, E., Forget, F., S., A., Navarro, T., Madeleine, J.-B., Montabone, L., Lefevre, F., Chaufray, J.-Y., L.-V. M., Gonzalez-Galindo, F., Lewis, S., Read, P., Desjean, M.-C., and Huot, J.-P. (2015). The Mars Climate Database (MCD Version 5.1). In *8th International Conference on Mars*.

Montenbruck, O. and Gill, E. (2000). *Satellite Orbits: Models, Methods and Applications*. Springer-Verlag, Heidelberg, Germany, first edition.

Mooij, E. (1994). *The motion of a vehicle in a planetary atmosphere*. Delft University of Technology, Faculty of Aerospace Engineering, Report LR-768.

Moss, J. N., Blanchard, R. C., Wilmoth, R. G., and Braun, R. D. (1999). Mars Pathfinder Rarefied Aerodynamics: Computations and Measurements. *Journal of Spacecraft and Rockets*, 36(3):330–339.

Musegaas, P. (2012). Optimization of Space Trajectories Including Multiple Gravity Assists and Deep Space Maneuvers . Master's thesis, Delft University of Technology, the Netherlands.

Nonweiler, T. (1959). The Control and Stability of Hypersonic Aircraft: An Analysis of the Criteria associated with Hypersonic Flight above the Stratosphere. *Aircraft Engineering and Aerospace Technology*, 31(11):322–329.

Noomen, R. (2016). *Lecture notes Mission Geometry and Orbit Design*. Astrodynamics and Space Missions, Delft University of Technology.

Ortelt, M., Weihs, H., Fischer, I., and Dogigli, M. (2012). Thermo-Mechanical Qualification Tests of Complex CMC Re-Entry Structures. In *27th Annual Cocoa Beach Conference on Advanced Ceramics and Composites: B: Ceramic Engineering and Science Proceedings*, volume 24, pages 281–287. John Wiley & Sons, Inc.

Papp, Z. (2014). Mission Planner for Heating Optimal Re-Entry Trajectories with Extended Range Capability. Master's thesis, Delft University of Technology, the Netherlands.

Picone, J. M., Hedin, A. E., Drob, D. P., and Aikin, A. C. (2002). NRLMSISE-00 empirical model of the atmosphere: Statistical comparisons and scientific issues. *Journal of Geophysical Research: Space Physics*, 107(A12):SIA 15–1–SIA 15–16.

Porco, C. C. (2006). Cassini Observes the Active South Pole of Enceladus. *Science*, 311(5766):1393–1401.

Press, W. H., Teukolsky, A. S., Vetterling, W. T., and Flanner, B. P. (1992). *Numerical Recipes in FORTRAN: The Art of Scientific Computing*. Press Syndicate of the University of Cambridge, The Pitt Building, Trumpington Street, Cambridge CB2 1RP, first edition.

Qingfu Zhang and Hui Li (2007). MOEA/D: A Multiobjective Evolutionary Algorithm Based on Decomposition. *IEEE Transactions on Evolutionary Computation*, 11(6):712–731.

Ronse, A. L. A. B. and Mooij, E. (2014). Statistical Impact Prediction of Decaying Objects. *Journal of Spacecraft and Rockets*, 51(6):1797–1810.

Secretin, T. A. L. P. (2012). Design of a Combinatorial Tool for Preliminary Space Mission Analysis, applied to the GTOC2 Problem. Master's thesis, Delft University of Technology, the Netherlands.

Sims, J. A., Longuski, J. M., and Patel, M. R. (2000). Aerogravity-Assist Trajectories to the Outer Planets and the Effect of Drag. *Journal of Spacecraft and Rockets*, 37(1):49–55.

Spencer, D. A. and Tolson, R. (2007). Aerobraking Cost and Risk Decisions. *Journal of Spacecraft and Rockets*, 44(6):1285–1293.

Spilker, T. R. and R., T. (2005). Significant science at Titan and Neptune from aerocaptured missions. *Planetary and Space Science*, 53(5):606–616.

Starkey, R. P. and Lewis, M. J. (1999). Simple analytical model for parametric studies of hypersonic waveriders. *Journal of Spacecraft and Rockets*, 36(4):516–523.

Sutton, K. and Graves, R. A. (1971). A General Stagnation-Point Convective-Heating Equation for Arbitrary Gas Mixtures. Technical report.

Svedhem, H., Titov, D., McCoy, D., Lebreton, J.-P., Barabash, S., Bertaux, J.-L., Drossart, P., Formisano, V., Häusler, B., Korablev, O., Markiewicz, W., Nevejans, D., Pätzold, M., Piccioni, G., Zhang, T., Taylor, F., Lellouch, E., Koschny, D., Witasse, O., Eggel, H., Warhaut, M., Accomazzo, A., Rodriguez-Canabal, J., Fabrega, J., Schirmann, T., Clochet, A., and Coradini, M. (2007). Venus Express—The first European mission to Venus. *Planetary and Space Science*, 55(12):1636–1652.

Tauber, M., Bowles, J., and Yang, L. (1989). The use of atmospheric braking during Mars missions. In *24th Thermophysics Conference*, Reston, Virigina. American Institute of Aeronautics and Astronautics.

Tauber, M. and Sutton, K. (1991). Stagnation-point radiative heating relations for earth and Mars entries. *Journal of Spacecraft and Rockets*, 28(1):40–42.

Tauber, M. E., Palmer, G. E., Prabhu, D., and Corp, E. R. C. (2012). Stagnation Point Radiative Heating Relations for Venus Entry. Technical report.

Tellmann, S., Pätzold, M., Häusler, B., Bird, M. K., and Tyler, G. L. (2009). Structure of the Venus neutral atmosphere as observed by the Radio Science experiment VeRa on Venus Express. *Journal of Geophysical Research*, 114(E9):E00B36.

Tincher, D. J. and Burnett, D. W. (1994). Hypersonic waverider test vehicle - A logical next step. *Journal of Spacecraft and Rockets*, 31(3):392–399.

Turchi, A., Congedo, P. M., and Magin, T. E. (2017). Thermochemical ablation modeling forward uncertainty analysis—Part I: Numerical methods and effect of model parameters. *International Journal of Thermal Sciences*.

Vasile, M. and Pascale, P. D. (2006). Preliminary Design of Multiple Gravity-Assist Trajectories. *Journal of Spacecraft and Rockets*, 43(4):794–805.

Venkatapathy, E., Szalai, C. E., Laub, B., Hwang, H. H., Conley, J. L., and Arnold, J. (2010). White Paper: Thermal Protection System Technologies for Enabling Future Sample Return Missions. Technical report, NASA Ames Research Center.

Villefranche, P., Evans, J., and Faye, F. (1997). Rosetta: The ESA comet rendezvous mission. *Acta Astronautica*, 40(12):871–877.

Voland, R. T., Huebner, L. D., and McClinton, C. R. (2006). X-43A Hypersonic vehicle technology development. *Acta Astronautica*, 59(1-5):181–191.

Wakker, K. (2015). *Fundamentals of Astrodynamics*. Delft University of Technology, Delft, The Netherlands.

Walker, S. H. (2008). The DARPA/AF Falcon Program: The Hypersonic Technology Vehicle #2 (HTV-2) Flight Demonstration Phase. In *15th AIAA International Space Planes and Hypersonic Systems and Technologies Conference*, Dayton, Ohio. American Institute of Aeronautics and Astronautics.

Wright, M. J., Bose, D., and Chen, Y.-K. (2007). Probabilistic Modeling of Aerothermal and Thermal Protection Material Response Uncertainties. *AIAA Journal*, 45(2):399–410.

Zitzler, E., Deb, K., and Thiele, L. (2000). Comparison of Multiobjective Evolutionary Algorithms: Empirical Results. *Evolutionary Computation*, 8(2):173–195.